UNIVERSIDAD COMPLUTENSE DE MADRID
FACULTAD DE CIENCIAS MATEMÁTICAS
DEPARTAMENTO DE MATEMÁTICA APLICADA

MATHEMATICAL MODELS IN FOOD ENGINEERING
MODELOS MATEMÁTICOS EN PROBLEMAS DE LA INDUSTRIA ALIMENTARIA

TESIS DOCTORAL DE:

NADIA ALEXANDRA SOFIA SMITH

BAJO LA DIRECCIÓN DE:

ÁNGEL MANUEL RAMOS DEL OLMO

Madrid, 2013

UNIVERSIDAD COMPLUTENSE DE MADRID

FACULTAD DE CIENCIAS MATEMÁTICAS

Departamento de Matemática Aplicada

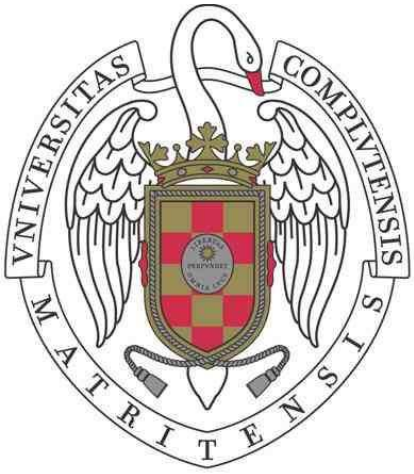

Mathematical Models in Food Engineering

Modelos Matemáticos en Problemas de la Industria Alimentaria

Tesis doctoral realizada por:

Nadia Alexandra Sofia Smith

Bajo la dirección de:

Ángel Manuel Ramos del Olmo

Madrid, 1 de febrero de 2013

To my family

Acknowledgements

En primer lugar quiero dar las gracias a mi director de tesis, Ángel Manuel Ramos, por toda su ayuda y dedicación durante estos años. Gracias por tus sabios consejos, y detalladas correcciones, por tu implicación y el tiempo que has invertido en los resultados presentados en esta memoria. Gracias por tu paciencia, y, sobre todo, por la confianza que has depositado en mí en los momentos más difíciles. Gracias por animarme en los primeros años, y en los últimos por apoyarme, a viajar a conferencias y cursos, y hacer estancias en otras universidades. Creo que esto ha sido muy enriquecedor para mí, tanto profesional como personalmente.

También quiero expresar mi agradecimiento a otros profesores e investigadores que han hecho valiosas aportaciones a este trabajo: a Benjamin Ivorra por su gran ayuda con COMSOL, sin la cual en muchos casos no habría sabido avanzar; a Gerardo Oleaga por todo el tiempo que invirtió hace unos años en enseñarme a resolver un problema de elementos finitos en Matlab; a Juan-Antonio Infante por su sugerencia acertada de hacer mi tesis con Ángel, por sus acertadas palabras hace años avisándome de que esto no iba a ser un camino fácil, y por su ayuda (ya fuese académica o personal) en numerosas ocasiones; a nuestros colaboradores del Instituto de Ciencia y Tecnología de Alimentos y Nutrición del CSIC (Pedro Sanz, Laura Otero, etc.) por las veces en las que me han atendido allí para enseñarme los experimentos que llevan a cabo, y por los datos experimentales proporcionados.

I would like to thank all my external collaborators without whom a lot of this work would not have been possible: Sarah Mitchell from University of Limerick, Kai Knoerzer from CSIRO, Stephen Peppin and Victor Burlakov from University of Oxford. In particular, a special thanks to Sarah for helping me in a very critical moment, making me enjoy some fun Maths and see the end was in sight.

A mis compañeros de despacho con los que he pasado tantos años, gracias por hacer este camino más llevadero. En especial a Luis, Silvia y Edwin, gracias por tantos buenos ratos tomando café, desahogando nuestras penas y compartiendo nuestras buenas experiencias.

Gracias a mis amigos de la carrera de matemáticas que siempre han estado apoyándome desde fuera, y a los que he echado de menos en muchas ocasiones en la facultad desde que terminamos. A mis amigas de toda la vida Bea, Vicky y Marta por siempre estar ahí y todos los buenos ratos juntas. A Irene por su confianza en mí y todas nuestros paseos juntas, que me han servido siempre de desahogo. A mis amigas de la Escolanía, que pase el tiempo que pase siempre sé que todo sigue igual.

I would like to thank my family for making my life so interesting and so much fun: my parents and their partners (Sonia and Hampaté) for their blind trust in me (special thanks to my Mum for her advice of putting work under the pillow and going to sleep); a mi hermana Rosanna también por su confianza ciega y apoyo (aunque a veces tenga que ser por Skype desde Australia); a Fran, Nico y Martina, porque me alegran la vida; my Aunt Marianne for all her support and enthusiasm; Granny for giving me that mathematical gene, for all her love and interest towards me; to Ronnie, who I wish could be here to see this work finished. Finally, to Mark: thank you for all of your mathematical help (which has been very important in crucial moments), but mainly for making my life so much better. I am very lucky to have you and very happy and excited about our future together.

Contents

List of Figures

Chapter 1

Introduction

There has been significant interest in the study of food engineering from the mid-twentieth century onwards [12, 13, 31, 43, 53, 63, 71, 74, 80, 82, 92]. Humans have been interested in food conservation since ancient times, using traditional techniques such as desiccation, conservation in oil, salting, smoking, cooling, etc. Due to the massive movement of populations to cities, a great supply of food in adequate conditions was necessary. Therefore, the food industry was developed in order to guarantee large-scale food techniques, to prolong its shelf life, and to make logistic aspects such as transport, distribution and storage, easier. Nowadays, the food industry is an increasingly competitive and dynamic arena, given that consumers are now more aware of what they eat. Food quality properties, such as taste, texture, appearance, and nutritional content are strongly dependent on the way the foods are processed [53].

Many classical industrial processes are based on thermal treatments, such as, for example, pasteurisation, sterilisation and freezing. In recent years, with the aim to improve these conventional processing technologies, in order to deliver higher-quality and better food products for the consumers, a number of innovative technologies, also referred to as "emerging" or "novel" technologies have been proposed, investigated, developed, and in some cases, implemented. These "emerging" technologies take advantage of other physics phenomena such as high hydrostatic pressure, electric and electromagnetic fields, and pressure waves. With these innovative technologies food engineers can not only develop new food products, but also improve the safety and quality of conventionally treated food through milder processing. When dealing with innovative processing technologies, several issues from concept development to implementation need addressing. In particular, proper application, development, and optimisation of suitable equipment and process conditions require a significant amount of further knowledge and understanding [53].

Innovative technologies provide additional complexity and challenges for modellers because of the interacting multiphysics phenomena. So no longer is there only the thermo- and fluid-dynamic principles of conventional processing, but these innovative technologies also incorporate additional multiphysics dimensions, for example, pressure, electric and electromagnetic fields, among others. To date, some of them still lack an adequate, complete understanding of the basic principles intervening in product and equipment during processing. Proper application of these technologies, development and optimisation of suitable equipment and process conditions, still require a significant amount of further knowledge [53].

The goal to achieve uniformity of each treatment is common to all innovative processing technologies. This goal can be already an issue at laboratory scale, and it can become progressively worse when scaling up to pilot plants and, subsequently, to commercial equipment. However, non-uniformity of the treatment is very commonly encountered. In fact, the non-uniformities of the process and the lack of process validation of innovative processes are the greatest limitations for industrial uptake [53].

We will see in Section 1.2, and afterwards throughout the thesis, that mathematical modelling is a very useful tool for characterising, improving, and optimising innovative food processing technologies. In particular, in this thesis we are going to focus only on processes that are based on High Hydrostatic Pressure. In Section 1.1 we describe the main features of these type of processes and give a brief overview of their benefits and advantages

List of Tables

over traditional technologies.

1.1 High Pressure Processing of Food

The appearance of High Pressure Processing (HPP) as a tool in the food industry started in the late 1980s [41]. Since then to date, extensive research has been done on possible application of HPP as a preservation method [12, 28], to change the physical and functional properties of food systems [11, 41] and to take advantage of the phase diagram of water: freezing, thawing and sub-zero temperature non-frozen storage under pressure [68, 71].

Nowadays, more than 70 companies are using HPP, producing more than 170,000 tons of products [53]. Several HPP-treated food products, including juices, jams, jellies, yogurts, ready-to-eat meat, and oysters, are already widely available in the United States, Europe, Japan, New Zealand, and Australia. These successful applications have led to a pronounced increase in commercial-scale HPP units around the world during the past 10 years [53].

Several studies [12, 13, 82] have proved that HPP at refrigeration, ambient or moderate heating temperature allows inactivation[1] of enzymes and pathogenic and spoilage microorganisms in food, while leaving small molecules intact, and therefore not modifying significantly the organoleptic properties (such as colour, odour, texture and flavour).

Two principles underlie the effect of High Pressure (HP): firstly, the Le Chatelier Principle, according to which any phenomenon (phase transition, chemical reaction, chemical reactivity, change in molecular configuration) accompanied by a decrease in volume will be enhanced by pressure; secondly, pressure is instantaneously and uniformly transmitted independently of the size and the geometry of the food (isostatic pressure). Unlike thermal processing and other classical conservation methods, HP effects are uniform and nearly instantaneous throughout the food and thus independent of food geometry and equipment size, which has facilitated the expansion from laboratory findings to full-scale production [89].

Thermal processing is the prevailing method to achieve microbial stability and safety, and although due to the isostatic principle, HPP has a great advantage as compared to thermal processing, HPP does not escape the classical limitations, imposed by heat transfer. Heat transfer characterises every process, accompanied by a period of pressure increase or decrease, which is associated with a proportional temperature change of the vessel's contents due to adiabatic heating. The magnitude of the adiabatic temperature increase or decrease depends on a number of factors, such as the food product thermo-physical properties (density, thermal expansion coefficient, and specific heat capacity) and initial temperature, as will be seen in further chapters. Heat transfer is caused by the resulting temperature gradients and can lead to large temperature differences, especially in large-volume industrial vessels. For a number of HP applications to food engineering, these limitations should be taken into account, trying to avoid as much as possible, non-uniformity at the end of the process.

According to [53], there are two approaches to achieve HP conditions: a direct approach, where a piston is used, which compresses the content of the HP chamber; and an indirect approach, where pressure-transmitting liquid (e.g., water) is pumped into the HP vessel using a HP pump followed by a "pressure intensifier". Liquids at extremely high pressures are compressible, requiring extra fluid to be pumped into the vessel. For all the models described throughout this thesis, we will assume that the HP has been achieved by the indirect method, as will be seen in Chapters 4, 5 and 6.

In general, a "conventional" batch HP process consists of a period of pressure build-up, followed by a period at constant pressure (holding time) and a period of pressure release. The holding time of a food product depends on the effectiveness of the treatment and the desired remaining level of the critical safety-, or quality-, related factor. It is agreed that, because of the extreme baroresistance of bacterial spores and some enzymes, HPP will most likely be accompanied by mild to high heating, or other treatments [21, 53]. In cases where HP is combined with elevated temperatures to minimise the pressure resistance of that safety-, or quality-, related aspect, the non-uniform temperature distribution, resulting from heat transfer generated at pressure build-up, will lead to a non-uniform distribution of the desired effect (inactivation of microorganisms, enzymes, etc.)

[1] Inactivation may be defined as the reduction of undesired biological activity, such as enzymatic catalysis and microbial contamination.

within the product. Depending on the temperature-pressure degradation kinetics of the component that is under study, this non-uniformity will be more or less pronounced. Especially in heterogeneous food materials, with the contents exhibiting differences in compression heating, the temperatures may not be equally distributed in the food products. Furthermore, the packaging material, the material of the product carrier, and the steel of the HP vessel are not heated to the same extent as the food; therefore, temperature gradients are developed throughout the system, leading to heat flux from the products to the cooler areas. These spatial temperature heterogeneities increase over the process time. Although, theoretically, the preheated product heats up uniformly during compression to sterilisation temperatures, during pressure holding time temperatures may decrease in certain areas of the vessel. This can affect enzymatic or spore inactivation, and some spores may survive the process if temperature loss is not prevented.

Therefore, an accurate evaluation of the effects of pressure, applied during conventional batch HPP, requires consideration of the phenomenon above described. If the non-uniform temperature distribution appearing during the process is taken into account, it can be assured that the objective of the process has been accomplished everywhere within the food product. With this in mind, equations describing the time-temperature-pressure history of a product must be coupled with the parameters describing the reaction kinetics for destruction of microorganisms, enzymes, and other factors. The optimisation of batch HP processes for nutrient retention should also be based on this approach.

Multiphysics modelling can help greatly in the characterisation of time-temperature-pressure distribution, subsequent microbial distributions, and other quality changes as a result of temperature inhomogeneities. These models can also be applied to the redesign and optimisation of equipment and determination of adequate processing conditions for optimum process/product performance.

1.2 Mathematical modelling of High-Pressure Processes

Mathematical modelling is a very useful tool for studying the effect of different systems and process parameters on the outcome of a process. Normally, it is the fastest and least expensive way, given that it minimises the number of experiments that need to be conducted to determine the influence of several parameters on the quality and safety of the process [24].

As previously discussed, most of HP applications in food are not only pressure dependent but also temperature dependent. This temperature evolution is very important to assure an uniform distribution of the pursued pressure effect (microbial and/or enzyme inactivation, etc.); also because some industrial processes must take place at a constant temperature or in a maximum-minimum threshold to avoid altering properties of the food (e.g. gelification or crystalline state, protein stability, fat migration, freezing, etc.) [71]. As pointed out in [20], from an engineering point of view, a theoretically based heat transfer model that allows predicting the temperature history within a product under pressure would be essential to homogenise and optimise HP processes (design of industrial processes and equipment as well as the quality of the end product).

Depending on the characteristics of the process, the type of food (liquid or solid), the dimensions of the HP vessel, the process conditions (initial temperature, maximum pressure, etc.), different mathematical models will be used. For example, for a large (when comparing with the pressurizing volume) solid-type food a heat transfer model with only conduction effects is sufficient [46, 69], whereas for a liquid-type food, convection effects have to also be included, and therefore equations that model the fluid flow also have to be coupled with the heat transfer equation. If we are studying HP freezing processes, a model that takes into account solidification also has to be considered. In some cases, the expression of the process outcome based on the attributes of the processed food, that is, e.g. the remaining microbial load, enzyme activity, and chemical reaction products, is required. Within multiphysics modelling, reaction kinetics (i.e., microbial inactivation, quality degradation, chemical reaction, and structural responses) can be coupled with the specific differential equations to provide the spatial distributions of reaction response.

Securing temperature uniformity in HP processed products is crucial for assuring uniform distribution of the pursued pressure effects (e.g. microbial and enzyme inactivation, as we will see in Chapter 2), and the prediction of thermal history within a product under pressure is essential for optimising and homogenising HP process. For this reason, research has focused on heat transfer models that simulate the combination of HP and thermal

treatments on food products [71]. Out of many works we highlight the following (references to more of these kind of models can be found in [18, 71]): Denys et al. [19, 21] suggest a numerical approach for modelling conductive heat transfer during batch HP processing of solid-type food products. The authors showed experimentally that non-uniform temperature distribution during HP processing of foods involved a non-uniform enzymatic inactivation. The proposed numerical model could accurately describe the conductive heat transfer during different, but fluid dynamics phenomena in the pressure medium were not included. In [36, 37] the authors analysed the thermodynamic and fluid-dynamic effects of HP treatments of liquid-type food systems by numerical simulation. The authors studied the spatial and temporal evolution of temperature and fluid velocity fields. They proved that the uniformity of a HP effect can be disturbed by convective and conductive heat and mass transport conditions that are affected by parameters such as the compression rate, the size of the pressure chamber or the solvent viscosity. In [69] a mathematical model describing the phenomena of heat and mass transfer taking place during the HP treatment of solid foods is obtained, showing the importance of including convection effects in some cases. In [46] the temperature distribution is analysed and used as an input for the inactivation of certain enzymes, for both solid- and liquid-type foods, and the behaviour and stability of the proposed models are checked by various numerical examples. Furthermore, various simplified versions of these models are discussed, showing accurate enough results when compared to the original models. Knoerzer *et al.* [52] considered a model that predicted flow and temperature fields inside a pilot-scale vessel during the pressure heating, holding and cooling stages. The model agreed well with experimental results in which thermocouples were used to measure temperature throughout a metallic composite carrier inserted into the vessel. Smith *et al.* [86] presented a generalised enthalpy model for a HP Shift Freezing process based on volume fractions dependent on temperature and pressure. The model included the effects of pressure on conservation of enthalpy and incorporates the freezing point depression of non-dilute food samples. In addition the significant heat transfer effects of convection in the pressurizing medium are accounted for by solving the two-dimensional Navier-Stokes equations.

Even though there has already been a significant amount of research in this area, there are still many situations that arise in HPP that have not been modelled. Therefore, throughout this thesis we have considered different types of HP processes, trying to cover as many situations as possible when working with HP food processing, presenting innovative models. Namely, models for large and small, solid and liquid type foods, for vertically and horizontally oriented machines, and also for HP freezing processes are analysed. We have developed the corresponding model for each case, solving each one accordingly. Because every Chapter deals with a different kind of process, a brief literature review for each of them is given, when relevant, in their individual Chapters.

In Chapter 2 we first start by presenting a model for bacterial and enzymatic inactivation, hence showing the necessity for knowing the temperature distribution throughout a HP process. A case study of one particular bacteria, for which experimental data is available, is modelled and validated.

In Chapter 3 we present the general aspects of the heat and mass transfer models for HP processes developed in [46, 69]. The new models we derived in Chapters 4, 5 and 6 are based on this one, and thus we decided to include this model-presentation chapter to avoid having to introduce the same model in each of the later ones.

In Chapter 4 we introduce one of the most basic type of model for time-temperature-pressure evolution, considering large samples of solid-type foods in a vertically oriented machine. With these, only conduction effects have to be included in the heat transfer model, which makes its resolution easier, and in some cases may even be possible to solve analytically. For vertically oriented machines, a reduction from three to two dimensions is possible due to the axis-symmetric geometry. Thus, in Chapter 4 several two dimensional models, with different kind of boundary conditions, are solved analytically and then compared to simplified versions. Also, some of the heat transfer models considered in this Chapter are coupled with an enzymatic inactivation model, showing how this coupling can be done. To date most of the published heat transfer models for solid-type foods had been solved numerically and not analytically.

In Chapter 5 a more complex problem is discussed. We consider liquid-type foods, for which convection effects also have to be included into the heat transfer model. Therefore, the equations for fluid flow (Navier–Stokes equations) have to be also solved. Due to the complexity, analytical solutions are no longer available and the model has to be solved numerically. An added complication to the problem in this Chapter is that we model processes and liquid-type foods placed in both vertically and horizontally oriented HP vessels. For the vertically oriented HP vessel we could reduce it to two dimensions, due to the axis-symmetry. However for the horizontally

oriented, there are no longer axis-symmetric features and a three dimensional model is necessary, adding an extra challenge to the numerical model. The differences between models have been analysed. Developing a model for a horizontally oriented HP vessel is interesting from an industrial point of view, as most of the industrial-scale vessels are in that position [63]. However, at a pilot-scale, they are vertically oriented and therefore most of the published research has been focused on these kind of machines, and the models are usually solved in two dimensions.

In Chapter 6 a freezing process that benefits from HP, namely a High-Pressure Shift Freezing (HPSF) process, is described, modelled and solved numerically. Modelling conventional solidification problems is not an easy task, and a lot of interest and research has been put into this area. HP freezing problems, however, have not been as studied, and in this Chapter we present a generalised enthalpy model for a HPSF process. The model can be used for large (when compared to the pressurising fluid volume) solid-type food (only conduction effects included) and also for small (when compared to the pressurising fluid volume) solid-type food (where the significant heat transfer effects of convection in the pressurizing medium are accounted for by solving the Navier–Stokes equations). The model is run for several numerical tests, and good agreement with experimental data from the literature is found.

The analysis in Chapter 6 shows that HPSF is more beneficial for ice crystal size and shape than traditional (at atmospheric pressure) freezing. This motivates the work in Chapter 7, which differs from previous Chapters as we do not solve a model to find the temperature distribution inside a food sample undergoing a HP process. A model for growth and coarsening of ice crystals inside a frozen food sample is developed and some numerical experiments are given, with which the model is validated by using experimental data. To the best of our knowledge this is the first model suited for freezing crystallisation in the context of HP.

In Chapter 8 the final conclusions and possible extensions of the presented work are outlined, and in Chapters 9 and 10 brief summary in English and Spanish, respectively, of the thesis is given.

Chapter 2

Motivation: Effects of High-Pressure on enzymes and microorganisms related to food conservation

Nomenclature for Chapter 2

A	Enzymatic activity
B	Kinetic parameter (K)
C	Kinetic parameter (MPa^{-1})
C_p	Specific heat capacity (J mol^{-1} K^{-1})
D	Decimal reduction time (min)
E_a	Activation energy (J mol^{-1})
n	Number of log-cycles (constant)
N	Microbial population (cfu g^{-1})
P	Pressure (MPa)
r	Linear regression coefficient (constant)
R	Universal gas constant (cm^3 MPa mol^{-1} K^{-1})
S	Entropy (J mol^{-1} K^{-1})
t	Time (min)
T	Temperature (K)
V	Volume (cm^3)
$\bar{x}$	x-component of centre of gravity
$\bar{y}$	y-component of centre of gravity
z	Pressure resistant coefficient (MPa)

Acronyms

HP	High Pressure

Greek symbols

$\Delta\nu$	Compressibility factor (cm^3 mol^{-1})
$\Delta\zeta$	Thermal expansibility (cm^3 mol^{-1} K^{-1})
ΔV^*	Volume of activation (cm^3 mol^{-1})
κ	Inactivation rate (min^{-1})

Indices

0	Initial
ref	Reference

As explained in Chapter 1, some studies [12, 82] have proven that HP causes inactivation of enzymes and microorganisms in food. The efficiency of a HP treatment on inactivation depends on several parameters [13, 82] such as the type of microorganism or enzyme under study, the physiological state of the microorganism (e.g. exponentially growing state, stationary state, frozen, etc.), the pressure applied, the temperature, the processing time, the pH of the sample and the composition of the food or the dispersion medium.

Let us review some of the general concepts that we mention in this Chapter, following the Encyclopedia Britannica:

Enzymes: Enzymes are large protein molecules that act as biological catalysts, accelerating chemical reactions without being consumed to any appreciable extent themselves. The activity of enzymes is specific for a certain set of chemical substrates, and it is dependent on both pH and temperature.

The living tissues of plants and animals maintain a balance of enzymatic activity. This balance is disrupted upon harvest or slaughter. In some cases, enzymes that play a useful role in living tissues may catalyze

spoilage reactions following harvest or slaughter. For example, the enzyme pepsin is found in the stomach of all animals and is involved in the breakdown of proteins during the normal digestion process. However, soon after the slaughter of an animal, pepsin begins to break down the proteins of the organs, weakening the tissues and making them more susceptible to microbial contamination. After the harvesting of fruits, certain enzymes remain active within the cells of the plant tissues. These enzymes continue to catalyze the biochemical processes of ripening and may eventually lead to rotting, as can be observed in bananas. In addition, oxidative enzymes in fruits continue to carry out cellular respiration (the process of using oxygen to metabolise glucose for energy). This continued respiration decreases the shelf life of fresh fruits and may lead to spoilage. Respiration may be controlled by refrigerated storage or modified-atmosphere packaging.

Microorganism: Microorganisms are a collection of organisms that share the characteristic of being visible only with a microscope. They constitute the subject matter of microbiology. Microorganism is a general term that becomes more understandable if it is divided into its principal types - bacteria, yeasts, molds, protozoa, algae, and rickettsia-predominantly unicellular microbes. Viruses are also included, although they cannot live or reproduce on their own. They are particles, not cells; they consist of deoxyribonucleic acid (DNA) or ribonucleic acid (RNA), but not both. Viruses invade living cells - bacteria, algae, fungi, protozoa, plants, and animals (including humans) - and use their hosts' metabolic and genetic machinery to produce thousands of new virus particles. Some viruses can transform normal cells to cancer cells. Rickettsias and chlamydiae are very small cells that can grow and multiply only inside other living cells. Although bacteria, actinomycetes, yeasts, and molds are cells that must be magnified in order to see them, when cultured on solid media that allow their growth and multiplication, they form visible colonies consisting of millions of cells.

Bacteria and fungi (yeasts and molds) are the principal types of microorganisms that cause food spoilage and food - borne illnesses. Foods may be contaminated by microorganisms at any time during harvest, storage, processing, distribution, handling, or preparation. The primary sources of microbial contamination are soil, air, animal feed, animal hides and intestines, plant surfaces, sewage, and food processing machinery or utensils.

Bacteria: Bacteria are unicellular organisms that have a simple internal structure compared with the cells of other organisms. The increase in the number of bacteria in a population is commonly referred to as bacterial growth by microbiologists. This growth is the result of the division of one bacterial cell into two identical bacterial cells, a process called binary fission. Under optimal growth conditions, a bacterial cell may divide approximately every 20 minutes. Thus, a single cell can produce almost 70 billion cells in 12 hours. The factors that influence the growth of bacteria include nutrient availability, moisture, pH, oxygen levels, and the presence or absence of inhibiting substances (e.g., antibiotics).

The nutritional requirements of most bacteria are chemical elements such as carbon, hydrogen, oxygen, nitrogen, phosphorus, sulfur, magnesium, potassium, sodium, calcium, and iron. The bacteria obtain these elements by utilizing gases in the atmosphere and by metabolizing certain food constituents such as carbohydrates and proteins.

Temperature and pH play a significant role in controlling the growth rates of bacteria. Bacteria may be classified into three groups based on their temperature requirement for optimal growth: thermophiles (55°C-75°C), mesophiles (20°C-45°C), or psychrotrophs (10°C-20°C). In addition, most bacteria grow best in a neutral environment (pH equal to 7).

Bacteria also require a certain amount of available water for their growth. The availability of water is expressed as water activity and is defined by the ratio of the vapour pressure of water in the food to the vapour pressure of pure water at a specific temperature. Therefore, the water activity of any food product is always a value between 0 and 1, with 0 representing an absence of water and 1 representing pure water. Most bacteria do not grow in foods with a water activity below 0.91, although some halophilic bacteria (those able to tolerate high salt concentrations) can grow in foods with a water activity lower than 0.75. Growth may be controlled by lowering the water activity - either by adding solutes such as sugar, glycerol, and salt or by removing water through dehydration.

The oxygen requirements for optimal growth vary considerably for different bacteria. Some bacteria require the presence of free oxygen for growth and are called obligate aerobes, whereas other bacteria are poisoned by the presence of oxygen and are called obligate anaerobes. Facultative anaerobes are bacteria that can grow in both the presence or absence of oxygen. In addition to oxygen concentration, the oxygen reduction potential

of the growth medium influences bacterial growth. The oxygen reduction potential is a relative measure of the oxidizing or reducing capacity of the growth medium.

When bacteria contaminate a food substrate, it takes some time before they start growing. This lag phase is the period when the bacteria are adjusting to the environment. Following the lag phase is the log phase, in which population grows in a logarithmic fashion. As the population grows, the bacteria consume available nutrients and produce waste products. When the nutrient supply is depleted, the growth rate enters a stationary phase in which the number of viable bacteria cells remains the same. During the stationary phase, the rate of bacterial cell growth is equal to the rate of bacterial cell death. When the rate of cell death becomes greater than the rate of cell growth, the population enters the decline phase.

When the conditions for bacterial cell growth are unfavourable (e.g., low or high temperatures or low moisture content), several species of bacteria can produce resistant cells called endospores. Endospores are highly resistant to heat, chemicals, desiccation (drying out), and ultraviolet light. The endospores may remain dormant for long periods of time. When conditions become favourable for growth (e.g., thawing of meats), the endospores germinate and produce viable cells that can begin exponential growth.

After reviewing the general concepts, in Section 2.1 we study a particular case of inactivation of the bacteria *Listeria monocytogenes* inoculated in raw minced ham, based on the experimental results described in [33]. This work was presented as a technical report (see [76]) to Esteban Espuña, S.A.

The methodology followed in Section 2.1 is valid not only for *Listeria monocytogenes*, which we use here as a practical real-life application, but for many other microorganisms or enzymes. One just needs to follow a similar approach to the one explained here, but with data corresponding to the new microorganism or enzyme. In Section 2.2 we present a generalised model for microbial or enzymatic inactivation for a more general process and/or microorganism or enzyme.

2.1 A case study: Inactivation of *Listeria monocytogenes* inoculated in minced raw ham

Let us start by reviewing what *Listeria monocytogenes* is:

Listeria monocytogenes: (source: [1, 3, 31]) These are the bacteria that cause the infection listeriosis. It is a facultative anaerobic bacterium, capable of growing and reproducing inside the host's cells, and is one of the most virulent food-borne pathogens, with 20 to 30 percent of clinical infections resulting in death. L. monocytogenes is a Gram-positive bacterium, motile via flagella at 30°C and below, but usually not at 37°C. L. monocytogenes can instead move within eukaryotic cells by explosive polymerisation of actin filaments (known as comet tails or actin rockets). It can survive in extreme conditions for long periods of time. It can reproduce in refrigerated foods, which increases risk during storage.

The bacterium has been isolated from humans and from more than 50 species of wild and domestic animals, including mammals, birds, fish, crustaceans, and ticks. It has also been isolated from environmental sources such as animal silage, soil, plants, sewage, and stream water. It has been found in milk, cheese, raw meat and sea food.

By using experimental data provided in [33] we want to build a mathematical model that allows us to predict the value of the microbial population N of a sample after going through a HP process. In [33] the population of *Listeria monocytogenes* is measured in cfu g^{-1}.[1]

The inoculation medium of the bacteria, together with the pressure, temperature and time of the process, are decisive factors for characterising the inactivation process. Due to data limitation we will not be able to include the dependence of the inoculation medium, as we only have results from test performed on *Listeria* strains

[1] In microbiology, colony-forming unit (CFU) is an estimate of viable bacterial or fungal numbers. Unlike direct microscopic counts where all cells, dead and living, are counted, CFU estimates viable cells. The appearance of a visible colony requires significant growth of the initial cells plated - at the time of counting the colonies it is not possible to determine if the colony arose from one cell or 1000 cells. Therefore, the results are given as CFU/mL (colony-forming units per milliliter) for liquids, and CFU/g (colony-forming units per gram) for solids to reflect this uncertainty (rather than cells/mL or cells/g).

inoculated in raw minced ham. The dependence of the inactivation of *Listeria* on the medium is discussed in [22, 31].

With these data the temperature dependence could not be included either as all experiments were performed at the same temperature ($T = 25°\text{C}$). In [31] this dependence is studied.

We will therefore start by finding a formula for microbial population $N(t)$ as a function of time, and then include the pressure dependence, giving the microbial population $N(t; P)$ as a function of time and pressure. The procedure that we follow is:

1. Experimental observation
2. Mathematical modelling
3. Identify kinetic parameters
4. Validation of model with data

2.1.1 Modelling of the population $N(t)$ for a fixed pressure P and temperature T

Experimental observation

HP processes are run on three different strains of *Listeria monocytogenes* (Lm. 1, Lm. 2, Lm. 17) isolated from raw ham and inoculated in minced raw ham (with water activity $A_w = 0.90$). The results of the tests (data obtained from [33]) are recorded into a table of values $(t_i, \log(N(t_i)))$ where t_i is the time (min) and $N(t_i)$ the bacterial population at time t_i (cfu g^{-1}).

Mathematical modelling

For a fixed temperature T and pressure P, experimental values $(t_i, \log(N(t_i)))$ decrease in a linear way, hence we use a first order mathematical model given by (see, e.g., [22, 27, 43, 92])

$$\begin{cases} \dfrac{\mathrm{d}N(t)}{\mathrm{d}t} = -\kappa N(t), \quad t \geq 0, \\ N(0) = N_0, \end{cases} \tag{2.1}$$

where t is the elapsed process time (min), $N(t)$, N_0 (cfu g^{-1}) are the bacterial population at time t and at the start, respectively, and κ (min^{-1}) is the kinetic inactivation rate constant or death velocity constant.

The solution to (2.1) is given by

$$\ln\left(\frac{N(t)}{N_0}\right) = -\kappa t \quad \text{or, equivalently,} \quad N(t) = N_0 \exp(-\kappa t). \tag{2.2}$$

In Food Engineering, it is common to use the concept of decimal reduction time (see [22]), D, which is defined as the time required to kill 90% of the microorganisms being studied.

Remark 1. In the literature (see, e.g., [31, 81]) D is also defined as the time required for the microorganisms to reduce by one log-cycle, which is equivalent to reduce them by 90% (i.e. $N(t) = \frac{N_0}{10}$). Hence if we need the population to reduce by n-log-cycles (i.e. $N(t) = \frac{N_0}{10^n}$) the processing time should be at least nD min.

For industrial food processes, it is usual to study 5-log-cycles reductions (see [33, 49, 77]), which is equivalent to having a processing time of at least $5D$ min.

From (2.2)

$$\log\left(\frac{N(t)}{N_0}\right) = \log(\exp(-\kappa t)) = -\kappa t \log(e) = -\kappa t \frac{\ln(e)}{\ln(10)} = \frac{-\kappa t}{\ln(10)}. \tag{2.3}$$

As D is the time required for $N(t) = \frac{N_0}{10}$, it holds that

$$D = \frac{\ln(10)}{\kappa} \log\left(\frac{N_0}{\frac{N_0}{10}}\right) = \frac{\ln(10)}{\kappa}, \tag{2.4}$$

leading to the relation between the decimal reduction time, D, and the kinetic inactivation rate constant, κ.

From (2.3) and (2.4), the process elapsed time can be expressed as

$$t = D \log\left(\frac{N_0}{N(t)}\right), \qquad \text{or, equivalently,} \qquad \log\left(\frac{N(t)}{N_0}\right) = -\frac{t}{D}. \tag{2.5}$$

Identify kinetic parameters

We are going to work with the solution given by the form of (2.5), and thus the kinetic parameter we need to identify is the decimal reduction time, D. This will allow us to predict the bacterial population after a process at fixed temperature T and pressure P, at an arbitrary time chosen by the model user.

To identify the value of D we use the experimental values and plot a scatter graph. The model validation carried out in the next step shows that the scattered points will be very close to a straight line with a negative slope. In this case, according to (2.5), the value of the slope is $\frac{-1}{D}$. To identify D we find the linear regression line by linear regression techniques.

Validation of model with data

We need to validate that the first order model together with the identified D, is good enough. To do so we build a table with the values of D calculated by linear regression, and check that, for each identified value of D (which depends on pressure, temperature and the *Listeria* strain we are analysing) provides a good approximation of the experimental results for bacterial population $N(t)$ at certain times t. Figures 2.1a, 2.1b, 2.1c and 2.1d

Trial	D(min)	r
1st	1.2778	0.9770
2nd	1.3769	0.9818
3rd	1.4172	0.9469
D(mean)	**1.3573**	

Lm1. $P = 600$ MPa

Trial	D(min)	r
1st	1.4511	0.9874
2nd	1.4505	0.9779
3rd	1.5285	0.9314
D(mean)	**1.4767**	

Lm12. $P = 600$ MPa

Trial	D(min)	r
1st	1.4799	0.99
2nd	1.5267	0.9817
3rd	1.4422	0.9772
D(mean)	**1.4829**	

Lm17. $P = 600$ MPa

Trial	D(min)	r
1st	4.6558	0.99
2nd	4.3791	0.9749
3rd	4.7603	0.9794
D(mean)	**4.5984**	

Lm17. $P = 500$ MPa

Table 2.1: Linear regression results for different strains of *Listeria monocytogenes*. D: decimal reduction time. r: regression coefficient. $T = 25°$C (fixed). Data source: [33]

show the experimental bacterial population ($*$) as a function of time for different trials, run on different strains of *Listeria*, at different pressures and a fixed temperature $T = 25°$C. The straight lines in the figures are the correspondent regression lines. Table 2.1 gives the predicted D values and the regression coefficient r, showing that the regression is good enough for each D calculated.

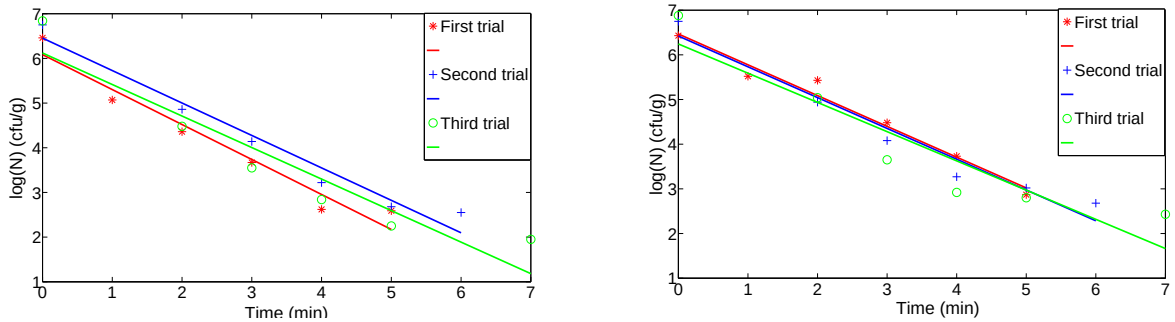

(a) Strain Lm.1. $P = 600$MPa

(b) Strain Lm.12 $P = 600$MPa

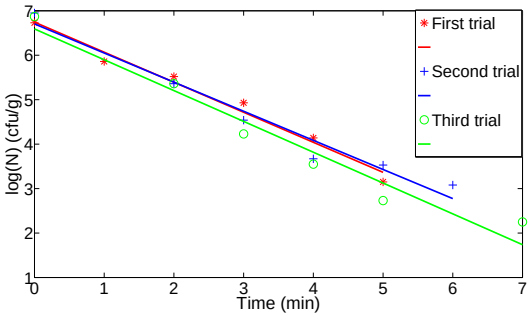

(c) Strain Lm.17 $P = 600$MPa

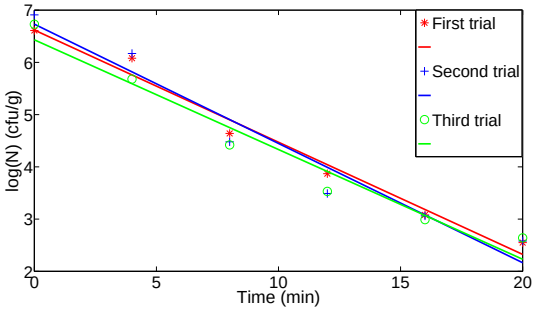

(d) Strain Lm.17 $P = 500$MPa

Figure 2.1: Reduction of the bacterial population and regression lines corresponding to the different strains of *Listeria monocytogenes* from the several trials. $T = 25°$C (fixed). Data source: [33]

We have seen that for fixed temperature T and pressure P, with available data of bacterial population at different time steps, we can identify kinetic parameter D by linear regression. This allows us to estimate bacterial population after t minutes of processing at the same temperature and pressure using (2.5). We can also easily estimate the required time for a n-log-cycle reduction in bacterial population, which is nD as stated in Remark 1.

The following step is to estimate, for a fixed temperature T, the bacterial population $N(t; P)$ at a given time t and for any pressure P, without having to do experimental measurements for that pressure. For this we will need to identify some new kinetic parameters, as explained in Section 2.1.2.

2.1.2 Modelling of the population $N(t; P)$ for a fixed temperature T

Experimental observation

We are going to use the experimental results from [33] of the trials run on strain Lm. 17 of *Listeria monocytogenes* at two different pressures, $P = 500$ MPa and $P = 600$ MPa. The temperature is fixed at $T = 25°$C.

Mathematical modelling

For fixed pressure P and temperature T we showed that (2.1) (or, equivalently (2.2) or (2.5)) is a valid model. If we now want to extend it for arbitrary pressures, in a suitable range, we need to identify the kinetic parameters that describe the influence of pressure on microbial population. Not many references to such parameters are available (as stated in [31]), however we have found two different models (see [27] and [31]) that focus on the effects of pressure on microbial population.

- The first one of these models gives a formula for $\kappa(P) := \kappa_P$ for each pressure. Hence we will be able to quantify how pressure affects the inactivation rate constant. To do so we introduce the concept of *volume of activation*, ΔV^* (cm^3/mol) defined as follows (see [2]): according to transition state theory,[2] the volume of activation is interpreted as the difference between the partial molar volumes of the transition state and the sums of the partial volumes of the reactants at the same temperature and pressure.

  The volume of activation, ΔV^*, can be derived from the pressure dependence of the inactivation rate constant of a reaction, defined by the equation (see [25]):

$$\Delta V^* = -RT \left(\frac{\mathrm{d} \ln \kappa}{\mathrm{d}P} \right)_T, \tag{2.6}$$

  where P is the pressure (MPa), $R = 8.314$ (cm^3 MPa mol^{-1} K^{-1}) is the universal gas constant, T is the temperature (K) and κ (min^{-1}) is the inactivation rate constant.

  Thus from (2.6) we can derive a formula for the inactivation rate constant κ as a function of pressure P:

$$\left(\frac{\mathrm{d} \ln \kappa}{\mathrm{d}P} \right)_T = -\frac{\Delta V^*}{RT}. \tag{2.7}$$

  The volume of activation ΔV^* is the kinetic parameter that we need to identify for this model. We will do this in the next Section.

Remark 2. In [31], equation (2.7) is written differently. Integrating (2.7) from a reference pressure P_{ref}, to an arbitrary pressure P, we can obtain what is known as Eyring's equation:

$$\ln(\kappa(P)) = \ln(\kappa_{P_{\text{ref}}}) - \frac{V(P - P_{\text{ref}})}{RT}, \tag{2.8}$$

where $\kappa_{P_{\text{ref}}}$ is the inactivation rate constant at the reference pressure P_{ref}, P the arbitrary pressure, T the fixed temperature and V the activation volume (which we denoted by ΔV^*).

Remark 3. In [27] the authors point out that it is difficult to give a physical meaning to ΔV^* when working with processes involving bacteria. It may be considered as the sum of chemical, structural and intermolecular changes. However, the identification of an apparent ΔV^* is useful to characterise the pressure dependence of the inactivation rate constant, and hence why we use it here.

The resulting mathematical model is

$$\begin{cases} \kappa(P) = \kappa_{P_{\text{ref}}} \exp\left(\dfrac{-\Delta V^*(P - P_{\text{ref}})}{RT} \right), & P \text{ in a suitable range}, \\ \dfrac{\mathrm{d}N(t;P)}{\mathrm{d}t} = -\kappa(P) N(t;P), & t \geq 0, \\ N(0,P) = N_0. \end{cases} \tag{2.9}$$

The solution of (2.9) is given by

$$\ln\left(\frac{N(t;P)}{N_0} \right) = -\kappa_{P_{\text{ref}}} t \ \exp\left(\left(\frac{-\Delta V^*}{RT} \right) (P - P_{\text{ref}}) \right), \tag{2.10}$$

or, equivalently,

$$N(t;P) = N_0 \exp\left(-\kappa_{P_{\text{ref}}} \ t \ \exp\left(\left(\frac{-\Delta V^*}{RT} \right) (P - P_{\text{ref}}) \right) \right). \tag{2.11}$$

[2] Transition state theory (source [1]): also called activated-complex theory, is a treatment of chemical reactions and other processes that regards them as proceeding by a continuous change in the relative positions and potential energies of the constituent atoms and molecules. On the reaction path between the initial and final arrangements of atoms or molecules, there exists an intermediate configuration at which the potential energy has a maximum value. The configuration corresponding to this maximum is known as the activated complex, and its state is referred to as the transition state

- The second model provides a formula for $D(P) := D_P$ (min) for each pressure. Following [31] we have

$$\log\left(\frac{D(P)}{D_{P_{\text{ref}}}}\right) = -\frac{P - P_{\text{ref}}}{z}, \tag{2.12}$$

where $D_{P_{\text{ref}}}$ is the decimal reduction time at a reference pressure P_{ref} (MPa), P the pressure (MPa), and z (MPa) is the *pressure resistant coefficient* or *z-pressure-value*, which is the kinetic parameter we have to identify for this model. From (2.12) it is clear that z is the pressure increment from P_{ref} necessary to reduce $D_{P_{\text{ref}}}$ by one-log-cycle.

Remark 4. In contrast to what was said in Remark 3 for ΔV^*, the physical meaning of z is obvious when working with bacterias.

The resulting mathematical model in this case is

$$\begin{cases} D(P) = D_{P_{\text{ref}}}\ 10^{\left(-\frac{P-P_{\text{ref}}}{z}\right)}, & P \text{ in a suitable range}, \\ \dfrac{\mathrm{d}N(t;P)}{\mathrm{d}t} = -\dfrac{\ln(10)}{D(P)}\ N(t;P), & t \geq 0, \\ N(0,P) = N_0. \end{cases} \tag{2.13}$$

Remark 5. Note that the second equation of (2.13) is equal to the second equation of (2.9), by taking into account (2.4).

The solution of (2.13) is given by

$$\log\left(\frac{N(t;P)}{N_0}\right) = -\frac{t}{D_{P_{\text{ref}}}}\ 10^{\left(\frac{P-P_{\text{ref}}}{z}\right)}, \tag{2.14}$$

or, equivalently,

$$N(t;P) = N_0\ 10^{-\frac{t}{D_{P_{\text{ref}}}} 10^{\left(\frac{P-P_{\text{ref}}}{z}\right)}}. \tag{2.15}$$

Remark 6. As was said in Remark 1, $D(P)$ is the time required to reduce the microbial population by one-log-cycle at an arbitrary pressure P. Therefore, by using the formula for $D(P)$ from the first equation of (2.13), the time $t(P,n)$ required to attain an n-log-cycle reduction is

$$t(P,n) = n\ D_{P_{\text{ref}}}\ 10^{\left(-\frac{P-P_{\text{ref}}}{z}\right)}. \tag{2.16}$$

Identify kinetic parameters

- For the first model the kinetic parameters we need to identify are P_{ref} (MPa) (which could also be chosen a priori), $\kappa_{P_{\text{ref}}}$ (min^{-1}) and ΔV^* ($\text{cm}^3\ \text{mol}^{-1}$). From (2.8) it holds that

$$\ln(\kappa(P)) = -\frac{\Delta V^*}{RT}P + \left(\frac{\Delta V^*}{RT}P_{\text{ref}} + \ln(\kappa_{P_{\text{ref}}})\right). \tag{2.17}$$

Using identified values of $\kappa(P_i)$ (we calculate them using the identified mean values $D(P_i)$ from the previous Section, and the relation $\kappa = \frac{\ln(10)}{D}$) we plot the scatter graph for $(P_i, \ln(\kappa(P_i)))$. The model validation carried out in the next step shows that the scattered points will be very close to a straight line with a positive slope. In this case, according to (2.17), the value of the slope is $-\frac{\Delta V^*}{RT}$, from where we can obtain ΔV^*. The linear regression line will go through the centre of gravity of the scatter plot, that is

$$(\overline{x}, \overline{y}) = \frac{1}{m}\sum_{i=1}^{m}(P_i, \ln(\kappa(P_i))), \tag{2.18}$$

thus, selecting P_{ref} and $\kappa_{P_{\text{ref}}}$ such that

$$(\overline{x}, \overline{y}) = (P_{\text{ref}}, \ln(\kappa_{P_{\text{ref}}})), \tag{2.19}$$

we have

$$P_{\text{ref}} = \overline{x}, \text{ and } \kappa_{P_{\text{ref}}} = e^{\overline{y}}. \tag{2.20}$$

This allows us to obtain a mathematical model for $\kappa(P)$ for any pressure in a suitable range using (2.8).

- For the second model, the kinetic parameters we need to identify are P_{ref} (MPa), $D_{P_{\text{ref}}}$ (min) and z (MPa). From (2.12) it holds that

$$\log(D(P)) = -\frac{P}{z} + \left(\frac{P_{\text{ref}}}{z} + \log(D_{P_{\text{ref}}})\right). \tag{2.21}$$

Using identified values of $D(P_i)$ we plot the scatter graph for $(P_i, \log(D(P_i)))$. The model validation carried out in the next step shows that the scattered points will be very close to a straight line with a negative slope. In this case, according to (2.21), the value of the slope is $-\frac{1}{z}$, from where we can obtain z. The linear regression line will go through the centre of gravity of the scatter plot, that is

$$(\overline{x}, \overline{y}) = \frac{1}{m}\sum_{i=1}^{m}(P_i, \log(D(P_i))), \tag{2.22}$$

thus, selecting P_{ref} and $D_{P_{\text{ref}}}$ such that

$$(\overline{x}, \overline{y}) = (P_{\text{ref}}, \log(D_{P_{\text{ref}}})), \tag{2.23}$$

we have

$$P_{\text{ref}} = \overline{x}, \text{ and } D_{P_{\text{ref}}} = 10^{\overline{y}}. \tag{2.24}$$

This allows us to obtain a mathematical model for $D(P)$ for any pressure in a suitable range using (2.12).

Validation of model with data

In a similar way to Section 2.1.1, we want to show that (2.9) together with the identified ΔV^* value, and (2.13) together with the identified z value, are good enough approximations for a certain range of pressure, when compared to experimental data. Then we can use (2.11) and (2.15) in order to obtain suitable estimates of the microbial population of strain Lm.17 of *Listeria monocytogenes* under those conditions.

- Figure 2.2a shows the linear regression line (calculated using the mean value of the trials) which were used to obtain the activation volume ΔV^*. Table 2.2 shows the values obtained using this method. Figure 2.2b shows the graphs of the functions $\kappa(P)$ for the mean value of the different trials, together with the scatter plot for $(P_i, \kappa(P_i))$, which had been previously calculated.

Trial	ΔV^*	P_{ref}	$\kappa_{P_{\text{ref}}}$	r
Mean	**-28.0389**	**550**	**0.8818**	1

Table 2.2: Identifying ΔV^*. Data used: mean values of three trials for strain Lm.17 of *Listeria monocytogenes*. $P = 500,600$ MPa. $T = 25°$C. Results obtained by linear regression. r: regression coefficient. Source of experimental data: [33]

- Figure 2.2c shows the linear regression line (calculated using the mean value of the trials) which were used to obtain the value of z. Table 2.3 shows the values obtained using this method. Figure 2.2d shows the graphs of the functions $D(P)$ for the mean value of the different trials, together with the scatter plot for $(P_i, D(P_i))$, which had been previously calculated.

Remark 7. The linear regressions performed for ΔV^* and for z have a regression coefficient of 1. This is due to the fact that we only had sets of data at two different pressure (500 and 600 MPa), and therefore the regression line necessarily goes through both points and hence the regression coefficient is 1. With more available data we would have been able to obtain more significant results.

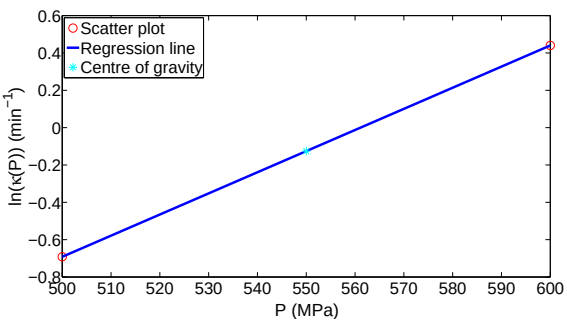

(a) Linear regression lines for obtaining ΔV^*

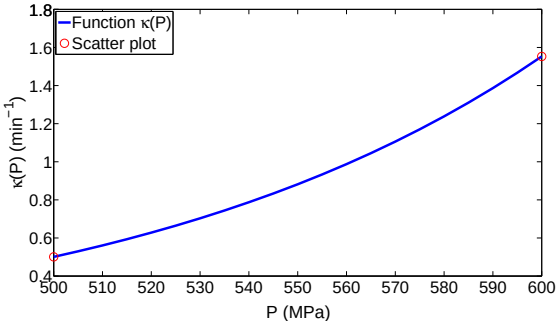

(b) Graph of function $\kappa(P)$

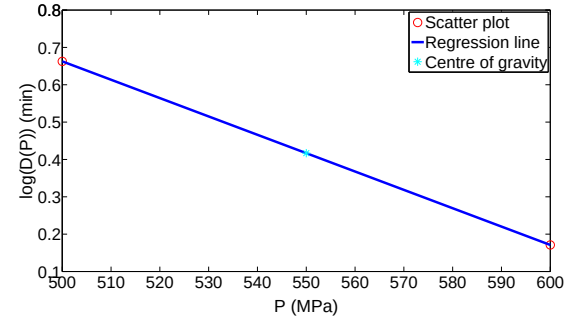

(c) Linear regression lines for obtaining z

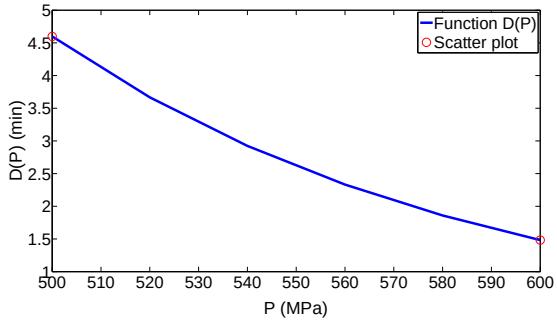

(d) Graph of function $D(P)$

Figure 2.2: Model validation with data for HP inactivation of strain Lm. 17 of *Listeria monocytogenes*. $T = 25°$C. Source for experimental data: [33].

Trial	z (MPa)	P_{ref}	$D_{P_{\text{ref}}}$	r
Mean	**203.4609**	550	**2.6113**	1

Table 2.3: Identifying z. Data used: mean values of three trials for strain Lm.17 of *Listeria monocytogenes*. $P = 500, 600$ MPa. $T = 25°$C. Results obtained by linear regression. r: regression coefficient. Source of experimental data: [33]

Relation between the two models

Let us now see how the two previous models are related. To do so we show that there is a simple mathematical relation between ΔV^* and z. Let us recall that for fixed pressure P and temperature T, the relation between κ and D is given by (2.4). As can be easily seen in Table 2.4 for the reference pressure, $P_{\text{ref}} = 550$ MPa, (2.4)

Trial	$\kappa_{P_{\text{ref}}}$ (calculated by regression)	$\frac{\ln(10)}{\kappa_{P_{\text{ref}}}}$	$D_{P_{\text{ref}}}$ (calculated by regression)
Mean	**0.8818**	**2.6113**	**2.6113**

Table 2.4: Checking that relation (2.4) between κ and D holds at the reference pressure $P_{\text{ref}} = 500$ MPa.

holds, and therefore

$$D_{P_{\text{ref}}} = \frac{\ln(10)}{\kappa_{P_{\text{ref}}}} \tag{2.25}$$

For an arbitrary pressure, P,

$$D(P) = \frac{\ln(10)}{\kappa(P)} \tag{2.26}$$

has to hold. Therefore, using the first equation of (2.9) and the first equation of (2.13) it follows

$$D_{P_{\text{ref}}}\ 10^{\left(-\frac{P-P_{\text{ref}}}{z}\right)} = \frac{\ln(10)}{\kappa_{P_{\text{ref}}}\exp\left(\frac{-\Delta V^*(P-P_{\text{ref}})}{RT}\right)} \implies 10^{\left(-\frac{P-P_{\text{ref}}}{z}\right)} = \exp\left(\frac{\Delta V^*(P-P_{\text{ref}})}{RT}\right),$$
$$\implies -\frac{P-P_{\text{ref}}}{z} = \log\left(\exp\left(\frac{\Delta V^*(P-P_{\text{ref}})}{RT}\right)\right) = \frac{\ln\left(\exp\left(\frac{\Delta V^*(P-P_{\text{ref}})}{RT}\right)\right)}{\ln(10)} \tag{2.27}$$
$$\implies -\frac{P-P_{\text{ref}}}{z} = \frac{\Delta V^*(P-P_{\text{ref}})}{RT\ln(10)},$$

from where we can find the relation between ΔV^* and z, given by

$$\Delta V^* = -\frac{RT\ln(10)}{z} \quad . \tag{2.28}$$

Table 2.5 shows that formula (2.28) is correct for our data

Trial	z (calculated by regression)	$\frac{-RT\ln(10)}{z}$	ΔV^* (calculated by regression)
Mean	**203.4609**	**-28.0389**	**-28.0389**

Table 2.5: Checking that the relation (2.28) between ΔV^* and z holds for the available experimental data.

Expressions (2.4) and (2.28) allow us to indistinctly use one model or the other, without having to do new regression calculations.

Observations

Kinetic pressure parameters ΔV^* and z (together with suitable reference values P_{ref}, $\kappa_{P_{\text{ref}}}$ and $D_{P_{\text{ref}}}$) have been identified. With these parameters the bacterial population $N(t;P)$, at any time t and pressure P (within the adequate range), can be calculated.

- In particular, for the first model, the bacterial population (of strain Lm.17 of *Listeria monocytogenes*) after elapsed time t, at any pressure P (preferably in the range 500 - 600 MPa or close to it) and at a temperature of 25°C is given by

$$N(t;P) = N_0\ e^{-\kappa(P)t}, \tag{2.29}$$

  where N_0 is the initial bacterial population $N_0 = 6.3096\cdot 10^6$ (cfu g^{-1}),

$$\kappa(P) = \kappa_{P_{\text{ref}}}\exp\left(\frac{-\Delta V^*(P-P_{\text{ref}})}{RT}\right), \tag{2.30}$$

  $\kappa_{P_{\text{ref}}} = 0.8818$ (min^{-1}), $P_{\text{ref}} = 550$ (MPa), $\Delta V^* = -28.0389$ (cm^{3}mol^{-1}), $R = 8.314$ (Jmol^{-1}K^{-1}), and $T = 298.15$ (K). It is easy to see from (2.30) that at a higher pressure, higher is the inactivation rate constant, $\kappa(P)$. In Figure 2.3 a graph of $N(t;P)$ for $t \in (0,7)$ min and $P \in (500,600)$ MPa can be seen. In the figure it is clear that the lowest values of bacterial population are obtained for higher pressure and time values.

  We point out that the values for ΔV^* and $\kappa_{P_{\text{ref}}}$ have been taken as the mean value of the three experiments. The value for N_0 has been taken from [33].

- For the second model, the bacterial population (of strain Lm.17 of *Listeria monocytogenes*) after elapsed time t, at any pressure P (preferably in the range 500 - 600 MPa or close to it) and at a temperature of 25°C is given by

$$N(t;P) = N_0\ 10^{-\frac{t}{D(P)}}, \tag{2.31}$$

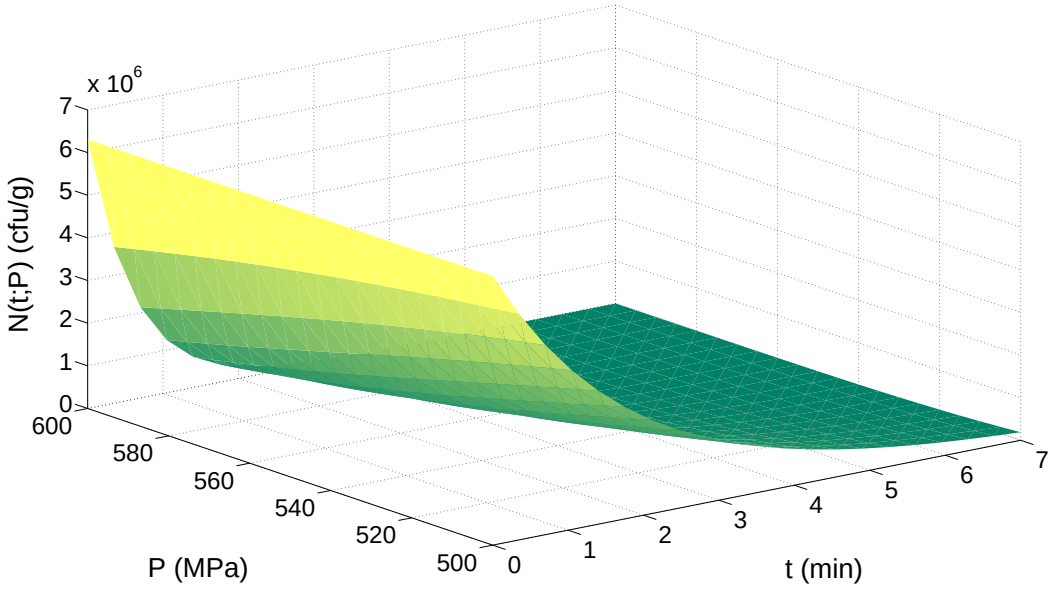

Figure 2.3: Graph of $N(t;P)$ (from the first model), for the mean values of the three experiments of strain Lm.17 of *Listeria monocytogenes* Lm.17. $T = 25°$C.

where N_0 is the initial bacterial population $N_0 = 6.3096 \cdot 10^6$ (cfu g^{-1}),

$$D(P) = D_{P_{\text{ref}}}\ 10^{\left(-\frac{P-P_{\text{ref}}}{z}\right)}, \tag{2.32}$$

$D_{P_{\text{ref}}} = 2.6113$ (min), $P_{\text{ref}} = 550$ (MPa), and $z = 203.4609$ (MPa). It is easy to see from (2.32) that at a higher pressure, lower is the decimal reduction time, $D(P)$.

Also, according to (2.16), the time required to obtain a n-log-cycle reduction is

$$t(P,n) = n\ D_{P_{\text{ref}}}\ 10^{-\frac{P-P_{\text{ref}}}{z}}. \tag{2.33}$$

We point out that the values for z and $D_{P_{\text{ref}}}$ have been taken as the mean value of the three experiments. The value for N_0 has been taken from [33].

The obvious next step would be to model the population $N(t;T,P)$ of bacteria for arbitrary pressures and temperatures, in an adequate range. To follow the same procedure as above we would need experimental measurements at different temperatures. However these were not provided to us in the same study as [33], hence we could not do the entire model validation. However, in Section 2.2 we present a mathematical model for microbial and enzymatic inactivation at arbitrary pressures and temperatures, which is a generalisation of the models presented above for arbitrary pressure and temperature conditions.

2.2 Generalised mathematical modelling of microbial and enzymatic inactivation

By analogy to the models derived in Section 2.1, in order to describe changes in the microbial population as a function of time t, when the food sample is processed at temperature T and pressure P, we can use the following

first order model[3] (see, e.g., [22, 27, 43, 92]):

$$\begin{cases} \dfrac{\mathrm{d}N(t;T,P)}{\mathrm{d}t} = -\kappa(T,P)N(t;T,P), \quad t \geq 0, \\ N(0;T,P) = N_0, \end{cases} \tag{2.34}$$

where N_0 is the initial microbial population and $\kappa(T,P)$ is the *inactivation rate* (min^{-1}) that now depends on temperature and pressure. The solution to (2.34) is given by

$$N(t;T,P) = N_0 \ \exp\left(-\int_0^t \kappa(T(s),P(s)) \ \mathrm{d}s\right), \tag{2.35}$$

Another equation used very often (see [31]) to calculate changes of microbial population as a function of time is the following:

$$\begin{cases} \dfrac{\mathrm{d}N(t;T,P)}{\mathrm{d}t} = -\dfrac{\log 10}{D(T,P)}N(t;T,P), & t \geq 0, \\ N(0;T,P) = N_0, & \\ \textbf{Solution: } N(t;T,P) = N_0 \ 10^{-\int_0^t \frac{1}{D(T(s),P(s))} \ \mathrm{d}s}, & \end{cases} \tag{2.36}$$

where $D(T,P)$ is the *decimal reduction time* (min) which also depends on temperature and pressure.

If instead of the microbial population we want to describe changes in enzymatic activity as a function of time, when the food sample is processed at temperature T and pressure P we can use the first-order kinetic model (see, for instance, [62, 87]):

$$\begin{cases} \dfrac{\mathrm{d}A(t;T,P)}{\mathrm{d}t} = -\kappa(T,P)A(t;T,P), & t \geq 0, \\ A(0;T,P) = A_0, & \\ \textbf{Solution: } A(t;T,P) = A_0 \ \exp\left(-\displaystyle\int_0^t \kappa(T(s),P(s)) \ \mathrm{d}s\right), & \end{cases} \tag{2.37}$$

where $A(t;T,P)$ is the enzymatic activity at time t, when the food sample is processed at temperature T and pressure P, A_0 is the initial enzymatic activity and $\kappa(T,P)$ is the *inactivation rate* (min^{-1}). To measure enzymatic activity several protocols may be used (for example, the unit of enzymatic activity is often used as the amount of enzyme that catalyses the conversion of 1 μmol of substrate in a minute), taking into account the variation of a suitable magnitude per unit of time. According to the chosen magnitude, this activity is expressed in the corresponding units. However, this is not a relevant issue, what is interesting from a practical point of view is to study the reduction of the non-dimensional value A/A_0.

To be able to apply these models we need to identify kinetic parameters $\kappa(T,P)$ and $D(T,P)$ for the microbes or enzymes we are interested in and adequate ranges of temperature and pressure, in a similar way to what was done in Section 2.1.

Remark 8. In Section 2.1 we carried out a study case of inactivation of the bacteria *Listeria monocytogenes*, but exactly the same study could have been done for an enzyme, if data were available.

We have seen above that one can use exactly the same kinetic models are exactly the same for microbial and enzymatic inactivation, and in the following we will show that the identification of kinetic parameters procedure follows the same approach as above.

For isostatic processes, $\kappa(T)$ can be given by Arrhenius' equation (see, for instance, [59]):

$$\kappa(T) = \kappa_{T_{\mathrm{ref}}} \exp\left(\left(\frac{-E_a}{R}\right)\left(\frac{1}{T} - \frac{1}{T_{\mathrm{ref}}}\right)\right), \tag{2.38}$$

[3]Higher-order models that describe changes in microbial populations as a function of time can also be found in the literature [92].

where $\kappa(T)$ (min^{-1}) is the inactivation rate for an arbitrary temperature T (K), $\kappa_{T_{\text{ref}}}$ (min^{-1}) is the inactivation rate at reference temperature T_{ref} (K), E_a (J mol^{-1}) is the activation energy[4] and $R = 8.314$ (J mol^{-1} K^{-1}) is the universal gas constant.

As defined in (2.9), for isothermal processes $\kappa(P)$ can be given by (see, for instance, [59]) the following equation (based on Eyring's equation):

$$\kappa(P) = \kappa_{P_{\text{ref}}} \exp\left(\frac{-\Delta V^*(P - P_{\text{ref}})}{RT}\right), \tag{2.39}$$

where $\kappa(P)$ (min^{-1}) is the inactivation rate for an arbitrary pressure P (MPa), $\kappa_{P_{\text{ref}}}$ (min^{-1}) is the inactivation rate at reference pressure P_{ref} (MPa) and ΔV^* (cm^3 mol^{-1}) is the volume of activation.

For temperature and pressure dependent processes, $\kappa(T, P)$ may be calculated by a combination of Arrhenius equation and Eyring equation, as follows (see e.g. [58]):

$$\kappa(P, T) = \kappa_{\text{ref}} \exp\left(-B\left(\frac{1}{T} - \frac{1}{T_{\text{ref}}}\right)\right) \exp(-C(P - P_{\text{ref}})), \tag{2.40}$$

where T_{ref} is a reference temperature (K), P_{ref} is a reference pressure (MPa), κ_{ref} is the inactivation rate at reference conditions (min^{-1}), B (K) and C (MPa^{-1}) are kinetic parameters that express the dependence of κ on temperature and pressure, respectively.

A more complex equation may be used, by considering Eyring's transition state theory adapted to enzymatic study (see e.g. [44, 61]):

$$\begin{aligned}\kappa(P,T) = \kappa_{\text{ref}} &\exp\left(\frac{-\Delta V_{\text{ref}}}{RT}(P - P_{\text{ref}})\right) \exp\left(\frac{\Delta S_{\text{ref}}}{RT}(T - T_{\text{ref}})\right) \\ + \ &\exp\left(\frac{-\Delta\nu}{2RT}(P - P_{\text{ref}})^2\right) \exp\left(\frac{-2\Delta\zeta}{RT}(P - P_{\text{ref}})(T - T_{\text{ref}})\right) \\ + \ &\exp\left(\frac{\Delta C_p}{RT}\left(T(\ln\frac{T}{T_{\text{ref}}} - 1) + T_{\text{ref}}\right)\right) + \text{high-order terms in } P \text{ and } T,\end{aligned} \tag{2.41}$$

where ΔV_{ref} is the volume change at reference conditions (cm^3 mol^{-1}), ΔS_{ref} is the entropy change at reference conditions (J mol^{-1} K^{-1}), ΔC_p is the heat capacity change (J mol^{-1} K^{-1}), $\Delta\zeta$ is the thermal expansibility factor (cm^3 mol^{-1} K^{-1}) and $\Delta\nu$ is the compressibility factor (cm^3 J^{-1} mol^{-1}). Depending on the enzyme that is being studied, higher-order terms can be added to (2.41) in order to refine the approximation of the pressure-temperature dependence of the enzymatic activity.

By construction $\kappa(T, P)$ and $D(T, P)$ are related by $\kappa = \frac{\ln(10)}{D}$, thereby it is possible to move from one model to the other. However, we may also calculate $D(T, P)$ directly by using suitable equations. For $D(T)$ and $D(P)$, we have, resp. [31]:

$$\log\left(\frac{D(T)}{D_{T_{\text{ref}}}}\right) = -\frac{T - T_{\text{ref}}}{z_T}, \tag{2.42}$$

$$\log\left(\frac{D(P)}{D_{P_{\text{ref}}}}\right) = -\frac{P - P_{\text{ref}}}{z_P}, \tag{2.43}$$

where z_T (K) (resp., z_P (MPa)) is the thermal (resp., pressure) resistance constant that can be defined as the temperature (resp., pressure) increase needed to accomplish a 1-log-cycle reduction in the decimal reduction time value D (min); $D_{T_{\text{ref}}}$ (resp., $D_{P_{\text{ref}}}$) (min) is the reference decimal reduction time at reference temperature T_{ref} (K) (resp., reference pressure P_{ref} (MPa)) within the range of temperatures (resp., pressures) used to generate experimental data.

Therefore, the problem of identifying function $\kappa(T, P)$ is a parameter estimation problem (we have to identify E_a, ΔV^*, etc...). This parameter identification may be done using regression techniques, like we did in Section 2.1 when we had available data.

[4] Activation energy (chemistry): the minimum amount of energy that is required to activate atoms or molecules to a condition in which they can undergo chemical transformation or physical transport.

Models for enzymatic inactivation have been successfully applied when studying the inactivation of various enzymes with different conditions of pressure and temperature (see e.g. [44, 59]). However, they can only be used when the temperature and pressure profiles are known. Therefore, these models do not allow to perform numerical simulations in general situations without temperature and pressure evolution data. In practice, for a HP process, the pressure evolution is known as it is imposed by the user and the limits of the equipment. In the case of the temperature evolution it is necessary to consider the adiabatic heating effects due to the work of compression/expansion in the considered HP device. Also the temperature may not be at a suitable initial temperature, and there may be cooling or heating of the sample to take into account. The temperature of the processed food may change with time and with space, therefore we need a heat transfer model capable of predicting the temperature for the processed food.

This leads to one of the main goal of this thesis, which has been to propose and analyse several heat and mass transfer models for HP processing of food. Once we have the temperature distribution, we can couple it to the inactivation models to work out the enzymatic or bacterial distribution at any point or time step. As stated in Chapter 1, throughout the following Chapters we have studied heat transfer models that cover as many situations as possible when working with HP food processing. In particular, in Chapter 4 several two dimensional models for solid type foods, with different kind of boundary conditions, are solved analytically. An example of how a heat transfer model is coupled to a enzymatic inactivation model is given, and some simplified versions are discussed. In Chapter 5 a three dimensional model for solid- and liquid-type foods has been solved numerically for both vertically and horizontally oriented HP vessels. In Chapter 6 a generalised enthalpy model for a HP shift freezing is presented and solved numerically. All of the models presented in Chapters 4, 5 and 6 are based on one common model that was derived by the authors in [46, 69]. For this reason, before giving the details of the heat transfer models studied in the subsequent Chapters, we present and describe this common model in Chapter 3.

Chapter 3

Common features of the heat and mass transfer models described in this thesis

Nomenclature for Chapter 3

$\mathbf{A}_1$, $\mathbf{A}_2$	Corner points
C_p	Specific heat capacity (J kg^{-1} K^{-1})
$\mathbf{g}$	Gravity vector (m s^{-2})
h	Heat transfer coefficient (W m^{-2} K^{-1})
H	Domain height (m)
k	Thermal conductivity (W m^{-1} K^{-1})
L	Domain width (m)
M	Mass (kg)
$\mathbf{n}$	Outward normal unit vector (m)
p	Mass transfer pressure (Pa)
P	Equipment Pressure (Pa)
r	Radial coordinate (m)
t	Time (s)
t_f	Final time (s)
T	Temperature (K)
T_0	Initial temperature (K)
T_env	Environment temperature (K)
T_r	Fixed temperature (K)
$\mathbf{u}$	Fluid velocity vector (m s^{-1})
V	Volume (m^3)
z	Vertical coordinate (m)

Acronyms

HP	High Pressure
2D	Two-dimensional
3D	Three-dimensional

Greek symbols

β	Thermal expansion coefficient (K^{-1})
Γ	Whole domain boundary
Γ_p	Boundary of Ω_P^*
Γ_r	Fixed temperature boundary
Γ_up	Heat transfer boundary
η	Dynamic viscosity (Pa s)
ρ	Density (kg m^{-3})
Ω	Whole domain
Ω_C	Cap of the sample holder
Ω_F	Food sample domain
Ω_P	Pressurising medium
Ω_S	Steel vessel

Other symbols

∇	Gradient
$\nabla\cdot$	Divergence
∇^2	Laplacian

Indices

*	Rotated domains
F	Food domain
P	Pressurising fluid

All of the models that will be derived in Chapters 4, 5 and 6 have a common feature: the geometry of all of them is inspired by the same HP machine (also used in [46, 67, 69]), which is the pilot-scale unit ACB GEC Alsthom (Nantes, France) (see Figure 3.1), located at the "Instituto de Ciencia y Tecnología de Alimentos y Nutrición" (ICTAN), part of the "Consejo Superior de Investigaciones Científicas" (CSIC). Even though different mathematical models are used in Chapters 4, 5 and 6, they are all derived from a common heat and mass transfer model [46, 69]. In this Chapter we are going to describe the model that we use throughout the entire thesis as it is the starting point for the rest of our models, and we will distinguish the cases of solid- and liquid-type foods, as we use the former in Chapters 4 and 6, and the latter in Chapter 5.

During a HP process that takes place in the pilot-scale machine previously mentioned, the food sample (orange

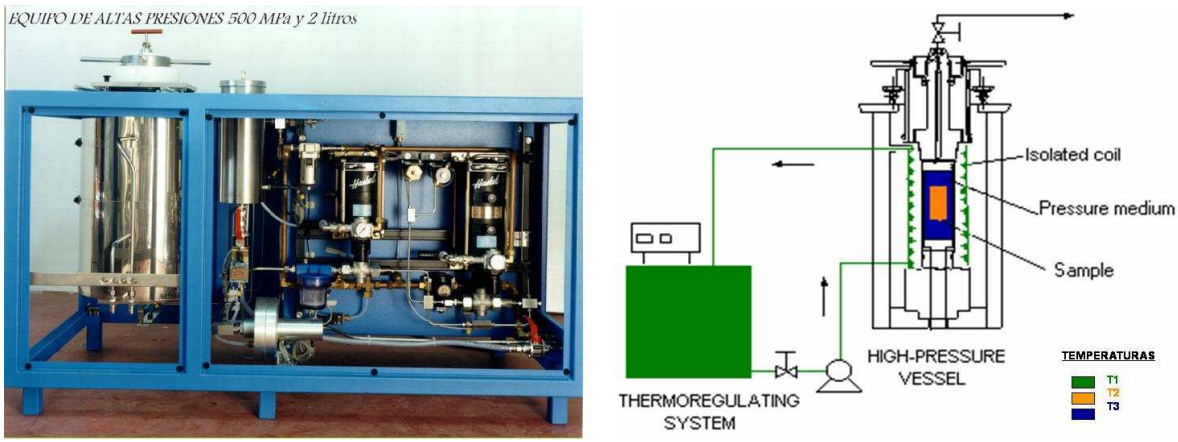

(a) Pilot-scale HP vessel (b) Diagram of its operation

Figure 3.1: Pilot-scale HP unit ACB GEC Alstom. Adapted from [69]

area in Figure 3.1b) is placed inside the steel cylindrical vessel, which is filled with the pressurising fluid (blue are in Figure 3.1b). The user can choose whether to heat or cool the sample during the process through the isolated coil which is controlled by the thermo-regulating system (green in Figure 3.1b). A typical HP treatment consists of a compression step, a holding phase at the target pressure, and a pressure release step. At the beginning, the sample, pressure medium and vessel are usually in equilibrium, all of them at an initial temperature. During compression, pressure is applied at certain rate up to the target pressure by a hydro-pneumatic pump. The holding phase finishes when expansion takes place. This process usually results in a laminar flow [45, 46], without turbulences appearing neither in the pressurising medium nor in the liquid-type food. These two conditions (cylindrical geometry and laminar flow) suggest the use of an axis-symmetry model. By using cylindrical coordinates, and eliminating the angular coordinate, the three dimensional model can be reduce to a two dimensional one, allowing the usage of a plane domain, which corresponds to half of an axial section (i.e. the intersection of the cylinder with a plane containing its axis).

We introduce the notation used in the following Chapters, regarding the planar domains where the problem will be studied [45, 46]. Firstly, we consider the following four sub-domains (see Figure 3.2):

- Ω_{F}: domain that contains the food sample.
- Ω_{C}: cap of the sample holder (typically rubber).
- Ω_{P}: domain occupied by the pressurising medium.
- Ω_{S}: domain of the steel that surrounds the rest of the domains.

The domain in the cylindrical (r, z)-coordinates is the rectangle $\Omega = [0, L] \times [0, H]$ and the axis of symmetry is defined by $(\{0\} \times (0, H))$. The boundary of Ω (this is, the whole domain, defined as $\overline{\Omega} = \overline{\Omega_{\mathrm{F}} \cup \Omega_{\mathrm{C}} \cup \Omega_{\mathrm{P}} \cup \Omega_{\mathrm{S}}}$) is denoted by Γ, where we can distinguish:

- $\Gamma_{\mathrm{r}} \subset \{L\} \times [0, H]$, where the temperature is known.
- $\Gamma_{\mathrm{up}} = [0, L] \times \{H\}$, where heat transfer with the room in which equipment is located may take place.
- $\Gamma \setminus \{\Gamma_{\mathrm{r}} \cup \Gamma_{\mathrm{up}}\}$, that has zero heat flux, either by axial symmetry or by isolation of the equipment.

Finally, we will use the super index $([\,]^*)$ to denote the domains generated by rotating all the previously described domains (and their corresponding boundaries) along the axis of symmetry $(\{0\} \times (0, H))$ in the 3D version of the problem. Namely, Ω^*, Ω_{F}^*, Ω_{P}^*, Ω_{S}^*, Ω_{C}^*, Γ^*, Γ_{r}^* and Γ_{up}^* are the three-dimensional and two-dimensional domains generated by rotating, along the axis of symmetry, Ω, Ω_{F}, Ω_{P}, Ω_{S}, Ω_{C}, Γ, Γ_{r} and Γ_{up}, respectively.

Now we have defined the domain, in the following Sections we are going to describe the equations for the model, distinguishing two significant cases: solid- and liquid-type foods, as in [46].

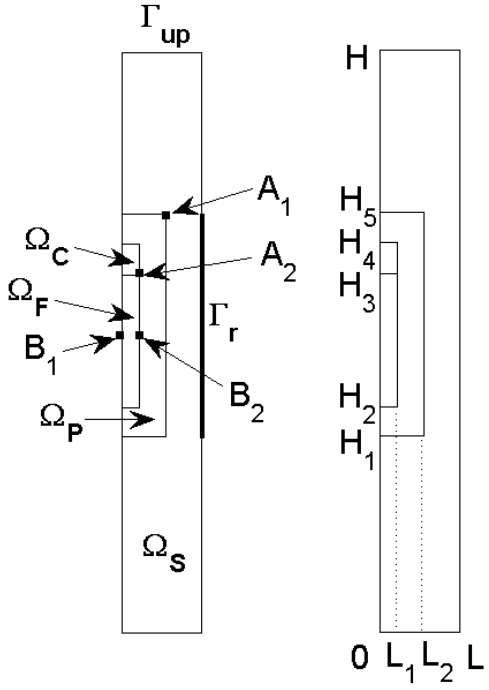

Figure 3.2: 2D axis-symmetric domain

3.1 Solid-type foods

3.1.1 Heat transfer by conduction

When solid type foods are considered, the starting point is the heat conduction equation for temperature T (K)

$$\rho C_p \frac{\partial T}{\partial t} - \nabla \cdot (k \nabla T) = \beta \, \frac{\mathrm{d}P}{\mathrm{d}t} \, T \quad \text{in } \Omega^* \times (0, t_\mathrm{f}), \tag{3.1}$$

where ρ is the density (kg m^{-3}), C_p the specific heat (J kg^{-1} K^{-1}), k the thermal conductivity (W m^{-1} K^{-1}) and t_f is the final time (s). The right-hand side of equation (3.1) is the heat production due to the change of pressure $P = P(t)$ (Pa) applied by the equipment (chosen by the user within the machine limitations) and β is the thermal expansion coefficient, that is given by

$$\beta = \begin{cases} \beta_\mathrm{F} : \text{ thermal expansion coefficient } (\mathrm{K}^{-1}) \text{ of the food in } \Omega^*_\mathrm{F}, \\ \beta_\mathrm{P} : \text{ thermal expansion coefficient } (\mathrm{K}^{-1}) \text{ of the pressurizing fluid in } \Omega^*_\mathrm{P}, \\ 0, \text{ elsewhere.} \end{cases} \tag{3.2}$$

This term results from the following relation (for derivation see, e.g. [52]), which is valid for isentropic processes[1]

$$\frac{\Delta T}{\Delta P} = \frac{\beta T V}{M C_p} = \frac{\beta T}{\rho C_p}, \tag{3.3}$$

where ΔT (K) denotes the temperature change due to the pressure change ΔP (Pa), V (m^3) is the volume and M (kg) the mass.

[1] A process during which the entropy remains constant is called an isentropic process, If a process is both reversible and adiabatic, then it is an isentropic process.

In order to solve equation (3.1), we must specify appropriate boundary and initial conditions depending on the HP machine and the problem under study. We use the same conditions as in [69] for the previously described pilot-scale unit (ACB GEC Alsthom, Nantes, France)

$$\begin{cases} k\dfrac{\partial T}{\partial \mathbf{n}} = 0 & \text{on} \quad \Gamma_0^* \times (0, t_\mathrm{f}), \\ k\dfrac{\partial T}{\partial \mathbf{n}} = h(T_\mathrm{env} - T) & \text{on} \quad \Gamma_\mathrm{up}^* \times (0, t_\mathrm{f}), \\ T = T_\mathrm{r} & \text{on} \quad \Gamma_\mathrm{r}^* \times (0, t_\mathrm{f}), \\ T = T_0 & \text{in} \quad \Omega^* \times \{0\}, \end{cases} \tag{3.4}$$

where $\mathbf{n}$ is the outward unit normal vector on the boundary of the domain, T_0 (K) is the initial temperature, T_r (K) is the fixed temperature on Γ_r^*, T_env (K) is the environment temperature (constant) and h (W m^{-2} K^{-1}) is the heat transfer coefficient.

By using cylindrical coordinates and taking into account axial symmetry, system (3.1), (3.4) may be rewritten as the following 2D problem

$$\begin{cases} \rho C_p \dfrac{\partial T}{\partial t} - \dfrac{1}{r}\dfrac{\partial}{\partial r}\left(rk\dfrac{\partial T}{\partial r}\right) - \dfrac{\partial}{\partial z}\left(k\dfrac{\partial T}{\partial z}\right) = \beta\dfrac{\mathrm{d}P}{\mathrm{d}t}T & \text{in} \quad \Omega \times (0, t_\mathrm{f}), \\ k\dfrac{\partial T}{\partial \mathbf{n}} = 0 & \text{on} \quad \Gamma_0 \times (0, t_\mathrm{f}), \\ k\dfrac{\partial T}{\partial \mathbf{n}} = h(T_\mathrm{env} - T) & \text{on} \quad \Gamma_\mathrm{up} \times (0, t_\mathrm{f}), \\ T = T_\mathrm{r} & \text{on} \quad \Gamma_\mathrm{r} \times (0, t_\mathrm{f}), \\ T = T_0 & \text{in} \quad \Omega \times \{0\}. \end{cases} \tag{3.5}$$

This model is suitable for what we will refer to as a "large sample", i.e. when the filling ratio of the food sample inside the vessel is much higher than that in the pressurizing medium (see Figure 3.3a), since convection effects due to the pressurizing fluid can be neglected. This has been confirmed to be true in [69], by validation with several comparisons between numerical and experimental results. In [69] the authors show that for "small samples", when the filling ratio of the food inside the vessel is not much higher than in the pressurizing medium (see Figure 3.3b), the solution of this model differs a lot from the experimental results. Therefore they improve the model by including convection effects in the pressurizing medium. We present this model in Section 3.1.2.

Another case when (3.5) may be used, even if we are dealing with a small sample, is for highly viscous fluids – which could be the case at low temperatures – where convection effects may be negligible. This would reduce the computing time without any significant loss in prediction.

3.1.2 Heat transfer by conduction and convection

The non-homogeneous temperature distribution induces a non-homogeneous density distribution in the pressurising medium and consequently a buoyancy fluid motion, i.e. free convection. In order to take into account the fact that the fluid motion influences the temperature distribution, a non-isothermal flow model is considered. We assume that the fluid velocity, $\mathbf{u}$ (m s^{-1}), satisfies the Navier–Stokes equations for compressible Newtonian fluid under Stokes' assumption (see, e.g., [5]). The resulting system, with appropriate point, boundary and

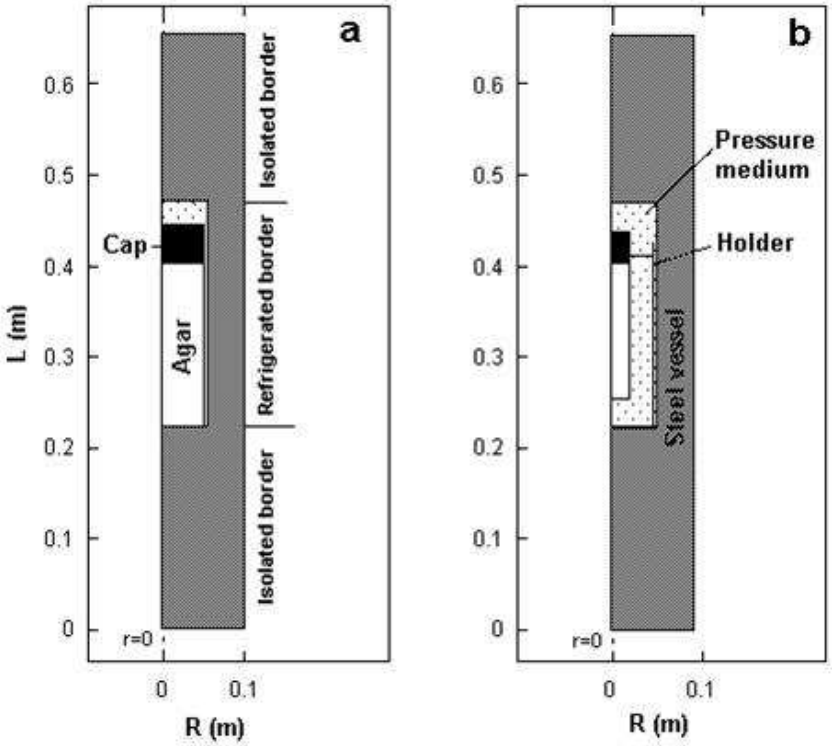

Figure 3.3: Different 2D computational domains: (a) large agar sample and (b) small agar sample. Extracted from [69]

initial conditions, is

$$
\begin{cases}
\rho C_p \dfrac{\partial T}{\partial t} - \nabla \cdot (k \nabla T) + \rho C_p \mathbf{u} \cdot \nabla T = \beta \dfrac{\mathrm{d}P}{\mathrm{d}t} T, & \text{in} \quad \Omega^* \times (0, t_\mathrm{f}), \\
\rho \dfrac{\partial \mathbf{u}}{\partial t} - \nabla \cdot \eta (\nabla \mathbf{u} + \nabla \mathbf{u}^\mathbf{t}) + \rho (\mathbf{u} \cdot \nabla) \mathbf{u} & \\
\qquad = -\nabla p - \dfrac{2}{3} \nabla (\eta \nabla \cdot \mathbf{u}) + \rho \mathbf{g} & \text{in} \quad \Omega_\mathrm{P}^* \times (0, t_\mathrm{f}), \\
\dfrac{\partial \rho}{\partial t} + \nabla \cdot (\rho \mathbf{u}) = 0 & \text{in} \quad \Omega_\mathrm{P}^* \times (0, t_\mathrm{f}), \\
k \dfrac{\partial T}{\partial \mathbf{n}} = 0 & \text{on} \quad \Gamma_0^* \times (0, t_\mathrm{f}), \\
k \dfrac{\partial T}{\partial \mathbf{n}} = h (T_\mathrm{env} - T) & \text{on} \quad \Gamma_\mathrm{up}^* \times (0, t_\mathrm{f}), \\
T = T_\mathrm{r} & \text{on} \quad \Gamma_\mathrm{r}^* \times (0, t_\mathrm{f}), \\
\mathbf{u} = 0 & \text{on} \quad \Gamma_\mathrm{P}^* \times (0, t_\mathrm{f}), \\
T(0) = T_0 & \text{in} \quad \Omega^*, \\
\mathbf{u}(0) = 0 & \text{in} \quad \Omega^*, \\
p = 10^5 & \text{at} \quad \mathbf{A}_1 \times (0, t_\mathrm{f}),
\end{cases}
\tag{3.6}
$$

where $\mathbf{g}$ is the gravity vector (m s^{-2}), η is the dynamic viscosity (Pa s), $p = p(x,t)$ is the pressure generated by the mass transfer inside the fluid, and $P + p$ is the total pressure (Pa) in the pressurizing medium Ω_P^*. $\mathbf{A}_1$ is a corner point of Γ_P^*, which is the boundary of Ω_P^* (see Figure 3.2). The authors in [46] pointed out that could

have written $\beta\frac{\mathrm{d}(P+p)}{\mathrm{d}t}T$ on the right-hand side of the first equation of (3.6), but it was assumed that the internal heat generation due to mass transfer is negligible. Also, on the right-hand side of the second equation of (3.6) ∇p is written, given that $P(t)$ depends only on time and thus $\nabla(P+p)=\nabla p$. The fact that p only appears in its gradient form in (3.6) means that such function is uniquely determined except for additive constants. This explains the necessity to fix its value at some point, and this is done by imposing the point condition at $\mathbf{A}_1$. Such condition means that the total pressure $(P+p)$ at this point is equal to the equipment pressure P plus the atmospherical pressure.

As in Section 3.1.1 for the conductive heat transfer model, system (3.6) can also be rewritten as an equivalent 2D problem by using cylindrical coordinates. In Chapter 6, where one case under study is for small solid-type foods, the numerical experiments considered related to this model were carried out using the 2D version of the corresponding equations.

3.2 Liquid-type foods

Again following [46] we are going to describe the model for a liquid-type food, which includes heat transfer by conduction and convection. The convection occurs in both the food sample and the pressurizing medium regions, Ω_{F} and Ω_{P}, in which two different velocity fields are considered, $\mathbf{u}_{\mathrm{F}}$ and $\mathbf{u}_{\mathrm{P}}$, respectively. The pressurizing medium and the food are separated by the sample holder and do not mix. It is assumed that both the pressurizing fluid and the liquid-type food are compressible and Newtonian fluids. Hence the governing equations are

$$\begin{cases} \rho C_p\dfrac{\partial T}{\partial t}-\nabla\cdot(k\nabla T)+\rho C_p\mathbf{u}\cdot\nabla T=\beta\,\dfrac{\mathrm{d}P}{\mathrm{d}t}\,T & \text{in} \quad \Omega^*\times(0,t_{\mathrm{f}}),\\ \rho\dfrac{\partial\mathbf{u}_{\mathrm{F}}}{\partial t}-\nabla\cdot\eta(\nabla\mathbf{u}_{\mathrm{F}}+\nabla\mathbf{u}_{\mathrm{F}}^{\mathbf{t}})+\rho(\mathbf{u}_{\mathrm{F}}\cdot\nabla)\mathbf{u}_{\mathrm{F}} & \\ \quad=-\nabla p-\dfrac{2}{3}\nabla(\eta\nabla\cdot\mathbf{u}_{\mathrm{F}})+\rho\mathbf{g} & \text{in} \quad \Omega_{\mathrm{F}}^*\times(0,t_{\mathrm{f}}),\\ \rho\dfrac{\partial\mathbf{u}_{\mathrm{P}}}{\partial t}-\nabla\cdot\eta(\nabla\mathbf{u}_{\mathrm{P}}+\nabla\mathbf{u}_{\mathrm{P}}^{\mathbf{t}})+\rho(\mathbf{u}_{\mathrm{P}}\cdot\nabla)\mathbf{u}_{\mathrm{P}} & \\ \quad=-\nabla p-\dfrac{2}{3}\nabla(\eta\nabla\cdot\mathbf{u}_{\mathrm{P}})+\rho\mathbf{g} & \text{in} \quad \Omega_{\mathrm{P}}^*\times(0,t_{\mathrm{f}}),\\ \dfrac{\partial\rho}{\partial t}+\nabla\cdot(\rho\mathbf{u}_{\mathrm{F}})=0 & \text{in} \quad \Omega_{\mathrm{F}}^*\times(0,t_{\mathrm{f}}),\\ \dfrac{\partial\rho}{\partial t}+\nabla\cdot(\rho\mathbf{u}_{\mathrm{P}})=0 & \text{in} \quad \Omega_{\mathrm{P}}^*\times(0,t_{\mathrm{f}}), \end{cases} \tag{3.7}$$

with point, boundary and initial conditions

$$\begin{cases} k\dfrac{\partial T}{\partial\mathbf{n}}=0 & \text{on} \quad \left(\Gamma^*\setminus(\Gamma_{\mathrm{r}}^*\cup\Gamma_{\mathrm{up}}^*)\right)\times(0,t_{\mathrm{f}}),\\ k\dfrac{\partial T}{\partial z}=h(T_{\mathrm{env}}-T) & \text{on} \quad \Gamma_{\mathrm{up}}^*\times(0,t_{\mathrm{f}}),\\ T=T_{\mathrm{r}} & \text{on} \quad \Gamma_{\mathrm{r}}^*\times(0,t_{\mathrm{f}}),\\ \mathbf{u}_{\mathrm{F}}=0 & \text{on} \quad \Gamma_{\mathrm{F}}^*\times(0,t_{\mathrm{f}}),\\ \mathbf{u}_{\mathrm{P}}=0 & \text{on} \quad \Gamma_{\mathrm{P}}^*\times(0,t_{\mathrm{f}}),\\ T(0)=T_0 & \text{in} \quad \Omega^*,\\ \mathbf{u}_{\mathrm{F}}(0)=0 & \text{in} \quad \Omega_{\mathrm{F}}^*,\\ \mathbf{u}_{\mathrm{P}}(0)=0 & \text{in} \quad \Omega_{\mathrm{P}}^*,\\ p=10^5 & \text{on} \quad \mathbf{A}_1\times(0,t_{\mathrm{f}}),\\ p=10^5 & \text{on} \quad \mathbf{A}_2\times(0,t_{\mathrm{f}}), \end{cases} \tag{3.8}$$

where Γ_{F}^* denotes the boundary of Ω_{F}^*, Γ_{P}^* denotes the boundary of Ω_{P}^* and $\mathbf{A}_1$, $\mathbf{A}_2$ are points of Γ_{P}^* and Γ_{F}^*, respectively (see Figure 3.2).

In this case convection plays a very important role, not only in the pressurising fluid, but also in the liquid-type food. Therefore, to neglect its effect (as in the big solid case), could lead to very different results from the real thermal behaviour, for both large and small samples.

3.3 Simplified models

In [46] the authors proposed several simplified models in order to reduce the computational complexity needed to solve the full models, and checked the validity of such models, showing that compared to the full models, the simplified ones give similar results and were proved to be faster and easier to implement. Therefore, following the work done in [46] we describe some simplified models that will be used in later Chapters, to make the implementation of freezing models and three-dimensional models, among others, a bit simpler.

3.3.1 For a large solid-type food

For a large solid-type food we consider a simplified version of system (3.5), which has constant coefficients by setting the thermo-physical parameters C_p, k, β and ρ to their mean value in the range of temperature and pressure considered in the process. This model is denoted by SCC in [46].

3.3.2 For a small solid-type food

For the small solid-type food, where convection effects in the pressurising medium are included, see system (3.6), apart from also considering constant thermo-physical properties, a simplification based on the Boussinesq approximation is made [46]. More precisely, coefficients C_p, k, β and η are considered to be constant (instead of temperature and pressure dependent), and are set to their mean value ($\bar{C}_p$, $\bar{k}$, $\bar{\beta}$ and $\bar{\eta}$, respectively) in the range of temperature and pressure considered in the process; ρ is also chosen as a constant value $\bar{\rho}$, except for the gravitational force $\rho\mathbf{g}$ that appears in the second system (3.6), where ρ remains dependent on temperature and pressure (in order to keep the effect of the gravitational forces). Furthermore, we assume the pressurising fluid is incompressible. With the simplifications system (3.6) can be written as

$$
\begin{cases}
\bar{\rho}\bar{C}_p\dfrac{\partial T}{\partial t} - \nabla\cdot(\bar{k}\nabla T) + \bar{\rho}\bar{C}_p\mathbf{u}\cdot\nabla T = \bar{\beta}\dfrac{\mathrm{d}P}{\mathrm{d}t}T, & \text{in} \quad \Omega^*\times(0,t_{\mathrm{f}}),\\
\bar{\rho}\dfrac{\partial \mathbf{u}}{\partial t} - \bar{\eta}\nabla^2\mathbf{u} + \bar{\rho}(\mathbf{u}\cdot\nabla)\mathbf{u} = -\nabla p + \rho\mathbf{g} & \text{in} \quad \Omega_{\mathrm{P}}^*\times(0,t_{\mathrm{f}}),\\
\nabla\cdot(\mathbf{u}) = 0 & \text{in} \quad \Omega_{\mathrm{P}}^*\times(0,t_{\mathrm{f}}),\\
\bar{k}\dfrac{\partial T}{\partial \mathbf{n}} = 0 & \text{on} \quad \Gamma_0^*\times(0,t_{\mathrm{f}}),\\
\bar{k}\dfrac{\partial T}{\partial \mathbf{n}} = h(T_{\mathrm{env}} - T) & \text{on} \quad \Gamma_{\mathrm{up}}^*\times(0,t_{\mathrm{f}}),\\
T = T_{\mathrm{r}} & \text{on} \quad \Gamma_{\mathrm{r}}^*\times(0,t_{\mathrm{f}}),\\
\mathbf{u} = 0 & \text{on} \quad \Gamma_{\mathrm{P}}^*\times(0,t_{\mathrm{f}}),\\
T(0) = T_0 & \text{in} \quad \Omega^*,\\
\mathbf{u}(0) = 0 & \text{in} \quad \Omega^*,\\
p = 10^5 & \text{at} \quad \mathbf{A}_1\times(0,t_{\mathrm{f}}).
\end{cases}
\tag{3.9}
$$

3.3.3 For a liquid-type food

For a liquid-type food we also use the same simplified model based on the Boussinesq approximation, this time for both the liquid food and pressurising medium (this approximation is denoted by LB in [46]). Thus system (3.7) is simplified to

$$\begin{cases} \bar{\rho}\bar{C_p}\dfrac{\partial T}{\partial t} - \bar{k}\nabla^2 T + \bar{\rho}\bar{C_p}\mathbf{u}\cdot\nabla T = \bar{\beta}\ \dfrac{\mathrm{d}P}{\mathrm{d}t}\ T & \text{in} \quad \Omega^* \times (0, t_\mathrm{f}), \\ \bar{\rho}\dfrac{\partial \mathbf{u}_\mathrm{F}}{\partial t} - \bar{\eta}\nabla^2\mathbf{u}_\mathrm{F} + \bar{\rho}(\mathbf{u}_\mathrm{F}\cdot\nabla)\mathbf{u}_\mathrm{F} = -\nabla p + \rho\mathbf{g} & \text{in} \quad \Omega^*_\mathrm{F} \times (0, t_\mathrm{f}), \\ \bar{\rho}\dfrac{\partial \mathbf{u}_\mathrm{P}}{\partial t} - \bar{\eta}\nabla^2\mathbf{u}_\mathrm{P} + \bar{\rho}(\mathbf{u}_\mathrm{P}\cdot\nabla)\mathbf{u}_\mathrm{P} = -\nabla p + \rho\mathbf{g} & \text{in} \quad \Omega^*_\mathrm{P} \times (0, t_\mathrm{f}), \\ \nabla\cdot(\mathbf{u}_\mathrm{F}) = 0 & \text{in} \quad \Omega^*_\mathrm{F} \times (0, t_\mathrm{f}), \\ \nabla\cdot(\mathbf{u}_\mathrm{P}) = 0 & \text{in} \quad \Omega^*_\mathrm{P} \times (0, t_\mathrm{f}), \end{cases} \tag{3.10}$$

with boundary and initial conditions given by (3.8).

Chapter 4

Dimensional analysis and simplifications

Nomenclature for Chapter 4

A	Enzymatic activity
$a,\ b,\ c,\ d$	Dimensionless groups of parameters
C_p	Specific heat capacity (J kg^{-1} K^{-1})
h	Heat transfer coefficient (W m^{-2} K^{-1})
H	Half of the food domain height (m)
H_2	Half of the complete domain height (m)
$J_n(\cdot)$	Bessel function of the first kind of order n
k	Thermal conductivity (W m^{-1} K^{-1})
L	Food domain width (m)
L_2	Complete domain width (m)
$\mathbf{n}$	Outward normal unit vector (m)
P	Equipment Pressure (Pa)
r	Radial coordinate (m)
R	Radial scale (m)
t	Time (s)
t_f	Final time (s)
t_p	Pressure-up time (s)
T	Temperature (K)
T_0	Initial temperature (K)
T_r	Fixed temperature (K)
z	Vertical coordinate (m)
Z	Height scale (m)

Indices

*	Rotated domains
0	Initial
F	Food domain
in	Inner solution for boundary layer
out	Outer solution for boundary layer
S	Steel vessel domain
up	Pressure-up solution

Acronyms

BSAA	Bacillus Subtilis α-Amylase
CPE	Carrot Pectin Methyl-Esterase
FEM	Finite Element Method
HP	High-Pressure
LOX	Lipoxygenase
ODE	Ordinary Differential Equation
PDE	Partial Differential Equation
1D	One-dimensional
2D	Two-dimensional
2D-all	2D averaged over all domain
2D-ave	2D averaged over all domain excluding top
2D-mid	2D at middle height
3D	Three-dimensional

Greek symbols

β	Thermal expansion coefficient (K^{-1})
χ	Characteristic function in $(0, t_\mathrm{p})$
ΔT	Temperature scale (K)
γ	Maximum pressure reached (Pa)
Γ^D	Whole domain boundary
$\Gamma^\mathrm{D}_\mathrm{exc}$	Heat transfer boundary
$\Gamma^\mathrm{D}_\mathrm{r}$	Fixed temperature boundary
$\Gamma^\mathrm{D}_\mathrm{sym}$	Axis-symmetric boundary
η	Dynamic viscosity (Pa s)
κ	Inactivation rate (min^{-1})
ρ	Density (kg m^{-3})
τ	Time scale (s)
Ω^D	Whole domain
$\Omega^\mathrm{D}_\mathrm{F}$	Food sample domain
$\Omega^\mathrm{D}_\mathrm{S}$	Steel vessel

4.1 Introduction

In this Chapter we focus only on solid type foods, with a large filling ratio, where convection effects do not need to be taken into account as pointed out in Chapter 3. We perform a dimensional analysis which highlights the dominant terms in the model, and shows that in some cases the equations can be simplified (in dimension) and yet provide a good approximation. These models for HP processes are much simpler than those found in the literature [21, 46, 52], but still have the correct qualitative features, and hence would be very important when designing suitable industrial equipments and optimizing the processes. Moreover, using the solutions we propose, there is no need to have an FEM solver in order to simulate the process. This Chapter is based on the analysis in [85].

In [54, 55] dimensional analysis of thermo-fluid-dynamic mechanisms taking place during HP treatment of bio-substances is carried out, and both forced and free convection case is described. As the authors point out in [54], dimensional analysis gives the possibility to reduce the large number of internal and external parameters related to a HP treatment of a bio-substance, and also to generalise the statement about the process mechanisms and phenomena, showing which have a significant influence and which plays a minor role on the thermo-fluid-dynamics of HP processes. A large value of the dimensionless group, points out an elevated importance of these mechanisms on the momentum and heat transfer in HP autoclaves. In contrast, if dimensionless parameters become very small, it means that these terms can be neglected. In [55] the thermo-fluid-dynamical mechanisms are analysed for three different sizes of a HP chamber, two different pressure generation systems and two model-fluids that differ in viscosity, again discussing the cases of forced and free convection. The results presented by the authors contain process parameter study based on dimensionless numbers derived from conservation equations of mass, momentum and energy, which as stated in [54], can be very useful for transformation of laboratory investigations and results into the industrial scale. In both papers, the authors point out that in further investigations the temporal and spatial distribution of process parameters in the chamber should be taken into consideration.

The dimensional analysis we perform throughout this Chapter is for simpler models than those described in [54, 55] (as we do not consider fluid-dynamics), but nevertheless, we do take into account the temporal and spatial temperature distribution. After identifying the relevant process parameters and neglecting the non-important ones, we proceed to solve the resulting non-dimensional systems. Furthermore, due to the simplicity of the reduced systems, we can find analytical solutions rather than only numerical ones.

In Section 4.2 we describe the problem and present the governing equations to calculate the temperature distribution. A dimensional analysis is then performed to simplify the model. Sections 4.3 and 4.4 contain a thorough investigation of the complete and simplified models for the pressure up and pressure hold times, respectively, and we are able to find exact and approximate solutions describing the whole process. In Section 4.5 we present some numerical results of a particular process, comparing all the models to exact and numerical solutions. In Section 4.6 we couple the simplified heat transfer models to an enzymatic inactivation model. Section 4.7 briefly considers an extension to third class boundary conditions and, finally, in Section 4.8 we give concluding remarks.

4.2 Problem Description

As already stated in Chapter 3, when HP is applied in food technology, it is necessary to take into account the thermal effects that are produced by variations of temperature due to the compression/expansion occurring in the food sample and the pressurizing medium. In practice, the pressure evolution, $P(t)$, is known as it is imposed by the user and the limits of the equipment. The temperature of the processed food may change with time and space, therefore we need a heat transfer model capable of predicting the temperature for the processed food. From Chapter 3 we know that for solid-type foods with a large filling ratio, a heat transfer model taking into account only conduction effects is sufficient for correctly predicting the temperature distribution. As the model is both time and spatially dependent, we also introduce a brief description of the domain describing the HP device considered in our simulations, which is a slight variation of the one presented in Chapter 3.

4.2.1 Mathematical Model

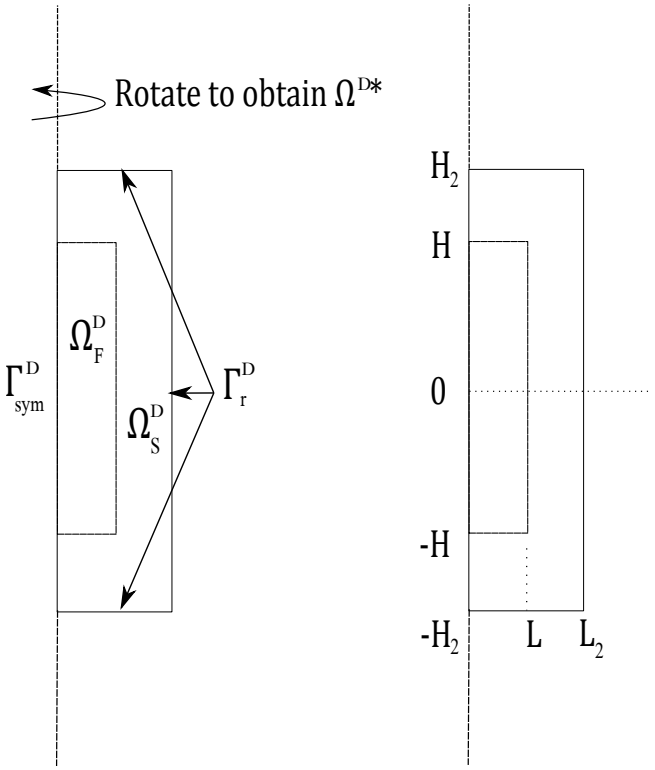

Figure 4.1: Simplified 2D axis-symmetric computational domain for dimensional analysis

In this Chapter we analyse an axis-symmetric two-dimensional geometry with only the food and the surrounding steel (see Figure 4.1). This is a simplified version of the geometry presented in Chapter 3 (see Figure 3.2), which also included the pressurising fluid and the rubber cap of sample holder. As a matter of fact, other authors have studied even more complex geometries, which included, e.g. the carrier [52]. However, in this Chapter our focus is on studying a solid-type food with a large filling ratio, where the pressure medium represents a low proportion of the vessel content, and so we assume that the pressurizing fluid can be ignored (the rubber cap is also ignored for the sake of simplicity).

The domain in the cylindrical (r, z)-coordinates is the rectangle $\Omega^{\mathrm{D}} = [0, L_2] \times [-H_2, H_2]$ defined by $\overline{\Omega^{\mathrm{D}}} = \overline{\Omega_{\mathrm{F}}^{\mathrm{D}} \cup \Omega_{\mathrm{S}}^{\mathrm{D}}}$, where $\Omega_{\mathrm{F}}^{\mathrm{D}} = [0, L] \times [-H, H]$ is the food domain, and $\Omega_{\mathrm{S}}^{\mathrm{D}}$ is the domain of the steel that surrounds the food. We use $\Omega^{\mathrm{D}*}$ to denote the 3D domain generated by rotating Ω^{D} along the axis of symmetry ($\{0\} \times (-H_2, H_2)$). The boundary of Ω^{D} is denoted by $\Gamma^{\mathrm{D}} = \Gamma_{\mathrm{r}}^{\mathrm{D}} \cup \Gamma_{\mathrm{sym}}^{\mathrm{D}}$, where we can distinguish $\Gamma_{\mathrm{r}}^{\mathrm{D}}$ on which the temperature is known, and $\Gamma_{\mathrm{sym}}^{\mathrm{D}}$ that has zero heat flux by axial symmetry.

We would like to remark that the notation used here is very similar to the one used in Chapter 3, however we have added the subscript $^{\mathrm{D}}$ to denote that we are in the geometry for the dimensional analysis Chapter, which has slightly change with respect to the one presented in the previous Chapter.

Since we are only concerned in analysing solid-type foods with a large filling ratio, we only take into account conduction effects (and neglect convection effects). Thus, when large solid-type foods are considered, as we saw in Section 3.1.1 of Chapter 3, we start with the heat conduction equation for temperature T (K)

$$\rho C_p \frac{\partial T}{\partial t} - \nabla \cdot (k \nabla T) = \beta \, \frac{\mathrm{d}P}{\mathrm{d}t} \, T \qquad \text{in} \quad \Omega^{\mathrm{D}*} \times (0, t_{\mathrm{f}}), \tag{4.1}$$

where now β is defined as in (3.2), but only has one non-zero component, β_{F} (due to the fact that we are no longer including the pressurising fluid region). For the sake of simplicity, we are going to use the assumption of constant thermo-physical properties described in Section 3.3.1.

By using cylindrical coordinates and taking into account axial symmetry, equation (4.1) may be re-written in 2D as

$$\rho\, C_p\, \frac{\partial T}{\partial t} - \frac{1}{r}\frac{\partial}{\partial r}\left(rk\frac{\partial T}{\partial r}\right) - \frac{\partial}{\partial z}\left(k\frac{\partial T}{\partial z}\right) = \beta\, \frac{\mathrm{d}P}{\mathrm{d}t}\, T \qquad \text{in} \quad \Omega^{\mathrm{D}} \times (0, t_{\mathrm{f}}). \tag{4.2}$$

Equation (4.2) must be completed with appropriate boundary and initial conditions. In this Chapter, for simplicity we assume that the outer walls of the domain are kept at a constant temperature T_{r}, and that the initial temperature T_0 is constant in each region, therefore giving

$$\begin{cases} \dfrac{\partial T}{\partial r} = 0 & \text{on} \quad \Gamma^{\mathrm{D}}_{\mathrm{sym}}, \\ T = T_{\mathrm{r}} & \text{on} \quad \Gamma^{\mathrm{D}}_{\mathrm{r}}, \\ T = T_0 & \text{at} \quad t = 0. \end{cases} \tag{4.3}$$

In Section 4.7 we briefly discuss an extended model with third class boundary conditions. Several authors have considered different boundary conditions to those described above. As we pointed out in Chapter 3, Infante *et al.* [46] and Otero *et al.* [69] assumed a boundary was kept at a refrigerated temperature, as well as a boundary allowing for heat transfer with the room. Denys *et al.* [21] considered an overall heat transfer coefficient at the surface of the cylinder to account for heat transfer through the walls of the HP vessel. Although our conditions (4.3) may seem overly simplistic from a practical consideration, it has been suggested in the literature that keeping the walls of machine at a constant temperature may be good for avoiding heat loss [71]. There can be a problem of heat loss through the wall of the HP vessel, and by anticipating the temperature increase of the processed product, resulting from compression, conductive heat transfer and temperature gradients can be avoided [21].

In the following Sections we study exact and approximate solutions for the model with first class boundary conditions. It is convenient to begin by non-dimensionalising the model to highlight whether any simplifications are possible.

4.2.2 Dimensional analysis

Given that the pressure function in equation (4.2) only appears in a derivative form, and that the pressure applied on these processes is typically a piecewise linear function in time (hence such a derivative is usually piecewise constant), we do not non-dimensionalise the pressure variable. Instead, we rewrite the pressure derivative $\frac{\mathrm{d}P}{\mathrm{d}t}(t)$ as

$$\frac{\mathrm{d}P}{\mathrm{d}t}(t) = \begin{cases} \dfrac{\gamma}{t_{\mathrm{p}}}, & 0 < t \le t_{\mathrm{p}}, \\ 0, & t > t_{\mathrm{p}}, \end{cases} \tag{4.4}$$

where, for the sake of simplicity, we suppose that $\frac{\mathrm{d}P}{\mathrm{d}t}(t) = \frac{\gamma}{t_{\mathrm{p}}} > 0$ (P linear) for all $t \in [0, t_{\mathrm{p}}]$, and γ (Pa) is the maximum pressure reached (for the sake of simplicity we assume that atmospheric pressure is 0 MPa, instead of 0.1 MPa, which is typically the real value). After time t_{p} the pressure is maintained constant at the maximum value, and therefore the derivative is zero (other cases can be also studied similarly). The release of pressure that takes place after t_{f} can be modelled with the same approach. Since it does not introduce any further difficulty we have not considered it here.

Therefore, for $0 < t \le t_{\mathrm{p}}$ equation (4.2) can be written as

$$\rho\, C_p\, \frac{\partial T}{\partial t} - \frac{1}{r}\frac{\partial}{\partial r}\left(rk\frac{\partial T}{\partial r}\right) - \frac{\partial}{\partial z}\left(k\frac{\partial T}{\partial z}\right) = \beta\, \frac{\gamma}{t_{\mathrm{p}}}\, T, \tag{4.5}$$

and for $t_{\mathrm{p}} < t \le t_{\mathrm{f}}$ the same equation holds, except with the right-hand side equal to zero.

The system is now non-dimensionalised by setting

$$\hat{r} = \frac{r}{R}, \qquad \hat{z} = \frac{z}{Z}, \qquad \hat{t} = \frac{t}{\tau}, \qquad \hat{T} = \frac{T - T_{\mathrm{r}}}{\Delta T},$$

where ΔT, R, Z and τ are suitable temperature, radius, height and time scales, respectively.

Thus, for $0 < \hat{t} \leq \frac{t_\mathrm{p}}{\tau}$, equation (4.5) becomes

$$\frac{\rho\ C_p\ \Delta T}{\tau}\frac{\partial \hat{T}}{\partial \hat{t}} - \frac{k\Delta T}{R^2\hat{r}}\frac{\partial}{\partial \hat{r}}\left(\hat{r}\frac{\partial \hat{T}}{\partial \hat{r}}\right) - \frac{k\Delta T}{Z^2}\frac{\partial^2 \hat{T}}{\partial \hat{z}^2} = \frac{\beta\gamma\Delta T}{t_\mathrm{p}}(\hat{T} + \frac{T_\mathrm{r}}{\Delta T}). \tag{4.6}$$

For ease of notation we drop the $\hat{}$ notation, and so T, z, r and t are now the non-dimensional variables.

We divide equation (4.6) by $\rho C_p \Delta T/\tau$, resulting in

$$\frac{\partial T}{\partial t} - \frac{k\tau}{R^2\rho C_p}\frac{1}{r}\frac{\partial}{\partial r}\left(r\frac{\partial T}{\partial r}\right) - \frac{k\tau}{Z^2\rho C_p}\frac{\partial^2 T}{\partial z^2} = \frac{\beta\gamma\tau}{\rho C_p t_\mathrm{p}}T + \frac{\beta\gamma\tau}{\rho C_p t_\mathrm{p}}\frac{T_\mathrm{r}}{\Delta T}. \tag{4.7}$$

The dimensionless groups of parameters in equation (4.7) are

$$a = \frac{k\tau}{R^2\rho C_p}, \qquad b = \frac{k\tau}{Z^2\rho C_p}, \qquad c = \frac{\beta\gamma\tau}{\rho C_p t_\mathrm{p}}, \qquad d = \frac{\beta\gamma\tau}{\rho C_p t_\mathrm{p}}\frac{T_\mathrm{r}}{\Delta T}. \tag{4.8}$$

The radius and height scales that we propose come from the dimensions of the food cylinder, giving $R = L$ and $Z = H$. Note that we are only considering half of the height of the domain as the z scale for the sake of simplicity. For the temperature scale we set $\Delta T = \max\{|T_0 - T_\mathrm{r}|, \frac{\beta\gamma T_0}{\rho C_p}\}$, where ρ and C_p are the density and specific heat of the food sample, respectively. The quantity $\frac{\beta\gamma T_0}{\rho C_p}$ is the maximum increase of temperature in the food sample due to the increase of pressure (according to (3.3)). The time scale τ is chosen from equation (4.7). We wish to investigate what happens when the pressure is increased and therefore balance the pressure term with the time derivative. This leads to

$$\tau = \frac{\rho C_p t_\mathrm{p}}{\beta\gamma}\min\left\{1, \frac{\Delta T}{T_\mathrm{r}}\right\}.$$

The system in non-dimensional form is therefore given by

$$\begin{cases} \dfrac{\partial T}{\partial t} - a\dfrac{1}{r}\dfrac{\partial}{\partial r}\left(r\dfrac{\partial T}{\partial r}\right) - b\dfrac{\partial^2 T}{\partial z^2} = (cT + d)\chi(t) & \text{in} \quad \hat{\Omega^\mathrm{D}} \times (0, t_\mathrm{f}), \\ \dfrac{\partial T}{\partial r} = 0 & \text{on} \quad \hat{\Gamma^\mathrm{D}}_{\mathrm{sym}}, \\ T = 0 & \text{on} \quad \hat{\Gamma^\mathrm{D}}_{\mathrm{r}}, \\ T = T_0^* & \text{at} \quad t = 0, \end{cases} \tag{4.9}$$

where $\hat{\Omega^\mathrm{D}} = (0, \frac{L_2}{L}) \times (\frac{-H_2}{H}, \frac{H_2}{H})$ is the non-dimensional form of the whole domain Ω^D. The function $\chi(t)$ is defined as

$$\chi(t) = \begin{cases} 1, & \text{if} \quad t \in (0, t_\mathrm{p}), \\ 0, & \text{elsewhere.} \end{cases}$$

Note that t_p/τ and t_f/τ have been redefined as t_p and t_f for convenience. The non-dimensional initial value is

$$T_0^* = \frac{T_0 - T_\mathrm{r}}{\Delta T}. \tag{4.10}$$

It should be pointed out that in (4.8), $b = a\frac{R^2}{Z^2}$ and hence with the chosen scales $b = a\frac{L^2}{H^2}$. This will mean that if the food sample holder is narrow and tall (which is usually the case for the HP pilot scale machines), the conduction parameter in the z direction, b, will be smaller than that in the r direction, a. Thus we wish to investigate whether the heat transfer due to conduction is dominant in the radial direction over the height direction, for a thin and tall machine. This will be studied in Sections 4.3.2 and 4.4.2.

System (4.9) is set in $\hat{\Omega^\mathrm{D}}$, which involves the two regions to determine the temperature in the food, T_F, and in the steel, T_S. Taking into account that parameters c and d defined in (4.8) are zero in the steel region, as

$\beta = 0$, (4.9) is defined as

$$\begin{cases} \dfrac{\partial T_{\mathrm{F}}}{\partial t} - a_{\mathrm{F}} \dfrac{1}{r} \dfrac{\partial}{\partial r} \left(r \dfrac{\partial T_{\mathrm{F}}}{\partial r} \right) - b_{\mathrm{F}} \dfrac{\partial^2 T_{\mathrm{F}}}{\partial z^2} = (c_{\mathrm{F}} T_{\mathrm{F}} + d_{\mathrm{F}}) \chi(t) & \text{in} \quad \hat{\Omega^{\mathrm{D}}}_{\mathrm{F}} \times (0, t_{\mathrm{f}}), \\ \dfrac{\partial T_{\mathrm{S}}}{\partial t} - a_{\mathrm{S}} \dfrac{1}{r} \dfrac{\partial}{\partial r} \left(r \dfrac{\partial T_{\mathrm{S}}}{\partial r} \right) - b_{\mathrm{S}} \dfrac{\partial^2 T_{\mathrm{S}}}{\partial z^2} = 0 & \text{in} \quad \hat{\Omega^{\mathrm{D}}}_{\mathrm{S}} \times (0, t_{\mathrm{f}}), \\ \dfrac{\partial T_{\mathrm{F}}}{\partial r} = 0, \qquad \dfrac{\partial T_{\mathrm{S}}}{\partial r} = 0 & \text{on} \quad \hat{\Gamma^{\mathrm{D}}}_{\mathrm{sym}}, \\ k_{\mathrm{F}} \dfrac{\partial T_{\mathrm{F}}}{\partial r} = k_{\mathrm{S}} \dfrac{\partial T_{\mathrm{S}}}{\partial r}, \qquad T_{\mathrm{F}} = T_{\mathrm{S}} & \text{on} \quad \hat{\Gamma^{\mathrm{D}}}_{\mathrm{FS}}, \\ T_{\mathrm{S}} = 0 & \text{on} \quad \hat{\Gamma^{\mathrm{D}}}_{\mathrm{r}}, \\ T_{\mathrm{F}} = T^*_{\mathrm{F}_0}, \qquad T_{\mathrm{S}} = T^*_{\mathrm{S}_0} & \text{at} \quad t = 0, \end{cases} \tag{4.11}$$

where $T^*_{\mathrm{F}_0}$ and $T^*_{\mathrm{S}_0}$ are the non-dimensional initial temperatures in the food and steel, respectively. $\hat{\Omega^{\mathrm{D}}}_{\mathrm{F}} = (0,1) \times (-1,1)$ is the non-dimensional food region, and $\hat{\Omega^{\mathrm{D}}}_{\mathrm{S}} = \hat{\Omega^{\mathrm{D}}} - \hat{\Omega^{\mathrm{D}}}_{\mathrm{F}}$ the steel one. On the non-dimensional food-steel boundary, $\hat{\Gamma^{\mathrm{D}}}_{\mathrm{FS}} = \big[(0,1) \times \{1\}\big] \cup \big[(0,1) \times \{-1\}\big] \cup \big[\{1\} \times (-1,1)\big]$, continuity of the solution and the fluxes has been imposed.

We begin by determining an approximate solution for the steel temperature. By assuming that the conductivity of steel is much larger than that of the food, we can simplify the flux boundary condition on $\hat{\Gamma^{\mathrm{D}}}_{\mathrm{FS}}$

$$\frac{\partial T_{\mathrm{S}}}{\partial r} = \frac{k_{\mathrm{F}}}{k_{\mathrm{S}}} \frac{\partial T_{\mathrm{F}}}{\partial r} \approx 0, \qquad \text{on } \hat{\Gamma^{\mathrm{D}}}_{\mathrm{FS}}. \tag{4.12}$$

If we also assume that we are working with a narrow and tall machine, i.e. that $L << H$, and hence $b_{\mathrm{S}} << a_{\mathrm{S}}$, the equation for the steel reduces to

$$\frac{\partial T_{\mathrm{S}}}{\partial t} - a_{\mathrm{S}} \frac{1}{r} \frac{\partial}{\partial r} \left(r \frac{\partial T_{\mathrm{F}}}{\partial r} \right) = 0, \qquad \text{in } \hat{\Omega^{\mathrm{D}}}_{\mathrm{S}} \times (0, t_{\mathrm{f}}). \tag{4.13}$$

Since steel has a high thermal diffusivity, a_{S}, the solution of (4.13) goes to steady state very rapidly, and the solution to the steady state problem is zero (using the zero flux and zero temperature boundary conditions). Hence we can conclude that $T_{\mathrm{S}} \approx 0$. Then the boundary condition for the food at $\hat{\Gamma^{\mathrm{D}}}_{\mathrm{FS}}$ can be approximated by $T_{\mathrm{F}} \approx 0$.

Thus, we now only have the temperature in the food problem to solve, and (4.11) reduces to

$$\begin{cases} \dfrac{\partial T_{\mathrm{F}}}{\partial t} - a_{\mathrm{F}} \dfrac{1}{r} \dfrac{\partial}{\partial r} \left(r \dfrac{\partial T_{\mathrm{F}}}{\partial r} \right) - b_{\mathrm{F}} \dfrac{\partial^2 T_{\mathrm{F}}}{\partial z^2} = (c_{\mathrm{F}} T_{\mathrm{F}} + d_{\mathrm{F}}) \chi(t) & \text{in} \quad (0,1) \times (-1,1) \times (0, t_{\mathrm{f}}), \\ \dfrac{\partial T_{\mathrm{F}}}{\partial r} = 0 & \text{on} \quad r = 0, \\ T_{\mathrm{F}} = 0 & \text{on} \quad r = 1, \\ T_{\mathrm{F}} = 0 & \text{on} \quad z = -1, \\ T_{\mathrm{F}} = 0 & \text{on} \quad z = 1, \\ T_{\mathrm{F}} = T^*_{\mathrm{F}_0} & \text{at} \quad t = 0. \end{cases} \tag{4.14}$$

One further simplification of system (4.14) can be made, and this is to divide the domain in half at $z = 0$ and impose a zero flux boundary condition. Due to symmetry we only need to solve the problem in the upper half

of the domain. Finally we have system for T_{F} (that we will simply refer to as T henceforth)

$$\begin{cases} \dfrac{\partial T}{\partial t} - a\dfrac{1}{r}\dfrac{\partial}{\partial r}\left(r\dfrac{\partial T}{\partial r}\right) - b\dfrac{\partial^2 T}{\partial z^2} = (cT+d)\chi(t) & \text{in} \quad (0,1)\times(0,1)\times(0,t_{\mathrm{f}}), \\ \dfrac{\partial T}{\partial r} = 0 & \text{on} \quad r=0, \\ T = 0 & \text{on} \quad r=1, \\ \dfrac{\partial T}{\partial z} = 0 & \text{on} \quad z=0, \\ T = 0 & \text{on} \quad z=1, \\ T = T_0^* & \text{at} \quad t=0. \end{cases} \tag{4.15}$$

4.3 Analysis for the pressure up time $0 \leq t \leq t_{\mathrm{p}}$

4.3.1 Exact solution

An exact solution can be found by solving the 2D system (4.15) using separation of variables. We can create a homogeneous problem by setting

$$T(r,z,t) = u(r,z,t) + v(r,z) + w(z). \tag{4.16}$$

Then the problem to solve for u is

$$\begin{cases} \dfrac{\partial u}{\partial t} = a\dfrac{1}{r}\dfrac{\partial}{\partial r}\left(r\dfrac{\partial u}{\partial r}\right) + b\dfrac{\partial^2 u}{\partial z^2} + cu & \text{in} \quad (0,1)\times(0,1)\times(0,t_{\mathrm{p}}), \\ \dfrac{\partial u}{\partial r} = 0 & \text{on} \quad r=0, \\ u = 0 & \text{on} \quad r=1, \\ \dfrac{\partial u}{\partial z} = 0 & \text{on} \quad z=0, \\ u = 0 & \text{on} \quad z=1, \\ u = T_0^* - v(r,z) - w(z) & \text{at} \quad t=0, \end{cases} \tag{4.17}$$

whilst the problem for v is

$$\begin{cases} 0 = a\dfrac{1}{r}\dfrac{\partial}{\partial r}\left(r\dfrac{\partial v}{\partial r}\right) + b\dfrac{\partial^2 v}{\partial z^2} + cv & \text{in} \quad (0,1)\times(0,1)\times(0,t_{\mathrm{p}}), \\ \dfrac{\partial v}{\partial r} = 0 & \text{on} \quad r=0, \\ v = -w(z) & \text{on} \quad r=1, \\ \dfrac{\partial v}{\partial z} = 0 & \text{on} \quad z=0, \\ v = 0 & \text{on} \quad z=1, \end{cases} \tag{4.18}$$

and the problem for w is

$$bw''(z) + cw(z) + d = 0, \qquad w'(0) = 0, \qquad w(1) = 0. \tag{4.19}$$

This has solution

$$w(z) = \frac{d}{c}\left(\frac{\cos(\mu z)}{\cos\mu} - 1\right), \tag{4.20}$$

where $\mu = \sqrt{c/b}$.

We use the method of separation of variables and set $v(r,z) = R(r)Z(z)$. Then the boundary conditions imply that $R'(0) = Z'(0) = Z(1) = 0$. From (4.18) we deduce that

$$\frac{\frac{a}{r}(R'(r) + rR''(r)) + cR(r)}{bR(r)} = -\frac{Z''(z)}{Z(z)} = \nu^2, \tag{4.21}$$

for suitable constants $\nu \in \mathbb{R}$, where $(\cdot)'$ denotes differentiation with respect to each variable. Solving the ODE for $Z(z)$ leads to

$$Z_p(z) = A_{Zp}\cos(\nu_p z), \qquad p = 1,\, 2,\, \ldots, \tag{4.22}$$

with $A_{Zp} \in \mathbb{R}$, and $\nu_p = (p - 1/2)\pi$. The ODE for $R(r)$ from (4.21) is

$$arR''(r) + aR'(r) + (c - \nu_p^2 b)rR(r) = 0, \tag{4.23}$$

which, after satisfying the boundary condition $R'(0) = 0$, has solution

$$R_p(r) = A_{Rp}J_0(\alpha_p r), \tag{4.24}$$

where J_n is the Bessel function of the first kind of order n, $A_{Rp} \in \mathbb{R}$, and

$$\alpha_p = \sqrt{\frac{c - \nu_p^2 b}{a}}. \tag{4.25}$$

The combined solution is therefore

$$v(r,z) = \sum_{p=1}^{\infty} A_p J_0(\alpha_p r)\cos(\nu_p z). \tag{4.26}$$

Coefficients A_p are found using the boundary condition $v = -w(z)$ from system (4.18). Thus

$$-w(z) = \sum_{p=1}^{\infty} A_p J_0(\alpha_p)\cos(\nu_p z), \tag{4.27}$$

where $w(z)$ is defined in (4.20). Integrating (4.27) and applying the orthogonality condition it follows that

$$A_p = -\frac{2}{J_0(\alpha_p)}\int_0^1 w(z)\cos(\nu_p z)\,\mathrm{d}z, \tag{4.28}$$

We finally turn to the problem for u in (4.17) and separate variables by setting $u(r,z,t) = R(r)Z(z)\Phi(t)$. Then the boundary conditions imply that $R'(0) = R(1) = Z'(0) = Z(1) = 0$. From (4.17) we deduce that now

$$\frac{\Phi'(t)}{\Phi(t)} = \frac{\frac{a}{r}(R'(r) + rR''(r))Z(z) + bR(r)Z''(z) + cR(r)Z(z)}{R(r)Z(z)} = -\lambda^2. \tag{4.29}$$

and so the first equation is solved to give $\Phi(t) = B\exp(-\lambda^2 t)$, for suitable constants $\lambda \in \mathbb{R}$. The solutions of R and Z are found in an identical manner to that described above, and so

$$Z_m(z) = C_{Zm}\cos(\nu_m z), \quad m = 1,\, 2,\, \ldots, \qquad R_n(r) = C_{Rn}J_0(\delta_n r), \quad n = 1,\, 2,\, \ldots, \tag{4.30}$$

where $\nu_m = (m - 1/2)\pi$ and

$$\delta_n = \sqrt{\frac{c + \lambda_{mn}^2 - \nu_m^2 b}{a}}. \tag{4.31}$$

These are found by solving $J_0(\delta_n) = 0$, in order to satisfy $R(0) = 0$, and then λ_{mn} can be determined from the formula $\lambda_{mn} = \sqrt{a\delta_n^2 + b\nu_m^2 - c}$.

The combined solution for u is therefore

$$u(r,z,t) = \sum_{n=1}^{\infty}\sum_{m=1}^{\infty} D_{mn}J_0(\delta_n r)\cos(\nu_m z)\exp(-\lambda_{mn}^2 t), \tag{4.32}$$

and coefficients D_{mn} are found using the initial condition in (4.17). Thus

$$T_0^* - v(r,z) - w(z) = \sum_{n=1}^{\infty}\sum_{m=1}^{\infty} D_{mn} J_0(\delta_n r)\cos(\nu_m z), \tag{4.33}$$

where $w(z)$ and $v(r,z)$ are defined in (4.20) and (4.26)-(4.28) respectively. Integrating with respect to r and z and using the orthogonality conditions leads to

$$D_{mn} = \frac{2\int_0^1\int_0^1 \left(T_0^* - v(r,z) - w(z)\right)\, rJ_0(\delta_n r)\cos(\nu_m z)\,\mathrm{d}r\,\mathrm{d}z}{\int_0^1 rJ_0^2(\delta_n r)\,\mathrm{d}r}. \tag{4.34}$$

The solutions for u, v and w are then added together to give the final solution for T in (4.16).

4.3.2 Approximation ignoring the z-dependence

If we assume that we are modelling a narrow and tall machine, and hence $b \ll a$, it is reasonable to ignore the z dependence in (4.15) and solve the 1D problem, which is therefore given by

$$\begin{cases} \dfrac{\partial T}{\partial t} - a\dfrac{1}{r}\dfrac{\partial}{\partial r}\left(r\dfrac{\partial T}{\partial r}\right) = (cT+d) & \text{in} \quad (0,1)\times(0,t_{\rm p}), \\ \dfrac{\partial T}{\partial r} = 0 & \text{on} \quad r=0, \\ T = 0 & \text{on} \quad r=1, \\ T = T_0^* & \text{at} \quad t=0. \end{cases} \tag{4.35}$$

We now consider various exact and approximate solutions to this simplified system.

Separation of variables solution

A separation of variables solution to system (4.35) can be found following the analysis given in Section 4.3.1. To create a homogeneous problem we substitute $T(r,t) = u(r,t) + v(r)$ into (4.35). Then the problem to solve for u is

$$\begin{cases} \dfrac{\partial u}{\partial t} = a\dfrac{1}{r}\dfrac{\partial}{\partial r}\left(r\dfrac{\partial u}{\partial r}\right) + cu & \text{in} \quad (0,1)\times(0,t_{\rm p}), \\ \dfrac{\partial u}{\partial r} = 0 & \text{on} \quad r=0, \\ u = 0 & \text{on} \quad r=1, \\ u = T_0^* - v(r) & \text{at} \quad t=0, \end{cases} \tag{4.36}$$

whilst the problem for v is

$$0 = \frac{a}{r}\big(v'(r) + rv''(r)\big) + cv + d, \tag{4.37}$$

with $v'(0) = 0$ and $v(1) = 0$. This has solution

$$v(r) = -\frac{d}{c} + \frac{dJ_0(\sqrt{\frac{c}{a}}r)}{cJ_0(\sqrt{\frac{c}{a}})}. \tag{4.38}$$

Following the procedure in Section 4.3.1 a straightforward calculation gives the solution for u as

$$u(r,t) = \sum_{n=1}^{\infty} \bar{D}_n J_0(\bar{\delta}_n r)\exp(-\bar{\lambda}_n^2 t), \tag{4.39}$$

where $\bar{\delta}_n \in \mathbb{R}$ satisfy $J_0(\bar{\delta}_n) = 0$, $\bar{\lambda}_n = \sqrt{a\bar{\delta}_n^2 - c}$, and coefficients $\bar{D}_n$ are given by

$$\bar{D}_n = \frac{2\int_0^1 (T_0^* - v(r))\ rJ_0(\bar{\delta}_n r)\,\mathrm{d}r}{\int_0^1 rJ_0^2(\bar{\delta}_n r)\,\mathrm{d}r}, \tag{4.40}$$

with $v(r)$ defined in (4.38). Finally, the solution T is simply the sum of u and v.

Boundary layer solution

Again the starting point is system (4.35). Let us assume that, as is true for some practical cases (an example of which will be shown in Section 4.5), $d = \mathcal{O}(1)$ and $b < a \ll 1$. Then ignoring the terms involving a and b, we find

$$\frac{\partial T}{\partial t} = cT + d \tag{4.41}$$

$$T(0) = T_0^*, \tag{4.42}$$

which gives the leading order solution

$$T(t) = -\frac{d}{c} + \left(T_0^* + \frac{d}{c}\right)\exp(ct). \tag{4.43}$$

Note that since solution (4.43) only depends on t it does satisfy the zero flux condition at $r = 0$, but it obviously cannot satisfy the zero temperature condition at $r = 1$. Thus we assume that (4.43) is an *outer* solution, $T \equiv T_{\text{out}}(t)$, and that there is a boundary layer at $r = 1$. In this region different terms will form the dominant balance and so to highlight this we re-scale the problem by introducing a boundary-layer coordinate as

$$\bar{r} = \frac{1 - r}{\delta}, \tag{4.44}$$

where $\delta \ll 1$ is to be determined. This change of variables has the effect of stretching the region near $r = 1$ when $\delta \to 0$, which in practice means that the boundary-layer problem (also known as inner problem) is solved on a infinite domain. If we let $T_{\text{in}}(\bar{r}, t)$ denote the solution of the problem when using the boundary-layer coordinate, then near $r = 1$ the PDE in (4.35) becomes

$$\frac{\partial T_{\text{in}}}{\partial t} - \frac{a}{\delta^2}\frac{1}{1 - \delta\bar{r}}\frac{\partial}{\partial \bar{r}}\left((1 - \delta\bar{r})\frac{\partial T_{\text{in}}}{\partial \bar{r}}\right) = cT_{\text{in}} + d, \tag{4.45}$$

which is

$$\frac{\partial T_{\text{in}}}{\partial t} + \frac{a}{\delta}\frac{1}{1 - \delta\bar{r}}\frac{\partial T_{\text{in}}}{\partial \bar{r}} - \frac{a}{\delta^2}\frac{\partial^2 T_{\text{in}}}{\partial \bar{r}^2} = cT_{\text{in}} + d. \tag{4.46}$$

To bring out the correct balance in the equation, we take $\delta = \sqrt{a}$, and so coupled with boundary and initial conditions the leading order problem is

$$\begin{cases} \dfrac{\partial T_{\text{in}}}{\partial t} = \dfrac{\partial^2 T_{\text{in}}}{\partial \bar{r}^2} - \sqrt{a}\dfrac{\partial T_{\text{in}}}{\partial \bar{r}} + cT_{\text{in}} + d & \text{in} \quad (0, \infty) \times (0, t_{\text{p}}), \\ T_{\text{in}} = 0 & \text{on} \quad \bar{r} = 0, \\ T_{\text{in}} \to T_{\text{out}}(t) & \text{as} \quad \bar{r} \to \infty, \\ T_{\text{in}} = T_0^* & \text{at} \quad t = 0, \end{cases} \tag{4.47}$$

where $T_{\text{out}}(t)$ is the outer solution given in (4.43). For convenience we subtract off the outer solution to give a new variable which decays to zero as $\bar{r} \to \infty$. Thus, if we define

$$T_{\text{in}}(\bar{r}, t) = T_{\text{out}}(t) + F(\bar{r}, t), \tag{4.48}$$

the system to solve for F reduces to

$$\begin{cases} \dfrac{\partial F}{\partial t} = \dfrac{\partial^2 F}{\partial \bar{r}^2} - \sqrt{a}\dfrac{\partial F}{\partial \bar{r}} + cF & \text{in} \quad (0,\infty)\times(0,t_{\rm p}), \\ F = -T_{\rm out}(t) & \text{on} \quad \bar{r}=0, \\ F \to 0 & \text{as} \quad \bar{r}\to\infty, \\ F = 0 & \text{at} \quad t = 0. \end{cases} \tag{4.49}$$

It is first convenient to transform the PDE in (4.49) into a standard heat equation by setting

$$F(\bar{r},t) = \exp\left(\frac{\sqrt{a}\,\bar{r}}{2} + ct - \frac{at}{4}\right) G(\bar{r},t). \tag{4.50}$$

Then (4.49) becomes

$$\begin{cases} \dfrac{\partial G}{\partial t} = \dfrac{\partial^2 G}{\partial \bar{r}^2} & \text{in} \quad (0,\infty)\times(0,t_{\rm p}), \\ G = -T_{\rm out}(t)\exp(-ct+\frac{at}{4}) & \text{on} \quad \bar{r}=0, \\ G \to 0 & \text{as} \quad \bar{r}\to\infty, \\ G = 0 & \text{at} \quad t = 0. \end{cases} \tag{4.51}$$

At first glance it appears that this system can be solved using Laplace transforms. However, the resulting transformed solution is not easy to invert using standard tables and so the solution would have to be given as a complex integral. To avoid this we instead use Fourier sine transforms, which is appropriate because there is a fixed boundary condition at $\bar{r}=0$. Given a function $f(x)$, $0 \le x < \infty$, the Fourier sine transform pair is defined as

$$\hat{f}(\omega) = \frac{2}{\pi}\int_0^\infty f(x)\sin(\omega x)\,{\rm d}x, \qquad f(x) = \int_0^\infty \hat{f}(\omega)\sin(\omega x)\,{\rm d}\omega. \tag{4.52}$$

Now if

$$\hat{G}(\omega,t) = \frac{2}{\pi}\int_0^\infty G(\bar{r},t)\sin(\omega\bar{r})\,{\rm d}\bar{r}, \tag{4.53}$$

then the PDE in (4.51) becomes

$$\frac{2}{\pi}\int_0^\infty \frac{\partial G}{\partial t}\sin(\omega\bar{r})\,{\rm d}\bar{r} = \frac{2}{\pi}\int_0^\infty \frac{\partial^2 G}{\partial \bar{r}^2}\sin(\omega\bar{r})\,{\rm d}\bar{r}, \tag{4.54}$$

or

$$\frac{\partial \hat{G}}{\partial t} + \omega^2\hat{G} = -\frac{2\omega T_{\rm out}(t)\exp\left(\frac{at}{4}-ct\right)}{\pi}. \tag{4.55}$$

Note that when differentiating $\hat{G}$ with respect to r twice, we have used the additional condition $\frac{\partial G}{\partial \bar{r}} \to 0$ as $\bar{r}\to\infty$, which follows from matching with the outer solution, that only depends on t.

The initial condition in (4.51) implies that $\hat{G}(\omega,0)=0$ and so equation (4.55) has solution

$$\hat{G}(\omega,t) = \frac{2\omega d}{\pi c(\omega^2+a/4-c)}\big[\exp(at/4-ct)-\exp(-\omega^2 t)\big] - \frac{2\omega(T_0^*+d/c)}{\pi(\omega^2+a/4)}\big[\exp(at/4)-\exp(-\omega^2 t)\big], \tag{4.56}$$

after substituting $T_{\rm out}(t)$ from (4.43). Finally the solution for G is given by

$$G(\bar{r},t) = \int_0^\infty \hat{G}(\omega,t)\sin(\omega\bar{r})\,{\rm d}\omega, \tag{4.57}$$

and so

$$T_{\rm in}(\bar{r},t) = T_{\rm out}(t) + \exp\left(\frac{\sqrt{a}\,\bar{r}}{2} - \frac{at}{4} + ct\right) G(\bar{r},t). \tag{4.58}$$

After adding the inner and outer solutions and subtracting the common part, we can write down the final solution in the whole domain as

$$T(r,t) = -\frac{d}{c} + \left(T_0^* + \frac{d}{c}\right)\exp(ct) + \exp\left(\frac{1-r}{2} + ct - \frac{at}{4}\right) G\left(\frac{1-r}{\sqrt{a}}, t\right). \tag{4.59}$$

4.3.3 Approximation including the z-dependence

Since the approximate solutions in Section 4.3.2 only depend on r and t it is clear that the boundary condition at $z = 1$ is not satisfied (unlike the zero flux boundary condition at $z = 0$, which is satisfied). We need to consider a boundary layer analysis near $z = 1$, and therefore follow a similar analysis to that given in Section 4.3.2. Thus we set $z = 1 - \sqrt{b}\bar{z}$ and denote $T_{\rm in}(r, \bar{z}, t)$ as the inner solution. Then, for leading order terms, system (4.15) becomes

$$\begin{cases} \dfrac{\partial T_{\rm in}}{\partial t} - a\dfrac{1}{r}\dfrac{\partial}{\partial r}\left(r\dfrac{\partial T_{\rm in}}{\partial r}\right) - \dfrac{\partial^2 T_{\rm in}}{\partial \bar{z}^2} = (cT_{\rm in} + d) & \text{in} \quad (0,1)\times(0,\infty)\times(0,t_{\rm p}), \\ \dfrac{\partial T_{\rm in}}{\partial r} = 0 & \text{on} \quad r = 0, \\ T_{\rm in} = 0 & \text{on} \quad r = 1, \\ T_{\rm in} \to T_{\rm out} & \text{as} \quad \bar{z} \to \infty, \\ T_{\rm in} = 0 & \text{on} \quad \bar{z} = 0, \\ T_{\rm in} = T_0^* & \text{at} \quad t = 0, \end{cases} \tag{4.60}$$

where $T_{\rm out}$ is the outer solution of the PDE, i.e. the solution that we solved in Section 4.3.2. We will use the series solution found in Section 4.3.2, namely

$$T_{\rm out}(r,t) = v(r) + \sum_{n=1}^{\infty} \bar{D}_n J_0(\bar{\delta}_n r)\exp(-\bar{\lambda}_n^2 t), \tag{4.61}$$

where $v(r)$ is given in (4.38). Whilst we could use the boundary layer solution (4.59), this form is simpler as it avoids a solution involving several integrals.

Using the same approach as in Section 4.3.2, if we set

$$T_{\rm in}(r,\bar{z},t) = T_{\rm out}(r,t) + F(r,\bar{z},t), \tag{4.62}$$

then the PDE in (4.60) becomes

$$\frac{\partial F}{\partial t} = a\frac{1}{r}\frac{\partial}{\partial r}\left(r\frac{\partial F}{\partial r}\right) + \frac{\partial^2 F}{\partial \bar{z}^2} + cF, \tag{4.63}$$

which follows since $T_{\rm out}(r,t)$ satisfies the outer PDE. If, as at the start of Section 4.3.2, we assume $a \ll 1$ and then ignore this term here, system (4.60) reduces to the following 1D problem:

$$\begin{cases} \dfrac{\partial F}{\partial t} - \dfrac{\partial^2 F}{\partial \bar{z}^2} = cF & \text{in} \quad (0,\infty)\times(0,t_{\rm p}), \\ F \to 0 & \text{as} \quad \bar{z} \to \infty, \\ F = h(t) & \text{on} \quad \bar{z} = 0, \\ F = 0 & \text{at} \quad t = 0, \end{cases} \tag{4.64}$$

where for convenience we have defined $h(t) = -T_{\rm out}(r,t)$ (considering r as a constant value and the solving the system for each r). Again using Fourier sine transforms we can find the exact solution to (4.64). This is given by

$$F(\bar{z},t) = \int_0^{\infty}\left(\frac{2}{\pi}\int_0^t h(t')\exp((\omega^2 - c)(t'-t))\,{\rm d}t'\right)\sin(\omega\bar{z})\,{\rm d}\omega, \tag{4.65}$$

or

$$F(\bar{z},t) = \int_0^{\infty}(f_1(\omega,t) + f_2(\omega,t))\sin(\omega\bar{z})\,{\rm d}\omega, \tag{4.66}$$

where

$$f_1(\omega,t) = -\frac{2\omega v(r)}{\pi(c-\omega^2)}\big[\exp((c-\omega^2)t)-1\big], \tag{4.67}$$

$$f_2(\omega,t) = \frac{2}{\pi}\sum_{n=0}^{\infty}\bar{D}_n J_0(\bar{\delta}_n r)\frac{\big[\exp(-\bar{\lambda}_n^2 t)-\exp((c-\omega^2)t)\big]}{\bar{\lambda}_n^2+c-\omega^2}. \tag{4.68}$$

Thus, the inner solution is simply the sum of F and $T_{\rm out}$. After adding the inner and outer solutions and subtracting the common part, we can write down the final solution in the whole domain as

$$T(r,z,t) = -\frac{d}{c} + \frac{dJ_0(\sqrt{\frac{c}{a}}r)}{cJ_0(\sqrt{\frac{c}{a}})} + \sum_{n=1}^{\infty}\bar{D}_n J_0(\bar{\delta}_n r)\exp(-\bar{\lambda}_n^2 t) + \int_0^{\infty}(f_1(\omega,t)+f_2(\omega,t))\sin\left(\frac{1-z}{\sqrt{b}}\omega\right)\mathrm{d}\omega. \tag{4.69}$$

4.4 Analysis for the pressure hold time $t_{\rm p} < t \le t_{\rm f}$

For $t \ge t_{\rm p}$, heating no longer occurs due to the increase in pressure, and hence the right-hand side of the PDE in system (4.15) is zero. Rescaling time as $\zeta = t - t_{\rm p}$, we have

$$\begin{cases} \dfrac{\partial T}{\partial \zeta} - a\dfrac{1}{r}\dfrac{\partial}{\partial r}\left(r\dfrac{\partial T}{\partial r}\right) - b\dfrac{\partial^2 T}{\partial z^2} = 0 & \text{in} \quad (0,1)\times(0,1)\times(0,t_{\rm f}-t_{\rm p}), \\ \dfrac{\partial T}{\partial r} = 0 & \text{on} \quad r=0, \\ T = 0 & \text{on} \quad r=1, \\ \dfrac{\partial T}{\partial z} = 0 & \text{on} \quad z=0, \\ T = 0 & \text{on} \quad z=1, \\ T = T_{\rm up}(r,z) & \text{at} \quad \zeta = 0, \end{cases} \tag{4.70}$$

where $T_{\rm up}(r,z)$ is the solution $T(r,z,t)$ of the problem (solved in Section 4.3.1) in the time interval $0 < t < t_{\rm p}$, at time $t = t_{\rm p}$, namely

$$T_{\rm up}(r,z) = \frac{d}{c}\left(\frac{\cos(\gamma z)}{\cos\gamma}-1\right) + \sum_{p=1}^{\infty}A_p J_0(\alpha_p r)\cos(\nu_p z) + \sum_{n=1}^{\infty}\sum_{m=1}^{\infty}D_{mn}J_0(\delta_n r)\cos(\nu_m z)\exp(-\lambda_{mn}^2 t_{\rm p}). \tag{4.71}$$

We now describe how to extend the analysis given above, for the pressure up time, to the system in the pressure hold time.

4.4.1 Exact solution

The analysis here is similar to that described in Section 4.3.1, but is in fact simpler because the right-hand side of the PDE is zero and so the problem is already homogeneous. Thus the solution is

$$T(r,z,t) = \sum_{j=1}^{\infty}\sum_{k=1}^{\infty}E_{kj}J_0(\eta_j r)\cos(\nu_k z)\exp(-\varphi_{kj}^2(t-t_{\rm p})), \tag{4.72}$$

where $\eta_j \in \mathbb{R}$ satisfy $J_0(\eta_j) = 0$, $\nu_k = (k-1/2)\pi$, and $\varphi_{kj} = \sqrt{a\eta_j^2 + b\nu_k^2}$. To determine coefficients E_{kj} we use the initial condition in (4.70), where $T_{\rm up}$ is defined in (4.71). Thus, after integrating and applying the orthogonality conditions, we have

$$E_{kj} = \frac{2\int_0^1\int_0^1 T_{\rm up}(r,z)rJ_0(\eta_j r)\cos(\nu_k z)\,\mathrm{d}r\,\mathrm{d}z}{\int_0^1 rJ_0^2(\eta_j r)\,\mathrm{d}r}. \tag{4.73}$$

4.4.2 Approximation ignoring the z-dependence

Again, assuming $b << a$, we ignore the z-dependence in (4.70) and solve the 1D problem, which is

$$\begin{cases} \dfrac{\partial T}{\partial \zeta} - a\dfrac{1}{r}\dfrac{\partial}{\partial r}\left(r\dfrac{\partial T}{\partial r}\right) = 0 & \text{in} \quad (0,1)\times(0,t_{\rm f}-t_{\rm p}), \\ \dfrac{\partial T}{\partial r} = 0 & \text{on} \quad r=0, \\ T = 0 & \text{on} \quad r=1, \\ T = T_{\rm up}(r) & \text{at} \quad \zeta = 0, \end{cases} \tag{4.74}$$

where $T_{\rm up}(r)$ is the 1D pressure up solution given in Section 4.3.2 at $t = t_{\rm p}$, i.e.

$$T_{\rm up}(r) = -\frac{d}{c} + \frac{dJ_0(\sqrt{\frac{c}{a}}r)}{cJ_0(\sqrt{\frac{c}{a}})} + \sum_{n=1}^{\infty} \bar{D}_n J_0(\bar{\delta}_n r)\exp(-\bar{\lambda}_n^2 t_{\rm p}). \tag{4.75}$$

A separation of variables solution to system (4.74) can be found using the same analysis as in previous sections. Thus we simply quote the solution as

$$T(r,t) = \sum_{j=1}^{\infty} \bar{E}_j J_0(\bar{\eta}_j r)\exp(-\bar{\varphi}_j^2(t-t_{\rm p})), \tag{4.76}$$

where $\bar{\eta}_j \in \mathbb{R}$ satisfy $J_0(\bar{\eta}_j) = 0$, and $\bar{\varphi}_j = \sqrt{a}\ \bar{\eta}_j$. To determine coefficients $\bar{E}_j$ we use the initial condition in (4.74). After integrating and applying the orthogonality condition, we have

$$\bar{E}_j = \frac{\int_0^1 T_{\rm up}(r)J_0(\bar{\eta}_j r)r\,{\rm d}r}{\int_0^1 rJ_0^2(\bar{\eta}_j r)\,{\rm d}r}, \tag{4.77}$$

where $T_{\rm up}(r)$ is defined in (4.75).

A boundary layer solution in 1D, like the one described in Section 4.3.2, was not given here because a boundary layer near $r = 1$ is no longer expected. This is due to the fact that the PDE in (4.74) has a right-hand side equal to zero, so now the a term becomes more important than in the pressure up time, where the c and d terms were dominant.

4.4.3 Approximation including the z-dependence

Following Section 4.3.3 we consider a boundary layer analysis near $z = 1$ by setting $z = 1 - \sqrt{b}\bar{z}$ and denote $T_{\rm in}(r,\bar{z},\zeta)$ as the inner solution. Then system (4.70) becomes

$$\begin{cases} \dfrac{\partial T_{\rm in}}{\partial \zeta} - a\dfrac{1}{r}\dfrac{\partial}{\partial r}\left(r\dfrac{\partial T_{\rm in}}{\partial r}\right) - \dfrac{\partial^2 T_{\rm in}}{\partial \bar{z}^2} = 0 & \text{in} \quad (0,1)\times(0,\infty)\times(0,t_{\rm f}-t_{\rm p}), \\ \dfrac{\partial T_{\rm in}}{\partial r} = 0 & \text{on} \quad r=0, \\ T_{\rm in} = 0 & \text{on} \quad r=1, \\ T_{\rm in} \to T_{\rm out}(r,t) & \text{as} \quad \bar{z}\to\infty, \\ T_{\rm in} = 0 & \text{on} \quad \bar{z}=0, \\ T = T_{\rm up}(r) & \text{at} \quad \zeta = 0, \end{cases} \tag{4.78}$$

where $T_{\rm up}(r)$ is given in (4.75), and $T_{\rm out}(r,t)$ in (4.76). Following the same setps as in Section 4.3.3 the solution is found to be

$$T(r,z,t) = T_{\rm out}(r,t) + \sum_{j=1}^{\infty}\int_0^{\infty} \frac{2\omega}{\pi}\bar{E}_j J_0(\bar{\eta}_j r)\frac{\left[\exp(-\bar{\varphi}_j^2\zeta) - \exp(-\omega^2\zeta)\right]}{\bar{\varphi}_j^2 - \omega^2}\sin\left(\frac{1-z}{\sqrt{b}}\omega\right). \tag{4.79}$$

4.5 Numerical tests

For the numerical tests we consider similar dimensions to the ones of the pilot unit (ACB GEC Alsthom, Nantes, France), described in Chapter 3, but we ignore the pressurising fluid domain and the rubber cap and focus on the food and surrounding steel domains. The dimensions for these are given in Table 4.1. Following [46, 69] we have chosen tylose (a food simile) as an example of solid type food. As pointed out in Section 4.2.1, the thermo-physical properties of the food sample are taken to be constant (and set to their mean value in the range of temperature and pressure considered in the process). The thermo-physical properties of the steel remain constant during the whole process.

The initial temperature is $T_0 = 313$ K $= 39.85°$C in both the food and the steel, and the pressure is linearly increased during the first 183 seconds until it reaches 360 MPa. Then the pressure is maintained constant until the final time (900 seconds) is reached. Thus, the pressure generated by the equipment satisfies $P(0) = 0$ and

$$\frac{\mathrm{d}P}{\mathrm{d}t}(t) = \begin{cases} \dfrac{360}{183} \cdot 10^6 \text{ Pa s}^{-1}, & 0 < t \leq 183, \\ 0 \text{ Pa s}^{-1}, & 183 < t < 900. \end{cases} \tag{4.80}$$

ρ_{F}	1006	ρ_{S}	7833	$C_{p_{\mathrm{F}}}$	3780	$C_{p_{\mathrm{S}}}$	465
k_{F}	0.49	k_{S}	55	β_{F}	$4.217 \cdot 10^{-4}$	γ	$360 \cdot 10^6$
L	0.045	L_2	0.09	H	0.091	H_2	0.327
T_0	313	T_{r}	292.3	t_{p}	183	t_{f}	900

Table 4.1: Parameter values for numerical simulations. The food properties are those of tylose. Data is obtained from [14, 46, 68].

Following the procedure described in Section 4.2.2, and considering the values given in Table 4.1, the scales used to non-dimensionalise the variables are: $R = 0.045$ m, $Z = 0.091$ m, $\Delta T = 20.7$ K and $\tau = 325$ s. The values of a, b, c and d are shown in Table 4.2 (we point out that they satisfy the assumptions considered in the previous sections). The non-dimensional initial condition is $T_0^* = 1$.

	a	b	c	d
$\hat{\Omega^{\mathrm{D}}}_{\mathrm{F}}$	0.02	0.005	0.07	1
$\hat{\Omega^{\mathrm{D}}}_{\mathrm{S}}$	2.423	0.593	0	0

Table 4.2: Non-dimensional parameter values for system (4.9).

In Sections 4.3 and 4.4 we have given an exact solution and several simplifications to our problem. In order to check the validity of such simplifications we compare them to the reference models, which are considered to be the exact solution given in Section 4.3.1 for the pressure up time, and the one given in Section 4.4.1 for the pressure hold. Also a numerical solution in both 1D (using radial coordinates) and 2D (using cylindrical coordinates) is calculated using the FEM solver COMSOL Multiphysics 3.5a. In [46, 69] similar, although more complex, models were solved numerically using this commercial software, and validated by comparing to experimental data. Our model is a simplification of ones proposed in those papers, and not based on a real experiment, so we choose a numerical solution solved with COMSOL rather than a comparison to experimental data.

All of our solutions were calculated using MATLAB 7.12.0.635 (R2011a) without requiring an FEM solver. For the separation of variables solutions, the transcendental equation $J_0(x) = 0$, which appears in Sections 4.3.1, 4.3.2, 4.4.1 and 4.4.2, was solved using this software, whose roots correspond to δ_n, $\bar{\delta}_n$, η_j, $\bar{\eta}_j$ for each section, respectively. Coefficients $\bar{D}_n$ and $\bar{E}_j$ that appear in equations (4.40) and (4.77), respectively, were calculated using integration formulas for Bessel functions. Coefficients D_{mn} and E_{kj} in equations (4.34) and (4.73) were calculated using a double trapezoidal rule for the sake of simplicity, although the same rules for Bessel functions

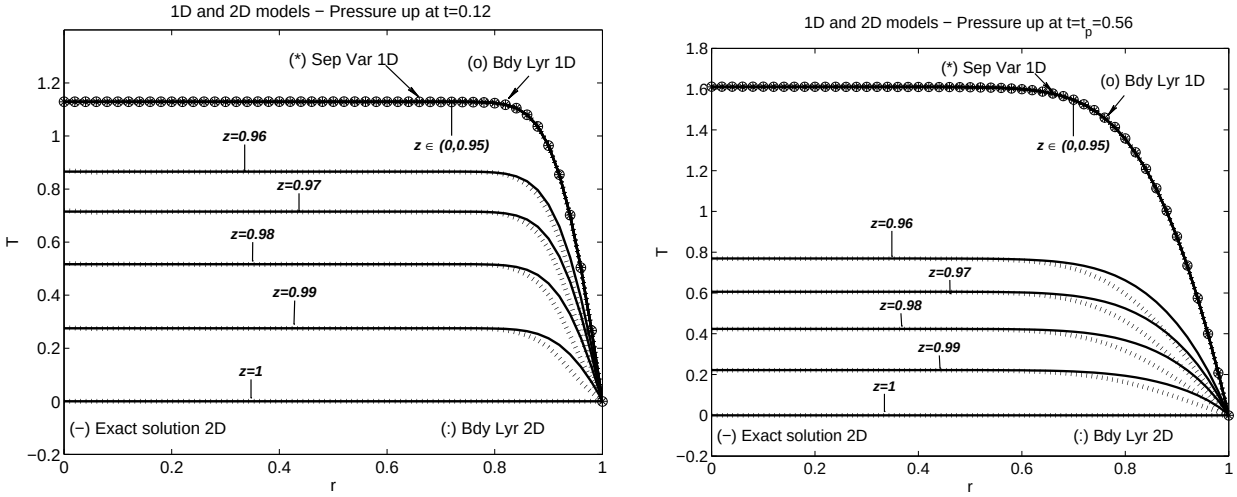

Figure 4.2: Dimensionless temperature profiles calculated with different methods in 1D and 2D for pressure up at $t = 0.12$ (left) and $t = t_{\mathrm{p}} = 0.56$ (right).

plus some for trigonometric functions could have been used for calculating it directly, or any other quadrature rule could also be used. We truncated each infinite sum and took as many terms as necessary to obtain a solution which did not vary to 16 decimal places from the solution with one term less. Thus, for equations (4.32) and (4.39) we took $N = 20$ terms, and for (4.72) and (4.75), $J = 20$ terms. For equations (4.26), $P = 35$ terms, for (4.32), $M = 35$ terms and for (4.72), $K = 35$ terms.

For the boundary layer solutions described in Sections 4.3.2 and 4.3.3, in which there are a semi-infinite integrals (namely (4.57) and (4.69)) to calculate, we followed [60], where a method to approximate integrals of the form $\int_a^\infty f(x)\,\phi(x)\,\mathrm{d}x$ is proposed, with $\phi(x)$ being either $\sin(\omega x)$ or $\cos(\omega x)$. The integral is approximated by a numerical integration over a finite domain (a, b), leaving a truncation error equal to the tail integration $\int_b^\infty f(x)\,\phi(x)\,\mathrm{d}x$, plus the discretisation error. Luo and Shevchenko [60] describe a very simple end-point correction to approximate the tail integration, which reduces significantly the truncation error, and which we have used in our calculations.

4.5.1 Results

Figure 4.2 shows the dimensionless temperature profiles given by the models presented in Section 4.3 for pressure up time. We have plotted the results of the 2D models at a fixed time ($t = 0.12$ on the left, $t = 0.56 = t_{\mathrm{p}}$ on the right) for different heights and for all r. As can be seen for all heights $z \in (0, 0.95)$ the solution is almost the same, and also matches perfectly with the 1D results from Sections 4.3.2 and 4.3.2. Then for the rest of heights up to $z = 1$, where the boundary layer is, it is clear that the solutions differ from the 1D model for the points very close to the top right corner of the 2D domain. There is a slight difference between the boundary layer solution given in Section 4.3.3 and the exact solution given in Section 4.3.1, especially near $r = 1$. This is because in (4.63) we are ignoring the a term, and therefore no heat conduction in the r direction is taken into account in this solution. Including this term leads to a problem which is more difficult to solve than the original one, and so the approximation would no longer be a simplification.

Figure 4.3 shows the dimensionless temperature profiles given by the models presented in Section 4.4 for pressure hold time. In this case the plots are at times $t = 1.50$ on the left and $t = 2.76 = t_{\mathrm{f}}$ on the right. For all heights $z \in (0, 0.94)$ the solution is almost the same and again matches perfectly with the 1D results from Section 4.4.2. In this case, however, for the rest of height up until $z = 1$ which are in the boundary layer, the approximation proposed in Section 4.4.3 differs more from the exact solution given in Section 4.4.1 than in the pressure up time case. This is because the conduction term in the r direction was ignored again, and, because there is no source term for the pressure hold case, this difference is more noticeable. We remark again that this slight discrepancy is for points that are very close to the top of the 2D domain.

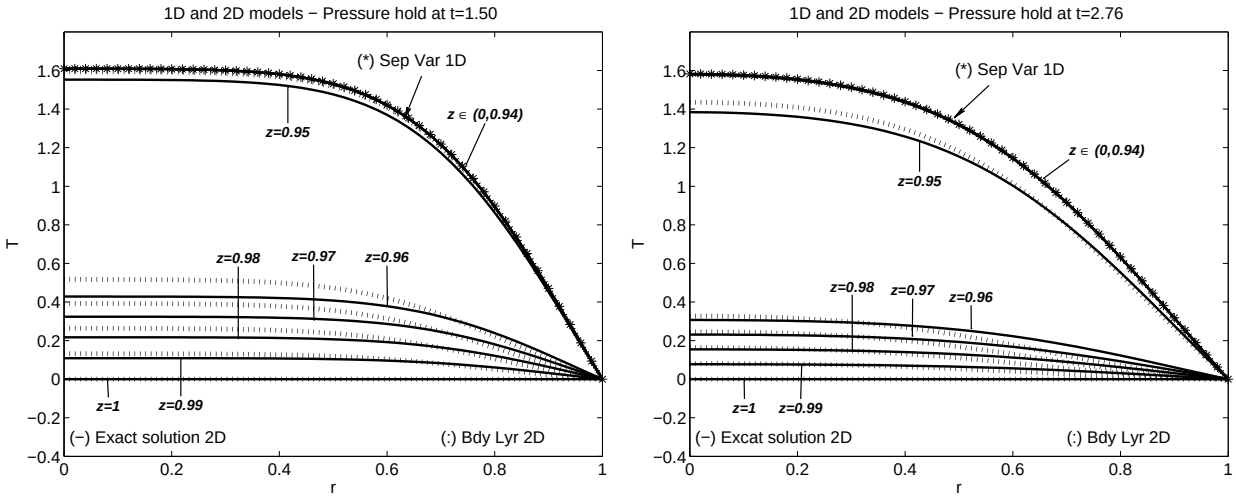

Figure 4.3: Dimensionless temperature profiles calculated with different methods in 1D and 2D for pressure hold at $t = 1.50$ (left) and $t = t_{\mathrm{f}} = 2.76$ (right).

Looking at the results we can see that the temperature profiles inside the food can be very well approximated by the 1D solution at nearly all heights inside the machine, except those very near the top, where a boundary layer exists. We point out that these are the results for the upper half of the domain (after our simplification in Section 4.2.2) and therefore by symmetry the same results hold for the lower half of the machine, i.e. the temperature profile for all heights except those near the bottom boundary can be very well approximated by a 1D model.

4.6 Coupling of Microbial-Enzymatic Inactivation and Heat Transfer Models

As explained in Chapter 2, one of the reasons for solving heat transfer models for HP processing of foods, is to find the temperature distribution for coupling with enzymatic or bacterial inactivation models. In this Section we give an example of how this can be done, and also compare the results obtained when using the simplified heat transfer models.

Following the work carried out in [45, 46], we couple the heat transfer models with kinetic equation (2.37) for enzymatic activity $A(t; T, P)$. This allows us to obtain a model that describes the non-homogeneous distribution of the enzymatic activity inside the food. Since we have proposed simplified 1D heat transfer models that give quite similar results to the different proposed 2D models, we want to compare the resulting enzymatic activity distribution that we obtain using the 2D heat transfer models with the 1D models. To do that, we perform a numerical study of the impact of a HP process on the inactivation of three different enzymes: Bacillus Subtilis α-Amylase (BSAA), Lipoxygenase (LOX) and Carrot Pectin Methyl-Esterase (CPE).

4.6.1 Resulting activity equation

For solid type food, we assume that particles do not move. Thus, according to (2.37), the enzymatic activity A of a particle located at a point $x \in \Omega_{\mathrm{F}}^{\mathrm{D}}$ at time t can be written as

$$A(x,t) = A(x,0) \exp\left(- \int_0^t \kappa(T(x,\sigma), P(\sigma)) \mathrm{d}\sigma \right). \tag{4.81}$$

The equipment pressure P (MPa) is a given pressure curve and the temperature T (K) is obtained by solving system (4.2)-(4.3), or a simplified version of it. If the temperature is solved using a non-dimensional model it is

important to convert the dimensionless temperature into a dimensional temperature before coupling with the enzymatic activity model.

4.6.2 Discretisation of the activity equation

We consider a time discretisation given by $0 = t_0 < t_1 < \cdots < t_n = t_\mathrm{f}$ with step $\varphi = \frac{t_\mathrm{f}}{n}$. Given $x \in \Omega_\mathrm{F}^\mathrm{D}$ and denoting $\kappa_j(x) = \kappa(T(x,t_j), P(t_j))$, a numerical approximation of (4.81) can be obtained considering, for instance, the trapezoidal formula

$$A(x,t_i) \approx A(x,0)\exp\left(-\frac{\varphi}{2}\sum_{j=0}^{i-1}(\kappa_j(x)+\kappa_{j+1}(x))\right), \quad i = 1,2,\cdots,n. \tag{4.82}$$

If the temperature distribution chosen to couple with (4.82) is one-dimensional, we consider the partition of the interval $(0,L)$, given by $0 = x_0 < x_1 < \cdots x_m = L$ with step $\bar{x} = \frac{L}{m}$, on which the enzymatic activity is evaluated. If instead, the temperature distribution is two-dimensional, the enzymatic activity is evaluated on a 10000 points equally distributed mesh in the food sample domain $\Omega_\mathrm{F}^\mathrm{D}$. By using linear interpolation we can get outputs for the whole domain as shown in Figure 4.4 and Table 4.3.

4.6.3 Enzymes considered for numerical simulation

For the numerical experiments, the following enzymes and the corresponding inactivation rates have been considered:

Bacillus Subtilis α-Amylase (BSAA): It is an enzyme produced by a bacteria called Bacillus Subtilis. This bacteria is present in the ground, and can contaminate food and in rare occasions cause intoxications. It catalyzes the hydrolysis of starch, generating sugars (such as maltose) that can modify the taste of food. The inactivation rate κ is modeled using equation (2.40) with $P_\mathrm{ref} = 500$ MPa, $T_\mathrm{ref} = 313$ K, $\kappa_\mathrm{ref} = 9.2\cdot 10^{-2}$ min^{-1}, $B = 10097$ K and $C = -8.7\cdot 10^{-4}$ MPa^{-1}. (For more details see [58]).

Lipoxygenase (LOX): This enzyme is present in various plants and vegetables such as green beans and green peas. It is responsible for the appearance of undesirable aromas in those products. In this case, the inactivation rate κ is modeled using equation (2.41) with $P_\mathrm{ref} = 500$ MPa, $T_\mathrm{ref} = 298$ K, $\kappa_\mathrm{ref} = 1.34\cdot 10^{-2}$ min^{-1}, $\Delta V_\mathrm{ref} = -30.814$ cm^{3}mol^{-1}, $\Delta S_\mathrm{ref} = 90.63$ J mol^{-1}K^{-1}, $\Delta C_p = 2466.71$ J mol^{-1}K^{-1}, $\Delta\zeta = 0.222$ cm^{3}mol^{-1}K^{-1}, $\Delta\nu = -0.0054$ cm^{6}J^{-1}mol^{-1}. (For more details see [44]).

Carrot Pectin Methyl-Esterase (CPE): Pectin Methyl-Esterase is an enzyme that is common to most vegetables. It can be present in vegetable juices producing low-methoxyl pectin. This process reduces juice viscosity and generates cloud loss (affecting juice flavor, color, texture and aroma). Here we concentrate on the Pectin Methyl-Esterase present in carrot juice (CPE). In this case, again the inactivation rate κ is modeled using equation (2.41) with $P_\mathrm{ref} = 700$ MPa, $T_\mathrm{ref} = 323.15$ K, $\kappa_\mathrm{ref} = 7.05\cdot 10^{-2}$ min^{-1}, $\Delta V_\mathrm{ref} = -44.0124$ cm^{3}mol^{-1}, $\Delta S_\mathrm{ref} = 168.4$ J mol^{-1}K^{-1}, $\Delta C_p = 1376.6$ J mol^{-1}K^{-1}, $\Delta\zeta = -0.0339$ cm^{3}mol^{-1}K^{-1}, $\Delta\nu = -0.1195$ cm^{6}J^{-1}mol^{-1}. (For more details see [61]).

4.6.4 Numerical results

For the numerical tests, we assume that the activity is 100% at $t = 0$ and consider $t_\mathrm{f} = 15$ min and $n = 900$. For the 1D-model, the activity is evaluated over the partition explained above with $L = 0.045$ (i.e. the radius of the food sample holder) and $m = 100$. For the 2D-model we consider 3 different cases: 2D-mid where the activity is evaluated at the same radial points as in the 1D case and at middle height of the food sample holder (at $z = 0$); 2D-all where the activity is evaluated over a 10000 points equally distributed mesh over the top half of $\Omega_\mathrm{F}^\mathrm{D}$ (i.e. over the same domain that the heat transfer models were solved on); 2D-ave where the activity is evaluated again over a 10000 points equally distributed mesh over the top half of $\Omega_\mathrm{F}^\mathrm{D}$, excluding all points higher than $z > 0.0864$m (or in non-dimensional $\hat{z} > 0.95$). The reason for distinguishing these two last cases

is because, as we saw in Figures 4.2 and 4.3, the temperature distributions can be very well approximated by the 1D solution at nearly all heights inside the machine, except those very near the top. We want to see if this also happens for the enzymatic activity.

For the 1D-model, the temperature is calculated using the 1D non-dimensional separation of variables solution given in Section 4.3.2 for P_{up}, and that of Section 4.4.2 for P_{hold}. Note that due to the similarity of the separation of variables and the boundary layer solutions calculated in Section 4.3.2, for P_{up}, the latter could have been used instead of the former. For all of the 2D models, the temperature is calculated using the 2D non-dimensional exact solution given in Section 4.3.1 for P_{up}, and that of Section 4.4.1 for P_{hold}.

As we can observe in Figure 4.4 and Table 4.3, the efficiency of the considered HP process for inactivating enzymes depends on the enzyme under study. For enzyme BSAA, this process is very efficient given that the final activity is very low, whilst enzyme CPE seems to be quite resistant to the process, as the final activity is very high. These results coincide qualitatively with those of [46].

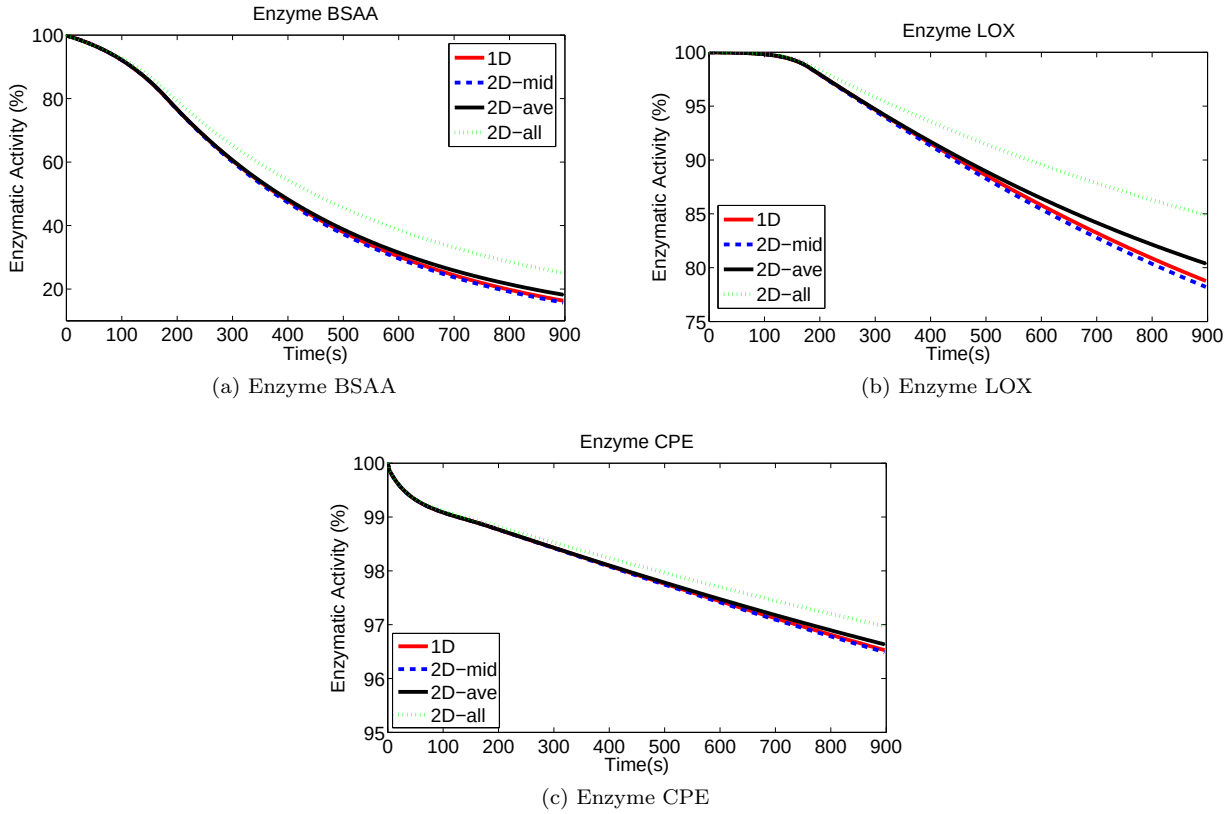

(a) Enzyme BSAA

(b) Enzyme LOX

(c) Enzyme CPE

Figure 4.4: Mean enzymatic activity evolution (%) over dimensional time for the considered models

If we compare the results we have obtained to calculate the enzymatic activity, we can see in Figure 4.4 that for the three enzymes under consideration the 1D, 2D-mid and 2D-ave give very similar results, whilst the 2D-all is slightly different. This is consistent with the results obtained in Section 4.5, where we saw that the temperature profiles for the 1D model were very similar to the 2D ones at every point except those near the very top. In Table 4.3 we can observe the differences in the final activity (given by the mean activity in the models at final time, i.e. $\mathcal{M}(A(\cdot, t_{\text{f}}); \Omega_{\text{F}}^{\text{D}}))$ for the three enzymes. Table 4.3 also shows the mean temperature $\mathcal{M}(T(\cdot, t_{\text{f}}); \Omega_{\text{F}}^{\text{D}}))$ (°C) inside the food domain during the process for the different cases.

Enzyme BSAA shows the largest differences between models. The 1D, 2D-mid and 2D-ave models give similar results (see Figure 4.4a) with a maximum difference of final mean activity of 2.5%. The 2D-all model however differs quite a lot, with a maximum difference of 9.5% compared to the other models (see Table 4.3). This is due to the fact that for the 2D-all case we are considering the points at the very top of the food domain, which, as we saw in Section 4.5, have different temperatures to the rest of the heights. Also enzyme BSAA is sensitive

to temperatures [58], hence the differences in the final activity.

The differences between models for enzyme LOX are less (see Figure 4.4b), with a maximum of 2.1% between the 1D, 2D-mid and 2D-ave models, and of 6.7% between the 2D-all and the other models (see Table 4.3), showing that LOX is not as sensitive to temperature as BSAA.

Enzyme CPE is clearly the least sensitive to temperature (see Figure 4.4c), as the differences between the models are very low, with a maximum of 0.143 % between the 1D, 2D-mid and 2D-ave models, and a maximum of 0.483 % between the 2D-all and the other models (see Table 4.3).

Model	BSAA	LOX	CPE	$\mathcal{M}(T;\Omega_{\mathrm{F}}^{\mathrm{D}}\times(0,t_{\mathrm{f}}))$ (°C)
1D	16.3319	78.7686	96.5264	44.8544
2D-mid	15.7557	78.2113	96.4911	45.0091
2D-ave	18.2006	80.3808	96.6343	44.3835
2D-all	25.0810	84.9130	96.9742	42.7215

Table 4.3: Mean activity at final time $t_{\mathrm{f}} = 15$ min $\mathcal{M}(A(\cdot,t_{\mathrm{f}});\Omega_{\mathrm{F}}^{\mathrm{D}})$ (%) for the four models considered and for BSAA, LOX and CPE enzymes. And mean temperature $\mathcal{M}(T;\Omega_{\mathrm{F}}^{\mathrm{D}}\times(0,t_{\mathrm{f}}))$ (°C) for all of the models.

Therefore we have seen that, in most cases, our simplified heat transfer models also give good results when coupling with enzymatic inactivation models.

4.7 Extension to third class boundary conditions

We now consider a model where only the food domain is included (see Figure 4.5), and assume that there is heat exchange between the walls of the food domain and the outside. Hence now the boundary and initial conditions for (4.2) are

$$\begin{cases} \dfrac{\partial T}{\partial r} = 0 & \text{on} \quad \Gamma_{\mathrm{sym}}^{\mathrm{D}}, \\ k\dfrac{\partial T}{\partial \mathbf{n}} = h(T_{\mathrm{r}} - T) & \text{on} \quad \Gamma_{\mathrm{exc}}^{\mathrm{D}} = \Gamma_{\mathrm{F}}^{\mathrm{D}} \setminus \Gamma_{\mathrm{sym}}^{\mathrm{D}}, \\ T = T_0 & \text{at} \quad t = 0, \end{cases} \tag{4.83}$$

where $\Gamma_{\mathrm{F}}^{\mathrm{D}}$ is the boundary of $\Omega_{\mathrm{F}}^{\mathrm{D}}$, h (W m^{-2} K^{-1}) is the heat transfer coefficient with the environment, and $\mathbf{n}$ is the outward unit normal vector on the boundary of the domain, $\Gamma_{\mathrm{exc}}^{\mathrm{D}}$.

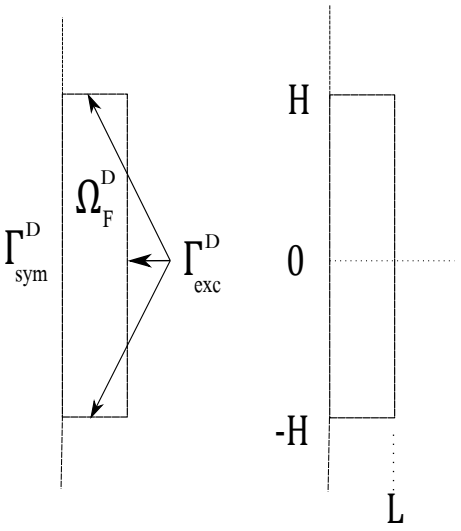

Figure 4.5: Simplified computational domain for third class boundary condition

Proceeding as in Section 4.2.2, we now have the following non-dimensional system to solve

$$\begin{cases} \dfrac{\partial T}{\partial t} - a\dfrac{1}{r}\dfrac{\partial}{\partial r}\left(r\dfrac{\partial T}{\partial r}\right) - b\dfrac{\partial^2 T}{\partial z^2} = (cT+d)\chi(t) & \text{in} \quad (0,1)\times(0,1)\times(0,t_{\rm f}), \\ \dfrac{\partial T}{\partial r} = 0 & \text{on} \quad r=0, \\ \epsilon_{\rm r}\dfrac{\partial T}{\partial r} = -T & \text{on} \quad r=1, \\ \dfrac{\partial T}{\partial z} = 0 & \text{on} \quad z=0, \\ \epsilon_{\rm z}\dfrac{\partial T}{\partial z} = -T & \text{on} \quad z=1, \\ T = T_0^* & \text{at} \quad t=0, \end{cases} \tag{4.84}$$

where $\epsilon_{\rm r} = \frac{k}{hR}$ and $\epsilon_{\rm z} = \frac{k}{hZ}$.

A similar analysis to that given for system (4.15), as described in Sections 4.3 and 4.4, can also be carried out for (4.84). Here we present only the results for the one dimensional approximation, ignoring the z-dependence for pressure up time.

4.7.1 Approximation ignoring the z-dependence for pressure up time

Following 4.3.2, if we assume that we are modelling a narrow and tall machine, and hence $b \ll a$, it is reasonable to ignore the z dependence in (4.84) and solve the 1D problem, which is given by

$$\begin{cases} \dfrac{\partial T}{\partial t} - a\dfrac{1}{r}\dfrac{\partial}{\partial r}\left(r\dfrac{\partial T}{\partial r}\right) = (cT+d) & \text{in} \quad (0,1)\times(0,t_{\rm p}), \\ \dfrac{\partial T}{\partial r} = 0 & \text{on} \quad r=0, \\ \epsilon_{\rm r}\dfrac{\partial T}{\partial r} = -T & \text{on} \quad r=1, \\ T = T_0^* & \text{at} \quad t=0. \end{cases} \tag{4.85}$$

We now consider an exact and an approximate solution to this simplified system.

Separation of variables 1D

The analysis here is similar to that described in Section 4.3.2 but with a different boundary condition. To create a homogeneous problem we substitute $T(r,t) = u(r,t) + v(r)$ into (4.85). Then the problem to solve for u is

$$\begin{cases} \dfrac{\partial u}{\partial t} = a\dfrac{1}{r}\dfrac{\partial}{\partial r}\left(r\dfrac{\partial u}{\partial r}\right) + cu & \text{in} \quad (0,1)\times(0,t_{\rm p}), \\ \dfrac{\partial u}{\partial r} = 0 & \text{on} \quad r=0, \\ \epsilon_{\rm r}\dfrac{\partial T}{\partial r} = -T & \text{on} \quad r=1, \\ u = T_0^* - v(r) & \text{at} \quad t=0, \end{cases} \tag{4.86}$$

whilst the problem for v is

$$0 = \frac{a}{r}\big(v'(r) + rv''(r)\big) + cv + d, \tag{4.87}$$

with $v'(0) = 0$ and $\epsilon_{\rm r}v'(1) = -v(1)$. This has solution

$$v(r) = \frac{d}{c}\Big[\frac{J_0(\sqrt{\frac{c}{a}}r)}{J_0(\sqrt{\frac{c}{a}}) - \epsilon_{\rm r}\sqrt{\frac{c}{a}}J_1(\sqrt{\frac{c}{a}})} - 1\Big]. \tag{4.88}$$

A straightforward calculation gives the solution for u as

$$u(r,t) = \sum_{n=1}^{\infty} \bar{\bar{D}}_n J_0(\bar{\bar{\delta}}_n r) \exp(-\bar{\bar{\lambda}}_n^2 t), \tag{4.89}$$

where $\bar{\bar{\delta}}_n \in \mathbb{R}$ satisfy

$$\epsilon_{\mathrm{r}} \bar{\bar{\delta}} J_1(\bar{\bar{\delta}}_n) = J_0(\bar{\bar{\delta}}_n), \tag{4.90}$$

$\bar{\bar{\lambda}}_n = \sqrt{a\bar{\bar{\delta}}_n^2 - c}$ and coefficients $\bar{\bar{D}}_n$ are given by

$$\bar{\bar{D}}_n = \frac{2\int_0^1 (T_0^* - v(r))\ rJ_0(\bar{\bar{\delta}}_n r)\,\mathrm{d}r}{\int_0^1 rJ_0^2(\bar{\bar{\delta}}_n r)\,\mathrm{d}r}, \tag{4.91}$$

with $v(r)$ defined in (4.88). Finally, the solution T is simply the sum of u and v.

Boundary layer in r

To consider a boundary layer in r we start with system (4.85). Analogously to Section 4.3.2 we assume $d = \mathcal{O}(1)$ and $b < a \ll 1$. Then ignoring the terms involving a and b, we again have at leading order the outer solution given by (4.43), i.e.

$$T(t) = -\frac{d}{c} + \left(T_0^* + \frac{d}{c}\right)\exp(ct). \tag{4.92}$$

It is clear that since solution (4.92) only depends on t it does satisfy the zero flux condition at $r = 0$, but it obviously cannot satisfy the third class boundary condition at $r = 1$. Therefore we consider a boundary layer near $r = 1$. Following the exact steps as in Section 4.3.2, we introduce the boundary-layer coordinate given by (4.44), take $\delta = \sqrt{a}$ to bring out the correct balance in the equation, which at leading order is

$$\begin{cases} \dfrac{\partial T_{\mathrm{in}}}{\partial t} = \dfrac{\partial^2 T_{\mathrm{in}}}{\partial \bar{r}^2} - \sqrt{a}\dfrac{\partial T_{\mathrm{in}}}{\partial \bar{r}} + cT_{\mathrm{in}} + d & \text{in} \quad (0,\infty)\times(0,t_{\mathrm{p}}), \\ \dfrac{\partial T_{\mathrm{in}}}{\partial \bar{r}} = \dfrac{\delta}{\epsilon_{\mathrm{r}}} T_{\mathrm{in}} & \text{on} \quad \bar{r} = 0, \\ T_{\mathrm{in}} \to T_{\mathrm{out}}(t) & \text{as} \quad \bar{r} \to \infty, \\ T_{\mathrm{in}} = T_0^* & \text{at} \quad t = 0, \end{cases} \tag{4.93}$$

where $T_{\mathrm{out}}(t)$ is the outer solution given by (4.92). We define

$$T_{\mathrm{in}}(\bar{r},t) = T_{\mathrm{out}}(t) + \exp\left(\frac{\sqrt{a}\,\bar{r}}{2} + ct - \frac{at}{4}\right) G(\bar{r},t), \tag{4.94}$$

and so the system for G reduces to

$$\begin{cases} \dfrac{\partial G}{\partial t} = \dfrac{\partial^2 G}{\partial \bar{r}^2} & \text{in} \quad (0,\infty)\times(0,t_{\mathrm{p}}), \\ -\dfrac{\partial G}{\partial \bar{r}} + \alpha G = h(t) & \text{on} \quad \bar{r} = 0, \\ G \to 0 & \text{as} \quad \bar{r} \to \infty, \\ G = 0 & \text{at} \quad t = 0, \end{cases} \tag{4.95}$$

where

$$\alpha = \frac{\sqrt{a}}{\epsilon_{\mathrm{r}}} - \frac{\sqrt{a}}{2}, \qquad h(t) = -\frac{\sqrt{a}}{\epsilon_{\mathrm{r}}} T_{\mathrm{out}}(t)\exp\left(-ct + at/4\right). \tag{4.96}$$

From [73] we know that (4.95) can be solved by taking the following integral transform

$$\hat{G}(\omega,t)=\int_0^\infty G(\bar{r},t)K(\omega,\bar{r})\,\mathrm{d}\bar{r}, \tag{4.97}$$

where $K(\omega,\bar{r})$ is the solution of

$$\begin{aligned}&\frac{\mathrm{d}^2R(\bar{r})}{\mathrm{d}^2\bar{r}^2}+\omega^2R(\bar{r})=0,\\&\alpha R(\bar{r})-\frac{\mathrm{d}R(\bar{r})}{\mathrm{d}\bar{r}}=0\qquad\text{on}\quad\bar{r}=0,\end{aligned} \tag{4.98}$$

namely

$$K(\omega,\bar{r})=\sqrt{\frac{2}{\pi}}\Big[\frac{\omega\cos(\omega\bar{r})+\alpha\sin(\omega\bar{r})}{\sqrt{\omega^2+\alpha^2}}\Big]. \tag{4.99}$$

Applying the integral transform (4.97) to the PDE in (4.95) gives

$$\int_0^\infty\frac{\partial G(\bar{r},t)}{\partial t}K(\omega,\bar{r})\,\mathrm{d}\bar{r}=\int_0^\infty\frac{\partial^2G(\bar{r},t)}{\partial\bar{r}^2}K(\omega,\bar{r})\,\mathrm{d}\bar{r}. \tag{4.100}$$

Now

$$\int_0^\infty\frac{\partial^2G(\bar{r},t)}{\partial\bar{r}^2}K(\omega,\bar{r})\,\mathrm{d}\bar{r}=-K\frac{\partial G}{\partial\bar{r}}\Big|_{\bar{r}=0}+\frac{\mathrm{d}K}{\mathrm{d}\bar{r}}G\Big|_{\bar{r}=0}-\omega^2\int_0^\infty G(\bar{r},t)K(\omega,\bar{r})\,\mathrm{d}\bar{r}. \tag{4.101}$$

From (4.95) and (4.98) it follows that at $\bar{r}=0$

$$-K\frac{\partial G}{\partial\bar{r}}+\frac{\mathrm{d}K}{\mathrm{d}\bar{r}}G=-K(\alpha G-h(t))+\alpha KG=h(t)K(\omega,0). \tag{4.102}$$

Hence

$$\int_0^\infty\frac{\partial^2G(\bar{r},t)}{\partial\bar{r}^2}K(\omega,\bar{r})\,\mathrm{d}\bar{r}=-\omega^2\hat{G}+h(t)K(\omega,0)=-\omega^2\hat{G}+\sqrt{\frac{2}{\pi}}h(t)\frac{\omega}{\sqrt{\omega^2+\alpha^2}}, \tag{4.103}$$

and so the PDE in (4.95) becomes

$$\frac{\partial\hat{G}}{\partial t}+\omega^2\hat{G}=\sqrt{\frac{2}{\pi}}h(t)\frac{\omega}{\sqrt{\omega^2+\alpha^2}}, \tag{4.104}$$

where $h(t)$ and α are defined in (4.96). The initial condition in (4.95) implies $\hat{G}(\omega,0)=0$, and so equation (4.104) has solution

$$\hat{G}(\omega,t)=\sqrt{\frac{2}{\pi}}\Big[\frac{\omega\sqrt{a}d}{\epsilon_{\mathrm{r}}c\sqrt{\omega^2+\alpha^2}}\frac{\exp(at/4-ct)-\exp(-\omega^2t)}{\omega^2+a/4-c}-\frac{\omega\sqrt{a}(T_0^*+d/c)}{\epsilon_{\mathrm{r}}\sqrt{\omega^2+\alpha^2}}\frac{\exp(at/4)-\exp(-\omega^2t)}{\omega^2+a/4}\Big], \tag{4.105}$$

after substituting $T_{\mathrm{out}}(t)$ from (4.92). Finally the solution for G (see [73]) is

$$G(\bar{r},t)=\sqrt{\frac{2}{\pi}}\Big[\int_0^\infty\hat{G}(\omega,t)\frac{\omega}{\sqrt{\omega^2+\alpha^2}}\cos(\omega\bar{r})\,\mathrm{d}\omega+\int_0^\infty\hat{G}(\omega,t)\frac{\alpha}{\sqrt{\omega^2+\alpha^2}}\sin(\omega\bar{r})\,\mathrm{d}\omega\Big], \tag{4.106}$$

and $T_{\mathrm{in}}(\bar{r},t)$ is given by (4.94). After adding the inner and outer solutions ans subtracting the common part, we can write down the final solution in the whole domain as

$$T(r,t)=-\frac{d}{c}+\left(T_0^*+\frac{d}{c}\right)\exp(ct)+\exp\left(\frac{1-r}{2}+ct-\frac{at}{4}\right)G\left(\frac{1-r}{\sqrt{a}},t\right). \tag{4.107}$$

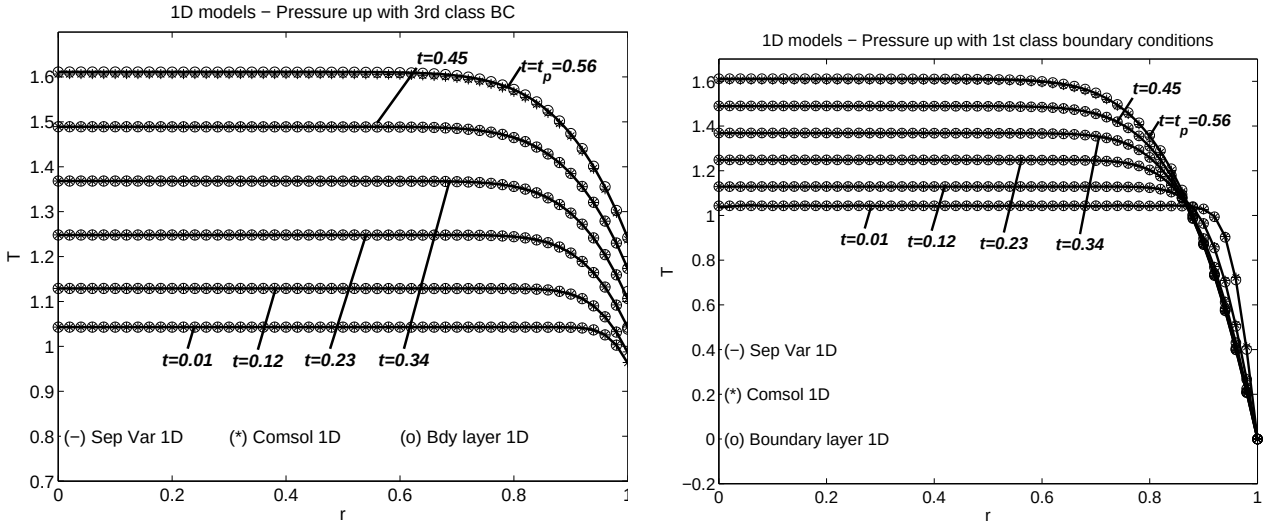

Figure 4.6: Dimensionless temperature profiles calculated with different methods in 1D for the third class (left) and first class (right) boundary conditions.

4.7.2 Results

We perform numerical tests for the problem with third class boundary conditions, using the same data and parameters as in Section 4.5. The heat transfer coefficient used in the tests is $h = 28$ W m^{-2} K^{-1}. Figure 4.6 shows the dimensionless temperature profiles that result from solving the pressure up time problem in 1D for boundary conditions of the third and first class (Sections 4.7.1 and 4.3.2, respectively). The temperature has been calculated using separation of variables in 1D (Sections 4.7.1 and 4.3.2, respectively), by a boundary layer in 1D approximation (Sections 4.7.1 and 4.3.2, respectively). Observe that both solutions match perfectly for all times, and also to the 1D COMSOL solution, which has been taken as a reference model. For the first class boundary conditions, an exact solution in 2D was given in Section 4.3.1. However, for the third class boundary condition we do not give all the possible solutions, as it is analogous to the ones derived throughout Sections 4.3 and 4.4, and we just concentrate on the 1D pressure up case. Also, for the first class boundary conditions, the heat transfer model was coupled with an enzymatic inactivation model in Section 4.6. Again, due to the analogy, we have not gone through the coupling in this case.

4.8 Conclusions

We have presented heat transfer models for predicting temperature profiles inside a solid-type food undergoing HP treatment. Two different kinds of boundary conditions have been considered depending on whether only the food holder is taken into account, or whether the surrounding steel is included. We have given a thorough analysis describing an exact 2D solution as well as several simplifications in both 2D and 1D. It has been shown that for the case of a tall and narrow HP machine, the temperature profile inside the food is very well approximated by a 1D model, except at points very close to the top and bottom boundaries. For the first class boundary conditions, the solutions of the 1D heat transfer models have been used to calculate the final enzymatic activity, also achieving very similar results to when the temperature of the 2D models are used. The reduction to 1D is very useful from a computational point of view, since faster simulations can be carried out. This is interesting, for instance, when performing optimisation algorithms, where very often the state equations need to be solved many times. In addition, the simplified model can help to calculate thermo-physical properties as a function of pressure, via inverse problems, which is an increasing need nowadays for food technologists. From an experimental point of view, results can also be used to determine where to place the thermocouples inside the food sample in order to measure the temperature experimentally. Finally, we point out that the solutions given here do not require the use of a "black-box" FEM solver and our approximations allow us to qualitatively describe the physical features involved.

Chapter 5

Modelling High-Pressure Processes in a Vertical and Horizontal chamber

Nomenclature for Chapter 5

$\mathbf{A}_1$, $\mathbf{A}_2$	Pressure points
C_p	Specific heat capacity (J kg^{-1} K^{-1})
$\mathbf{g}$	Gravity vector (m s^{-2})
h	Heat transfer coefficient (W m^{-2} K^{-1})
H	Domain height (m)
k	Thermal conductivity (W m^{-1} K^{-1})
L	Domain width (m)
L_r	Radial length scale (m)
L_z	Vertical length scale (m)
M	Mass (kg)
$\mathbf{n}$	Outward normal unit vector (m)
p	Mass transfer pressure (Pa)
P	Equipment Pressure (Pa)
$P_{\max}$	Maximum target pressure (Pa)
r	Radial coordinate (m)
t	Time (s)
t_{f}	Final time (s)
t_{up}	Pressure-up time (s)
T	Temperature (K)
T_0	Initial temperature (K)
T_{env}	Environment temperature (K)
T_{r}	Fixed temperature (K)
$\mathbf{u}$	Fluid velocity vector (m s^{-1})
u_x, u_y, u_z	Components of the velocity vector $\mathbf{u}$
U	Velocity scale (m s^{-1})
V	Volume (m^3)
x, y, z	Cartesian coordinates (m)

Indices

*	Rotated domains
F	Food domain
hold	Pressure-hold solution
P	Pressurising fluid
up	Pressure-up solution

Greek symbols

β	Thermal expansion coefficient (K^{-1})
Γ	Whole domain boundary
Γ_{p}	Boundary of Ω_{P}^*
Γ_{r}	Fixed temperature boundary
Γ_{up}	Heat transfer boundary
η	Dynamic viscosity (Pa s)
θ	Cylindrical angular coordinate
Θ	Temperature scale (K)
ρ	Density (kg m^{-3})
τ	Time scale (s)
Ω	Whole domain
Ω_{C}	Cap of the sample holder
Ω_{F}	Food sample domain
Ω_{P}	Pressurising medium
Ω_{S}	Steel vessel

Other symbols

∇	Gradient
$\nabla\cdot$	Divergence
∇^2	Laplacian

Acronyms

CFD	Computational Fluid Dynamics
FEM	Finite Element Method
HP	High Pressure
HPP	High Pressure Processing
OS	Operation system
RAM	Random access memory
2D	Two-dimensional
3D	Three-dimensional

5.1 Introduction

In this Chapter we are going to consider liquid-type foods, for which, as we showed in Chapter 3, convection effects also have to be included into the heat transfer model. Due to the complexity of solving Navier-Stokes equations, we know that analytical solutions are no longer available and the model will have to be solved numerically. Several authors have done extensive research in developing models to predict transient temperature and flow distributions, uniformity, and the loss of compression heating through high pressure vessel walls during all HPP steps. In [19, 21, 37, 38, 39, 40] the authors used discrete numerical modelling and computational fluid dynamics (CFD) to predict temperature and flow distribution inside the HP vessel. More recent models include solid materials [46, 48, 52, 69]. In [32] the authors predict temperature and flow distribution of a HP process in a three-dimensional vessel, and in [48, 52] the flow and temperature fields inside a pilot-scale unit for HP sterilisation conditions are predicted and validated numerically. In most of these works, special attention has also been given to the distribution of enzyme and microbial inactivation throughout the chamber and packages, aiming to ensure uniformity.

To the best of our knowledge, all of the models developed and published to date on prediction of temperature and flow distribution of a HPP, have one common feature, and that is they are models based on vertically oriented high pressure units. This is because, as stated in [63], the original HPP equipment units were vertical (see Figure 3.1 in Chapter 3). However, the current trend is to supply horizontal units at industrial scale (see Figure 5.1). A horizontal orientation avoids sub-level construction requirements, eliminates height, and floor load restrictions, makes system installation and relocation more feasible, facilitates product flow in the plant and reduces the risk of confusing treated and unprocessed product [63].

Figure 5.1: Example of horizontal, large commercial HPP vessel. Model Hiperbaric 55. Hiperbaric, Burgos, Spain. [42]

Because of this increase of horizontal units in the industry, but yet the lack of published work on horizontal models, we decided it would be interesting to begin to cover this research gap. Nowadays, most of the experimental data available from researchers is for HP processes which have taken place in a vertical unit, due to the fact that laboratory or pilot-scale units are mostly vertical. We did not have the experimental resources to be able to setup a horizontal laboratory-scale unit to obtain experimental data. Therefore, designing a horizontal model from scratch was not plausible at this point. Instead, we decided to develop a horizontal model by adapting an existing vertical one, which had previously been validated. In this way, what we can show are the differences between the vertical and horizontal models, stating the research need for developing horizontal models, which would be very helpful for the industry.

It is clear that the major reason why the vertical and horizontal models are different, even if they have exactly the same process conditions, is due to the fluid flow pattern, which we know that for the case of a liquid-type food has a significant influence on homogeneity of the final pressurised product. During compression, the increase in temperature induces heat exchange within the liquid and solid and also heat exchange with the walls of the pressure chamber. Consequently, density difference occurs which lead to free convection of the fluid.

For upward flow in vertical tubes, the effect of free convection is to accelerate the fluid particles near the wall. This creates steeper velocity and temperature gradients near the wall, and hence higher heat transfer rates. To satisfy continuity considerations, the increased velocity near the wall results in flow retardation at the tube centre and, in extreme cases, a reversal of flow at the tube centre may even occur (see, e.g., [57, 65]). The flow pattern produced by free convection inside a horizontal tube is quite different than the vertical case; transverse fluid movement is more important. When a fluid in a horizontal tube is heated, the buoyancy forces cause movement of the fluid upwards at the sides and downwards at the centre. If combined with forced flow (which we do not consider in this work), this effect sets up forward moving spirals and the resulting flow pattern may not be entirely steady (see, e.g., [65]).

Through the work developed in this Chapter we want to show that the horizontal and vertical flow inside a liquid-type food undergoing a HP process are indeed different, and therefore so is the temperature distribution, which could be problematic for the food industry, if uniformity of pursued effects such as enzymatic or microbial inactivation are required. This work is based on that from [84]. In the following Sections we are going to further develop a heat transfer model to determine the temperature and flow distribution inside a sample treated with HP in a horizontally oriented vessel, and compare the results to the ones obtained with the heat transfer model of a HP device placed vertically, with exactly the same process conditions.

5.2 The process models

The starting point is the vertical two-dimensional (2D) axis-symmetric geometry presented in Chapter 3, which was modelled and solved numerically in [46]. The selection of an axis-symmetric model is very common in HPP modelling of vertically oriented devices, given that in many cases the system comprises axis-symmetric features, and has been successfully used and validated in several papers (see, e.g. [50, 51, 52, 69]). This model derived by [46] for liquid-type foods includes conduction and convection effects, and the flow is assumed to be laminar (as we saw in Section 3.2). Other more complex models, which also include turbulence effects (such as, e.g. [50, 51, 52]), could have been chosen as the starting model. However due to the complexity of solving a horizontal model, we decided to keep it as simple as possible.

For a horizontally oriented HP device, however, there are no longer only axis-symmetric features, and therefore a three-dimensional (3D) model seems necessary. For this reason, in this Chapter we develop both vertical and horizontal 3D models, in order to compare them. We will first compare the 2D to the 3D vertical model to see how good the agreement is and to check the efficiency of the 3D model solver that we are going to use. Then we will proceed to compare the 3D horizontal to the 3D vertical model, and show how different the results are.

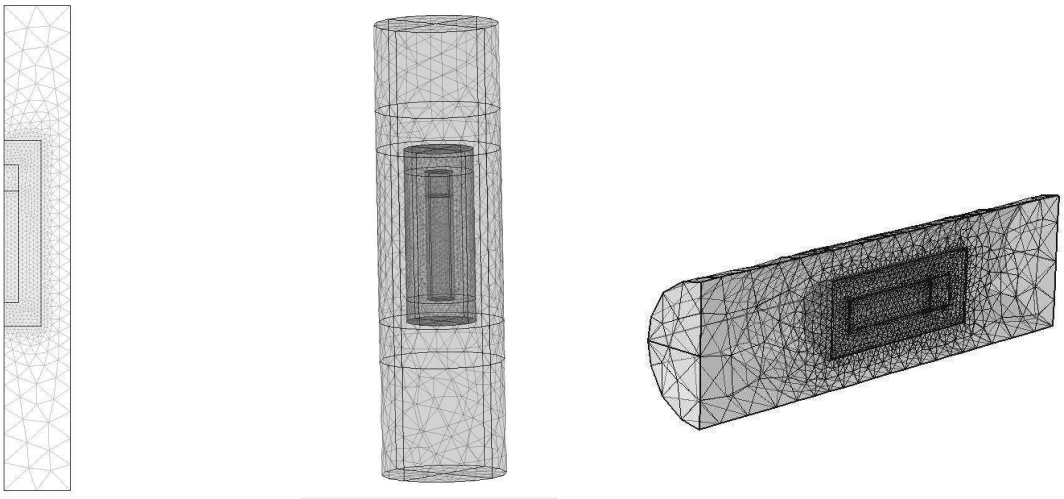

(a) 2D axis-symmetric (b) Full 3D vertical (c) Half 3D horizontal

Figure 5.2: Computational configurations

5.2.1 Geometries

Vertically oriented geometries

The computational vertical 2D axis-symmetric geometry consider is the one described in Chapter 3. The computational domain is shown in Figure 5.2a. From this 2D model we generate the 3D vertical model by rotating this geometry along the axis of symmetry; the resulting 3D vertical geometry is depicted in Figure 5.2b. We will show in Section 5.4.1 that the solution given by the axis-symmetric 2D vertical model is equal to the 3D model (ignoring numerical errors).

Horizontally oriented geometry

In the horizontal case there are no longer only axis-symmetric features, and so we obviously cannot reduce the model to 2D and expect to have the same solution as in the vertical case. However, there is a computational simplification that can be made: the model can be solved in only half a cylinder (cutting it longitudinally), hence reducing the number of degrees of freedom. The resulting "half" 3D horizontal geometry is depicted in Figure 5.2c.

5.2.2 Heat and mass transfer model

As stated in Section 5.1, for the purpose of this work we are only going to consider liquid-type foods. If we also have convection effects inside the food sample, the differences between the vertical and horizontally oriented chambers will be even more pronounced than if we only considered conduction effects inside the food sample, which is the case for solid-type foods. In this Chapter we are going to solve the full 3D model, to then compare the results to the 2D-axially symmetric model. Given the difficulties of solving a 3D model we have chosen to use the simplified model proposed in Chapter 3, Section 3.3.3, that is

$$\begin{cases} \bar{\rho}\bar{C_p}\dfrac{\partial T}{\partial t} - \bar{k}\nabla^2 T + \bar{\rho}\bar{C_p}\mathbf{u}\cdot\nabla T = \bar{\beta}\,\dfrac{\mathrm{d}P}{\mathrm{d}t}\,T & \text{in} \quad \Omega^* \times (0,t_\mathrm{f}), \\ \bar{\rho}\dfrac{\partial \mathbf{u}_\mathrm{F}}{\partial t} - \bar{\eta}\nabla^2\mathbf{u}_\mathrm{F} + \bar{\rho}(\mathbf{u}_\mathrm{F}\cdot\nabla)\mathbf{u}_\mathrm{F} = -\nabla p + \rho\mathbf{g} & \text{in} \quad \Omega^*_\mathrm{F} \times (0,t_\mathrm{f}), \\ \bar{\rho}\dfrac{\partial \mathbf{u}_\mathrm{P}}{\partial t} - \bar{\eta}\nabla^2\mathbf{u}_\mathrm{P} + \bar{\rho}(\mathbf{u}_\mathrm{P}\cdot\nabla)\mathbf{u}_\mathrm{P} = -\nabla p + \rho\mathbf{g} & \text{in} \quad \Omega^*_\mathrm{P} \times (0,t_\mathrm{f}), \\ \nabla\cdot(\mathbf{u}_\mathrm{F}) = 0 & \text{in} \quad \Omega^*_\mathrm{F} \times (0,t_\mathrm{f}), \\ \nabla\cdot(\mathbf{u}_\mathrm{P}) = 0 & \text{in} \quad \Omega^*_\mathrm{P} \times (0,t_\mathrm{f}), \end{cases} \tag{5.1}$$

with the following point, boundary and initial conditions

$$\begin{cases} k\dfrac{\partial T}{\partial \mathbf{n}} = 0 & \text{on} \quad \left(\Gamma^* \setminus (\Gamma^*_\mathrm{r} \cup \Gamma^*_\mathrm{up})\right) \times (0,t_\mathrm{f}), \\ k\dfrac{\partial T}{\partial z} = h(T_\mathrm{env} - T) & \text{on} \quad \Gamma^*_\mathrm{up} \times (0,t_\mathrm{f}), \\ T = T_\mathrm{r} & \text{on} \quad \Gamma^*_\mathrm{r} \times (0,t_\mathrm{f}), \\ \mathbf{u}_\mathrm{F} = 0 & \text{on} \quad \Gamma^*_\mathrm{F} \times (0,t_\mathrm{f}), \\ \mathbf{u}_\mathrm{P} = 0 & \text{on} \quad \Gamma^*_\mathrm{P} \times (0,t_\mathrm{f}), \\ T(0) = T_0 & \text{in} \quad \Omega^*, \\ \mathbf{u}_\mathrm{F}(0) = 0 & \text{in} \quad \Omega^*_\mathrm{F}, \\ \mathbf{u}_\mathrm{P}(0) = 0 & \text{in} \quad \Omega^*_\mathrm{P}, \\ p = 10^5 & \text{on} \quad \mathbf{A}_1 \times (0,t_\mathrm{f}), \\ p = 10^5 & \text{on} \quad \mathbf{A}_2 \times (0,t_\mathrm{f}). \end{cases} \tag{5.2}$$

System (5.1) together with its boundary and initial conditions (5.2) are valid for all the proposed geometries in Section 5.2.1. For the 2D axis-symmetric model it may be rewritten in cylindrical coordinates [46]. For the 3D horizontal "half" model, heat flux and flow symmetric boundary conditions have to be added to (5.2) at the "cutting" boundary.

5.2.3 Comparing dimensionless convection effects for vertical and horizontal model

Before we proceed with our simulations, we want to find a dimensionless quantity for convection effects for both the vertical and horizontal models, to see which is expected to be more important. For this, we look at the first equation of (5.1), i.e. the convective heat transfer equation

$$\bar{\rho}\bar{C_p}\frac{\partial T}{\partial t} - \bar{k}\nabla^2 T + \bar{\rho}\bar{C_p}\mathbf{u}\cdot\nabla T = \bar{\beta}\ \frac{\mathrm{d}P}{\mathrm{d}t}\ T, \tag{5.3}$$

where $\bar{\rho}$, $\bar{C_p}$, $\bar{k}$, $\bar{\beta}$ are considered to be constant (they are set to their mean value in the temperature and pressure range we are working in). We want to non-dimensionalise equation (5.3).

Following Section 4.2.2, we write the pressure derivative that appears in equation (5.3) using (4.4). Because the equation to non-dimensionalise now is different to the one in Section 4.2.2 (it includes a convective term and is in Cartesian coordinates instead of cylindrical ones), we choose new scales, and hence equation (5.3) is non-dimensionalised by setting

$$\hat{x} = \frac{x}{L_r}, \qquad \hat{y} = \frac{y}{L_r}, \qquad \hat{z} = \frac{z}{L_z}, \qquad \hat{t} = \frac{t}{\tau}, \qquad \hat{T} = \frac{T}{\Theta}, \qquad (\hat{u}_x, \hat{u}_y, \hat{u}_z) = \frac{1}{U}(u_x, u_y, u_z)$$

where Θ, U, and τ are suitable temperature, velocity, and time scales, respectively. L_r is a radial length scale and L_z a vertical length scale.

Thus, equation (5.3) becomes

$$\begin{aligned}\frac{\bar{\rho}\bar{C_p}\Theta}{\tau}\ \frac{\partial \hat{T}}{\partial \hat{t}} - \bar{k}\Theta\left(\frac{1}{L_r^2}\left(\frac{\partial^2\hat{T}}{\partial\hat{x}^2} + \frac{\partial^2\hat{T}}{\partial\hat{y}^2}\right) + \frac{1}{L_z^2}\frac{\partial^2\hat{T}}{\partial\hat{z}^2}\right)\\ + \bar{\rho}\bar{C_p}\Theta U(\hat{u}_x,\hat{u}_y,\hat{u}_z)\cdot\left(\frac{1}{L_r}\frac{\partial\hat{T}}{\partial\hat{x}}, \frac{1}{L_r}\frac{\partial\hat{T}}{\partial\hat{y}}, \frac{1}{L_z}\frac{\partial\hat{T}}{\partial\hat{z}}\right) = \frac{\beta\gamma\Theta}{t_\mathrm{p}}\ \hat{T}.\end{aligned} \tag{5.4}$$

We divide equation (5.4) by $\bar{\rho}\bar{C_p}\Theta/\tau$, resulting in

$$\frac{\partial\hat{T}}{\partial\hat{t}} - \frac{\bar{k}\tau}{\bar{\rho}\bar{C_p}}\left(\frac{1}{L_r^2}\left(\frac{\partial^2\hat{T}}{\partial\hat{x}^2} + \frac{\partial^2\hat{T}}{\partial\hat{y}^2}\right) + \frac{1}{L_z^2}\frac{\partial^2\hat{T}}{\partial\hat{z}^2}\right) + \tau U\left(\frac{\hat{u}_x}{L_r}\frac{\partial\hat{T}}{\partial\hat{x}} + \frac{\hat{u}_y}{L_r}\frac{\partial\hat{T}}{\partial\hat{y}} + \frac{\hat{u}_z}{L_z}\frac{\partial\hat{T}}{\partial\hat{z}}\right) = \frac{\beta\gamma\tau}{\bar{\rho}\bar{C_p}t_\mathrm{p}}\ \hat{T}. \tag{5.5}$$

We want to compare the convection effects between the vertical and horizontal models. If we picture the chamber placed vertically (see Figure 3.2), we can imagine that the fluid in the vertical model is moving up and down the chamber, whilst in the horizontal case it will move from left to right. Therefore, we assume that the velocity in the vertical case is mainly moving in the vertical direction, i.e. $u_z \gg u_x, u_y$ (or equivalently, $\hat{u}_z \gg \hat{u}_x, \hat{u}_y$) whilst in the horizontal case it mainly moves in the radial direction, hence $u_z \ll u_x, u_y$ (or equivalently, $\hat{u}_z \ll \hat{u}_x, \hat{u}_y$). We assume, in order to be able to compare the vertical and horizontal convection effects, that the velocity field $\mathbf{u}$ in both cases is of the same order (even though it has perpendicular directions).

To choose our length scales, we know that the fluid moves between H_1 and H_5 (see Figure 3.2) in the vertical direction, and hence $L_z = H_5 - H_1$; radially it moves between L_1 and L_2, and, if the food is of liquid-type, between 0 and L_1, and therefore the radial length scale is taken to be the maximum between L_1 and $L_2 - L_1$ or, for the sake of simplicity, $L_r = L_2$.

Assuming we are in the vertical case, equation (5.5) can be written as

$$\frac{\partial\hat{T}}{\partial\hat{t}} - \frac{\bar{k}\tau}{\bar{\rho}\bar{C_p}}\left(\frac{1}{L_r^2}\left(\frac{\partial^2\hat{T}}{\partial\hat{x}^2} + \frac{\partial^2\hat{T}}{\partial\hat{y}^2}\right) + \frac{1}{L_z^2}\frac{\partial^2\hat{T}}{\partial\hat{z}^2}\right) + \frac{\tau U}{L_z}\hat{u}_z\frac{\partial\hat{T}}{\partial\hat{z}} = \frac{\beta\gamma\tau}{\bar{\rho}\bar{C_p}t_\mathrm{p}}\ \hat{T}, \tag{5.6}$$

where the terms with $\hat{u}_x$ and $\hat{u}_y$ have been neglected because of our previous assumption $\hat{u}_z \gg \hat{u}_x, \hat{u}_y$. So, in this case we have a convective coefficient $c_v = \frac{\tau U}{L_z}$.

If instead we are in the horizontal case, equation (5.5) results in

$$\frac{\partial \hat{T}}{\partial \hat{t}} - \frac{\bar{k}\tau}{\bar{\rho}\bar{C}_p}\left(\frac{1}{L_r^2}\left(\frac{\partial^2 \hat{T}}{\partial \hat{x}^2} + \frac{\partial^2 \hat{T}}{\partial \hat{y}^2}\right) + \frac{1}{L_z^2}\frac{\partial^2 \hat{T}}{\partial \hat{z}^2}\right) + \frac{\tau U}{L_r}\left(\hat{u}_x \frac{\partial \hat{T}}{\partial \hat{x}} + \hat{u}_y \frac{\partial \hat{T}}{\partial \hat{y}}\right) = \frac{\beta\gamma\tau}{\bar{\rho}\bar{C}_p t_{\mathrm{p}}}\,\hat{T}, \tag{5.7}$$

where now the $\hat{u}_z$ term has been neglected due to our previous assumption $\hat{u}_z \ll \hat{u}_x, \hat{u}_y$. So, in this case we have a convective coefficient $c_h = \frac{\tau U}{L_r}$. We can see that the relation between c_v and c_h is $c_v = c_h\left(\frac{L_r}{L_z}\right)$.

From looking at the dimensions of our machine, we have $H_5 = 0.472$ m and $H_1 = 0.222$ m, which gives $L_z = 0.25$ m, and $L_2 = 0.05$ m, which gives $L_r = 0.05$ m. Using these values we see that $c_v = \frac{c_h}{5}$, so the convection effects are about 5 times larger in the horizontal case than in the vertical one. We remark that if we had chosen L_r to be $L_2 - L_1$, instead of L_2, then this difference would increase from 5 to nearly 10 times.

Also, we would like to point out that in the horizontal case, the convective currents reach the food sample sooner than in the vertical case, as they move mainly in the radial direction (see Figures 5.6a, 5.6b, 5.10a, 5.10b), which is smaller than the vertical direction. A fluid particle that is closer to the cold wall (especially to the top wall - this is, in the horizontal case) will in general take less time to reach the food sample than the same particle in the vertical case. This is why the machine placed horizontally cools the sample much faster than the vertically oriented one, resulting in lower temperatures throughout the process.

5.3 Numerical tests

5.3.1 Dimensions of the HP pilot unit

For the numerical tests, we have considered a similar size to the pilot unit (ACB GEC Alsthom, Nantes, France) that was used in [69]. The dimensions of the machine are given in Table 5.1. The numerical tests we present are computed in cylindrical coordinates for the 2D model, assuming cylindrical coordinates and Cartesian coordinates for the 3D-model. We use the Finite Element Method (FEM) solver COMSOL Multiphysics 3.5a to compute the solutions. More details of the computations will be given in Section 5.4.

5.3.2 Process conditions

Process P_1: Moderate temperature and pressure

We consider the following HP processes with different initial temperature and pressure curve (see process P_2 in [46]): The initial temperature is $T_{0_1} = 40°\mathrm{C}$ in the whole domain Ω and the pressure is linearly increased during the first 183 seconds until it reaches $P_{\max_1} = 360$ MPa. Thus, the pressure generated by the equipment satisfies $P(0) = 0$ and

$$\frac{\mathrm{d}P_1}{\mathrm{d}t}(t) = \begin{cases} \dfrac{360}{183} \cdot 10^6 \text{ Pa s}^{-1}, & 0 < t \leq 183, \\ 0 \text{ Pa s}^{-1}, & t > 183. \end{cases} \tag{5.8}$$

Process P_2: High temperature and pressure

We also consider a HP process with higher temperature and pressure curve (typical pasteurisation values): The initial temperature is $T_{0_2} = 65°\mathrm{C}$ in the whole domain Ω and the pressure is linearly increased during the first 200 seconds until it reaches $P_{\max_2} = 600$ MPa. Thus, the pressure generated by the equipment satisfies $P(0) = 0$

and

$$\frac{\mathrm{d}P_2}{\mathrm{d}t}(t) = \begin{cases} \dfrac{600}{200} \cdot 10^6 \text{ Pa s}^{-1}, & 0 < t \leq 200, \\ 0 \text{ Pa s}^{-1}, & t > 200. \end{cases} \tag{5.9}$$

5.3.3 Thermo-physical parameters

For the sake of simplicity, the physical parameters of the pressurising medium and the liquid-type food are assumed to be those of water. The mean values in the relevant range of temperature and pressure for each of the processes are given in Table 5.1. The thermo-physical properties of the steel and rubber cap of the sample holder are assumed to be constant, and obviously the same for both processes, and their values are also in Table 5.1. The refrigeration temperature T_r for both processes is taken to be equal to the initial temperature; and the environment temperature, T_env is taken as 19.3°C (which is a reasonable room temperature).

$\bar{\rho}_{\mathrm{F}_1}, \bar{\rho}_{\mathrm{P}_1}$	973.856	$\bar{\rho}_{\mathrm{F}_2}, \bar{\rho}_{\mathrm{P}_2}$	1068.2	ρ_S	7833	ρ_C	1110	kg m^{-3}
$\bar{C}_{p\mathrm{F}_1}, \bar{C}_{p\mathrm{P}_1}$	4686.65	$\bar{C}_{p\mathrm{F}_2}, \bar{C}_{p\mathrm{P}_2}$	3900.9	$C_{p\mathrm{S}}$	465	$C_{p\mathrm{C}}$	1884	J kg^{-1} K^{-1}
$\bar{k}_{\mathrm{F}_1}, \bar{k}_{\mathrm{P}_1}$	0.649	$\bar{k}_{\mathrm{F}_1}, \bar{k}_{\mathrm{P}_2}$	0.7848	k_S	55	k_C	0.173	W m^{-1} K^{-1}
$\bar{\beta}_{\mathrm{F}_1}, \bar{\beta}_{\mathrm{P}_1}$	$4.574 \cdot 10^{-4}$	$\bar{\beta}_{\mathrm{F}_2}, \bar{\beta}_{\mathrm{P}_2}$	$5.0297 \cdot 10^{-4}$	K^{-1}		h	28	W m^{-2} K^{-1}
$\bar{\eta}_1$	$8.069 \cdot 10^{-4}$	$\bar{\eta}_2$	$4.36 \cdot 10^{-4}$	Pa s		T_env	19.3	°C
P_{max_1}	360 MPa	L_1	0.02	L_2	0.05	L	0.09	m
P_{max_2}	600 MPa	H_1	0.222	H_2	0.254	H_3	0.404	m
$T_{0_1} = T_{\mathrm{r}_1}$	40°C	H_4	0.439	H_5	0.472	H	0.654	m
$T_{0_2} = T_{\mathrm{r}_2}$	65°C	t_{p_1}	183	t_{p_2}	200	t_f	900	s

Table 5.1: Typical parameter values for both processes. The food and the pressurising fluid properties are those of water in the adequate range of temperature and pressure. Data obtained from [14, 46, 68].

5.3.4 Computational methods

The partial differential equations describing the model were solved with the Finite Element Method (FEM) using COMSOL Multiphysics$^{\mathrm{TM}}$ (COMSOL AB, Stockholm, Sweden) a commercial software package. Different toolboxes (namely, heat transfer and fluid flow) were used for simultaneously solving Multiphysics problems. For each geometry the mesh was different, using tetrahedral elements for the 3D models and triangular elements for the 2D models. The computations were carried out on different workstations and the solving time for all cases was different (obviously for the 3D models it was much longer than the 2D models). Details can be seen in Table 5.2. We remark that even though the number of elements for the 3D vertical case was a bit larger than for the 3D horizontal case, the computational solving time was much longer for the horizontal model. This is due to the fact that the horizontal flow moves faster than the vertical one, and therefore the Navier-Stokes equations are more complex to solve and take longer.

Model	Comsol Version	Number of elements in mesh	Workstation characteristics	Computational time (s)
2D vertical axis-symmetric	3.5a	1526	Two dual-core processors (2.33 GHz each) 4 GB RAM 64bit OS Windows 2003	220
3D vertical	3.5a	73843	Two dual-core processors (2.33 GHz each) 4 GB RAM 64bit OS Windows 2003	144000
3D horizontal (half)	4.2a	66306	Four dual-core processors (3.40 GHz each) 8 GB RAM 64bit OS Windows 7	330949

Table 5.2: Characteristics of the computational methods for the different models

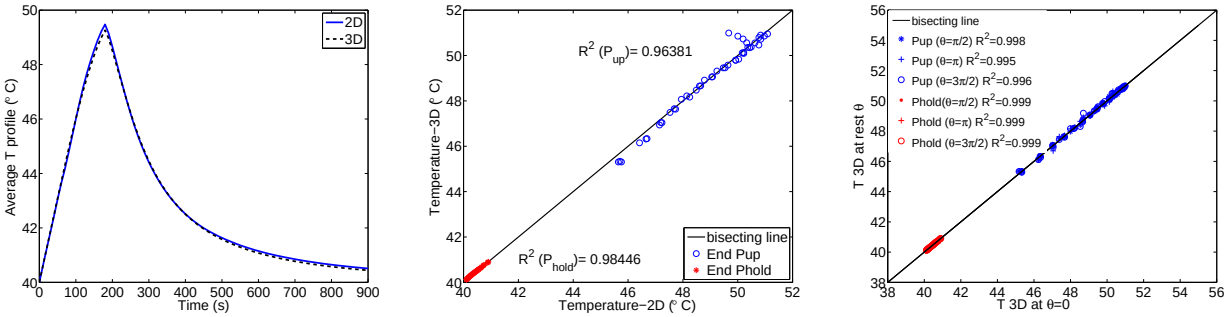

(a) Mean temperature (b) Parity plot 2D/3D (c) Parity plot 3D

Figure 5.3: Different plots for 2D and 3D vertical models. Process 1

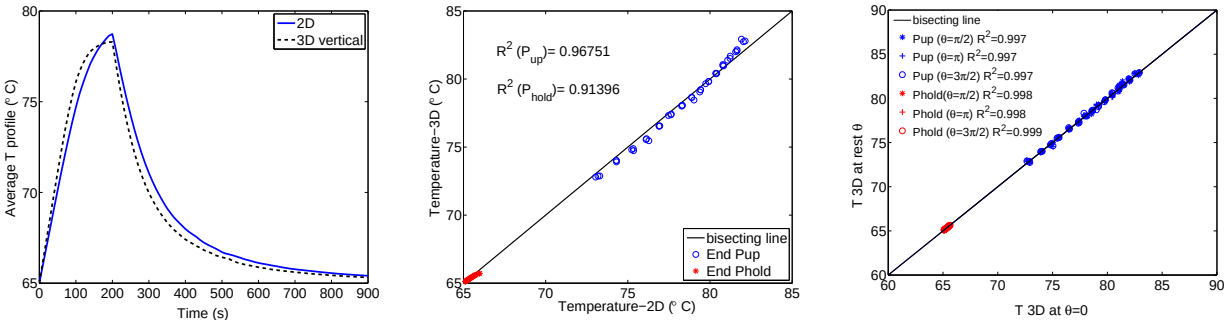

(a) Mean temperature (b) Parity plot 2D/3D (c) Parity plot 3D

Figure 5.4: Different plots for 2D and 3D vertical models. Process 2

5.4 Numerical results and discussion

5.4.1 Comparison between 2D axis-symmetric and 3D vertical models

Firstly, we compared the results of the 2D axis-symmetric and 3D vertical models, which we expect to be nearly identical. The comparison was performed in 45 locations (covering an axis-symmetric plane with a 3 x 15 matrix) at three different radial coordinates (symmetry axis, 9 mm distance from symmetry axis and 18mm distance from symmetry axis) and fifteen different heights (10 mm steps, from 6 mm above the sample holder bottom to 4 mm below the sample holder top) of the food sample region. This comparison with the same points was repeated for different planes in the 3D model (at angles $\theta = 0, \pi/2, \pi, 3\pi/2$). The 3D temperature variable is taken as the average of the temperature over these different planes. A comparison of the 2D and 3D Multiphysics models shows that the model outcome for the temperature was very similar. Figures 5.3a and 5.4a show the average temperature over time of the 2D axis-symmetric and 3D vertical model for processes P_1 and P_2, respectively, with very good agreement. Figures 5.3b and 5.4b show the parity plots for the predicted temperature from the 2D axis-symmetric and 3D vertical model for processes P_1 and P_2, respectively. The coefficient of determination R^2 were greater than 0.9, for both processes, at the end of pressurisation ($\mathrm{P_{up}}$) and at the end of the process ($\mathrm{P_{hold}}$). Figures 5.3c and 5.4c show the parity plot for the predicted temperatures of the 3D model along the different planes (at angles $\theta = 0, \pi/2, \pi, 3\pi/2$), for processes P_1 and P_2, respectively. The coefficients of determination R^2 were greater than 0.99, for both process, at the end of pressurisation ($\mathrm{P_{up}}$) and at the end of the process ($\mathrm{P_{hold}}$).

We point out that the 2D axis-symmetric solution could be even more similar to the 3D vertical solution if we had further refined the 3D mesh. However, given that our goal in this paper was to compare the 3D vertical to 3D horizontal model, and taking into account the large computational time the 3D models took (see Table 5.2),

we considered that further refinements to improve the 2D axis-symmetric to 3D vertical solution similarity was unnecessary, as the results already obtained are good enough.

5.4.2 Comparison between 3D vertical and 3D horizontal models

Let us now compare the 3D vertical and 3D horizontal models. Obviously, the results of these models will no longer be the same. We expect the temperature to be different, due to the difference in the flow. To compare the results from the different models, we developed a MATLAB routine to extract temperature data from the models in COMSOL, in several configurations:

- Over the entire liquid food domain with a 1 mm^3 resolution (i.e. we look at the same points for both cases), which will give us a good idea of the overall difference in temperature performance.
- On the central radial slice of the liquid food domain for both orientations, to help visualise the spatial differences radially.
- For further information on spatial differences we select 5 radial slices (and points on them at $1mm^2$ resolution) along the height in the vertical case (starting from the bottom of the food sample holder and separated by 0.0375m), and the same slices along the length in the horizontal case. The central radial slice of the previous point coincides with the third slice here. This will give us an idea of the temperature behaviour radially but also at different heights.
- Along the central axis of the food sample domain, which will help to illustrate the temperature differences with height at the same radial point.

For all of these data sets we plot the averaged temperature over time with standard deviations at ten time steps for both models, and for both processes P_1 and P_2. Tables 5.3 and 5.4 show the temperature mean values (measure of performance) and standard deviation values (measure of uniformity) at the end of pressurisation (P_{up}) and end of the process (P_{hold}), for all of these sets of data, for the 3D vertical and horizontal models, for process P_1 and P_2, respectively

We also look at slice plots of the temperature and velocity field inside the food sample and pressurising media at the end of the pressurisation (P_{up}) and also at the end of the process (P_{hold}), separately for the vertical and horizontal cases to illustrate the differences in temperature distribution inside the vessel and also the qualitative difference in the flow distribution.

Process P_1: Moderate temperature and pressure

Figures 5.5 and 5.6 show the slice plots for process P_1 at the end of P_{up} and P_{hold} for the vertical and horizontal model, respectively. As can be seen, the distribution for the vertical model is homogeneous in the radial direction and changes with height, whereas for the horizontal model the changes in length (equivalent to height for the vertical case) are insignificant, but there are differences in the radial direction. If we focus on a certain length for the horizontal case we can see that the temperature at the top is warmer than at the bottom, which did not happen in the vertical case (for the vertical case at a given height the temperature distribution inside the sample was more uniform). This can be explained by saying that the cooling is coming from the boundary Γ_r, which in the horizontal case is at the top and bottom of the sample (as it is depicted in the slice plot), but when you put the machine in a vertical position this boundary is at the left and right of the sample. In the vertical case, because the cooling was coming from the sides, it affected the flow homogeneously, but now it is coming from above and below, and because of gravity the lower part is getting cooler faster than the top part.

For both models, at the end of P_{up} the differences are larger than at the end of P_{hold} due to the fact that the pressurisation induces a heat source, so the overall temperature is larger, and hence so are the differences. At the end of P_{hold} the sample has had enough time to cool down to the boundary temperature T_{r} almost everywhere and therefore the differences at different locations have reduced. Overall, the temperature of the vertical model is higher than that of the horizontal one, especially at the end of P_{up}. This is due to the fact that the flow is faster in the horizontal case, and therefore the sample temperature reaches the boundary temperature at Γ_{r}

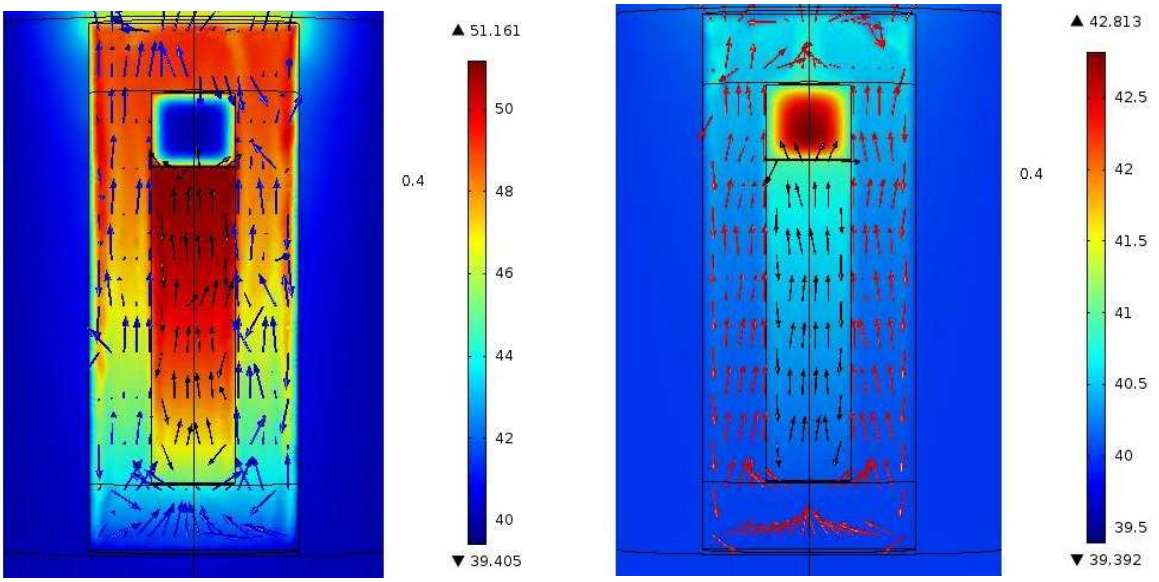

(a) End of P_{up} (b) End of P_{hold}

Figure 5.5: Slice plots 3D vertical model. Process P_1

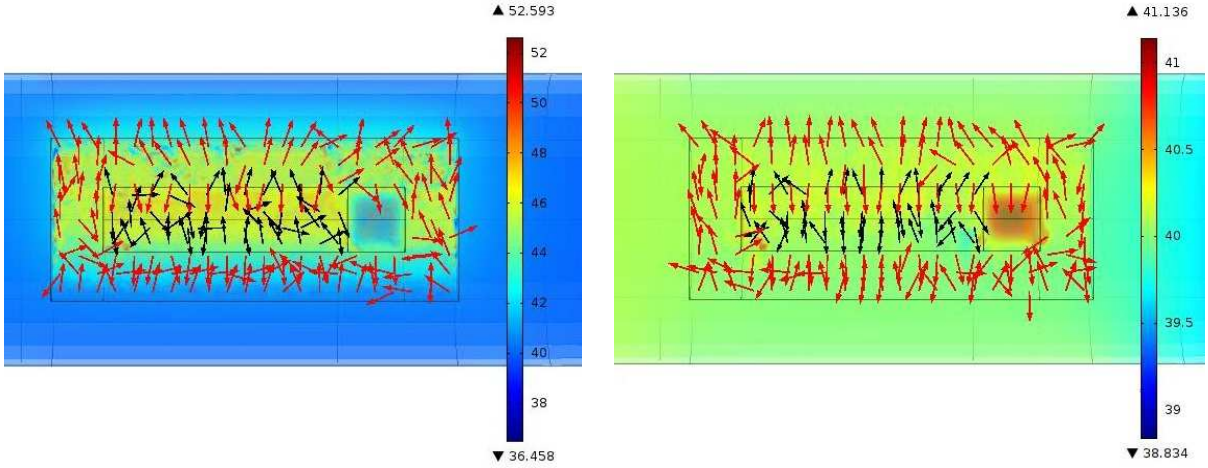

(a) End of P_{up} (b) End of P_{hold}

Figure 5.6: Slice plots 3D horizontal model. Process P_1

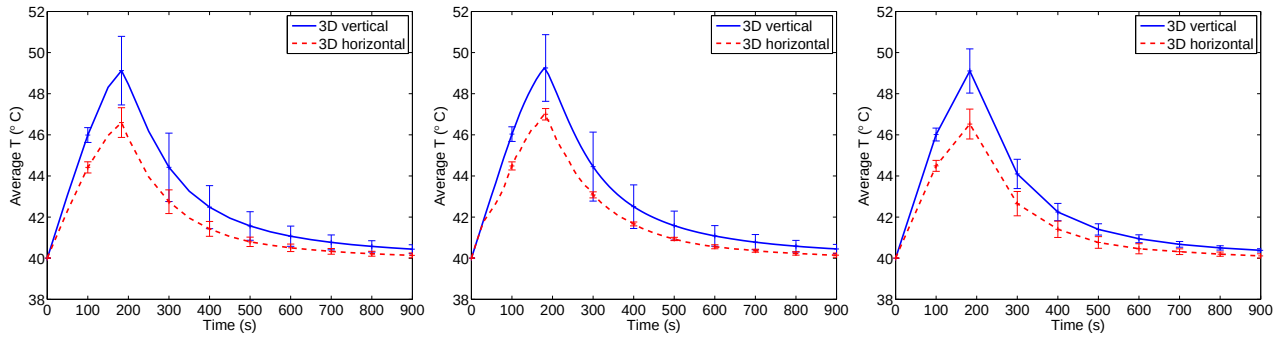

(a) Over 1mm^3 resolution (b) Along central axis (c) Over central slice

Figure 5.7: Averaged temperature evolution for different data sets. Process P_1

faster. In [46, 69] they proved that the cooling is faster when convection is included in the model than when it is not. So for faster flows this result also holds.

Looking at the qualitative distribution of the flow we can also see a difference between the vertical and horizontal model. For the vertical model the flow moves longitudinally, whereas for the horizontal model the flow moves mainly radially. This is due to gravity and the location of the cooler boundary, as we mentioned above. For the vertical model the cooler boundary is on the sides of the machine, therefore the flow move downwards when it gets near to the outside of the machine and upwards near the centre of the sample, where it is warmer. For the horizontal model, the cooler boundary in now above and below the sample, resulting in a radial flow.

Figure 5.7 shows the averaged temperature evolution for the different data sets for process P_1, with standard deviation bars every 100 seconds. Figure 5.7a is the average over the 1mm^3 resolution matrix and as can be seen the temperature of the vertical model is higher than the horizontal, and so are the standard deviations. This is due to the fact that overall the differences in temperatures throughout the whole domain will be higher in the vertical than in the horizontal case, because the horizontal flow is faster and therefore temperature uniformity is reached sooner. Figure 5.7b is the average along the central axis of the food domain, and again the temperature is higher in the vertical than the horizontal model, and so are the standard deviations, which is to be expected as it shows that the temperature varies more with height in the vertical case than with length in the horizontal one. Figure 5.7c is the average over the central slice of the food domain. Again, the temperature in the vertical model is higher than the horizontal, but now the standard deviation bars are nearly equal for both processes. We expected them to be larger in the horizontal case, due to the fact that at a given length the temperature will vary more radially in the horizontal case than in the vertical one (where at a given height we expect uniform temperatures). However for process P_1 these variations are similar for both models. We think this is due to the fact that the temperature of this process is in quite a small range (between 40 and 52°C), and temperature uniformity is easily achieved.

Figure 5.8 shows the averaged temperature evolution over the 5 different slices of the food domain, with standard deviation bars every 100 seconds, for process P_1. Figure 5.8a is for the vertical model and Figure 5.8b the horizontal. The temperature again is higher for the vertical model, and the differences of averaged temperature at different height is also larger in the vertical case, showing, once again, that temperature varies more with height in the vertical case than with length in the horizontal case. As would be expected, the nearer to the top of the food sample, the temperature of the vertical model is higher. In general, the standard deviations bars are also larger in the vertical case, which shows again the higher uniformity of the horizontal model in every direction, especially in this process were the range of temperatures used is not very wide.

Looking at Table 5.3 it can be seen that the horizontal model for process P_1 is more uniform throughout most of the process and for all of the data sets. Nearer to the end, i.e. near P_{hold}, both the horizontal and vertical models have similar mean values and uniformity measurements, which agrees with what we have seen in the plots.

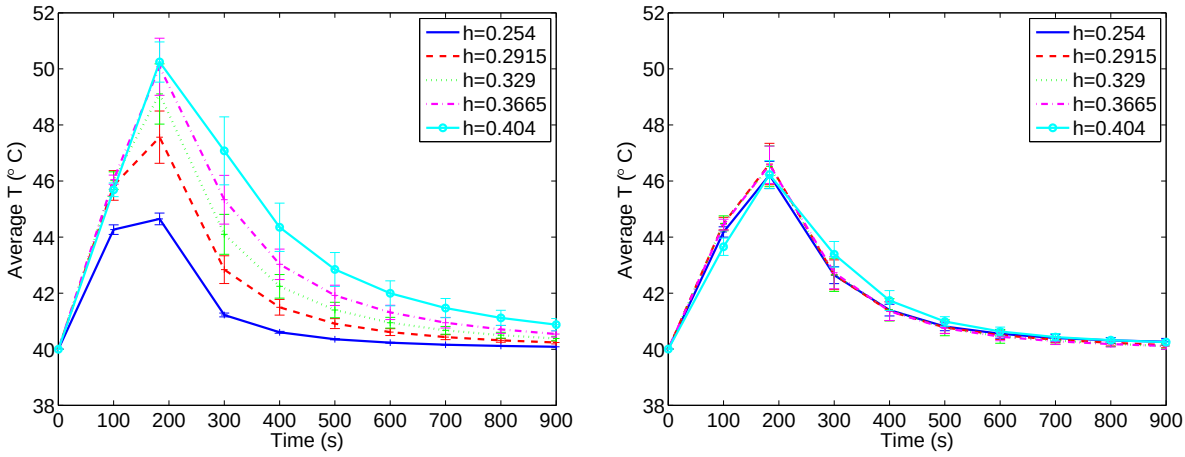

(a) Vertical model

(b) Horizontal model

Figure 5.8: Averaged temperature over 5 radial slices. Process P_1

	3D vertical		3D horizontal	
Process 1	End P_{up}	End P_{hold}	End P_{up}	End P_{hold}
1 mm^3 matrix	49.1221 ± 1.6683°C	40.4408 ± 0.2154°C	46.5964 ± 0.7216°C	40.1379 ± 0.1182°C
Slice 1	44.648 ± 0.2082°C	40.0895 ± 0.0062°C	46.2161 ± 0.4857°C	40.2686 ± 0.1117°C
Slice 2	47.5640 ± 0.9324°C	40.2410 ± 0.0508°C	46.605 ± 0.7389°C	40.1468 ± 0.0939°C
Slice 3 (central)	49.1055 ± 1.0751°C	40.3832 ± 0.0808°C	46.5246 ± 0.7272°C	40.1110 ± 0.1047°C
Slice 4	50.0764 ± 1.0181°C	40.5429 ± 0.1105°C	46.5801 ± 0.6666°C	40.1151 ± 0.1183°C
Slice 5	50.2452 ± 0.7175°C	40.8770 ± 0.2194°C	46.2281 ± 0.5006°C	40.2534 ± 0.0955°C
Central axis	49.2519 ± 1.6205°C	40.4496 ± 0.2225°C	47.001 ± 0.2771°C	40.1494 ± 0.0995°C

Table 5.3: Measure of performance and uniformity for 3D vertical and horizontal models. Process P_1

Process P_2: Higher temperature and pressure

For process P_2 an analogous analysis can be done. Figures 5.9 and 5.10 show the slice plots for temperature and flow distribution at the end of P_{up} and P_{hold}. The situation is very similar to the one described for the slice plots of process P_1. The one thing to remark is that now the differences are qualitatively the same, but quantitatively higher, due to the fact that process P_2 has a wider range of temperatures (between 65 and 85°C) than process P_1 (between 40 and 52°C) because the maximum pressure reached is higher for process P_2 (600 MPa) than for process P_1 (360 MPa).

Figure 5.11 shows the averaged temperature evolution for the different data sets for process P_2, with standard deviation bars every 100 seconds. Figure 5.11a is the average over the 1mm^3 resolution matrix and as can be seen, the temperature of the vertical is higher than in the horizontal model, and so are the standard deviations bars, same as for process P_1. Figure 5.11b is the average along the central axis of the food domain, and again the temperature in the vertical is higher than in the horizontal model, and so are the standard deviations. Figure 5.11c is the average over the central slice of the food domain. Again, the temperature in the vertical is higher than in the horizontal model, but now the standard deviation bars are larger for the horizontal case, which is what we expected as mentioned previously. We think this now happens due to the fact that process P_2 has a wider range of temperatures than process P_1 and therefore the temperature is not as uniform as before.

Figure 5.12 shows the averaged temperature evolution for process P_2, over the 5 different slices of the food domain, with standard deviation bars every 100 seconds. Figures 5.12a and 5.12b are for the vertical and horizontal models respectively. The temperature again is higher for the vertical model, and the differences of averaged temperature at different height is also larger in the vertical case, showing, once again, that temperature varies more with height in the vertical case than with length in the horizontal case. However, now we have, as for the central slice case for process P_2, that the standard deviations bars are larger in the horizontal case.

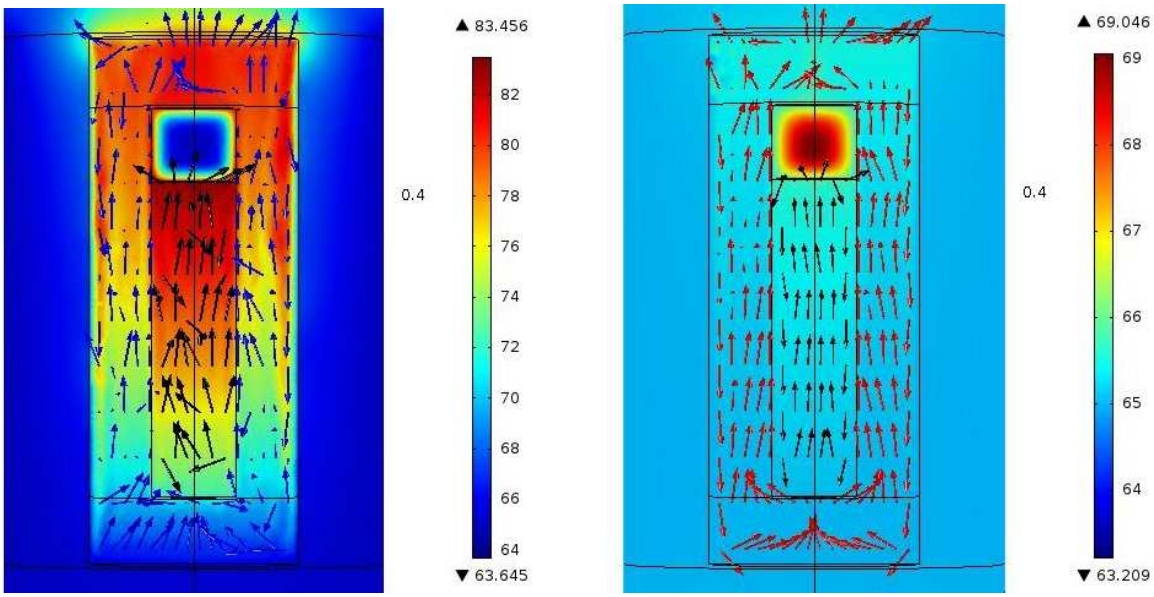

(a) End of P_{up} (b) End of P_{hold}

Figure 5.9: Slice plots 3D vertical model. Process P_2

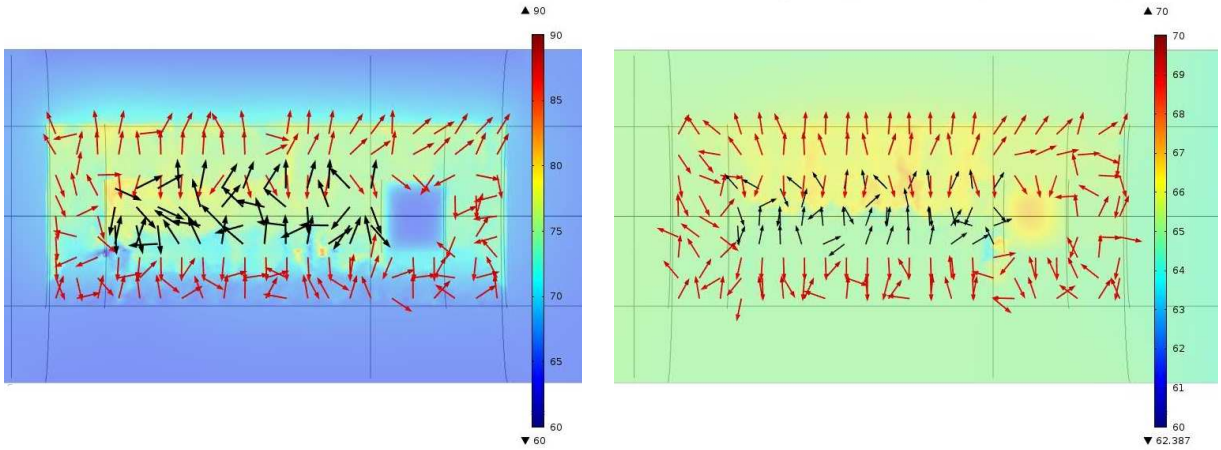

(a) End of P_{up} (b) End of P_{hold}

Figure 5.10: Slice plots 3D horizontal model. Process P_2

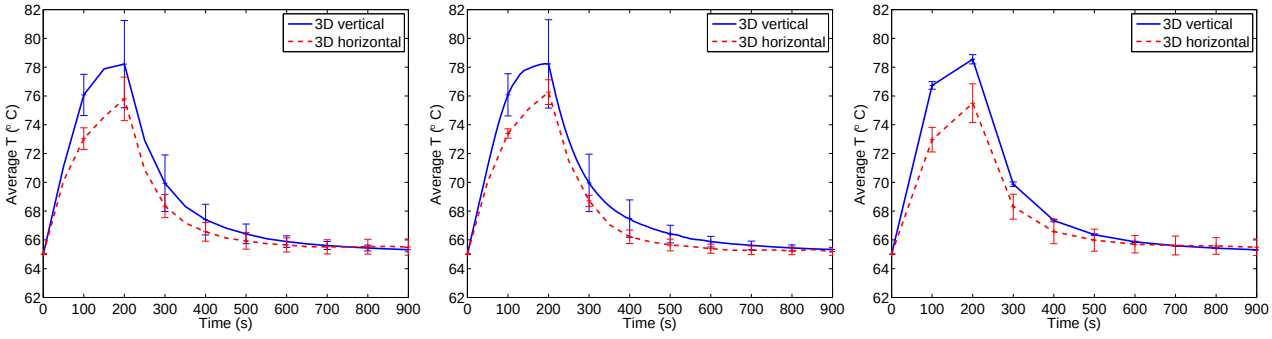

(a) Over 1mm^3 resolution (b) Along central axis (c) Over central slice

Figure 5.11: Averaged temperature evolution for different data sets. Process P_2

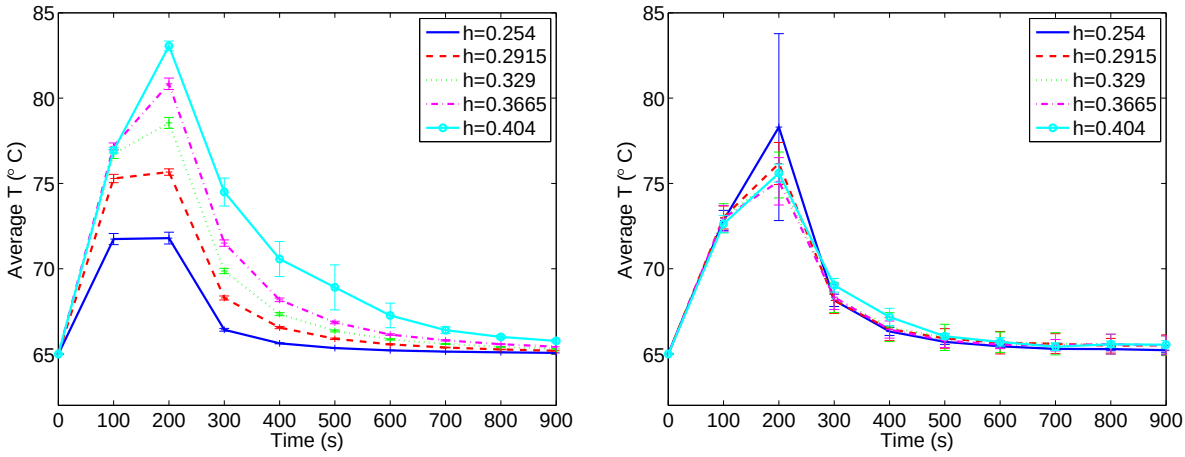

(a) Vertical model

(b) Horizontal model

Figure 5.12: Averaged temperature over 5 radial slices. Process P_2

This makes sense since at a given height (or length) the radial differences are lower in the vertical case. For process P_1 it did not happen because the temperature range was not as wide, and temperature uniformity was reached very quickly. However, process P_2 has a wider temperature range, and these differences can now be seen in Figure 5.12b and also in Table 5.4.

Looking at Table 5.4 it can be seen that the horizontal model for process P_2 is more uniform throughout most of the process and for all of the data sets, except for the slices. Nearer to the end, i.e. near P_{hold}, both the horizontal and vertical models have similar mean values and uniformity measurements, which agrees with what we have seen in the plots.

	3D vertical		3D horizontal	
Process 2	End P_{up}	End P_{hold}	End P_{up}	End P_{hold}
1 mm^3 matrix	78.2146 ± 3.0297°C	65.3206 ± 0.1524°C	75.7975 ± 1.153°C	65.5047 ± 0.5634°C
Slice 1	71.7993 ± 0.3457°C	65.0736 ± 0.0042°C	78.3037 ± 5.4769°C	65.2296 ± 0.1198°C
Slice 2	75.6690 ± 0.1889°C	65.1978 ± 0.0166°C	76.1683 ± 1.2328°C	65.5208 ± 0.6083°C
Slice 3 (central)	78.550 ± 0.3214°C	65.3076 ± 0.0175°C	75.4973 ± 1.3427°C	65.4906 ± 0.5718°C
Slice 4	80.8409 ± 0.3349°C	65.4281 ± 0.0224°C	75.1260 ± 1.3891°C	65.5108 ± 0.5610°C
Slice 5	83.0556 ± 0.2833°C	65.7739 ± 0.1022°C	75.6061 ± 0.5331°C	65.5527 ± 0.2359°C
Central axis	78.1882 ± 2.9916°C	65.3272 ± 0.1599°C	76.2656 ± 0.8592°C	65.1852 ± 0.2250°C

Table 5.4: Measure of performance and uniformity for 3D vertical and horizontal models. Process P_2

5.5 Concluding remarks

Three dimensional vertical and horizontal models for High-Pressure Food Processing have been set up and compared. The results have shown that, as expected, the temperature performance and uniformity is different for both geometries, which shows that there is a need to further develop horizontal models, given that most industrial processes take place in horizontally oriented HP devices, and the published related results up to date are all for vertically oriented HP devices. For a liquid-type food (in this work we have considered water) and for a long and thin machine we have shown that the temperature in general is more uniform for the horizontal case, for the processes we have discussed. For the vertical model temperatures change along height, whilst for the horizontal model they change more radially.

Chapter 6

High-Pressure Shift Freezing Processes

Nomenclature for Chapter 6

B	Ratio of unfrozen water to solids (constant)
C_p	Specific heat capacity (J kg^{-1} K^{-1})
e	Enthalpy (J m^{-3})
E	Weight ratio of water and solids (constant)
f	Mass fraction (constant)
f_s	Mass fraction of ice (constant)
g	Volume fraction (constant)
g_b	Volume fraction of solids in the food (constant)
$\mathbf{g}$	Gravity vector (m s^{-2})
h	Heat transfer coefficient (W m^{-2} K^{-1})
H	Domain height (m)
k	Thermal conductivity (W m^{-1} K^{-1})
L	Domain width (m)
m_i	Mass fraction of ice after expansion (constant)
M	Mass (kg)
$\mathbf{n}$	Outward normal unit vector (m)
p	Mass transfer pressure (Pa)
P	Equipment Pressure (Pa)
P_atm	Atmospheric pressure (Pa)
P_max	Pressure before expansion (Pa)
P_N	Nucleation pressure (Pa)
r	Radial coordinate (m)
t	Time (s)
t_{p_1}	Time at which the target pressure is reached (s)
t_{p_2}	Time at which we start to release pressure (s)
t_{p_3}	Time at which all the pressure has been released (s)
t_f	Final time (s)
T	Temperature (K)
T_env	Environment temperature (K)
T_F	Freezing temperature of food (K)
T_min	Lowest temperature before nucleation (K)
T_prev	Temperature before expansion (K)
T_r	Fixed boundary temperature (K)
T_w	Freezing point of water (K)
$\mathbf{u}$	Fluid velocity vector (m s^{-1})
V	Volume (m^3)
x	Mass fraction of solids in food (constant)
z	Vertical coordinate (m)

Greek symbols

α_w	Molar freezing point of water (kg K mol^{-1})
β	Thermal expansion coefficient (K^{-1})
δe	Liquid/solid enthalpy difference (J m^{-3})
ΔT_sc	Extent of supercooling (K)
ϵ	Small time interval over which ice suddenly nucleates (s)
γ_w	Molecular weight of water (kg mol^{-1})
Γ	Whole domain boundary
Γ_r	Fixed temperature boundary
Γ_up	Heat transfer boundary
η	Dynamic viscosity (Pa s)
λ	Latent heat (J kg^{-1})
ρ	Density (kg m^{-3})
Ω	Whole domain
Ω_C	Cap of the sample holder
Ω_F	Food sample domain
Ω_P	Pressurising medium
Ω_S	Steel vessel

Indices

0	Initial values
*	Rotated domains
C	Rubber cap
F	Food domain
l	Liquid
P	Pressurising fluid
ref	Reference value
s	Solid
S	Steel
vol	Volumetric
w	Water

Acronyms

FEM	Finite Element Method
HP	High-Pressure
HPSF	High-Pressure Shift Freezing
2D	Two-dimensional
3D	Three-dimensional

6.1 Introduction

In this Chapter we describe, model and solve numerically a High-Pressure Shift Freezing (HPSF) process, based on the published work [86]. As we will see later further ahead, modelling a general solidification problem is already a complicated task, mainly because the interface between the solid and liquid phases moves as latent heat is liberated at the interface. All of these problems are non-linear and therefore exact solutions are extremely difficult. In early years, analytical methods were the only means available to understand mathematically a physical process involving the moving boundary. Although analytical methods offer an exact solution, they have many limitations, and thus analytical solutions are mainly for the one-dimensional cases of an infinite or semi-infinite region with simple boundary conditions and constant thermal properties. Practical solidification problems are rarely one dimensional, initial and boundary conditions are always complex and thermo-physical properties can vary with phases, temperature, pressure, etc. For these reasons, nowadays in most engineering applications, the moving boundary problem is solved by means of numerical analysis. Due to the amount of real-world processes that involve freezing (such as, e.g., ice making, freezing of foods, solidification of metals in a cast process, etc.) and the challenge that modelling them poses, a lot of interest and research has been done in this area [15, 16, 17, 88, 74, 91].

If we focus on the freezing of food, further complications are added. One of the main problems is the highly non-linearity of the partial differential equations, due to the sudden change of thermo-physical properties such as specific heat and thermal conductivity around the freezing point. If the food sample has a complex shape, the progress of the freezing front can be highly unpredictable. Also, freezing is associated with large and sudden volume change, mass transfer, stress and cracking, cellular dehydration, supercooling, ice nucleation and propagation [74]. Furthermore, when modelling HP food freezing processes, the effect of pressure on thermal properties (such as latent heat, freezing point, thermal conductivity, specific heat) must also be taken into account [20, 29, 64, 71].

All of these issues will be considered in the generalised enthalpy model for a HPSF process that we present in this Chapter.

6.1.1 Food freezing with HP

Freezing is a widespread food preservation technology, as it ensures high food quality with long storage duration, and also because it has an extended implementation area (meat, fish, fruit, vegetables, dairy and egg products, etc.). Despite the benefits, freezing of foods can also cause undesirable changes in their texture and organoleptic properties, and its main drawback is the risk of food damage due to the formation of big ice crystals. Freezing can be defined as the crystallisation of liquid water into its solid form (ice). Nucleation of ice is a stochastic phenomenon. However, after nucleation, crystallisation always initially occurs under a known temperature defined as the initial freezing temperature. Crystal characteristics (size, location) are dependent on the freezing rate (slow freezing produces large crystals, whilst rapid freezing produces small ice crystals). The general purpose of food technologists working on this area has been to develop a freezing process that creates a homogeneous matrix of small ice crystals [20]. Improvement of known freezing methods and development of new techniques are important research goals for the food industry at present. With the recent increasing impact of HP technology on food processing, there has been a lot of research dealing with the potential applications of HP effects on ice-water transitions, given that pressure decreases the freezing and melting point of water to a minimum of $-22°$C at 207.5 MPa [8]. Therefore several HP freezing and thawing processes have been developed [20, 70].

According to the path followed by the process in the phase diagram of water [8], three different types of HP freezing processes can be distinguished in terms of the way in which the phase transition occurs [29]:

- **High-Pressure Assisted Freezing** (**HPAF**): Phase transition occurs under constant pressure, higher than atmospheric pressure, whilst the temperature is lowered to the corresponding freezing point. This process is identical to traditional freezing at atmospheric conditions except that it takes place under HP. The process is governed by thermal gradients because the cooling of the sample proceeds from the surface to the centre. Ice nucleation only takes place at the outer zone of the sample, which is in direct contact with the cooling medium. Needle-shaped ice crystals grow radially into the centre. Once the freezing plateau is complete and the sample reaches the final temperature, the pressure is released. As the latent

heat of crystallisation is reduced when pressure increases, reductions in phase transition times may be achieved.

- **High-Pressure Shift Freezing** (**HPSF**): Phase transition occurs due to a pressure change that promotes metastable[1] conditions and instantaneous ice production. On expansion, pressure release occurs instantaneously throughout the product (Pascal principle), and subsequently, its temperature decreases. Large-scale supercooling[2] takes place throughout the sample, which implies high ice nucleation velocities. Different authors have proved experimentally that ice nucleation occurs homogeneously throughout the whole volume of the product and not only on the surface, as they have found small granular shape ice crystals disperse throughout the resulting sample for several products. When comparing HPSF to classical freezing processes, important reductions of freezing times have been reported.
- **High-Pressure Induced Freezing** (**HPIF**): Phase transition is initiated by a pressure increase and continues at constant pressure.

A few studies on HPIF have been done to date [56, 90], and there are numerous papers and reviews dealing with HPAF [29, 64, 71] and HPSF [70, 72, 78]. Comparisons between them can only be made in processes where the amounts of latent heat[3] released and the difference in temperature between the initial freezing point of the sample and the cooling medium are identical. It is generally accepted that for the purposes described above, HPSF processes are the most advantageous [29]. Therefore, in this Chapter we concentrate only on HPSF processes. In Section 6.1.2 we describe the main features of HPSF processes and in Section 6.1.3 the state-of-the-art is described. In Section 6.2 we present a mathematical model to describe a generic freezing process, and then couple it with a heat transfer model, to finally give a new model describing a HPSF process. In Section 6.3 we present numerical results using known data from real experiments. In Section 6.4 we outline the final remarks.

6.1.2 Main features of a HPSF process

A sample subjected to a HPSF process (Figure 6.1), is cooled under pressure at less than 0°C and kept in the non-frozen state according to the corresponding phase diagram (A-B-C in Figure 6.1). When the desired temperature is reached in the product (point C), pressure is released. Two different processes may be distinguished depending on the pressure release rate: **rapid expansion** (in seconds) or **slow expansion** (in minutes). Phase transition occurs due to the pressure release, that induces uniform supercooling throughout the whole sample (point D for rapid expansions, point 1 for slow expansions) due to the isostatic nature of pressure. This supercooling induces uniform formation of nuclei throughout the sample (regardless of its shape or size), then latent heat is released, raising the sample temperature to the corresponding freezing point (point E for rapid expansion, 2 for slow expansion). Freezing is then completed at constant pressure, usually at atmospheric conditions; for practical reasons of applicability, expansions are usually made from high to atmospheric pressure (i.e. rapid expansion A-B-C-D-E in Figure 6.1) and therefore the phase transition mainly occurs at atmospheric pressure in this kind of experiment. As a general rule (but taking into account the phase diagram of water), the higher the pressure and the lower the temperature before expansion, the more ice nuclei are formed, and hence the shorter is the phase transition time.

Different authors [4, 29, 66, 79] have proved experimentally that in a HPSF process ice nucleation occurs homogeneously throughout the whole volume of the product and not only on the surface, as they have found small granular shape ice crystals dispersed throughout the resulting sample for several products. When comparing HPSF to classical freezing processes, important reductions of freezing times have been reported [29, 72, 79]. Applications of HPSF for food are still under development and the amount of available data are increasing accordingly. Most of the studies that are being carried out focus on the advantageous effects that HPSF has on

[1] Metastable state [1]: particular excited state of an atom, nucleus, or other system that has a longer lifetime than the ordinary excited states and that generally has a shorter lifetime than the lowest, often stable, energy state, called the ground state. A metastable state may thus be considered a kind of temporary energy trap or a somewhat stable intermediate stage of a system the energy of which may be lost in discrete amounts.

[2] Supercooling [29]: Process of cooling below the freezing point without solidification or crystallisation. Supercooling is a non-equilibrium, metastable state, which is analogous to an activation energy necessary for the nucleation process.

[3] Latent heat [1]: amount of energy released or absorbed by a chemical substance during a change of state that occurs without changing its temperature, meaning a phase transition such as the melting of ice or the boiling of water.

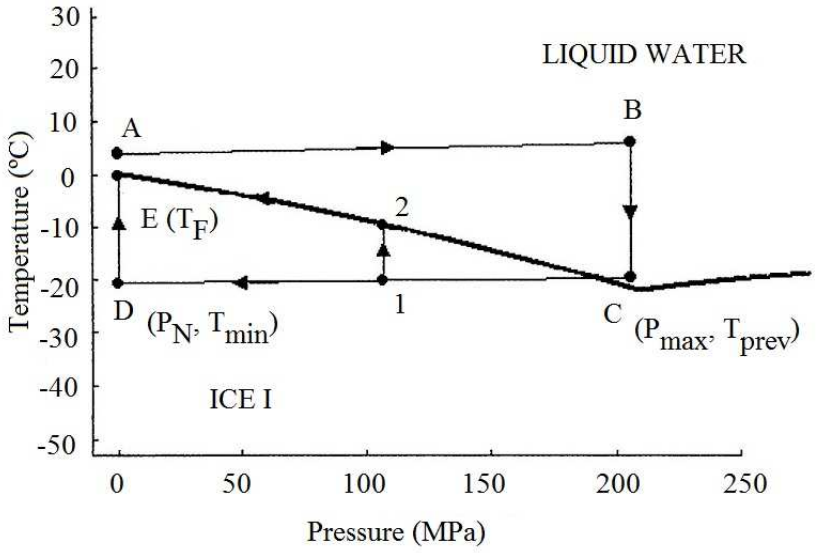

Figure 6.1: High-pressure shift freezing processes represented over the phase diagram of water. Rapid expansion is represented by A-B-C-D-E; (slow expansion is represented by A-B-C-1-2-E). A-B is compression; B-C is pre-cooling; C-D (or in the case of slow expansion C-1) is pressure release; at D (or at 1 in the case of slow expansion) the sample is highly supercooled – no latent heat has yet been released; for rapid expansion D-E latent heat is released and sample temperature increases up to the corresponding freezing point at atmospheric conditions. In the case of slow expansion 1-2 latent heat is released and the sample temperature increases up to the corresponding freezing point under pressure, 2-E the remaining pressure is released and the sample temperature stays on the melting line.

the texture and structure of various products. In [20] the authors compared the HPSF process to a conventional (at atmospheric pressure) freezing process, and concluded that the nucleation is faster and more uniform in the HPSF processes, producing a homogeneous crystallisation and therefore a better product in terms of texture. In [29] the authors compared the HPAF and HPSF processes on gelatin gel samples and concluded that the HPSF was clearly more advantageous: shorter phase transition times and homogeneous distribution of small ice crystals throughout the sample. HPSF has been successfully applied in the processing of fruits, pork, lobster and tofu, among other products.

6.1.3 Modelling of HPSF processes: state-of-the-art and needs

Due to the advantages of this method (mainly, its potential to improve the kinetics of the process and the characteristics of the ice crystals thus formed) compared to other freezing methods, apart from the published research focused on the impact of HP on quality aspects of the particular processed food, some modelling studies considering the temperature evolution during treatment of HPSF processes have been published to date. This is important in all HP processes, as pointed out by the authors in [71], because some industrial processes have to occur at a constant temperature or between a minimum-maximum threshold to avoid altering some properties of the food (gelification or crystalline state, protein stability, fat migration, freezing...) or to assure a uniform distribution of the pursued pressure effects (microbial or enzymatic inactivation, uniform nucleation...). In particular, when studying HPSF processes, since phase changes are driven by both pressure and temperature, heat transfer effects play a major role in this field. Therefore the research in this area has been focused on theoretically based heat transfer models that allow to predict the temperature history within a product freezing under pressure.

Some notable modelling studies are those of [20], where the authors used an explicit two dimensional finite difference scheme to simulate temperature profiles during HP freezing of a food simile (tylose) and got good agreement with experimental data, but remarked that an improvement needed is the contribution of convection

heat transfer by the HP fluid. In [78] the authors modelled a HPSF process of a finite cylinder using equations based on the crossed product of infinite slabs and infinite cylinders. The time needed to complete the precooling and change of phase stages is reproduced satisfactorily by the model, however there are misalignments in the tempering phase because experimental and theoretical conditions were not the same, due to the thermal gradients. The authors remark that for this stage a more accurate model (based on finite elements/differences) would be needed. In [54] the authors performed dimensional analysis of the governing equations describing HP processes with forced and free convection, giving a general overview of thermo-fluid-dynamical mechanisms of these kind of processes. In [64] a one dimensional finite difference numerical model based on the enthalpy formulation was developed to simulate HP freezing of tylose, agar gel and potatoes. This model in [64] uses a version of the enthalpy equation derived for constant pressure systems, adapting it to their system by accounting for pressure effects on the latent heat. In addition their model of freezing point depression of the food samples relies on the Schwartzberg equation [80], which was derived for dilute solutions. At the high ice fractions realised in HPSF systems, the unfrozen gel between ice crystals is non-dilute and a more general model may be required. In this Chapter we introduce a new enthalpy model by starting from the pressure-dependent conservation of enthalpy equation and determining the non-dilute freezing point depression directly from experimental measurements.

6.2 Building a new model for a HPSF process

We propose a two dimensional axially symmetric mathematical model for a HPSF process, derived from an enthalpy formulation based on volume fractions dependent on temperature and pressure. This model is valid for solid-type foods with a large and small filling sample versus pressurising media ratio. Convection effects in the pressurising fluid are taken into account when necessary.

In order to simulate a HPSF process, we first present a general heat transfer model in a HP process, and then we modify it, to take into account the solidification process, by deriving a model based on the enthalpy formulation at non-constant pressure. Also, we present the equations we use to calculate the amount of ice instantaneously produced just after expansion in a HPSF process, the amount of ice formed during the rest of the process, and the liquid volume fraction. Finally, we give the complete models used to simulate a HPSF process.

6.2.1 Modelling heat transfer in a general HP process

The geometry of the HP device consider for the models derived in this Chapter is the same as the one described in Chapter 3 (see Figure 3.2). In this Chapter, we are going to deal only with the case of solid-type foods. First we study large solid-type foods, and therefore a model that only takes into account conduction effects like the one presented in Section 3.1.1 will be used. For the small solid-type foods, the model includes the convection effects in the pressurising medium, like the one described in Section 3.1.2.

Heat transfer for a large solid-type food

Following Section 3.3.1 the heat transfer for a large solid-type food can be modelled by the following system in cylindrical coordinates

$$\begin{cases} \bar{\rho}\bar{C}_p\dfrac{\partial T}{\partial t} - \dfrac{1}{r}\dfrac{\partial}{\partial r}\left(r\bar{k}\dfrac{\partial T}{\partial r}\right) - \dfrac{\partial}{\partial z}\left(\bar{k}\dfrac{\partial T}{\partial z}\right) = \bar{\beta}\dfrac{\mathrm{d}P}{\mathrm{d}t}T & \text{in} \quad \Omega \times (0, t_\mathrm{f}), \\ \bar{k}\dfrac{\partial T}{\partial \mathbf{n}} = 0 & \text{on} \quad \Gamma_0 \times (0, t_\mathrm{f}), \\ \bar{k}\dfrac{\partial T}{\partial \mathbf{n}} = h(T_\mathrm{env} - T) & \text{on} \quad \Gamma_\mathrm{up} \times (0, t_\mathrm{f}), \\ T = T_\mathrm{r} & \text{on} \quad \Gamma_\mathrm{r} \times (0, t_\mathrm{f}), \\ T = T_0 & \text{in} \quad \Omega \times \{0\}. \end{cases} \tag{6.1}$$

Heat transfer for a small solid-type food

Following Section 3.3.2 the heat transfer for a small solid-type food can be modelled by the following system

$$\begin{cases} \bar{\rho}\bar{C}_p\dfrac{\partial T}{\partial t} - \nabla\cdot(\bar{k}\nabla T) + \bar{\rho}\bar{C}_p\mathbf{u}\cdot\nabla T = \bar{\beta}\dfrac{\mathrm{d}P}{\mathrm{d}t}T, & \text{in} \quad \Omega^*\times(0,t_\mathrm{f}),\\ \bar{\rho}\dfrac{\partial \mathbf{u}}{\partial t} - \bar{\eta}\nabla^2\mathbf{u} + \bar{\rho}(\mathbf{u}\cdot\nabla)\mathbf{u} = -\nabla p + \rho\mathbf{g} & \text{in} \quad \Omega^*_{\mathrm{P}}\times(0,t_\mathrm{f}),\\ \nabla\cdot(\mathbf{u}) = 0 & \text{in} \quad \Omega^*_{\mathrm{P}}\times(0,t_\mathrm{f}),\\ \bar{k}\dfrac{\partial T}{\partial \mathbf{n}} = 0 & \text{on} \quad \Gamma^*_0\times(0,t_\mathrm{f}),\\ \bar{k}\dfrac{\partial T}{\partial \mathbf{n}} = h(T_{\mathrm{env}} - T) & \text{on} \quad \Gamma^*_{\mathrm{up}}\times(0,t_\mathrm{f}),\\ T = T_\mathrm{r} & \text{on} \quad \Gamma^*_\mathrm{r}\times(0,t_\mathrm{f}),\\ \mathbf{u} = 0 & \text{on} \quad \Gamma^*_\mathrm{P}\times(0,t_\mathrm{f}),\\ T(0) = T_0 & \text{in} \quad \Omega^*,\\ \mathbf{u}(0) = 0 & \text{in} \quad \Omega^*,\\ p = 10^5 & \text{at} \quad \mathbf{A}_1\times(0,t_\mathrm{f}). \end{cases} \tag{6.2}$$

As we know from Chapter 3, system (6.2) can also be rewritten as an equivalent 2D problem by using cylindrical coordinates (system not shown in this Chapter). The numerical experiments considered in this Chapter were carried out using the 2D version of the corresponding equations.

In what follows, because we will be using constant thermo-physical properties throughout the rest of the Chapter, we remove the $\bar{}$ notation, and will refer to them as per usual, i.e. C_p, k, β, ρ and η.

6.2.2 Modelling a solidification process using the enthalpy formulation

In general, the difficulties of any solidification process are to control the position of the solid/liquid interface and to deal with the release of latent heat, which evolves over a very small temperature range. Crank [17] classifies the numerical methods for solving the 'moving-boundary' problem into *front-tracking* methods and *fixed-grid* methods. The former methods may be used when there is a distinct phase change and a smooth continuous front [91]. However, as the solid/liquid interface becomes less distinct (e.g. if it does not move smoothly or monotonically with time), it may sometimes be difficult or even impossible to track the moving boundary directly. It may have sharp peaks, or it may even disappear. Therefore, the possibility of reformulating the problem in such a way that there is no need to track the position of the solid/liquid interface, but instead it is bound up in a new form of the equations, which applies over the whole of a fixed domain, is an attractive one. These are the so called *fixed-grid* methods in which the position of the moving boundary appears, a posteriori, as a part of the solution.

The essential feature of the fixed-grid methods is that the latent heat evolution is accounted for in the governing energy equation by defining either a total enthalpy, an apparent specific heat or a heat source term [91]. Consequently, the numerical solution can be carried out on a space grid that remains fixed throughout the calculations. Another advantage of these methods is that the numerical treatment of the phase change can be achieved through simple modifications of existing heat transfer numerical methods and/or software. To model HPSF processes we use a combination of such methods, adapted to the case of non-constant pressure.

For a pure non-convecting material obeying Fourier's law of heat conduction, conservation of enthalpy can be written as [7]:

$$\frac{\partial e}{\partial t} = \nabla\cdot(k\nabla T) + \frac{\partial P}{\partial t}, \tag{6.3}$$

where e is the enthalpy per unit volume (J m^{-3}). If the pressure is constant equation (6.3) reduces to the

enthalpy equation used in [91]. In the enthalpy model of a HPSF process developed in [64] the pressure term on the right-hand side of (6.3) was neglected.

In the general case of non-constant pressure the enthalpy is a function of both temperature and pressure, and from thermodynamics we may derive the relation (see, e.g., [26]):

$$\mathrm{d}e = \rho C_p \mathrm{d}T + (1 - \beta T)\mathrm{d}P. \tag{6.4}$$

Integrating (6.4) from some reference temperature T_{ref} and reference pressure P_{ref} to the current temperature and pressure yields an expression for the enthalpy:

$$e(T, P) = e(T_{\mathrm{ref}}, P_{\mathrm{ref}}) + \int_{T_{\mathrm{ref}}}^{T} \rho C_p \mathrm{d}\theta + \int_{P_{\mathrm{ref}}}^{P} (1 - \beta T)\mathrm{d}\Pi. \tag{6.5}$$

In the case of a mixed-phase region composed of ice crystals (that we will refer to here as the solid part) and the solid and liquid part of the food that has not frozen yet (that we will refer to here as the liquid part), we may extend previous enthalpy models based on phase fractions (see [91]) by defining a 'mixture enthalpy' as:

$$\begin{aligned} e(T, P, g_{\mathrm{l}}) = e(T_{\mathrm{ref}}, P_{\mathrm{ref}}, g_{l,\mathrm{ref}}) + (1 - g_{\mathrm{l}}) \int_{T_{\mathrm{ref}}}^{T} \rho_s C_{p_s} \mathrm{d}\theta + g_{\mathrm{l}} \int_{T_{\mathrm{ref}}}^{T} \rho_{\mathrm{l}} C_{p_{\mathrm{l}}} \mathrm{d}\theta \\ + (g_{\mathrm{l}} - g_{\mathrm{b}})\rho_{\mathrm{l}}\lambda + (1 - g_{\mathrm{l}}) \int_{P_{\mathrm{ref}}}^{P} (1 - \beta_s T)\mathrm{d}\Pi + g_{\mathrm{l}} \int_{P_{\mathrm{ref}}}^{P} (1 - \beta_{\mathrm{l}} T)\mathrm{d}\Pi, \end{aligned} \tag{6.6}$$

where g_{l} is the volume fraction of the liquid part, g_{b} is the volume fraction of solids in the food (therefore $g_{\mathrm{l}} - g_{\mathrm{b}}$ is the volume fraction of water in the food) and λ is the latent heat of freezing of water (J kg^{-1}). We consider that $g_{l,\mathrm{ref}} = g_{\mathrm{b}}$, that T_{ref} is the temperature (K) at which all the latent heat has been released (typically $T_{\mathrm{ref}} = -40°$ C$= 233.15$ K, see [80]), and that $P_{\mathrm{ref}} = P_{\mathrm{atm}}$ (Pa), the atmospheric pressure. Similarly, a 'mixture conductivity' is defined as:

$$k = (1 - g_{\mathrm{l}})k_s + g_{\mathrm{l}}k_{\mathrm{l}}. \tag{6.7}$$

In the previous equations subscripts $[\,]_{\mathrm{s}}$ and $[\,]_{\mathrm{l}}$ refer to the solid and liquid phases respectively. Taking the total derivative of (6.6) gives:

$$\mathrm{d}e = C_{\mathrm{vol}}\ \mathrm{d}T + (1 - \beta_{\mathrm{vol}}T)\ \mathrm{d}P + \delta e\ \mathrm{d}g_{\mathrm{l}}, \tag{6.8}$$

where $C_{\mathrm{vol}} = (1 - g_{\mathrm{l}})\rho_{\mathrm{s}}C_{p_{\mathrm{s}}} + g_{\mathrm{l}}\rho_{\mathrm{l}}C_{p_{\mathrm{l}}}$, $\delta e = \int_{T_{\mathrm{ref}}}^{T}(\rho_{\mathrm{l}}C_{p_{\mathrm{l}}} - \rho_{\mathrm{s}}C_{p_{\mathrm{s}}})\mathrm{d}\theta + \int_{P_{\mathrm{ref}}}^{P} T(\beta_{\mathrm{s}} - \beta_{\mathrm{l}})\mathrm{d}\Pi + \rho_{\mathrm{l}}\lambda$ and $\beta_{\mathrm{vol}} = (1 - g_{\mathrm{l}})\beta_{\mathrm{s}} + g_{\mathrm{l}}\beta_{\mathrm{l}}$. Inserting (6.8) into the enthalpy equation (6.3) leads to:

$$C_{\mathrm{vol}}\frac{\partial T}{\partial t} - \nabla \cdot (k\nabla T) = \beta_{\mathrm{vol}}T\frac{\partial P}{\partial t} - \delta e\frac{\partial g_{\mathrm{l}}}{\partial t}. \tag{6.9}$$

For a HPSF process with rapid expansion (see ABCDE in Figure 6.1), typically the pressure profile is as follows:

$$P(t) = \begin{cases} \dfrac{P_{\max} - P_{\mathrm{atm}}}{t_{p_1}}t + P_{\mathrm{atm}} & t \le t_{p_1}, \\ P_{\max} & t_{p_1} < t \le t_{p_2}, \\ -\dfrac{P_{\max} - P_{\mathrm{atm}}}{t_{p_3} - t_{p_2}}(t - t_{p_2}) + P_{\max} & t_{p_2} < t < t_{p_3}, \\ P_{\mathrm{atm}} & \text{elsewhere}, \end{cases} \tag{6.10}$$

where t_{p_1} is the time at which the maximum pressure, $P_{\max}$, has been reached; t_{p_2} is the time at which we start releasing pressure; and t_{p_3} is the time at which all the pressure has been released down to atmospheric pressure, $P_{\mathrm{atm}} \approx 0.1$ MPa.

Experiments suggest (see [72]) that as the pressure is rapidly released ($t \in (t_{p_2}, t_{p_3})$), nucleation is at first delayed (leaving the system in a metastable state with respect to the formation of ice) until the pressure nears atmospheric when ice suddenly nucleates and forms in some small time interval. Therefore we assume there is no ice while the pressure is changing (until $t = t_{p_3}$), so during this stage equation (6.9) becomes:

$$\rho_{\mathrm{l}}C_{p_{\mathrm{l}}}\frac{\partial T}{\partial t} - \nabla \cdot (k\nabla T) = \beta_l T\frac{\partial P}{\partial t}, \qquad t \le t_{p_3}. \tag{6.11}$$

Once the pressure has been released, ice suddenly nucleates and forms in some small time interval (ε), where we assume that the change in ice fraction owing to the drop in pressure is some known function of time, hence now (6.9) becomes:

$$C_{\text{vol}}\frac{\partial T}{\partial t} - \nabla\cdot(k\nabla T) = -\delta e\frac{\partial g_{\text{l}}}{\partial t}, \qquad t\in(t_{p_3}, t_{p_3}+\varepsilon), \tag{6.12}$$

where now $\delta e = \int_{T_{\text{ref}}}^{T}(\rho_{\text{l}}C_{p_{\text{l}}} - \rho_{\text{s}}C_{p_{\text{s}}})\mathrm{d}\theta + \rho_{\text{l}}\lambda$, since $P = P_{\text{atm}}$. After this point and until the end of the process, we assume that the rest of the ice is computed as a function of temperature (an explicit formula for g_{l} is given in Section 6.2.3), which leads to:

$$\left[C_{\text{vol}} + \delta e\left(\frac{\partial g_{\text{l}}}{\partial T}\right)\right]\frac{\partial T}{\partial t} - \nabla\cdot(k\nabla T) = 0, \qquad t\geq t_{p_3}+\varepsilon. \tag{6.13}$$

As will be shown in Section 6.3 the model given by (6.9) (equivalent, under the previous assumptions, to (6.11), (6.12) and (6.13)) yields satisfactory agreement between theory and experiment. All the parameters involved in the model can be easily found in the literature for many food similes, except for the liquid fraction, g_{l}. In Section 6.2.3 we explain different characteristics of a HPSF that will enable us to derive a formula for g_{l} for a gel food simile as a function of time and temperature. We note, though, that a more rigorous approach would be to combine with equation (6.9) a stochastic nucleation law for $g_{\text{l}}(T,P)$ quantifying the ice formed at each instant as the pressure is released. As no such expression for $g_{\text{l}}(T,P)$ is currently available we leave this to future work.

6.2.3 Deriving an expression for the volume fraction g_{l} for a gel food simile

Supercooling reached after expansion

In [72] the authors define the extent of supercooling, ΔT_{sc} (°C), as the difference between the lowest temperature at the sample centre just before nucleation, T_{min}, and the sample freezing temperature, T_{F}, at pressure P_{N}, where the nucleation takes place. The extent of supercooling is a crucial factor in the dynamics of a freezing process. In conventional freezing at atmospheric pressure, it is generally admitted that supercooling and nucleation only occurs at the surface of the sample. In [72] the authors show that in HPSF experiments, upon pressure release, a metastable state was reached throughout the sample before nucleation. As can be seen in Figure 6.1, after expansion from $(P_{\text{max}}, T_{\text{prev}})$, the pressure/temperature coordinates of the sample move to $(P_{\text{N}}, T_{\text{min}})$, indicating extensive supercooling. Therefore, the extent of supercooling only depends on the minimum temperature reached after expansion and on the pressure at which nucleation occurs. The minimum temperature, T_{min}, reached at nucleation pressure, P_{N}, after a rapid pressure release can be estimated according to (3.3), and is accounted for in our heat transfer model. However, the prediction of T_{min} using (3.3) implies foreknowledge of the nucleation pressure P_{N}, and this is, in general, very difficult due to the stochastic nature of the nucleation phenomenon. In Section 6.2.3 we explain how to avoid this problem.

Modelling the amount of ice formed instantaneously after expansion

In [72] the authors explain that the pressure release in HPSF processes can be divided, ideally, in two different phases (see Figure 6.1). In the first phase, expansion takes place under metastable conditions. A percentage of water is instantaneously frozen when P_{N} is reached. The latent heat raises the sample temperature to the corresponding freezing point. The amount of ice formed at P_{N} can be calculated from the following equation (other equations are given in [72]):

$$m_i\lambda(P_{\text{N}}) = (m_i\overline{C}_{p_i} + (1-m_i)\overline{C}_{p_w})\Delta T_{\text{sc}}, \tag{6.14}$$

where m_i is the mass fraction of ice (defined as mass of ice divided by initial mass of water) formed after expansion, $\overline{C}_{p_i}$ (J kg^{-1} °C^{-1}) is the specific heat capacity of ice at the nucleation pressure (taken as the mean value of the specific heat capacity at the minimum temperature reached after expansion and the specific heat capacity at the corresponding melting point), $\overline{C}_{p_w}$ (J kg^{-1} °C^{-1}) is the specific heat capacity of water at the

nucleation pressure (taken as the mean value of the specific heat capacity at the minimum temperature reached after expansion and the specific heat capacity at the corresponding melting point), ΔT_{sc} (°C) is the extent of supercooling, and $\lambda(P_{\mathrm{N}})$ (J kg^{-1}) is the latent heat at nucleation pressure P_{N}.

Latent heat of freezing of water (J kg^{-1}) as a function of pressure P (MPa) can be estimated by the following equation (for more details, see [72]):

$$\lambda(P) = 3.114 \times 10^{-3} P^3 - 1.292 P^2 - 3.379 \times 10^2 P + 3.335 \times 10^5. \tag{6.15}$$

Therefore, we can calculate the percentage of instantaneously frozen water, m_i, by using equations (6.14) and (6.15), taking into account the extent of supercooling attained and the latent heat released at nucleation pressure. However, this is just a theoretical evaluation and it is not useful for modelling purposes because experimental data of nucleation pressure and temperature during expansion ($P_{\mathrm{N}}, T_{\mathrm{min}}$) are needed and, as was pointed out in Section 6.2.3, it is in general very difficult to predict the nucleation pressure. To overcome this problem, in [72] the authors proposed a simplified method for HPSF processes with rapid expansions: to assume that nucleation occurs at atmospheric pressure. On this basis, by using experimental pressure and temperature values immediately prior to expansion ($P_{\mathrm{max}}, T_{\mathrm{prev}}$), instead of ($P_{\mathrm{N}}$, T_{min}), the amount of ice formed after expansion can be determined. They do as follows: the minimum temperature after expansion, T_{min}, is calculated using (3.3); the corresponding supercooling is attained as $\Delta T_{\mathrm{sc}} = T_{\mathrm{F}} - T_{\mathrm{min}}$; equation (6.15) is used to calculated the latent heat released at atmospheric pressure, and finally we introduced these values in (6.14) to determine the percentage of ice instantaneously formed in HPSF experiments with rapid expansions. We use this simplification in our simulations.

Modelling the mass fraction of ice of the rest of the process

Once we have calculated the amount of ice formed instantaneously after expansion, we need an expression to calculate how the rest of the ice is formed as a function of temperature. As it occurs at atmospheric pressure, we do not have to worry about taking into account pressure effects this time. After expansion, an amount m_i of ice is instantaneously formed, which can be calculated, as we explained in Section 6.2.3. The temperature is raised to the corresponding freezing point at atmospheric pressure due to the release of latent heat.

Remark 9. The mass fraction of ice f_{s} as a function of temperature can be calculated with the following expression:

$$f_{\mathrm{s}}(T) = 1 - x_0/x(T), \tag{6.16}$$

where x_0 is the initial mass fraction of solids in the food and $x(T)$ is the mass fraction of solids in the food (without including the ice generated after the initial reference instant) at temperature T.

This can be easily seen by taking m as the initial mass of solids, m_{w_0} the initial mass of water and $m_w(T)$ be the mass of water in the food at temperature T, then:

$$x_0 = \frac{m}{m + m_{w_0}}, \quad x(T) = \frac{m}{m + m_w(T)}$$

and therefore:

$$1 - x_0/x(T) = 1 - \frac{m + m_w(T)}{m + m_{w_0}} = \frac{m_{w_0} - m_w(T)}{m + m_{w_0}} = \frac{\text{mass of ice}}{\text{total mass}} = f_{\mathrm{s}}(T)$$

Next we derive an equation for $x(T)$. In [75], the following extended Clausius-Clapeyron equation is presented to calculate the freezing point depression ($T_{\mathrm{w}} - T$) of gel, as a function of mass fraction of solids (x):

$$T_{\mathrm{w}} - T = -\frac{\alpha_w}{\gamma_w} \ln\left(\frac{1 - x - Bx}{1 - x - Bx + Ex}\right). \tag{6.17}$$

In (6.17) T_{w} is the freezing point of water at atmospheric pressure (i.e. 0°C), T is the freezing point of the food (°C), α_w is the molar freezing point constant of water (1860 kg K mol^{-1}), γ_w is the molecular weight of water (18 kg mol^{-1}), E is the molecular weight ratio of water and solids ($\gamma_w/\gamma_{\mathrm{s}}$) and B is the ratio of unfrozen

water to total solids. E and B are model parameters that the authors of [75] estimate using SAS non-linear regression.

From (6.17) we can calculate the freezing point depression depending on the mass fraction of solids, but we want to calculate the inverse, i.e., given a certain freezing point temperature T, what is the mass fraction of solids at that temperature. From (6.17) it is easy to find an expression for x as a function of T:

$$x(T) = \frac{\exp^{\frac{\gamma_w}{\alpha_w}(T-T_{\mathrm{w}})} - 1}{\exp^{\frac{\gamma_w}{\alpha_w}(T-T_{\mathrm{w}})}(1+B-E) - 1 - B}. \tag{6.18}$$

Substituting (6.18) into (6.16) we finally get the equation for the mass fraction of ice as a function of temperature:

$$f_{\mathrm{s}}(T) = \frac{\exp^{\frac{\gamma_w}{\alpha_w}(T-T_{\mathrm{w}})} - 1 - x_0(\exp^{\frac{\gamma_w}{\alpha_w}(T-T_{\mathrm{w}})}(1+B-E) - 1 - B)}{\exp^{\frac{\gamma_w}{\alpha_w}(T-T_{\mathrm{w}})} - 1}. \tag{6.19}$$

Expression for the volume fractions

In our model we work with volume fractions instead of mass fractions. The relation between them is given in the following remark.

Remark 10. In a mixture of two phases the volume fractions ($g_{\mathrm{l}},\ g_{\mathrm{s}}$) as functions of the mass fractions ($f_{\mathrm{l}},\ f_{\mathrm{s}}$) are:

$$g_{\mathrm{l}} = \frac{f_{\mathrm{l}}\rho_{\mathrm{s}}}{f_{\mathrm{l}}\rho_{\mathrm{s}} + f_{\mathrm{s}}\rho_{\mathrm{l}}}, \quad g_{\mathrm{s}} = \frac{f_{\mathrm{s}}\rho_{\mathrm{l}}}{f_{\mathrm{s}}\rho_{\mathrm{l}} + f_{\mathrm{l}}\rho_{\mathrm{s}}}. \tag{6.20}$$

The density of the mixture can be written as $\rho = \rho_{\mathrm{l}}g_{\mathrm{l}} + \rho_{\mathrm{s}}g_{\mathrm{s}}$ and the relationships between the mass and volume fractions in liquid and solid phases are:

$$f_{\mathrm{l}} = \frac{\rho_{\mathrm{l}}g_{\mathrm{l}}}{\rho}, \quad f_{\mathrm{s}} = \frac{\rho_{\mathrm{s}}g_{\mathrm{s}}}{\rho}.$$

As $\rho = \frac{\rho_{\mathrm{l}}g_{\mathrm{l}}}{f_{\mathrm{l}}}$ and also $\rho = \rho_{\mathrm{l}}g_{\mathrm{l}} + \rho_{\mathrm{s}}g_{\mathrm{s}} = g_{\mathrm{l}}(\rho_{\mathrm{l}} - \rho_{\mathrm{s}}) + \rho_{\mathrm{s}}$, after some straight forward calculations we have that:

$$g_{\mathrm{l}} = \frac{f_{\mathrm{l}}\rho_{\mathrm{s}}}{f_{\mathrm{s}}\rho_{\mathrm{l}} + f_{\mathrm{l}}\rho_{\mathrm{s}}} \text{ and } g_{\mathrm{s}} = 1 - g_{\mathrm{l}} = 1 - \frac{f_{\mathrm{l}}\rho_{\mathrm{s}}}{f_{\mathrm{s}}\rho_{\mathrm{l}} + f_{\mathrm{l}}\rho_{\mathrm{s}}} = \frac{f_{\mathrm{s}}\rho_{\mathrm{l}}}{f_{\mathrm{s}}\rho_{\mathrm{l}} + f_{\mathrm{l}}\rho_{\mathrm{s}}}.$$

As we said in Section 6.2.2, the liquid and solid volume fractions for our model depend on temperature and time. For a classical freezing process they are considered to be only dependent on temperature, but in a HPSF process we have information a priori about when the sample starts to freeze. We know that the sample remains unfrozen (even at subzero temperatures) until the pressure has been completely released (i.e. at $t = t_{p_3}$), and at that point there is a percentage of ice instantaneously formed, m_i, the mass of which we calculate using (6.14) and (6.15). After this point, the rest of the ice, $f_{\mathrm{s}}(T)$, is computed as a function of temperature following (6.19). We consider that the initial mass of solids in the food is the one before the expansion plus the mass of ice instantaneously formed after releasing pressure. Therefore, we take $x_0 = f_b + (f_{\mathrm{l}} - f_b)m_i$, where f_b is the mass fraction of solids in the food and f_{l} is the mass fraction of liquid in the food. Finally, we have that:

$$g_{\mathrm{l}}(t,T) = \begin{cases} 1 & t \le t_{p_3}, \\ 1 - \left(\dfrac{m_i\rho_{\mathrm{l}}}{m_i\rho_{\mathrm{l}} + (1-m_i)\rho_{\mathrm{s}}}\right)\dfrac{t - t_{p_3}}{\varepsilon} & t_{p_3} < t < t_{p_3} + \varepsilon, \\ 1 - \dfrac{f_{\mathrm{s}}(T)\rho_{\mathrm{l}}}{f_{\mathrm{s}}(T)\rho_{\mathrm{l}} + (1 - f_{\mathrm{s}}(T))\rho_{\mathrm{s}}} & t \ge t_{p_3} + \varepsilon, \end{cases} \tag{6.21}$$

where ε is the small time interval in which the mass fraction m_i of ice is instantaneously formed after the pressure release.

6.2.4 Resulting full model for a HPSF process

We focus on two different situations: HPSF of a large solid-type food and a small solid-type food.

For a large solid-type food

We use system (6.1), but we replace the first equation with (6.9), resulting in:

$$\begin{cases} C_{\rm vol}\dfrac{\partial T}{\partial t} - \dfrac{1}{r}\dfrac{\partial}{\partial r}\left(rk\dfrac{\partial T}{\partial r}\right) - \dfrac{\partial}{\partial z}\left(k\dfrac{\partial T}{\partial z}\right) = \beta_{\rm vol}\ \dfrac{{\rm d}P}{{\rm d}t}\ T - \delta e\dfrac{\partial g_{\rm l}}{\partial t} & \text{in} \quad \Omega\times(0,t_{\rm f}), \\ k\dfrac{\partial T}{\partial \mathbf{n}} = 0 & \text{on} \quad \Gamma_0\times(0,t_{\rm f}), \\ k\dfrac{\partial T}{\partial \mathbf{n}} = h(T_{\rm env}-T) & \text{on} \quad \Gamma_{\rm up}\times(0,t_{\rm f}), \\ T = T_{\rm r} & \text{on} \quad \Gamma_{\rm r}\times(0,t_{\rm f}), \\ T = T_0 & \text{in} \quad \Omega\times\{0\}, \end{cases} \tag{6.22}$$

where $g_{\rm l}$ is given by (6.21), P is given by (6.10), and $C_{\rm vol},\ \delta e,\ k,\ \beta_{\rm vol}$ are defined in Section 6.2.2.

For a small solid-type food

We use system (6.2), but we change the first equation for (6.9) plus the convective term of (6.2), resulting in:

$$\begin{cases} C_{\rm vol}\dfrac{\partial T}{\partial t} - \nabla\cdot(k\nabla T) + \rho C_p\mathbf{u}\cdot\nabla T = \beta_{\rm vol}\ \dfrac{{\rm d}P}{{\rm d}t}\ T - \delta e\dfrac{\partial g_{\rm l}}{\partial t} & \text{in} \quad \Omega^*\times(0,t_{\rm f}), \\ \rho\dfrac{\partial \mathbf{u}}{\partial t} - \eta\nabla^2\mathbf{u} + \rho(\mathbf{u}\cdot\nabla)\mathbf{u} = -\nabla p + \rho\mathbf{g} & \text{in} \quad \Omega^*_{\rm P}\times(0,t_{\rm f}), \\ \nabla\cdot(\mathbf{u}) = 0 & \text{in} \quad \Omega^*_{\rm P}\times(0,t_{\rm f}), \\ k\dfrac{\partial T}{\partial \mathbf{n}} = 0 & \text{on} \quad \Gamma^*_0\times(0,t_{\rm f}), \\ k\dfrac{\partial T}{\partial \mathbf{n}} = h(T_{\rm env}-T) & \text{on} \quad \Gamma^*_{\rm up}\times(0,t_{\rm f}), \\ T = T_{\rm r} & \text{on} \quad \Gamma^*_{\rm r}\times(0,t_{\rm f}), \\ \mathbf{u} = 0 & \text{on} \quad \Gamma^*_{\rm P}\times(0,t_{\rm f}), \\ T(0) = T_0 & \text{in} \quad \Omega^*, \\ \mathbf{u}(0) = 0 & \text{in} \quad \Omega^*, \\ p = 10^5 & \text{at} \quad \mathbf{A}_1\times(0,t_{\rm f}). \end{cases} \tag{6.23}$$

We point out that in these considered cases (that is, for solid and liquid-type foods) the pressurising medium used in HPSF processes does not freeze (therefore $g_{\rm l}=1$ in $\Omega_{\rm P}$). For both cases, in order to reduce computational complexity, as explained in Chapter 3, we have assumed that the thermo-physical properties of the food sample are constant, but different in the unfrozen and frozen states. The thermo-physical properties of the steel and the rubber cap remain constant during the whole process ($g_{\rm l}=1$ in those domains). We have also assumed that the thermo-physical properties of the pressurising fluid are constant for the large sample case, and for the small sample case, they are all constant except for ρ which is chosen as a constant value everywhere except in the gravitational force (i.e. we are using the Boussinesq approximation previously explained).

6.3 Numerical tests

We consider for the numerical tests the size of the pilot unit described in Chapter 3. The dimensions of the machine are $L=0.09$ m, $H=0.654$ m, $L_2=0.05$ m, $H_1=0.222$ m and $H_5=0.472$ m (see Figure 3.2). We simulate in this section the two cases described in Section 6.2.4. The size and location of the sample and the

rubber cap are given by $H_3 = 0.404$ m and $H_4 = 0.439$ m in both cases; $L_1 = 0.045$ m and $H_2 = H_1$ in the large sample case, and $L_1 = 0.02$ m and $H_2 = 0.294$ m in the small sample case (see Figure 3.2). The numerical tests we present are computed in cylindrical coordinates assuming axial symmetry. We use the Finite Element Method (FEM) solver COMSOL Multiphysics 3.5a. Velocity and pressure spatial discretisation is based on P2-P1 Lagrange Finite Elements satisfying the Ladyzhenskaya, Babuska and Brezzi (LBB) stability condition. The time integration is performed using the Variable-Step-Variable-Order (VSVO) BDF-based strategy implemented in the platform. The nonlinear systems are solved using UMFPACK (Unsymmetric MultiFrontal method for sparse linear systems) combined with the stabilisation technique GLS (Galerkin Least Squares).

For both cases, we consider agar gel as the solid-type food sample (this gel is a solid food simile that contains 99% water and therefore its properties are taken as those of water). The thermo-physical properties for the agar gel, in both unfrozen and frozen state, are respectively, $\rho_{\mathrm{F_l}} = 997$ kg m^{-3}, $\rho_{\mathrm{F_s}} = 918$ kg m^{-3}, $C_{p\mathrm{F_l}} = 4179$ J kg^{-1} K^{-1}, $C_{p\mathrm{F_s}} = 2052$ J kg^{-1} K^{-1}, $k_{\mathrm{F_l}} = 0.613$ W m^{-1} K^{-1}, $k_{\mathrm{F_s}} = 2.31$ W m^{-1} K^{-1}, $\beta_{\mathrm{F_l}} = 3.351 \cdot 10^{-4}$ K^{-1}, $\beta_{\mathrm{F_s}} = 7.97 \cdot 10^{-4}$ K^{-1}. The parameters for equation (6.19) are taken from [75] to be $E = 0.026$, $B = 0.050$, $\alpha_{\mathrm{w}} = 1860$ kg K mol^{-1} and $\gamma_{\mathrm{w}} = 18$ kg mol^{-1}. Parameters B and E given in [75] were estimated for bovine gel, and we are simulating the freezing of agar gel. We did not find in the literature any fitting parameters for agar gel, and this is why we used the ones for bovine gel, as they give good results. For x_0 in (6.19), we need the mass fraction of bounded solids in the food f_{sb}, which we can calculate using (6.20) with $g_{\mathrm{b}} = 0.01$, as agar gel contains 99% of water.

The thermo-physical properties of the steel and rubber cap are $\rho_{\mathrm{S}} = 7833$ kg m^{-3}, $C_{p\mathrm{S}} = 465$ J kg^{-1} K^{-1} and $k_{\mathrm{S}} = 55$ W m^{-1} K^{-1} for steel, and $\rho_{\mathrm{C}} = 1110$ kg m^{-3}, $C_{p\mathrm{C}} = 1884$ J kg^{-1} K^{-1} and $k_{\mathrm{C}} = 0.173$ W m^{-1} K^{-1} for rubber are taken. The environment temperature and the heat transfer coefficient used in all the tests are $T_{\mathrm{env}} = 19.3$ °C and $h = 28$ W m^{-2} K^{-1}, respectively. All of these data have been obtained from [29] and [71]. For the two cases, different pressurising fluids are considered, and for each case different temperature and pressure conditions are considered. We have considered these exact conditions and pressurising mediums in order to be able to compare our results with experimental published data (see [29, 71]).

For the large sample, following the experiments described in [70, 78], the pressurising fluid is considered to be a mixture of ethylene glycol and water (75/25, v/v), that has a very low freezing point and therefore does not freeze during the process (see [71]). The thermo-physical properties of this fluid are taken to be constant (as explained in Section 6.2.4 we take their mean values in the range of pressure and temperatures of the experiments) and using data from [34] we get $\rho_{\mathrm{P}} = 1127.91$ kg m^{-3}, $C_{p\mathrm{P}} = 2972.6$ J kg^{-1} K^{-1}, $k_{\mathrm{P}} = 0.345$ W m^{-1} K^{-1} and $\beta_{\mathrm{P}} = 5.655 \cdot 10^{-4}$ K^{-1}. As explained in [70, 78], before the experiment started, the pilot unit was tempered to the final subzero freezing temperature (T_{prev}) in order to avoid heat loss during freezing of the agar gel. The pressurising fluid was also kept at the final freezing temperature, i.e., $T_{0_{\mathrm{S}}} = T_{0_{\mathrm{P}}} = T_{\mathrm{prev}}$. The initial temperature of the food sample and the rubber cap are $T_{0_{\mathrm{F}}} = T_{0_{\mathrm{C}}} = 2$ °C. Several HPSF processes were carried out at different final subzero temperatures and maximum pressures, from which we have chosen $T_{\mathrm{prev}} = -18$ °C/$P_{\max} = 180$ MPa and $T_{\mathrm{prev}} = -21$ °C/$P_{\max} = 210$ MPa to simulate. Pressure was applied at a rate of 2.5 MPa s^{-1}. The temperature of the cooling medium, T_{r}, was 0.5 °C lower than the subzero final freezing temperature, T_{prev}, for each experiment. In [78] the authors determine the initial freezing temperature of agar gel from the freezing plateaus of all the experimental processes and on the basis of the recorded data, $T_{\mathrm{F}} = -0.3$ °C was considered.

For the small sample, following the experiments described in [72], we consider a mixture of ethylene glycol, water and ethanol (40/40/20, v/v/v), as the pressurising medium. This also has a very low freezing point and therefore does not freeze during the process (see [29]). As we explained in Section 6.2.4, all the thermo-physical properties are considered to be constants, except for ρ in the gravitational force term. The constant values have been taken from [35] as $\rho_{\mathrm{P}} = 1011.77$ kg m^{-3}, $C_{p\mathrm{P}} = 3042.3$ J kg^{-1} K^{-1}, $k_{\mathrm{P}} = 0.381$ W m^{-1} K^{-1} and $\beta_{\mathrm{P}} = 6.219 \cdot 10^{-4}$ K^{-1}. The viscosity has be taken as $\eta_{\mathrm{P}} = 0.02$ Pa s. For the density of the fluid as a function of temperature and pressure we follow [34], where the volumetric properties for binary mixtures of Pressure-Transmitting Fluids are given, and also equations for calculating these properties for other mixtures from those of their pure components. In this case, as explained in [72], again before the experiment started, the HP pilot unit was tempered to the final subzero freezing temperature (T_{prev}) in order to avoid heat loss during freezing of the agar gel. The pressurising fluid was also kept at the final freezing temperature, i.e., $T_{0_{\mathrm{S}}} = T_{0_{\mathrm{P}}} = T_{\mathrm{prev}}$. The initial temperature of the food sample and the rubber cap are $T_{0_{\mathrm{F}}} = T_{0_{\mathrm{C}}} = 5$ °C. Several HPSF experiments were performed at different final subzero temperatures and at various pressures, from which we have chosen

T_{prev} (°C)	$P_{\max}$ (MPa)	Experimental time (s)	Model prediction (s)	Other models (s)
Large sample		[70]		[70]
-18	180	5611 ± 493	**5195**	5957
-21	210	4817 ± 385	**4586**	4830
Small sample		[72]		[64]
-8	120	3850 ± 61	**3760**	3797
-20	210	1038 ± 120	**970**	1134

Table 6.1: Experimental and simulated time needed to complete freezing plateau in different HPSF experiments

to simulate the following: $T_{\text{prev}} = -8°$ C/$P_{\max} = 120$ MPa and $T_{\text{prev}} = -20°$ C/$P_{\max} = 210$ MPa. The temperature of the cooling medium, T_{r}, was 0.5 °C lower than the subzero final freezing temperature, T_{prev}, for each experiment. Pressure was also applied at a rate of 2.5 MPa s^{-1}. In [72] the authors determine the initial freezing temperature of agar gel from the freezing plateaus of all the experimental processes and on the basis of the recorded data, in this case, $T_{\text{F}} = -0.1$ °C was considered.

For both cases, as we know the rate at which pressure is applied and the maximum pressure we have to reach, t_{p_1}, i.e. the time in which we are increasing pressure, is calculated as $P_{\max}/P_{\text{rate}}$. For the sake of simplicity (we could have also used models (6.1) or (6.2) to compute it), we have obtained time t_{p_2} (the time when pressure is at its maximum and the temperature of the sample has reached the desired freezing temperature, T_{prev} from the experimental data (see [70, 72, 78]). Finally, $t_{p_3} = t_{p_2} + 2$, as we are considering the case of rapid pressure release, that is considered to be in 1-2 seconds.

6.3.1 Results

We have simulated the experiments described in Section 6.3 using the models explained in Section 6.2. The results of solving (6.22) for a HPSF process of a large sample of agar gel are shown in Figure 6.2. These experiments with agar gel and the different temperature and pressure profiles are described in [70, 78]. We do not have the experimental data to compare our simulations to (graphically), so instead we compared the phase transition times of our simulations to the ones published in [70, 78]. Following [72] we have calculated the phase transition times (plateau times shown in Table 6.1) as the time span between nucleation and reaching a temperature 5° C below the corresponding initial freezing point at the centre of the sample. We compare the predicted plateau times of our model to the experimental data, and also to the plateau times predicted by other HPSF models (see Table 6.1). For the large sample, we compare them to the theoretical times calculated in [70]; for the small sample , we compare them to those predicted in [64]. The times in Table 6.1 are not given as such in [64], where instead a "reduction in plateau time" (%) was given; this refers to how long the plateau time has reduced when compared to atmospheric pressure freezing (APF) process. The APF times are given in [72].

In Figure 6.3 the results of solving equation (6.23) for a HPSF process of a small sample of agar gel are shown compared to experimental data, and agree very well. These experiments with agar gel and the different temperature and pressure profiles are described in [72]. In that paper the authors remark that the free convection in the pressure fluid can acquire relative importance, as the pressure medium occupies 88.7% of the total vessel volume. In our model we include the convective effects, and we simulated exactly the same experiments without including convection effects, i.e. with only conduction effects, and the results (not shown here) were very different and did not agree with the experimental data. Without including convection effects, the small sample takes much longer to cool.

Our model predictions capture the trend in measured plateau times with applied temperature and pressure, and tend to underpredict the data slightly (see Figures 6.2–6.3 and Table 6.1), although in only one case of the four, the simulated time is not within experimental uncertainty but the remaining difference is on the order of half a minute, thus it should be considered acceptable for a process that takes about one hour. In any case, we discuss possible reasons for this underprediction in the conclusions. The other published models tend to overpredict

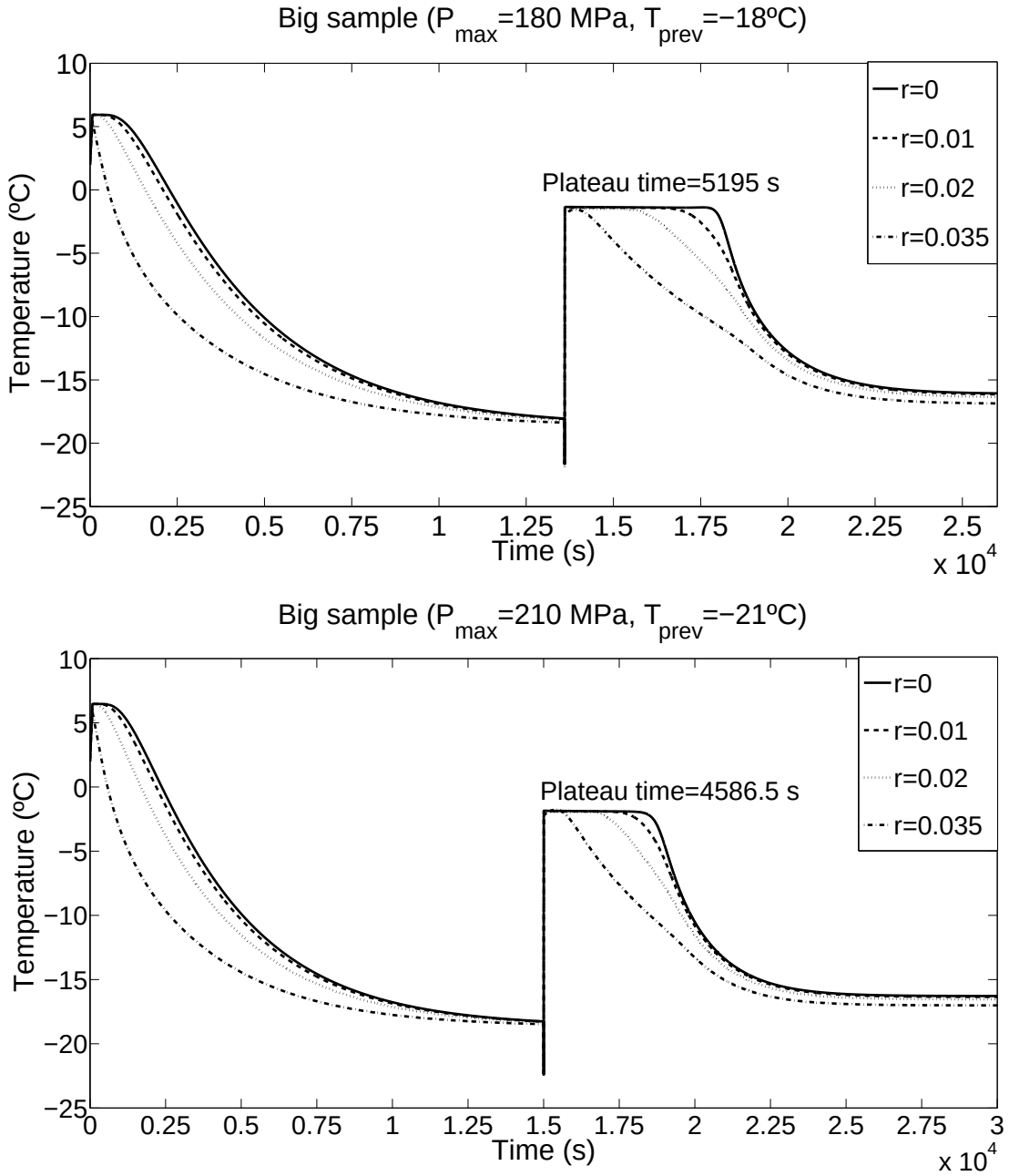

Figure 6.2: Temperature evolution at different radial locations of a large agar sample during a HPSF process for different temperature and pressure conditions. All results are predicted values from model (6.22).

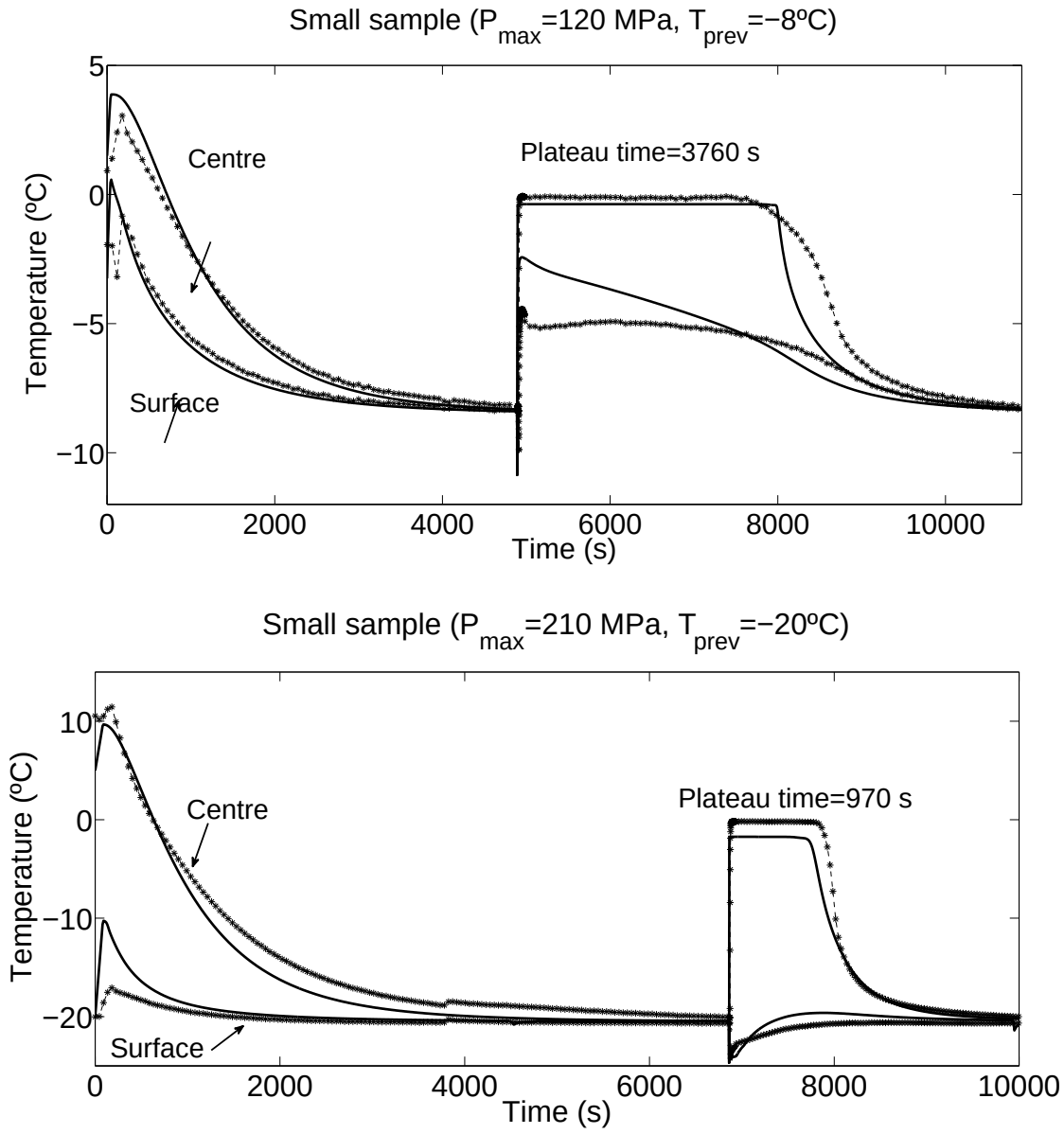

Figure 6.3: Temperature evolution at the centre and surface of a small agar sample during a HPSF process for different temperature and pressure conditions. (–) predicted values from model (6.23); (∗) experimental data.

the plateau times slightly, but also give quite satisfactory results. However, we remark that the authors in [70] calculated the plateau times taking into account the amount of ice instantaneously produced after expansion, and the time required to freeze the sample at atmospheric pressure, but did not obtain them as a result from a heat transfer model. In [64], for the small sample case, the authors proposed a one dimensional heat transfer model for the food sample, but they did not model the heat transfer in the pressurising medium. They assumed a boundary condition of the third class at the surface between the food and the pressurising fluid, and had to choose the surface heat transfer coefficient to best fit the experimental curve, i.e. they had a fitting parameter. Also, they did not validate the precooling stage, so their model is validated only from the temperature at which the pressure was released.

6.4 Conclusions

The models described in this Chapter provide a useful tool to simulate the temperature profile at all points inside both large and small solid food samples going through a HPSF process. The model for solidification is based on the enthalpy formulation at non-constant pressure and volume phase fractions. The models are two dimensional axis-symmetric, and can therefore predict the temperature distribution at any point inside the food sample, not just at any radial component, which happens with one dimensional models, but also at any height. Convection effects in the pressurising fluid are considered for the small sample case (and shown to be important).

For the small sample case, the numerical tests agree with the experimental data very well, especially at the centre of the sample. We emphasise that no fitting parameters were used in the simulations. At the surface there is not an accurate match between the data and the model. However we consider that the modelling efforts are good enough, given the relatively large experimental errors. It is important to point out, that locating a thermocouple exactly at the surface is very difficult, and often generates significant measurement errors coming from the neighbouring material temperature, which is colder than the food sample. For the large sample case, there is no experimental data to plot against the simulated temperature profile, but the results look very similar to the temperature profiles plotted in [78]. When comparing the model plateau times to the published experimental ones, we find that they are in general shorter, but in the range of the latter. In all cases, the prediction errors are on the order of minutes, which is not too bad given that the processing time is on the order of hours.

Future improvements, in case experimental measurements become more precise, could potentially be obtained by including temperature and pressure dependence of material properties, anisotropy effects in the frozen region, and extending our 2D convection simulations to 3D.

Chapter 7

Growth and coarsening of ice crystals

Nomenclature for Chapter 7

C_{R_i}	Coefficients for radii in numerical scheme (μm s^{-1})
$C_{v_{\text{ice}}}$	Coefficients for ice volume concentration in numerical scheme (s^{-1})
dt	Time step for numerical scheme (s)
G	System Gibb's free energy (eV)
I_{in} / I_{out}	Molecule inward / outward flow ($\mu m^{-2} s^{-1}$)
k	Boltzmann constant (eV K^{-1})
K	Surface reaction rate (μm s^{-1})
L	Latent heat (eV per molecule)
M	Mass (mg)
n	Molecular number concentration (μm^{-3})
N	Number of molecules in the system
$n$max	$(2\nu_{\text{hyd}} + \nu_{\text{oxy}})^{-1}$ (μm^{-3})
r	minimum ice particle radius
R	Ice particle–cluster radius (μm)
S	Surface (μm^2)
t	Time (s)
T	Temperature (K)
$\bar{t}$	Time when the melting temperature reaches the experimental temperature and no more ice precipitates (s)
v	Volume concentration (dimensionless)
V	Volume (μm^3)
x	Mass concentration (mg μm^{-3})

Acronyms

APF	Atmospheric pressure freezing
HPSF	High-Pressure Shift freezing

Greek symbols

β	Rate of change of $\mu_{\text{s.water}}$ with respect to x_{s} (eV μm^3 mg^{-1} per molecule)
γ	Surface energy per unit area (eV μm^{-2})
μ	Chemical potential (eV per molecule)
ν	Molecular or atomic volume (μm^3)
ε	Cohesive energy (eV per molecule)

Other symbols

$\langle f \rangle$	mean value of the set $\{f_i\}_i$

Indices

0	Initial modelling time
cl	Ice particle–cluster
exp	experimental
GT	Gibbs–Thomson
hyd	Hydrogen
i	Ice particles index
ice	Non precipitated ice
melt	Melt
mf	Mean field
OR	Ostwald Ripening
oxy	Oxygen
s	Salt
s.water	Salty water
thr	Threshold
water	Pure water

7.1 Motivation for studying growth and coarsening of ice particles

After studying High Pressure Shift Freezing (HPSF) processes in Chapter 6 it is clear that HPSF is a good method to produce frozen food with small ice crystal size that are uniformly distributed, and therefore, with reduced tissue damage and higher overall quality [30].

The goal of this Chapter, which is based on the work from [83], is to develop a model to study the growth and coarsening of ice particles in a frozen food sample, and hence look at the temporal evolution of HPSF frozen ice

crystals. This idea came from the work published in [30], where the authors investigated if HPSF frozen systems follow the same ice recrystallisation kinetics than those conventionally frozen (at atmospheric conditions). For this the authors of [30] designed a system which could hold HPSF frozen samples of suitable size for microscopic observation without their alteration. Then using direct microscopic examination at different temperatures, they could follow the evolution of ice crystals with time and study the influence of the freezing method and storage temperature on recrystallisation. In [30] a 1.86N NaCl solution was used as a food model sample. For this reason, we model a very simple system consisting of salty water. If we assume that initially the ice particles are homogeneously distributed and have the spherical shape, which occurs with a HPSF frozen sample as explained in Chapter 6, our model is valid for any kind of freezing process and not only HPSF. This will allow us to compare the evolution of HPSF frozen samples to that of samples that have been classically frozen.

In Section 7.2 we describe how to calculate the melting temperature of salty water and show some expressions regarding the salt mass concentration and the volume concentration of dissolved ice. In Section 7.3 we present a model that accounts for the growth and ripening of ice crystals in this simple system by developing a theory somewhat similar to Ostwald ripening [9]. Our model predicts crystal size evolution with time, and also ice crystal size distribution. In Section 7.4 we describe the numerical simulations we have performed and in Section 7.5 we present the particular numerical experiments and results for salty water and ice-cream. In Section 7.6 we outline the conclusions.

7.2 Melting temperature of salty water

Consider a system consisting of salty water at an experimental temperature T_{exp}. If the temperature is low enough (below the melting point) the system has a potential to produce a certain amount of ice (which depends on the temperature [6]) via isothermal crystallisation. Let us assume that at time t_0 (s) the system has already produced part of this ice, which has precipitated in spherical particles of radii R_i (μm). For modelling purposes it is also convenient to assume that all the ice which can potentially still precipitate, is, at time t_0, initially dissolved in salty water, without it having precipitated yet. Such consideration allows developing a theory somewhat similar to Ostwald ripening to account for both growth and coarsening of the pre-existing ice particles. During some time there will be two physical processes occuring: growth of ice particles due to the new ice that is being produced (since the experimental temperature is below the melting temperature) and ripening between ice particles.

As we will see below, the salt concentration increases along the process pushing the melting temperature T_{melt} down towards T_{exp}. At some instant $\bar{t}$ (s), $T_{\text{melt}}(\bar{t})$ (K) reaches the experimental temperature T_{exp}, no more ice is produced and $T_{\text{melt}}(t) = T_{\text{exp}}$ for any $t \geq \bar{t}$. Therefore, for $t \geq \bar{t}$ only ripening takes place. Our goal in this Chapter is to study the evolution of the ice particles present in the system for times $t \in [t_0, \infty)$.

Let us suppose that at time t (s) the system is composed of salty water, spherical (for simplicity) precipitated ice particles of radii $R_i(t)$ (μm) larger than a minimum value r (for instance, the minimal radius than our experimental equipment is able to measure). Figure 7.1 shows a graphical description of the system.

Let us also assume that the system has a salt mass concentration given by

$$x_s(t) = \frac{M_s}{V_{\text{s.water}} + V_{\text{ice}}(t)}, \tag{7.1}$$

where M_s (mg) is the total salt mass dissolved in water and non-precipitated dissolved ice, $V_{\text{s.water}}$ (μm^3) is the volume occupied by salty water that is not part of the non-precipitated ice dissolved in water, and $V_{\text{ice}}(t)$ (μm^3) is the volume occupied by the non-precipitated ice dissolved in water.

First we illustrate the dependence of the melting temperature upon the salt concentration. Looking at the interaction between salty water and non–dissolved ice in thermodynamic equilibrium, at melting temperature $T_{\text{melt}}(x_s)$ the chemical potentials of H_2O molecules in the non-precipitated ice (μ_{ice}) and in salty water ($\mu_{\text{s.water}}$) are equal.

Ice forms very compact structures avoiding H_2O molecules to move in void space. Therefore we can neglect entropy and, assuming it does not contain any salt, its chemical potential (measured in eV per molecule) is

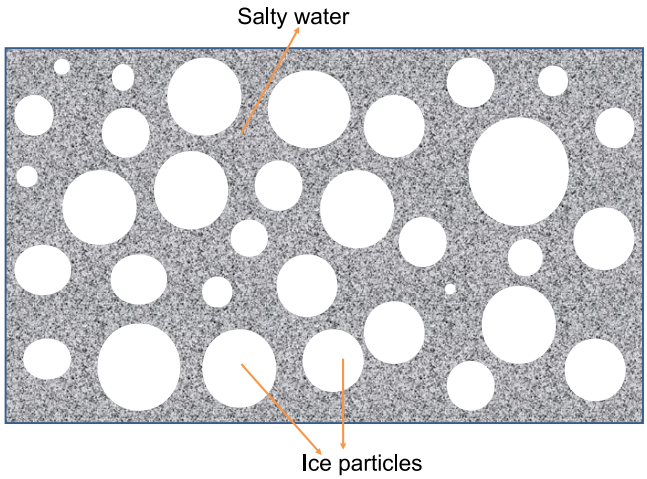

Figure 7.1: Salty water system configuration.

given by

$$\mu_{\text{ice}} = -\varepsilon_{\text{ice}} \tag{7.2}$$

which is constant for the range of temperatures and pressures under consideration, where ε_{ice} (measured in eV per molecule) is the cohesive energy of H_2O molecules in ice, i.e. the inter–molecular energy required to break all the bonds associated with one molecule.

On the other hand, the chemical potential of the liquid salty water depends on x_s and then, following Section 5 of [47], we have that

$$\mu_{\text{s.water}}(x_s) = \mu_{\text{water}} - \beta x_s, \tag{7.3}$$

where $-\beta$ (eV μm^3 mg^{-1} per molecule) is the rate of change of $\mu_{\text{s.water}}$ with respect to x_s.

The chemical potential of liquid substances has a component due to the cohesive energies of its molecules and it also has another component due to the entropy generated by the "voids" appearing in their open structures. This component is specially important for water, since it is a liquid with extraordinary properties, which has an open structure that is full of voids (see [10]). Therefore, water chemical potential has a component due to the cohesive energy of H_2O molecules and it also has another component due to the entropy generated by the "voids" mentioned above. Thus (see Section 7 of [47]),

$$\mu_{\text{water}}(T) = -\varepsilon_{\text{water}} + kT \ln\left(\frac{n_{\text{water}}}{n\text{max}}\right), \tag{7.4}$$

for any temperature T (K), where $\varepsilon_{\text{water}}$ is the cohesive energies of H_2O molecules in pure water, k is the Boltzmann constant ($k \approx 1.3806488\text{x}10^{-23}$J K^{-1} $= 8.617332410^{-5}$eV K^{-1}), $n_{\text{water}} = \nu_{\text{water}}^{-1}$ (molecules per μm^3) is the number concentration of H_2O molecules in water and $n$max is the maximum number concentration of H_2O molecules in water that would be attained in the hypothetical case of water molecules occupying only the volume occupied by their atoms (i.e. $n$max is the inverse of the volume that is occupied by the atoms of a water molecule or $n\text{max} = (2\nu_{\text{hyd}}+\nu_{\text{oxy}})^{-1}$, where ν_{hyd} and ν_{oxy} (μm^3) are the atomic volumes of hydrogen and oxygen, respectively). According to [10], typical values are $\nu_{\text{water}} = 0.02992$ x 10^{-9} μm^3 and $2\nu_{\text{hyd}} + \nu_{\text{oxy}} = 0.0146$ x 10^{-9} μm^3, which gives a ratio $\frac{n_{\text{water}}}{n\text{max}} = \frac{2\nu_{\text{a,hyd}}+\nu_{\text{a,oxy}}}{\nu_{\text{water}}} \approx 0.49$, whereas a dense packing of spherical molecules would yield 0.74. Thus, a large part of the volume of liquid water is actually made of voids.

Then, using that $\mu_{\text{ice}} = \mu_{\text{s.water}}$ and (7.2)–(7.4), we obtain that

$$kT_{\text{melt}}(x_s) = \frac{L_{\text{melt}} - \beta x_s}{\ln\left(\frac{n\text{max}}{n_{\text{water}}}\right)}, \tag{7.5}$$

with $L_{\text{melt}} = \varepsilon_{\text{ice}} - \varepsilon_{\text{water}}$ being the latent heat of melting (expressed in eV per molecule). From this equation,

we can obtain a more useful expression for the shift of the melting point:

$$\frac{T_{\text{melt}}(x_s)}{T_{\text{melt}}(0)} = \frac{L_{\text{melt}} - \beta\ x_s}{L_{\text{melt}}} = 1 - \frac{\beta x_s}{L_{\text{melt}}}. \tag{7.6}$$

This equation illustrates that the higher x_s, the lower $T_{\text{melt}}(x_s)$. In reality, once crystallisation/melting starts, x_s begins to change. In a crystallisation process it increases pushing $T_{\text{melt}}(x_s)$ down, which eventually stops crystallisation. It looks like all the ice dissolved has now precipitated.

It is instructive to define x_s as a function of the volume concentration of dissolved ice

$$v_{\text{ice}} = \frac{V_{\text{ice}}}{V_{\text{s.water}} + V_{\text{ice}}}. \tag{7.7}$$

From here we have that

$$V_{\text{ice}} = \frac{v_{\text{ice}} V_{\text{s.water}}}{1 - v_{\text{ice}}} \tag{7.8}$$

and then

$$x_s(t) = \frac{M_s(1 - v_{\text{ice}}(t))}{V_{\text{s.water}}} = x_s(\bar{t})(1 - v_{\text{ice}}(t)), \tag{7.9}$$

where we recall that $\bar{t}$ (s) is the time when the maximum salt mass concentration is attained, which is achieved when all dissolved ice has precipitated. According to Equation (7.6) we have

$$\frac{T_{\text{melt}}(x_s(\bar{t}))}{T_{\text{melt}}(0)} = 1 - \frac{\beta x_s(\bar{t})}{L_{\text{melt}}}.$$

Then, taking into account that $T_{\text{melt}}(x_s(\bar{t})) = T_{\text{exp}}$, we obtain

$$x_s(\bar{t}) = \frac{L_{\text{melt}}}{\beta}\left(1 - \frac{T_{\text{exp}}}{T_{\text{melt}}(0)}\right). \tag{7.10}$$

Let us suppose that, at the initial time t_0 the salt concentration is $x_s(t_0) = x_{s,0}$ and the volume of water plus dissolved ice is $V_{\text{s.water}} + V_{\text{ice}}(t_0) = V_0$. Then, we can find the amount of ice crystallised at temperature T_{exp}. From (7.1) we have

$$x_s(\bar{t}) = \frac{x_{s,0} V_0}{V_0 - V_{\text{ice}}(t_0)},$$

which implies that

$$V_{\text{ice}}(t_0) = V_0\left(1 - \frac{x_{s,0}}{x_s(\bar{t})}\right).$$

Then, from (7.7) we deduce that

$$v_{\text{ice}}(t_0) = \frac{V_{\text{ice}}(t_0)}{V_0} = 1 - \frac{x_{s,0}}{x_s(\bar{t})}. \tag{7.11}$$

Substituting Equation (7.10) into (7.11) we obtain

$$v_{\text{ice}}(t_0) = 1 - \frac{x_{s,0}}{\frac{L_{\text{melt}}}{\beta}\left(1 - \frac{T_{\text{exp}}}{T_{\text{melt}}(0)}\right)} = 1 - \frac{\beta x_{s,0}}{L_{\text{melt}}}\frac{T_{\text{melt}}(0)}{(T_{\text{melt}}(0) - T_{\text{exp}})}. \tag{7.12}$$

We can also find the salt mass concentration at any time, as a function of the corresponding volume concentration of dissolved ice, by using the following expression, deduced from (7.9) and (7.11):

$$x_s(t) = x_s(\bar{t})(1 - v_{\text{ice}}(t)) = \frac{x_{s,0}(1 - v_{\text{ice}}(t))}{1 - v_{\text{ice}}(t_0)}. \tag{7.13}$$

7.3 Growth and ripening

Here we use the idea about dissolved ice in the water and find equations describing growth and ripening of pre-existing ice particles. For simplicity we assume that all the particles have spherical shape and retain it during the whole process. In the mean field theory of ordinary Ostwald ripening (OR) the conservation of fluxes (total incoming and outgoing) is normally assumed. If there is supersaturation of one component (ice) in the other (water) such conservation does not take place anymore, i.e. the total particles mass increases. The equations for particle radii R (μm) are

$$\frac{\mathrm{d}R}{\mathrm{d}t} = \nu_{\mathrm{ice}} \left(I_{\mathrm{in}} - I_{\mathrm{out}}(R) \right), \tag{7.14}$$

where ν_{ice} (μm^3 per molecule) is the molecular volume of an H_2O molecule in ice and I_{in} (molecules per μm^2 and per s), respectively I_{out}, is the number of ice molecules deposited on, respectively removed from, an ice particle per unit surface and per unit time. In the Wagner limit (see, e.g., [9]) the fluxes can be written as

$$I_{\mathrm{in}} = K \; n_{\mathrm{mf}}, \qquad I_{\mathrm{out}}(R) = K \; n_{\mathrm{GT}}(R),$$

where n_{mf} (ice molecules per μm^3) is the mean field number concentration of dissolved ice, $n_{\mathrm{GT}}(R)$ is the Gibbs–Thomson number concentration and K (μm s^{-1}) is the surface reaction rate.

The main assumption of our approach is that the mean field number concentration can be represented as a sum

$$n_{\mathrm{mf}} = n_{\mathrm{OR}} + n_{\mathrm{ice}}, \tag{7.15}$$

where the component n_{OR} (molecules per μm^3) is responsible for ripening, and n_{ice} (molecules per μm^3) is the number concentration of H_2O molecules in the dissolved ice, which is responsible for ice growth.

7.3.1 Ripening

The ripening mean field component can be obtained from the fluxes balance, assuming that all emitted molecular fluxes are absorbed accounting for the ripening process. The number of ice molecules deposited on an ice particle of radius R per unit time is $4\pi R^2 \left(I_{\mathrm{in}} - I_{\mathrm{out}}(R) \right)$. Therefore, taking into account all particles and assuming that the total number of ice molecules in all particles is conserved, we have

$$\sum_i R_i^2 \left(n_{\mathrm{OR}} - n_{\mathrm{GT}}(R_i) \right) = 0,$$

which implies, using mean values, that

$$n_{\mathrm{OR}} = \frac{\left\langle R^2 \; n_{\mathrm{GT}}(R) \right\rangle}{\langle R^2 \rangle}. \tag{7.16}$$

Looking at the interaction between salty water and a dissolved ice particle–cluster with radius R in thermodynamic equilibrium, at melting temperature $T_{\mathrm{melt}}(x_s)$ the chemical potentials in the ice particle–cluster ($\mu_{\mathrm{cl}}(R)$) and in salty water ($\mu_{\mathrm{s.water}}$) are equal. Let us see how to compute $\mu_{\mathrm{cl}}(R)$.

When the initial ice molecules or tiny small particles with chemical potential μ_{ice} grow to a big cluster with radius R, its chemical potential needs to incorporate a term due to the increase of energy surface. In order to compute this term we recall that, according to the Gibbs fundamental equation for a thermodynamical system, (see, e.g., [26]), assuming that pressure and temperature are constant during the process we have

$$\mathrm{d}G = \mu \mathrm{d}N,$$

where G and N are the system Gibbs free energy and number of molecules in the system. On the other hand (see, e.g., [26])

$$\mathrm{d}G = -\varepsilon \mathrm{d}V + \gamma \mathrm{d}S,$$

where ε is the cohesive energy per unit volume, S is the system surface and γ is the the system surface energy per unit area. Then, if we apply this to the system formed by a cluster particle with radius R, we have that

$$\mu_{\rm cl}(R) = \frac{{\rm d}G_{\rm cl}}{{\rm d}N} = \frac{{\rm d}G_{\rm cl}}{{\rm d}V}\frac{{\rm d}V}{{\rm d}N} = \left(-\varepsilon_{\rm cl} + \gamma\frac{{\rm d}S}{{\rm d}N}\right)\nu_{\rm ice} = -\varepsilon_{\rm ice} + \gamma\frac{{\rm d}(4\pi R^2)}{{\rm d}(4\pi R^3/3)}\nu_{\rm ice}.$$

Therefore we obtain

$$\mu_{\rm cl}(R) = -\varepsilon_{\rm ice} + \frac{2\gamma\nu_{\rm ice}}{R}, \tag{7.17}$$

where γ is the cluster surface energy per unit area.

Following the approach used in [9], the outgoing flux $I_{\rm out}(R)$, which is due to emission of ice molecules from the cluster surface, at a given temperature surely should be the same as in the situation when the particle is in equilibrium with the surrounding salty water. Therefore, the Gibbs-Thomson concentration, $n_{\rm GT}(R)$, can be then determined from the equilibrium condition $\mu_{\rm cl} = \mu_{\rm water}$. Then, from (7.3), (7.4), (7.13) and (7.17), it follows that

$$-\varepsilon_{\rm ice} + \frac{2\gamma\nu_{\rm ice}}{R(t)} = -\varepsilon_{\rm water} + kT_{\rm exp}\ln\left(\frac{n_{\rm GT}(t)}{n\max}\right) - \frac{\beta x_{s,0}(1-v_{\rm ice}(t))}{1-v_{\rm ice}(0)}.$$

From this we obtain

$$n_{\rm GT}(R(t)) = n\max\,\exp\left[-\frac{L_{\rm melt} - \frac{\beta x_{s,0}(1-v_{\rm ice}(t))}{1-v_{\rm ice}(0)}}{kT_{\rm exp}} + \frac{2\gamma\nu_{\rm ice}}{kT_{\rm exp}R(t)}\right]. \tag{7.18}$$

Expression (7.18) for $n_{\rm GT}(R(t))$ can be simplified, as was done in [9], by making the following standard assumption of the classical OR theory

$$2\gamma\nu_{\rm ice} << kT_{\rm exp}R(t). \tag{7.19}$$

We will see in Section 7.5 that (7.19) holds for the particular cases under study. Thus, (7.18) can be approximated by

$$n_{\rm GT}(R(t)) \approx n\max\,\exp\left[-\frac{L_{\rm melt} - \frac{\beta x_{s,0}(1-v_{\rm ice}(t))}{1-v_{\rm ice}(0)}}{kT_{\rm exp}}\right]\left(1 + \frac{2\gamma\nu_{\rm ice}}{kT_{\rm exp}R(t)}\right). \tag{7.20}$$

Substituting (7.20) into equation (7.16) we find

$$n_{\rm OR} \approx n\max\,\exp\left[-\frac{L_{\rm melt} - \frac{\beta x_{s,0}(1-v_{\rm ice}(t))}{1-v_{\rm ice}(0)}}{kT_{\rm exp}}\right]\left(1 + \frac{2\gamma\nu_{\rm ice}\,\langle R(t)\rangle}{kT_{\rm exp}\,\langle R(t)^2\rangle}\right). \tag{7.21}$$

7.3.2 Growth

The growth fraction $n_{\rm ice}$ of the mean field given in (7.15) can be determined from a separate equation. It is clear that

$${\rm d}V_{\rm ice} = -{\rm d}\left(\sum_i \frac{4\pi}{3}R_i^3\right) = -\sum_i 4\pi R_i^2{\rm d}R_i,$$

which implies that

$$\frac{{\rm d}V_{\rm ice}}{{\rm d}t} = -\sum_i 4\pi R_i^2\frac{{\rm d}R_i}{{\rm d}t}.$$

Then, using (7.14) but accounting only for growth and without ripening (i.e. with $I_{\rm out} = 0$ and $n_{\rm OR} = 0$) we find the following equation for $V_{\rm ice}(t)$

$$\frac{{\rm d}V_{\rm ice}}{{\rm d}t} = -\nu_{\rm ice}Kn_{\rm ice}\sum_i 4\pi R_i^2. \tag{7.22}$$

Let us now rewrite (7.22) in terms of v_{ice}. From (7.8) and (7.11) we obtain

$$\frac{\mathrm{d}}{\mathrm{d}t}\left(\frac{v_{\text{ice}}V_0(1-v_{\text{ice}}(t_0))}{1-v_{\text{ice}}}\right) = -\nu_{\text{ice}}Kn_{\text{ice}}\sum_i 4\pi R_i^2 = -Kv_{\text{ice}}\sum_i 4\pi R_i^2$$

$$\Longrightarrow \qquad \frac{\mathrm{d}v_{\text{ice}}}{\mathrm{d}t}\left(\frac{1}{1-v_{\text{ice}}}+\frac{v_{\text{ice}}}{(1-v_{\text{ice}})^2}\right) = -\frac{Kv_{\text{ice}}}{V_0(1-v_{\text{ice}}(t_0))}\sum_i 4\pi R_i^2.$$

7.3.3 Ripening and growth

Thus, the full set of equations is

$$\begin{cases} \dfrac{\mathrm{d}v_{\text{ice}}(t)}{\mathrm{d}t} = -\dfrac{Kv_{\text{ice}}(t)(1-v_{\text{ice}}(t))^2}{V_0(1-v_{\text{ice}}(t_0))}\displaystyle\sum_i 4\pi R_i(t)^2 \\ \dfrac{\mathrm{d}R_i(t)}{\mathrm{d}t} = Kv_{\text{ice}}(t) + \dfrac{2\gamma\nu_{\text{ice}}^2 Kn\text{max}}{kT_{\text{exp}}}\exp\left[-\dfrac{L_{\text{melt}}}{kT_{\text{exp}}}+\dfrac{\beta x_{s,0}(1-v_{\text{ice}}(t))}{kT_{\text{exp}}(1-v_{\text{ice}}(t_0))}\right]\left(\dfrac{\langle R(t)\rangle}{\langle R(t)^2\rangle}-\dfrac{1}{R_i(t)}\right). \end{cases}$$

Parameter $n\text{max}$ can be eliminated from the above equation by this using that, from (7.5),

$$n\text{max} = n_{\text{water}}\exp\left(\frac{L_{\text{melt}}}{kT_{\text{melt}}(0)}\right).$$

Thus, the system can be written as

$$\begin{cases} \dfrac{\mathrm{d}v_{\text{ice}}(t)}{\mathrm{d}t} = -\dfrac{Kv_{\text{ice}}(t)(1-v_{\text{ice}}(t))^2}{V_0(1-v_{\text{ice}}(t_0))}\displaystyle\sum_i 4\pi R_i(t)^2 \\ \dfrac{\mathrm{d}R_i(t)}{\mathrm{d}t} = Kv_{\text{ice}}(t)+ \\ \quad \dfrac{2\gamma\nu_{\text{ice}}^2\nu_{\text{water}}^{-1}K}{kT_{\text{exp}}}\exp\left[\dfrac{L_{\text{melt}}}{k}\left(\dfrac{1}{T_{\text{melt}}(0)}-\dfrac{1}{T_{\text{exp}}}\right)+\dfrac{\beta x_{s,0}(1-v_{\text{ice}}(t))}{kT_{\text{exp}}(1-v_{\text{ice}}(t_0))}\right]\left(\dfrac{\langle R(t)\rangle}{\langle R(t)^2\rangle}-\dfrac{1}{R_i(t)}\right). \end{cases} \tag{7.23}$$

This system must be completed with initial conditions at a suitable time t_0 (s). The initial ice volume concentration $v_{\text{ice}}(t_0)$ is calculated using Equation (7.12). $R_i(0)$ and the number of index i have to be estimated from experiments

$$\begin{cases} v_{\text{ice}}(t_0) = 1-\dfrac{\beta x_{s,0}}{L_{\text{melt}}}\dfrac{T_{\text{melt}}(0)}{(T_{\text{melt}}(0)-T_{\text{exp}})}, \\ R_i(t_0) \text{ estimated from experiments.} \end{cases} \tag{7.24}$$

We have, therefore, developed a model given by (7.23)–(7.24).

7.4 Numerical simulations

7.4.1 Estimation of some parameters for simulations

Model (7.23)–(7.24) needs the value of the well–known constants (which we give in the relevant units for this Chapter) $k \approx 8.617$ x 10^{-5} (eV K^{-1}), $T_{\text{melt}}(0) \approx 273.15$ (K), $L_{\text{melt}} \approx 0.0625$ (eV molecule^{-1}), $\gamma \approx 1.5605$ x 10^5 (eV μm^{-2}), $\nu_{\text{water}} \approx 0.02992$ x 10^{-9} (μm^3) and $\nu_{\text{ice}} \approx 0.03263\ 10^{-9}$ (μm^3). It also needs the following input parameters: T_{exp}, K, V_0, β, $x_{s,0}$ and $R_i(0)$, for all i.

Now,

$$\frac{2\gamma\nu_{\text{ice}}^2\nu_{\text{water}}^{-1}}{k} \approx \frac{2\cdot 1.5605\cdot 10^5\cdot 0.03263^2\cdot 10^{-18}}{0.02992\cdot 10^{-9}\cdot 8.617\cdot 10^{-5}} \approx 0.12887\ \mu\text{m K},$$

$$\frac{L_{\text{melt}}}{k} \approx \frac{0.0625}{8.617\cdot 10^{-5}}\ \text{K molecule}^{-1} \approx 725.31\ \text{K molecule}^{-1},$$

$$\frac{L_{\text{melt}}}{kT_{\text{melt}}(0)} \approx \frac{725.31}{273.15} \text{ molecule}^{-1} \approx 2.6554 \text{ molecule}^{-1},$$
$$\frac{1}{k} = \frac{1}{8.617 \cdot 10^{-5}} \text{ K eV}^{-1} \approx 11604.967 \text{ K eV}^{-1},$$

and

$$\frac{T_{\text{melt}}(0)}{L_{\text{melt}}} \approx \frac{273.15}{0.0625} =\approx 4370.4 \text{ K eV}^{-1} \text{ molecule}.$$

Therefore, system (7.23) can be approximated for the simulations by

$$\begin{cases} \dfrac{\mathrm{d}v_{\text{ice}}(t)}{\mathrm{d}t} = C_{v_{\text{ice}}}(t) \\ \dfrac{\mathrm{d}R_i(t)}{\mathrm{d}t} = C_{R_i}(t), \end{cases} \tag{7.25}$$

where

$$\begin{cases} C_{v_{\text{ice}}}(t) = -\dfrac{Kv_{\text{ice}}(t)(1-v_{\text{ice}}(t))^2}{V_0(1-v_{\text{ice}}(t_0))} \displaystyle\sum_i 4\pi R_i(t)^2 \\ C_{R_i}(t) = Kv_{\text{ice}}(t)+ \\ \qquad 0.12887\dfrac{K}{T_{\text{exp}}} \exp\left[2.6554 - \dfrac{725.31}{T_{\text{exp}}} + 11604.967\dfrac{\beta x_{s,0}(1-v_{\text{ice}}(t))}{T_{\text{exp}}(1-v_{\text{ice}}(t_0))}\right]\left(\dfrac{\langle R_i(t)\rangle}{\langle R(t)^2\rangle} - \dfrac{1}{R_i(t)}\right). \end{cases} \tag{7.26}$$

The initial conditions given in (7.24) can be approximated by

$$\begin{cases} v_{\text{ice}}(t_0) = 1 - 4370.4\dfrac{\beta x_{s,0}}{(273.15 - T_{\text{exp}})}, \\ R_i(t_0) \text{ estimated from experiments.} \end{cases} \tag{7.27}$$

The rest of the input parameters have to be given in the following units: T_{exp} (K), K (μm s^{-1}), V_0 (μm^3), β (eV μm^3 mg^{-1} per molecule) $x_{s,0}$ (mg μm^{-3}) and $R_i(0)$ (μm), for all i.

7.4.2 Numerical approximation

The numerical model was implemented in Fortran using a first-order explicit Euler scheme. The estimation of parameters described in Section 7.4.1 was used in the numerical algorithm. Time was discretised from the initial time, t_0, to final time, t_{f}, using a step $\mathrm{d}t$. The numerical scheme was initiated using (7.27) and at a given time t, if we know $v_{\text{ice}}(t)$ and $R_i(t)$ we calculate those values at the following time step as

$$\begin{cases} v_{\text{ice}}(t+\mathrm{d}t) = v_{\text{ice}}(t) + \mathrm{d}t \cdot C_{v_{\text{ice}}}(t) \\ R_i(t+\mathrm{d}t) = R_i(t) + \mathrm{d}t \cdot C_{R_i}(t), \end{cases} \tag{7.28}$$

with $C_{v_{\text{ice}}}(t)$ and $C_{R_i}(t)$ given by (7.26).

In an analogous way to [9], when particle radius decreases below a certain threshold, R_{thr}, the particle is declared as evaporated in our model, with its residual content being transferred to other particles in proportion to their surface area. For our simulations we have considered $R_{\text{thr}} = 0.01$ μm.

7.5 Numerical experiments

We set up two different numerical experiments to validate our model. For the first one we used experimental data from [30]. In this work they use a salty water solution as a food model. Because our model was designed specifically for salty water, we will see that the experimental data fits very well. The second model validation was done using ice-cream as our food model and was based on the published work [23]. Even though ice cream is a much more complex system that salty water, we tried to adjust our model to this case, and we see reasonable agreement.

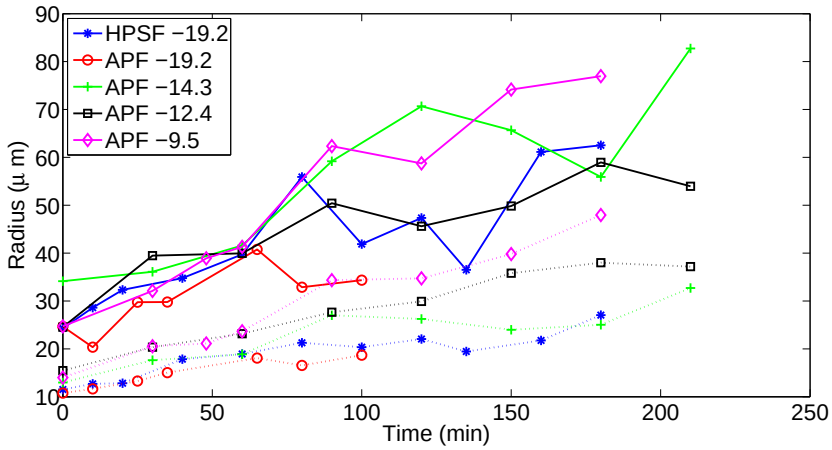

Figure 7.2: Mean (dotted lines) and maximum (solid lines) experimental ice particle radius values for salty water data

7.5.1 Salty water food model

Following [30], a 1.86N NaCl solution is used as a food model solution. The authors selected this concentration so that at -19.2°C, the temperature at which HPSF recrystallisation behavior takes place, the frozen fraction was approximately 50%. The samples were then introduced into the chamber for HPSF or atmospheric pressure immersion freezing. The HPSF samples were pressurised to 210 MPa and cooled down to -20 °C. Once equilibrium was reached, pressure was quickly released, inducing nucleation. The rest of the freezing process was completed at atmospheric pressure. Freezing at atmospheric pressure (APF) was done by immersion in silicone oil inside the vessel kept at -20°C.

Once the samples were frozen they were placed in the chamber for observations to be carried out with a microscope. Temperature was raised from -19.2°C, the lower attained at the chamber, to the target experimental temperature and kept constant for a period of 3 h to study recrystallisation phenomena. The authors consider this time period long enough to represent the more intense phase of the recrystallisation process. These target experimental temperatures were -19.2°C for comparison of HPSF and APF frozen samples (which we will refer to as HPSF-19.2 and APF -19.2) and -14.3°C, -12.4°C, -9.5°C (which will be referred to as APF -14.3, APF -12.4 and APF -9.5, respectively) for system temperature dependence study. The evolution of the ice crystals during this period was followed by the micrographs that were automatically taken every 30 minutes. An image analysis software was used to detect crystal boundaries from the micrographs, and from this a diameter for each crystal was determined.

Discrete experimental data

The data we have available are the diameters of the crystals at each time step. Figure 7.2 shows the maximum and mean radius evolution for each of the experiments. We would like to remark that the maximum radii data is not very reliable, as it should be a monotonic increasing function over time, and as can be seen for some cases it is not. We think this is due to the fact that in the experimental observations a very small sample was analyzed (due to the limitations of the equipment, given the complexity of performing these kind of observations without alteration of the ice fraction and crystal size distribution, as pointed out in [30]), which meant that on average there were 150-200 initial crystals, not enough to get more accurate results. The mean radii evolution, however, looks more reliable.

To simulate these same experiments with our model, we know from Section 7.4.1 that the input parameters needed are V_0, $R_i(t_0)$, T_{exp}, K, β and $x_{s,0}$. From the experimental data we have $R_i(t_0)$ (in μm), and T_{exp} we take as -19.2°C=253.95 K, temperature at which we know, from [30], the frozen fraction of the solution was approximately 51%. V_0 (μm^3) is the initial volume of the sample, which we work out for each case in the

following way: we assume that the initial amount of frozen ice is 16% and that the final amount of frozen ice is approximately 51% (i.e. for each experiment there is a total ice fraction of 0.51 and a dissolved ice fraction of 0.35); we can choose the number of particles we want the system to have and then we fit the total volume so these amounts of ice are obtained (obvioulsy, because we are calculating a volume, this depends also on the initial radii distribution). For each experiment the number of particles, and hence volumes, were different, and will be pointed out separately in each graph. The initial salt mass concentration, $x_{s,0}$, was calculated using the fact that we are working with a 1.86 N NaCl solution. By converting normality to solute mass concentration in the relevant units, we get $x_{s,0} = 1.0881 \cdot 10^{-10}$ mg μm^{-3}. Finally, K and β are model fitting parameters. For all of the salty water experiments we take $K = 1$ μm s^{-1} and $\beta = 2.757 \cdot 10^{7}$ eV μm^4 mg^{-1} molecule^{-1}.

Let us see, for the case under study, if inequality (7.19) holds. As $k \approx 8.617$ x 10^{-5} (eV K^{-1}), $T_{\text{exp}} = 253.95$ (K), $\gamma \approx 1.5605$ x 10^5 (eV μm^{-2}) and $\nu_{\text{ice}} \approx 0.03263$ 10^{-9} (μm^3), we have that for (7.19) to hold, necessarily,

$$R_i >> \frac{2\gamma\nu_{\text{ice}}}{kT_{\text{exp}}} = 4.6538 \text{ x } 10^{-4} \ \mu\text{m}, \ \forall i,$$

which is true given that all particles in the model have a larger radius than the threshold one (otherwise they disappear) and $R_{\text{thr}} = 0.01$ μm.

As mentioned previously, the experimental data was measured for 3 h and we have the radii of the crystals every 30 minutes. With our model we can run it for much longer times, which we believe will give a better idea of the long term behaviour of the ice crystal coarsening. Actually the authors in [30] also point this out, by saying that the ice crystal size distribution attained after much longer storage times would be drastically different for both models. Our model also predicts crystal size distribution at a given time. To start our model we extracted the initial experimental crystal size distribution, which is the input parameter $R_i(t_0)$. In what follows, for all the above mentioned experiments, we plot the average and maximum radius evolution over time of the simulation and experimental results to see how well they match. For the salty water model, we do not plot the distributions, given that they do not match well to the experimental ones. This is due to the fact that the experimental distributions are discrete (not enough data), and the model predicts continuous distributions, hence the non matching.

Figures 7.3a and 7.3b show the simulated and experimental radius evolution over time for HPSF -19.2 and the APF -19.2 processes, respectively. For both cases the simulated average radius matches the experimental average radius very well, and as can be seen we let the simulated radius evolve for longer than 3 h. The maximum radius is not that good at every point, but the experimental data is not that reliable. If we want to compare the long term behaviour of the sample frozen using HPSF and the one with APF, we can see that they are very similar, which agrees with what was reported in [30]. We can see that the simulated radii evolution curves are not smooth, especially near the end; this again is due to the discreteness of the initial data.

Figures 7.4a, 7.4b and 7.4c show the simulated and experimental radius evolution over time for the APF -14.3, APF -12.4 and the APF -9.5 processes. Again we can see the very good agreement for experimental and simulated average radii evolution over time.

Continuous experimental data

To test the validity of our model for predicting ice crystal size distributions at a given time, we designed a new set of data from experiment APF -12.4 described in Section 7.5.1. We created a continuous initial distribution from the experimental discrete initial one. To do so we calculated the mean value and standard deviation of the discrete data, and used these values to create a continuous distributions, assuming it followed a normal distribution. The initial radii distribution was then extracted from this normal distribution, by taking the same radii sizes as in the discrete case, but changing the frequency from the discrete ones to the continuous ones. In this way, as we are using a continuous initial distribution as an input for the model, we will be able to predict continuous distributions for different time steps (see Figure 7.5a) . Figure 7.5 shows the distributions (7.5a) and the average and maximum simulated and experimental radius evolution over time (7.5b). Again the average radii match very well. As can be seen the simulated radii curves are now much smoother than in the discrete case (see Figure 7.4b). The simulated distributions are now very smooth too. If we had more available experimental data, and hence continuous distributions, these simulated distributions could be compared to the

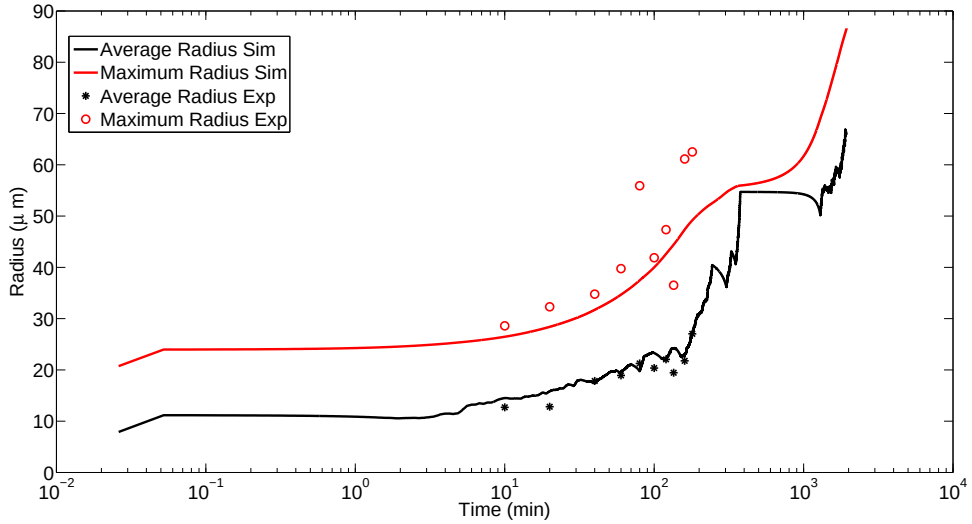

(a) HPSF -19.2. (Number of particles=8000; $V_0 = 1.05$ x 10^8 μm^3)

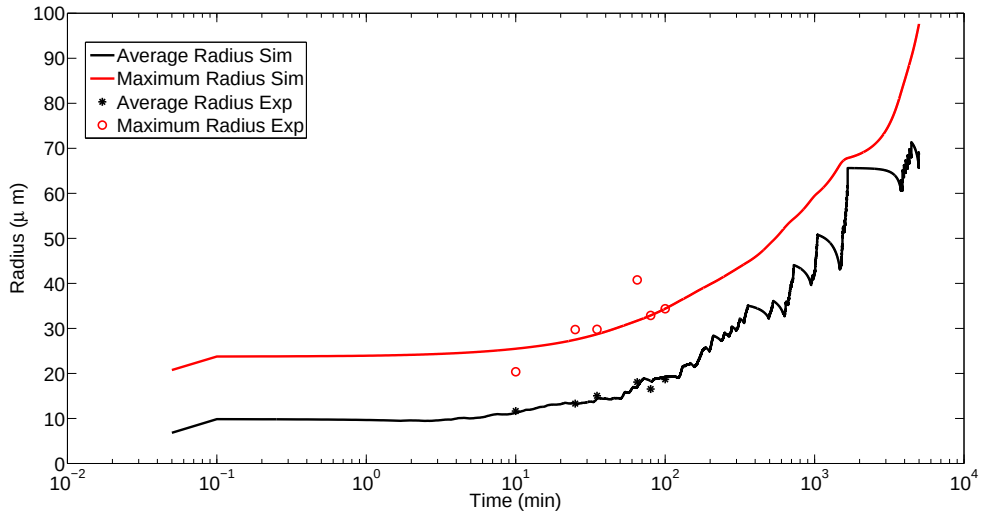

(b) APF -19.2 (Number of particles=5000; $V_0 = 4.8$ x 10^7 μm^3)

Figure 7.3: Experimental and simulated average and maximum ice particle radius evolution (in logarithmic scale) for salty water experiment

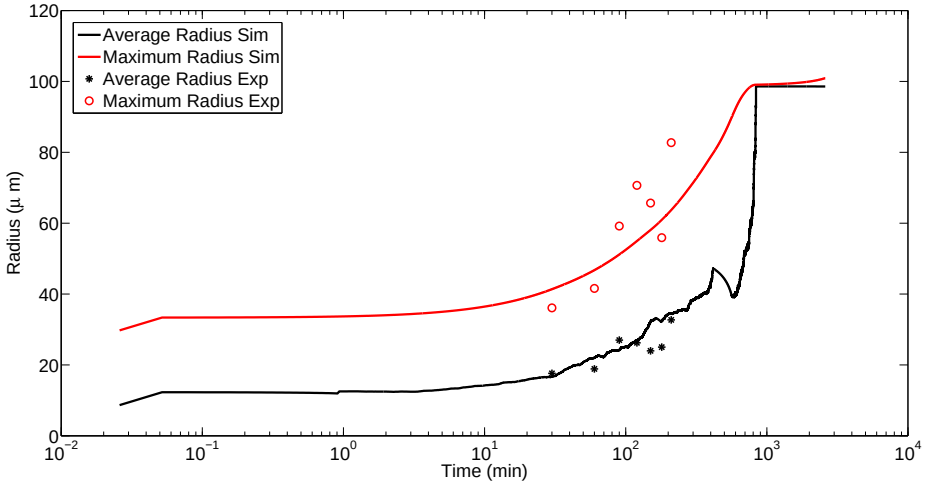

(a) APF -14.3 (Number of particles=10000; $V_0 = 1.8$ x 10^8 μm^3)

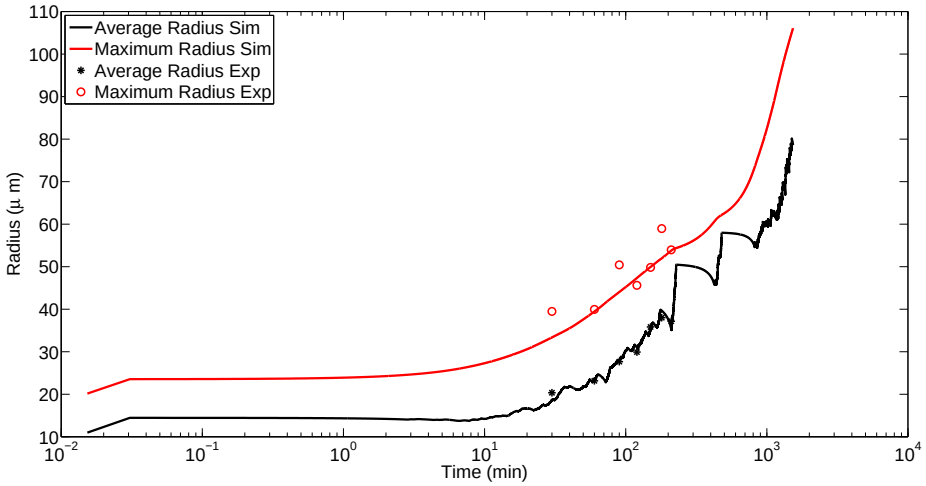

(b) APF -12.4 (Number of particles=5000; $V_0 = 1.05$ x 10^8 μm^3)

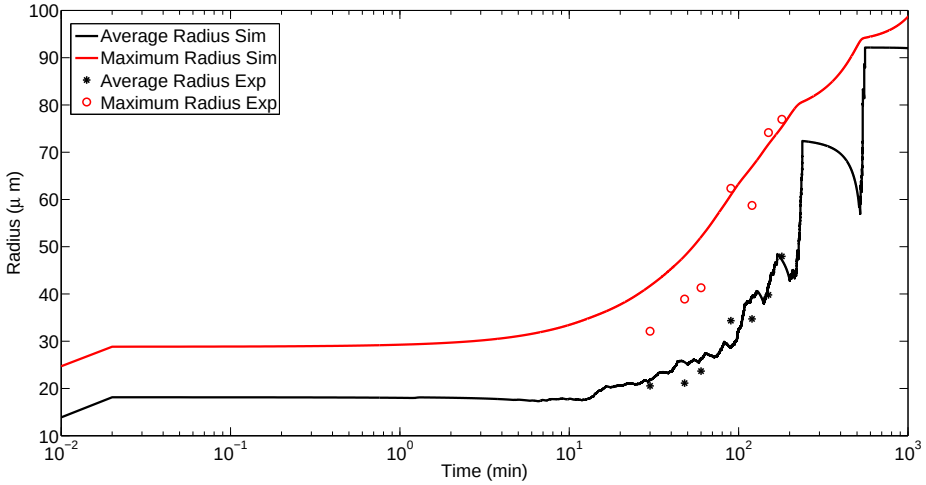

(c) APF -9.5 (Number of particles=10000; $V_0 = 4$ x 10^8 μm^3)

Figure 7.4: Experimental and simulated average and maximum ice particle radius evolution (in logarithmic scale) for salty water experiment

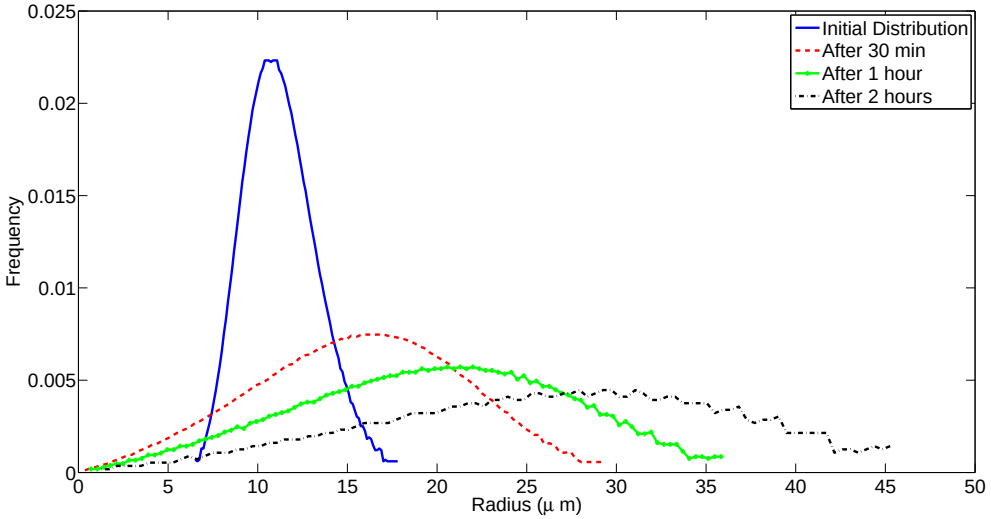

(a) Ice particle distributions

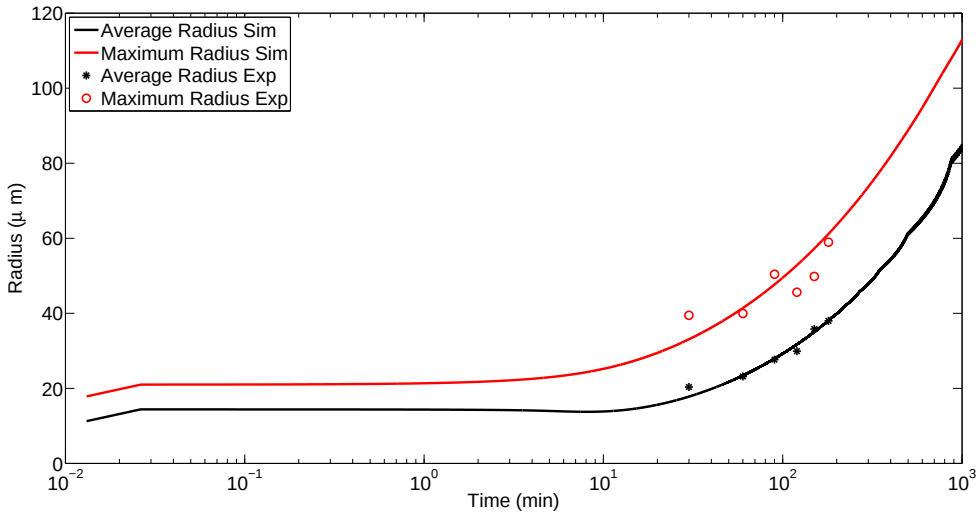

(b) Ice particle radius evolution (in logarithmic scale)

Figure 7.5: APF $-12.4°$C Continuous model (Number of particles=12000; $V_0 = 2.2$ x 10^8 μm^3)

experimental ones.

7.5.2 Ice-cream food model

Following [23] our second numerical experiment uses ice-cream as a food model. As previously stated, ice-cream is a much more complex system than salty water, but we still want to try our model with ice-cream to see if it can be fitted. In [23] a methodology to characterise the ice crystal size distribution was developed and several ice-cream and ice milk formulations were analyzed to test the methodology. A refrigerated glove box was constructed to allow temperature control of the sample during preparation and viewing. This glove box allowed samples to be analyzed at any temperature down to -20°C and permitted analysis of samples directly drawn from an ice-cream freezer. Once the frozen ice-cream samples were ready (at the right temperature) they were placed in the glove box and left there for enough time to equilibrate to the glove box temperature [23]. Afterwards the sample was viewed using conventional brightfield light microscopy, and then size measurements of the ice crystals were made directly from photomicrographic prints.

Several ice-cream and ice milk formulations varying in total solids level were prepared in [23]. We use the 40% total solids (TS) ice-cream formulation, for no more particular reason than for this formulation a plot of the distributions at different time steps was given in the cited paper, and we will use it to compare our simulated results to. Samples were frozen, then drawn from the freezer and hardened for 24 h, and finally stored in a storage freezer for several weeks. Samples were analyzed for crystal size immediately after drawing from the freezer (the glove box temperature was set to the draw temperature, -7.3 ± 0.3°C); after hardening (at -14°C) and after 7 and 14 weeks of storage (also at -14°C).

To set up the numerical experimental for our model from this data we make the following assumptions: we take $T_{\text{exp}} = -14$°C=259.15 K, which is the temperature at which all the measurements were done, except for the first one, immediately after drawing from the freezer. Because of the differences in temperature between the drawing and hardening stages, a significant increase in ice crystal size was observed, as pointed out in [23]. Our model does not account for differences in temperature, so we assume that the temperature is constant throughout the whole experiment ($T_{\text{exp}} = -14$°C), but we will see that our results are still good enough given that the model does account for growth. We take the initial radii distribution, $R_i(t_0)$, from Figure 4 in [23] (we extrapolate some points from the published curve and then create a histogram using those points, which we use as an initial distribution for our code). We assume that the initial amount of ice formed after drawing is approximately 25% and that the dissolved ice concentration is the same amount, which gives a total ice fraction of 50%. As we want smooth distributions we consider quite a large number of particles, 4500, and therefore the system volume is taken as $1.2{\cdot}10^9$ μm^3, to get the correct ice fractions. In this case we do not have a value for the $x_{s,0}$ from the experimental data, as we are no longer working with salty water but with ice-cream instead, which has many more components. This means that we now have three fitting parameters, β, $x_{s,0}$ and K. However, if we note that in system (7.25)-(7.27), β and $x_{s,0}$ always appear as $\beta x_{s,0}$ (never separate) we can write the multiplication of both as one fitting parameter. Thus, we consider $\beta x_{s,0} = 0.0024$ eV molecule^{-1}, which is very close to the value used for the salty water $\beta x_{s,0} = 0.003$ eV molecule^{-1}. For K we stick to the same value as for the salty water experiments, i.e. $K = 1$ μm s^{-1}.

Again for this case, inequality (7.19) holds. The only parameters that has changed with respect to the salty-water model is T_{exp} which is now 259.15 K, leading to

$$R_i >> 4.5604 \text{ x } 10^{-4} \ \mu\text{m}, \ \forall i,$$

which is true given $R_{\text{thr}} = 0.01$ μm.

Figure 7.6 shows the simulated (lines) and experimental (lines with symbols) distributions (7.6a) and the average and maximum simulated and experimental radius evolution over time (7.6b). The model distribution prediction agrees well with the experimental distributions, except after 14 weeks when the experimental crystals have stopped coarsening (the 7 weeks and 14 weeks distributions are practically the same), whereas the simulated ones continue to coarsen. We think that this is due to the fact that ice-cream contains fat and emulsifiers which provide a mechanical obstruction to crystal growth (see [23]), something that our model does not take into account. For example, the possibility of using temperatures changing with time during the process or the

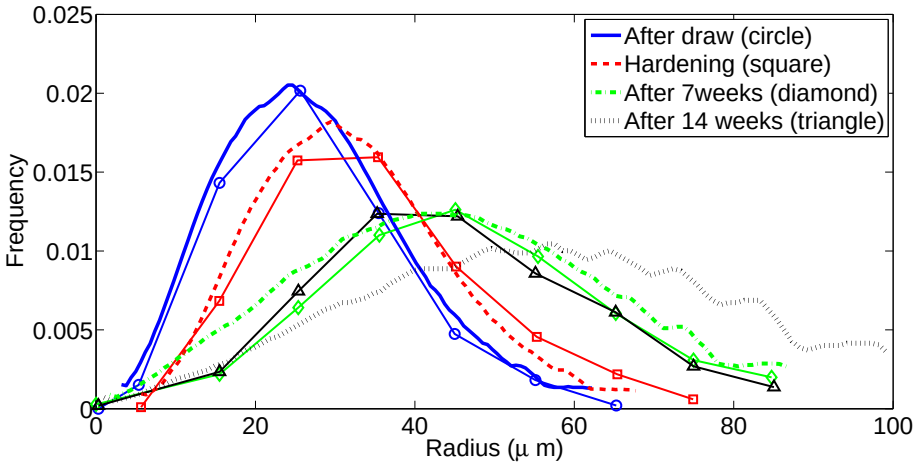

(a) Simulated (lines) and experimental (lines with symbols) ice particle distributions

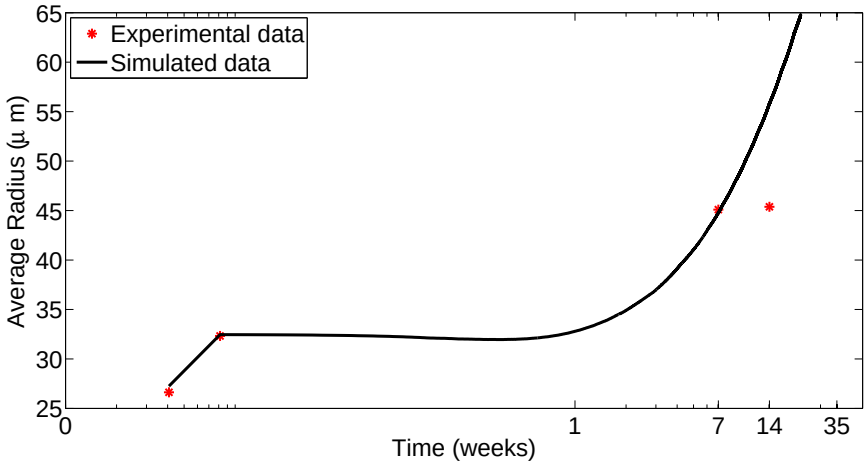

(b) Ice particle radius evolution (in logarithmic scale)

Figure 7.6: Ice-cream model

inclusion of mechanisms avoiding crystal growth (such as the fat and emulsifiers mentioned above) are some of the new features that could be added to the model.

7.6 Conclusions

We have developed a very simple model that studies growth and coarsening of ice crystals, and validated it for two different food similes: salty water and ice-cream. The results have shown that the model is accurate enough to predict correctly average radial evolution for all cases, and crystal size distribution, if the initial data is continuous. Further improvements to the model could be to include more components into the systems, and therefore use it for more complex foods. For example, the possibility of using temperatures that change with time throughout the process, or the inclusion of mechanisms avoiding crystal growth (such as the fat and emulsifiers mentioned above) are new features that could also be added to the model.

Chapter 8

Conclusions and future work

In this thesis we have described, modelled and analysed several problems related to High-Pressure processes in Food Engineering. There is a very wide range of problems that can be studied in this field, depending on factors such as the type of food, the size and geometry of the High-Pressure vessel, and the desired effects of the process. In particular, in this thesis we have concentrated on problems concerning large and small, solid- and liquid-type foods, vertically and horizontally oriented machines. Also, High-Pressure freezing processes and the growth and coarsening of ice crystals inside a frozen food sample have been studied.

One of the main goals of food processing is the inactivation of microorganisms and enzymes, to ensure food is safe and of good quality for the consumer to eat. In Chapter 2 we presented a bacterial inactivation model (which can also be used for enzymatic inactivation), and gave an example, using experimental data, of how the kinetic parameters can be identified. It was made clear that once these are identified, in order to calculate the final bacterial count (or final enzymatic activity) inside a food sample, the temperature and pressure distribution has to be known, and then both models should be coupled. The pressure profile is known a priori in these type of processes (it can be chosen by the user), but the temperature distribution changes with time and space, and therefore heat transfer models for predicting temperature profiles are necessary. Developing such models has been the purpose of this thesis.

Heat transfer models for predicting temperature profiles inside a large solid-type food were presented in Chapter 4, and several two- and one-dimensional simplified versions of these models were given, after performing dimensional analysis. These simplified models provide a good approximation of the full model, but are not as complex and need less computational time. Also, the solutions given do not require the use of a "black-box" FEM solver and our approximations allow us to qualitatively describe the physical features involved. It has been shown that for the case of a tall and narrow High-Pressure machine, the temperature profile inside the food is very well approximated by a one-dimensional model, except at points very close to the top and bottom boundaries. Furthermore, the solutions of the one-dimensional heat transfer models have been used to calculate the final enzymatic activity, also achieving very similar results to those found when the temperature of the two-dimensional models are used. This has great advantages for other problems that arise in the High-Pressure processing context (which could be possible future work), such as optimisation procedures for equipment design and identification of pressure and temperature dependent thermo-physical parameters of these processes, by means of solving inverse problems.

In Chapter 5, we discussed processes that take place in vertically and horizontally oriented High-Pressure machines for liquid-type foods. To the best of our knowledge, to date, horizontal vessels have not been modelled, but are of great relevance for the food industry, given most industrial-scale machines are horizontal. The computational complexity of these models is very high, as they have to be solved in three dimensions. We compared a vertical and horizontal model with exactly the same process conditions, highlighting the important differences arising between the two models. These include modifications to the temperature distribution and flow field of the fluid. In particular, for a liquid-type food (in this work we have considered water), for the vertical model temperatures change with height, whilst for the horizontal model they change more radially. Therefore, for a long and thin machine we have shown that the temperature in general is more uniform for the

horizontal case, for the processes we have discussed. With the work done in this Chapter 5 we are now able to present an accurate horizontal representation, from which experimentalist can benefit.

Models for a High-Pressure shift freezing process for large and small solid-type foods were given in Chapter 6. The model for solidification is based on the enthalpy formulation at non-constant pressure and volume phase fractions. The model describes the temperature profiles throughout the process and can predict the plateau times, which are both relevant parameters for food experimentalists. Without using any fitting parameters, the simulated results for the numerical tests we performed agreed very well with the experimental data for the small sample case, especially at the centre of the sample. At the surface there is not an accurate match between the data and the model. However, we considered the modelling approach to be sufficient, given the relatively large experimental errors. For the large sample case there is no experimental data to plot against the simulated temperature profile, but when comparing the model plateau times to the published experimental ones, we find that they are in general shorter, but in the range of the latter. In all cases, the prediction errors are on the order of minutes, which is reasonable given that the processing time is on the order of hours.

The development of a model for growth and coarsening of ice crystals, presented in Chapter 7, was motivated by studies of recrystallisation of frozen food samples. Food engineers want to ensure high quality of products after long term storage. The model presented is valid for food samples which have been frozen using High-Pressure Shift Freezing or conventional freezing, assuming that initially the ice particles are homogeneously distributed and have the same size and shape. The model was solved numerically and validated for two different food similes: salty water and ice-cream. We showed that the model is accurate enough to correctly predict the average radial evolution and crystal size distribution. Future work could be to include more components into the systems, and therefore use it for more complex foods, to introduce non-constant temperatures or to include mechanisms avoiding crystal growth.

Throughout this thesis we have covered a wide range of problems related to Food Engineering, using a large variety of mathematical techniques in the process. Nevertheless, there is still a large amount of problems that can be solved in this area. For example, in Chapters 4, 5 and 6, the models could be further developed so they are all valid for any type of food sample (i.e. large or small, solid or liquid), and the resulting temperature distributions from these models could be coupled with the enzymatic or bacterial inactivation models presented in Chapter 2, as was briefly highlighted in Chapter 4. Other improvements could potentially be obtained by including the temperature and pressure dependence of material properties in all of the heat transfer models presented. Also, in Chapter 6, anisotropy effects could be included in the frozen region, and our two-dimensional convection simulations extended to three-dimensions. As mentioned above, possible improvements to the model presented in Chapter 7 could be to include more components into the systems, and therefore use it for more complex foods. The previously listed examples of future work, together with those mentioned in each Chapter individually, are just some of the possible extensions.

Chapter 9

Summary in English

Introduction and goals of the thesis

There has been significant interest in the study of food engineering from the mid-twentieth century onwards [12, 13, 31, 43, 53, 63, 71, 74, 80, 82, 92]. Humans have been interested in food conservation since ancient times, using traditional techniques such as desiccation, conservation in oil, salting, smoking, cooling, etc. Due to the massive movement of populations to cities, a great supply of food in adequate conditions was necessary. Therefore, the food industry was developed in order to guarantee large-scale food techniques, to prolong its shelf life, and to make logistic aspects such as transport, distribution and storage, easier. Nowadays, the food industry is an increasingly competitive and dynamic arena, given that consumers are now more aware of what they eat. Food quality properties, such as taste, texture, appearance, and nutritional content are strongly dependent on the way the foods are processed.

Many classical industrial processes are based on thermal treatments, such as, for example, pasteurisation, sterilisation and freezing. In recent years, with the aim to improve these conventional processing technologies, in order to deliver higher-quality and better food products for the consumers, a number of innovative technologies, also referred to as "emerging" or "novel" technologies have been proposed, investigated, developed, and in some cases, implemented. These "emerging" technologies take advantage of other physics phenomena such as high hydrostatic pressure, electric and electromagnetic fields, and pressure waves. With these innovative technologies food engineers can not only develop new food products, but also improve the safety and quality of conventionally treated food through milder processing [53].

In particular, in this thesis we have focused on one of these new emerging technologies, High Pressure Processing (HPP) of food. The appearance of HPP as a tool in the food industry started in the late 1980s [41]. Since then to date, extensive research has been done on possible application of HPP as a preservation method [12, 28], to change the physical and functional properties of food systems [11, 41] and to take advantage of the phase diagram of water: freezing, thawing and sub-zero temperature non-frozen storage under pressure [68, 71].

Several studies [12, 13, 82] have proved that HPP allows inactivation of enzymes and pathogenic and spoilage microorganisms in food, while leaving small molecules intact, and therefore not modifying significantly the organoleptic properties (such as colour, odour, texture and flavour).

Two principles underlie the effect of High Pressure (HP): firstly, the Le Chatelier Principle, according to which any phenomenon (phase transition, chemical reaction, chemical reactivity, change in molecular configuration) accompanied by a decrease in volume will be enhanced by pressure; secondly, pressure is instantaneously and uniformly transmitted independently of the size and the geometry of the food (isostatic pressure).

Therefore, unlike thermal processing, HP effects are uniform and nearly instantaneous throughout the food and thus independent of food geometry and equipment size. However, HPP does not escape the classical limitations, imposed by heat transfer. Heat transfer characterises every process, accompanied by a period of pressure increase or decrease, which is associated with a proportional temperature change of the vessel's contents due

to adiabatic heating. The magnitude of the adiabatic temperature increase or decrease depends on a number of factors, such as the food product thermo-physical properties (density, thermal expansion coefficient, and specific heat capacity) and initial temperature. Heat transfer is caused by the resulting temperature gradients and can lead to large temperature differences, especially in large-volume industrial vessels. For a number of HP applications to food engineering, these limitations should be taken into account, trying to avoid as much as possible, non-uniformity at the end of the process.

Therefore, an accurate evaluation of the effects of pressure, applied during conventional batch HPP, requires the knowledge of the non-uniform temperature distribution inside the sample. With this in mind, equations describing the time-temperature-pressure history of a product must be coupled with the parameters describing the reaction kinetics for destruction of microorganisms, enzymes, and other factors. The optimisation of batch HP processes for nutrient retention should also be based on this approach.

Mathematical modelling is a very useful tool for characterising this temperature distribution. Normally, it is the fastest and least expensive way, given that it minimises the number of experiments that need to be conducted to determine the influence of several parameters on the quality and safety of the process. Depending on the characteristics of the process, the type of food (liquid or solid), the dimensions of the HP vessel, the process conditions (initial temperature, maximum pressure, etc.), different mathematical models are used. For example, for a large (when comparing with the pressurising volume) solid-type food a heat transfer model with only conduction effects is sufficient [46, 69], whereas for a liquid-type food, convection effects have to also be included, and therefore equations that model the fluid flow also have to be coupled with the heat transfer equation. If we are studying HP freezing processes, a model that takes into account solidification also has to be considered. In some cases, the expression of the process outcome based on the attributes of the processed food, that is, e.g. the remaining microbial load, enzyme activity, and chemical reaction products, is required. Within multiphysics modelling, reaction kinetics (i.e., microbial inactivation, quality degradation, chemical reaction, and structural responses) can be coupled with the specific differential equations to provide the spatial distributions of reaction response.

Even though there has already been a significant amount of research in this area, there are still many situations that arise in HPP that have not been modelled. Therefore, throughout this thesis we have considered different types of HP processes, trying to cover as many situations as possible when working with HP food processing, presenting innovative models. Namely, models for large and small, solid and liquid type foods, for vertically and horizontally oriented machines, and also for HP freezing processes are analysed. We have developed the corresponding model for each case, solving each one accordingly.

In Chapter 2 we first start by presenting a model for bacterial and enzymatic inactivation, hence showing the necessity for knowing the temperature distribution throughout a HP process. A case study of one particular bacteria, for which experimental data is available, is modelled and validated.

In Chapter 3 we present the general aspects of the heat and mass transfer models for HP processes developed in [46, 69]. The new models we derived in Chapters 4, 5 and 6 are based on this one, and thus we decided to include this model-presentation chapter to avoid having to introduce the same model in each of the later ones.

In Chapter 4 we introduce one of the most basic type of model for time-temperature-pressure evolution, considering large samples of solid-type foods in a vertically oriented machine. With these, only conduction effects have to be included in the heat transfer model, which makes its resolution easier, and in some cases may even be possible to solve analytically. For vertically oriented machines, a reduction from three to two dimensions is possible due to the axis-symmetric geometry. Thus, in Chapter 4 several two dimensional models, with different kind of boundary conditions, are solved analytically and then compared to simplified versions. Also, some of the heat transfer models considered in this Chapter are coupled with an enzymatic inactivation model, showing how this coupling can be done. To date most of the published heat transfer models for solid-type foods had been solved numerically and not analytically.

In Chapter 5 a more complex problem is discussed. We consider liquid-type foods, for which convection effects also have to be included into the heat transfer model. Therefore, the equations for fluid flow (Navier–Stokes equations) have to be also solved. Due to the complexity, analytical solutions are no longer available and the model has to be solved numerically. An added complication to the problem in this Chapter is that we model processes and liquid-type foods placed in both vertically and horizontally oriented HP vessels. For the vertically

oriented HP vessel we could reduce it to two dimensions, due to the axis-symmetry. However for the horizontally oriented, there are no longer axis-symmetric features and a three dimensional model is necessary, adding an extra challenge to the numerical model. The differences between models have been analysed. Developing a model for a horizontally oriented HP vessel is interesting from an industrial point of view, as most of the industrial-scale vessels are in that position [63]. However, at a pilot-scale, they are vertically oriented and therefore most of the published research has been focused on these kind of machines, and the models are usually solved in two dimensions.

In Chapter 6 a freezing process that benefits from HP, namely a High-Pressure Shift Freezing (HPSF) process, is described, modelled and solved numerically. Modelling conventional solidification problems is not an easy task, and a lot of interest and research has been put into this area. HP freezing problems, however, have not been as studied, and in this Chapter we present a generalised enthalpy model for a HPSF process. The model can be used for large (when compared to the pressurising fluid volume) solid-type food (only conduction effects included) and also for small (when compared to the pressurising fluid volume) solid-type food (where the significant heat transfer effects of convection in the pressurizing medium are accounted for by solving the Navier–Stokes equations). The model is run for several numerical tests, and good agreement with experimental data from the literature is found.

The analysis in Chapter 6 shows that HPSF is more beneficial for ice crystal size and shape than traditional (at atmospheric pressure) freezing. This motivates the work in Chapter 7, which differs from previous Chapters as we do not solve a model to find the temperature distribution inside a food sample undergoing a HP process. A model for growth and coarsening of ice crystals inside a frozen food sample is developed and some numerical experiments are given, with which the model is validated by using experimental data. To the best of our knowledge this is the first model suited for freezing crystallisation in the context of HP.

Main contributions of the thesis

The most important results and contributions of this thesis can be found in Chapters 4, 5, 6 and 7. As said above, Chapter 2 is for motivation of the rest of the problems of the thesis, and in Chapter 3 the general heat transfer model used further along on is given.

The heat transfer models presented in Chapter 4 are valid for predicting temperature profiles inside a large solid-type food undergoing HP treatment. Two different kinds of boundary conditions have been considered depending on whether only the food holder is taken into account, or whether the surrounding steel is included. We perform a dimensional analysis which highlights the dominant terms in the model, and shows that in some cases the equations can be simplified (in dimension) and yet provide a good approximation. These models for HP processes are much simpler than those found in the literature, but still have the correct qualitative features. Using the solutions we propose, there is no need to have an FEM solver in order to simulate the process. We have given a thorough analysis describing an exact 2D solution as well as several simplifications in both 2D and 1D. It has been shown that for the case of a tall and narrow HP machine, the temperature profile inside the food is very well approximated by a 1D model, except at points very close to the top and bottom boundaries. For the first class boundary conditions, the solutions of the 1D heat transfer models have been used to calculate the final enzymatic activity, also achieving very similar results to when the temperature of the 2D models are used. The reduction to 1D is very useful from a computational point of view, since faster simulations can be carried out. This is interesting, for instance, when performing optimisation algorithms, where very often the state equations need to be solved many times. In addition, the simplified model can help to calculate thermo-physical properties as a function of pressure, via inverse problems, which is an increasing need nowadays for food technologists. From an experimental point of view, results can also be used to determine where to place the thermocouples inside the food sample in order to measure the temperature experimentally.

In Chapter 5 we consider liquid-type foods, for which convection effects also have to be included into the heat transfer model. Due to the complexity of solving Navier-Stokes equations, we know that analytical solutions are no longer available and the model will have to be solved numerically. Several authors have done extensive research in developing models to predict transient temperature and flow distributions, but to the best of our knowledge, all of the models developed and published to date on prediction of temperature and flow distribution

of a HPP, are based on vertically oriented high pressure units. This is because the original HPP equipment units were vertical. However, the current trend is to supply horizontal units at industrial scale. Because of this increase of horizontal units in the industry, but yet the lack of published work on horizontal models, we decided it would be interesting to begin to cover this research gap. Nowadays, most of the experimental data available from researchers is for HP processes which have taken place in a vertical unit, due to the fact that laboratory or pilot-scale units are mostly vertical. We did not have the experimental resources to be able to setup a horizontal laboratory-scale unit to obtain experimental data. Therefore, designing a horizontal model from scratch was not plausible at this point. Instead, we decided to develop a horizontal model by adapting an existing vertical one, which had previously been validated. In this way, what we can show are the differences between the vertical and horizontal models, stating the research need for developing horizontal models, which would be very helpful for the industry. It is clear that the major reason why the vertical and horizontal models are different, even if they have exactly the same process conditions, is due to the fluid flow pattern, which we know that for the case of a liquid-type food has a significant influence on homogeneity of the final pressurised product. The results of the numerical simulations show that, as expected, the temperature performance and uniformity is different for both geometries, mainly due to the differences in the flow. For a liquid-type food (in this work we have considered water) and for a long and thin machine we have shown that the temperature in general is more uniform for the horizontal case, for the processes we have discussed. For the vertical model temperatures change along height, whilst for the horizontal model they change more radially.

In a High-Pressure Shift Freezing (HPSF) process, like the one described in Chapter 6, phase transition occurs due to a pressure change that promotes metastable conditions and instantaneous ice production. On expansion, pressure release occurs instantaneously throughout the product (Pascal principle), and subsequently, its temperature decreases. Large-scale supercooling takes place throughout the sample, which implies high ice nucleation velocities. Different authors have proved experimentally that ice nucleation occurs homogeneously throughout the whole volume of the product and not only on the surface, as they have found small granular shape ice crystals disperse throughout the resulting sample for several products. Due to the advantages of this method (mainly, its potential to improve the kinetics of the process and the characteristics of the ice crystals thus formed) compared to other freezing methods, some modelling studies considering the temperature evolution during treatment of HPSF processes have been published to date. This is important in all HP processes, and in particular in freezing processes. In Chapter 6 we introduce a new model based on the enthalpy formulation at non-constant pressure and volume phase fractions. The model is two dimensional axis-symmetric (many of the published ones are one dimensional), and is valid both large and small solid food samples. Convection effects in the pressurising fluid are considered for the small sample case (which is also a novelty when compared to published models). The numerical results agree with the experimental data very well and no fitting parameters were used in the simulations.

In Chapter 7 a model to study the growth and coarsening of ice particles in a frozen food sample is developed. We assume that initially the ice particles are homogeneously distributed and have the same spherical shape, which occurs with a HPSF frozen sample, our model is valid for any kind of freezing process and not only HPSF. This will allow us to compare the evolution of HPSF frozen samples to that of samples that have been classically frozen. We present a model that accounts for the growth and ripening of ice crystals in this simple system by developing a theory somewhat similar to "Ostwald ripening". The model predicts crystal size evolution with time, and also ice crystal size distribution. We validate it for two different food similes: salty water and ice-cream. The results have shown that the model is accurate enough to predict correctly average radial evolution for all cases, and crystal size distribution, if the initial data is continuous.

Conclusions

In this thesis we have described, modelled and analysed several problems related to High-Pressure processes in Food Engineering. There is a very wide range of problems that can be studied in this field, depending on factors such as the type of food, the size and geometry of the High-Pressure vessel, and the desired effects of the process. In particular, in this thesis we have concentrated on problems concerning large and small, solid- and liquid-type foods, vertically and horizontally oriented machines. Also, High-Pressure freezing processes and the growth and coarsening of ice crystals inside a frozen food sample have been studied.

Throughout this thesis we have covered a wide range of problems related to Food Engineering, using a large variety of mathematical techniques in the process. Nevertheless, there is still a large amount of problems that can be solved in this area. For example, in Chapters 4, 5 and 6, the models could be further developed so they are all valid for any type of food sample (i.e. large or small, solid or liquid), and the resulting temperature distributions from these models could be coupled with the enzymatic or bacterial inactivation models presented in Chapter 2, as was briefly highlighted in Chapter 4. Other improvements could potentially be obtained by including the temperature and pressure dependence of material properties in all of the heat transfer models presented. Also, in Chapter 6, anisotropy effects could be included in the frozen region, and our two-dimensional convection simulations extended to three-dimensions. Possible improvements to the model presented in Chapter 7 could be to include more components into the system, and therefore use it for more complex foods. The previously listed examples of future work, together with those mentioned in each Chapter individually, are just some of the possible extensions.

Chapter 10

Resumen en español

Introducción y objetivos de la tesis

Desde mediados del Siglo XX en adelante ha habido un gran interés en problemas relacionados con la industria alimentaria [12, 13, 31, 43, 53, 63, 71, 74, 80, 82, 92]. La conservación de alimentos ha sido importante para los humanos desde la antigüedad, cuando se utilizaban técnicas tradicionales como la desecación, el curado, la salazón, el encurtido, el ahumado, etc. La industria alimentaria se desarrolló cuando se produjo el desplazamiento masivo de la población al medio urbano, ya que era preciso contar con un suministro masivo de alimentos en condiciones de consumo adecuadas. De esta manera se pudo prolongar la vida útil de los alimentos, garantizar tratamientos a gran escala y mejorar aspectos logísticos como el transporte, la distribución y el almacenamiento.

Muchos de los métodos clásicos utilizados para la conservación de los alimentos consisten en la aplicación de tratamientos térmicos, como por ejemplo la pasteurización, esterilización y congelación. El problema de estos tratamientos es que pueden suponer una reducción importante de las propiedades organolépticas y nutricionales del alimento. Por ello, ya que hoy en día no sólo importa alargar la vida útil de los alimentos, sino que también se pretende que sean de buena calidad, se están desarrollando nuevas técnicas que se aprovechan de otros fenómenos físicos como por ejemplo las altas presiones, los campos eléctricos y electromagnéticos, y las ondas de presión. Con estas tecnologías novedosas, los ingenieros trabajando en este campo no sólo pueden mejorar la calidad de los alimentos tratados, sino que también pueden desarrollar nuevos productos [53].

En particular, en esta tesis, nos hemos centrado en estudiar una de estas tecnologías emergentes, los tratamientos a altas presiones. Éstos comenzaron a usarse como herramienta de la industria alimentaria a finales de los años 80 [41]. Desde entonces hasta el día de hoy, se han investigado las posibles aplicaciones de las altas presiones como una técnica de conservación [12, 28], el efecto que tienen sobre las propiedades físicas y funcionales de los alimentos [11, 41], y cómo se puede aprovechar el diagrama de fases del agua para la congelación, sublimación y almacenamiento a temperaturas bajo cero de alimentos no congelados bajo presión [68, 71].

Varios estudios [12, 13, 82] muestran que las altas presiones pueden inactivar enzimas y microorganismos, sin alterar sustancialmente las propiedades organolépticas del alimento, ya que la alta presión no afecta, al menos de forma significativa, a las moléculas pequeñas como las que proporcionan el sabor y las vitaminas.

Hay dos principios generales que son de gran interés cuando se habla de la aplicación de altas presiones: por una parte, el principio de Le Chatelier, según el cual el aumento de presión favorece (respectivamente, desfavorece) cualquier fenómeno (cambio de estado, reacción química, cambio en la estructura molecular, etc.) que esté acompañado de un descenso (respectivamente, aumento) de volumen; y por otra, el principio isostático, según el cual la presión se transmite de manera uniforme y quasi-instantánea a través de toda la muestra que esté bajo presión.

Por tanto, a diferencia de los procesos térmicos, los efectos de las altas presiones son uniformes e instantáneos en el alimento, con independencia de la geometría y el tamaño de éste. Aún así, los procesos de altas presiones tienen limitaciones que vienen impuestas por la transferencia de calor. En todo tratamiento con altas presiones, en el

que hay un incremento o descenso de presión, se genera un cambio proporcional en la temperatura dentro de la vasija de alta presión debido a la generación de calor adiabático. La magnitud de este cambio depende de varios factores, como las propiedades termofísicas del alimento (densidad, calor específico, coeficiente de expansión térmica) y la temperatura inicial del proceso. La transferencia de calor se produce debido a los gradientes térmicos resultantes y puede provocar grandes diferencias de temperatura dentro del alimento, especialmente en vasijas grandes de tamaño industrial. Para muchas aplicaciones de la ingeniería alimentaria es importante tener en cuenta estas limitaciones, dado que suele ser conveniente conseguir procesos lo más uniformes posibles.

Por esto, si se busca entender de manera precisa los efectos de la presión sobre un alimento que es tratado con altas presiones, hay que tener en cuenta que los procesos con altas presiones son dependientes no sólo de la presión, sino también de la temperatura, y conocer la distribución no uniforme de temperaturas que se genera durante el proceso. Es necesario estudiar las ecuaciones que describen la evolución de temperaturas y presión en función del tiempo, y posteriormente acoplarlas con, por ejemplo, los modelos cinéticos de inactivación de enzimas y microorganismos u otros factores que se quieran estudiar. También es importante conocer la distribución de temperaturas si se quiere optimizar los tratamientos de altas presiones.

La modelización matemática es una herramienta muy útil para hallar esta distribución de temperaturas, y normalmente es la manera más rápida y económica de hacerlo, ya que minimiza el número de experimentos que hay que llevar a cabo. Dependiendo de las características del proceso, el tipo de alimento (sólido o líquido), las dimensiones de la vasija de alta presión, las condiciones del proceso (temperatura inicial, presión máxima, etc.), el modelos matemático usado será distinto. Por ejemplo, para un alimento sólido grande (en comparación con la cantidad de líquido presurizante) un modelo de transferencia de calor por conducción es suficiente [46, 69], mientras que para un alimento líquido es necesario incluir también los efectos de la convección, acoplando por tanto la ecuación de transferencia de calor con las ecuaciones de Navier–Stokes. Si se estudiasen procesos de congelación por altas presiones, un modelo que tuviese en cuenta el fenómeno de solidificación sería necesario. En algunos casos, lo que se busca es un resultado del proceso como la actividad enzimática resultante o la cantidad final de microorganismos, y la modelización matemática también es útil para esto, ya que se pueden acoplar las ecuaciones de estas reacciones cinéticas con las de transferencia de calor, dando lugar a la distribución espacial de la reacción buscada.

Hasta la fecha, se ha llevado a cabo mucha investigación en este campo de modelización matemática, pero aún quedan muchos problemas por estudiar. El objetivo de esta tesis doctoral ha sido abordar la mayor cantidad de problemas posibles relacionados con procesos de alimentos tratados a altas presiones. En particular, se han desarrollado y resuelto modelos para alimentos grandes y pequeños, sólidos y líquidos, para máquinas orientadas vertical y horizontalmente, y también para procesos de congelación por altas presiones.

En el capítulo 2 se presenta un modelo de inactivación bacteriana, y se resuelve para un caso particular, queriendo hacer hincapié en la necesidad de conocer la distribución de temperaturas durante el proceso, y por tanto motivando el resto de los capítulos presentados en esta tesis.

El modelo de transferencia de calor y masa presentado en el capítulo 3, desarrollado por los autores en [46, 69], es la base para los modelos que se describen en los capítulos 4, 5 y 6, y por ello se presenta en un capítulo aparte, para poder hacer referencia a él y no tener que repetirlo por separado en cada capítulo posterior.

En el capítulo 4 se desarrolla un modelo de evolución temporal de la temperatura y la presión, para alimentos sólidos grandes tratados en una máquina colocada en posición vertical. Para éstos, como se muestra en el capítulo 3 sólo hay que incluir los efectos de la conducción en el modelo de transferencia de calor, lo cual hace más sencilla su resolución, y en algunos casos hasta se puede resolver analíticamente. Para máquinas posicionadas en vertical, gracias a la simetría axial, se puede reducir el modelo de tres a dos dimensiones. Teniendo esto en cuenta, en el capítulo 4 se desarrollan varios modelos bidimensionales, para diferentes tipos de condiciones de contorno, que se resuelven analíticamente y posteriormente se comparan con versiones simplificadas de los mismos. Mostramos que en algunos casos es posible reducir aún más el modelo de dos dimensiones a una. Además, algunos de los modelos presentados en este capítulo se acoplan con un modelo de inactivación enzimática. Hasta la fecha la gran mayoría de los modelos publicados de transferencia de calor para alimentos sólidos que son tratados con altas presiones se han resuelto numéricamente, pero no analíticamente.

En el capítulo 5 se estudia un modelo más complejo. Por una parte se consideran alimentos líquidos, y por tanto los efectos de la convección deben incluirse también en el modelo de transferencia de calor, por lo que

las ecuaciones de Navier–Stokes también se resuelven. Debido a la complejidad de este modelo, ya no pueden encontrarse soluciones analíticas, y el modelo debe resolverse numéricamente. Otra complicación añadida a este problema es que queremos modelizar procesos para alimentos líquidos en máquinas colocadas vertical y horizontalmente. Para las máquinas verticales, como hemos dicho antes, se podría reducir el modelo a dos dimensiones, pero para las horizontales esto no es posible, dado que ya no hay simetría axial, por lo que es necesario resolver un modelo tridimensional. Una vez resueltos se comparan las diferencias entre los modelos vertical y horizontal. El planteamiento de un modelo para una máquina de alta presión colocada en posición horizontal es muy interesante para la industria, ya que la gran mayoría de las máquinas industriales son horizontales [63]. Sin embargo, las máquinas piloto suelen ser verticales y por ello la mayor parte de la investigación llevada a cabo en este campo ha sido para máquinas de este tipo.

En el capítulo 6 hemos descrito, modelizado y resuelto numéricamente un proceso de congelación a altas presiones, en particular por congelación por cambio brusco de presión, lo que en inglés se conoce por High-Pressure Shift Freezing (HPSF). La modelización de un problema de solidificación por sí sólo no es una tarea fácil, lo que queda demostrado por la gran cantidad de estudios realizados sobre este tema. Sin embargo, la congelación por altas presiones, no ha sido tan estudiada y por ello en este capítulo presentamos un modelo generalizado de entalpía para un proceso de congelación por cambio brusco de presión. El modelo se puede utilizar para alimentos sólidos grandes y pequeños. Se valida el modelo con varios experimentos numéricos, obteniendo buenos resultados cuando se compara con datos experimentales, sin necesidad de utilizar parámetros de ajuste.

Finalmente, el capítulo 7 se diferencia de los demás porque no resolvemos un modelo para encontrar la distribución de temperaturas dentro de un alimento sometido a un tratamiento de altas presiones. En cambio, lo que hacemos es presentar un modelo que estudia el crecimiento y la maduración de los cristales de hielo dentro de un alimento congelado mediante los procesos HPSF estudiados en el capítulo 6.

Aportaciones fundamentales de la tesis

Los resultados novedosos de esta tesis pueden encontrarse en los capítulos 4, 5, 6 y 7. Como ya hemos señalado antes, los capítulos 2 y 3 son de motivación y presentación de un modelo general, respectivamente.

Los modelos presentados en el capítulo 4 son válidos para alimentos sólidos grandes, para los que es suficiente un modelo de transferencia de calor por conducción. Se ha estudiado el modelo con dos tipos distintos de condiciones de contorno. Mediante técnicas de análisis dimensional, hemos obtenido los términos dominantes del modelo, y en algunos casos hemos podido simplificar las ecuaciones (dimensionalmente), obteniendo una buena aproximación. Los modelos presentados en este capítulo son más sencillos que otros que se pueden encontrar en la literatura, pero tienen las características cualitativas correctas, y por tanto serían de gran importancia a la hora de diseñar equipos industriales y optimizar procesos. Además, con las soluciones que proponemos en el capítulo 4, no se necesita disponer de un solver de elementos finitos para simular los procesos. De hecho, debido a la simplificación de los sistemas, en algunos casos se pueden encontrar soluciones analíticas aparte de numéricas. Hemos hecho un análisis exhaustivo del modelo en dos dimensiones, dando una solución exacta, y proponiendo varias simplificaciones tanto en dos dimensiones como en una. Se muestra que para el caso de una máquina vertical larga y estrecha, la distribución de temperaturas bidimensional se puede aproximar adecuadamente con un modelo unidimensional, en casi todos los puntos del alimento salvo los muy cercanos a las tapas superior e inferior. Se han acoplado las soluciones del modelo de transferencia de calor en una dimensión con un modelo de inactivación enzimática, y los resultados obtenidos son muy parecidos a los que se obtienen usando la distribución de temperaturas bidimensional. Hemos visto, por tanto, que con la reducción a una dimensión se obtienen resultados muy razonables, y tiene ventajas computacionales evidentes, ya que simulaciones más rápidas pueden llevarse a cabo. Esto sería interesante, por ejemplo, para algoritmos de optimización, donde las ecuaciones del estado tiene que resolverse muchas veces. Los modelos en una dimensión también serían más manejables para calcular, mediante problemas inversos, las propiedades termofísicas en función de la presión, lo cual es de gran relevancia para los ingenieros de alimentos. Desde un punto de vista experimental, estos resultados también pueden usarse para determinar dónde deberían ir colocados los termopares dentro del alimento para medir de manera correcta y eficaz la temperatura dentro del alimento.

En el capítulo 5 se consideran alimentos líquidos, para los que es necesario resolver numéricamente las ecuaciones de Navier–Stokes. Muchos estudios se han realizado en este campo para determinar la distribución de temperatura y flujo, pero por lo que sabemos, todos los modelos publicados hasta la fecha son para máquinas de alta presión colocadas en vertical. Esto se debe, como se señala en [63], a que tradicionalmente los equipos de alta presión han sido diseñados en vertical, como por ejemplo el de la Figura 3.1 del capítulo 3. Sin embargo, las tendencias están cambiando, y hoy en día la gran mayoría de los equipos industriales son horizontales, como por ejemplo el de la Figura 5.1 del capítulo 5. Debido a este incremento de máquinas horizontales, pero en cambio a la falta de investigación desarrollada en este tema, consideramos que sería interesante hacer un primer modelo para ello. La mayoría de los datos experimentales disponibles son de experimentos llevados a cabo en máquinas verticales, y además no disponemos de los recursos experimentales necesarios para montar una máquina piloto horizontal, por lo que diseñar un modelo horizontal desde cero no era viable. En cambio lo que hemos desarrollado es un modelo horizontal a partir de uno vertical, que ya había sido validado. Como el modelo en horizontal no puede reducirse a un modelo bidimensional, lo que sí podía hacerse en el caso vertical por simetría axial, hemos resuelto los dos modelos (vertical y horizontal) en tres dimensiones. De este modo, podemos mostrar las diferencias entre los modelos, resaltando la necesidad de desarrollar modelos horizontales, que serían de gran ayuda para la industria. Es evidente que aún con exactamente las mismas condiciones de procesado, los modelos verticales y horizontales van a ser distintos debido al comportamiento del flujo. Cuando se estudian alimentos líquidos sabemos que además este flujo repercute sobre la distribución de temperaturas de manera considerable. Después de llevar a cabo los experimentos numéricos, hemos probado que la distribución de temperaturas y uniformidad es muy distinta para las dos geometrías, debido principalmente al distinto comportamiento del flujo. Las temperaturas del modelo vertical cambian a lo largo de la altura, mientras que las del modelo horizontal lo hacen radialmente, y por ello para una máquina larga y estrecha, en general el modelo horizontal tiene resultados más uniformes.

Un proceso de congelación por cambio brusco de presión, como el que se describe en el capítulo 6, es en el que el cambio de fase ocurre debido a un cambio de presión que provoca condiciones metaestables y una producción instantánea de hielo. En estos procesos tiene lugar un subenfriamiento en toda la muestra, lo cual implica que la nucleación ocurre de manera homogénea por toda la muestra, dando lugar a cristales pequeños y redondeados distribuidos uniformemente. Debido a que este método es ventajoso comparado con métodos de congelación más tradicionales, se han hecho bastantes estudios sobre el efecto que tiene la alta presión sobre la calidad final del alimento congelado, pero también sobre la evolución de temperaturas dentro de la muestra durante el proceso. Conocer la distribución de temperaturas, como ya hemos visto, es importante para cualquier tipo de proceso a altas presiones, y por supuesto también para uno de congelación. En el capítulo 6 introducimos un modelo nuevo basado en la conservación de la entalpía (que suponemos dependiente de la presión) y en fracciones de volumen de alimento congelado y sin congelar. Los modelos que presentamos son bidimensionales (muchos de los modelos publicados en este área son unidimensionales), y son válidos para alimentos sólidos grandes o pequeños. Para el caso pequeño nuestro modelo incluye los efectos de la convección en el líquido presurizante (lo cual es también novedoso comparado con los resultados publicados). Los resultados numéricos encajan muy bien con los experimentales, y nos gustaría destacar que no se han utilizado parámetros de ajuste.

En el capítulo 7 se ha desarrollado un modelo que estudia el crecimiento y la maduración de los cristales de hielo dentro de un alimento congelado, válido tanto para alimentos congelados a presión atmosférica o a alta presión. Para que esto sea posible, hay que suponer que inicialmente las partículas de hielo tienen la misma forma (esférica), y están homogéneamente distribuidas en toda la muestra (como ocurre con los procesos de congelación por cambio brusco de presión). De esta forma podremos comparar, pasado un determinado tiempo, si hay diferencias en el producto final, entre un alimento congelado de manera tradicional y otro congelado usando altas presiones. Debido a que disponíamos de datos experimentales para una solución de sal en agua, comenzamos modelizando un sistema muy simple compuesto por agua salada. Para ello se desarrolla un modelo que estudia el crecimiento y la maduración de los cristales de hielo basándonos en la teoría de "Ostwald ripening". El modelo puede predecir la evolución temporal del radio de los cristales, así como la distribución por tamaño de éstos. Para validar el modelo usamos los datos experimentales que tenemos de agua salada, y también probamos con otros datos de la literatura en los que el alimento considerado es helado. Los resultados muestran que, para ambos experimentos, el modelo predice de manera correcta la evolución temporal del radio, y la distribución de tamaño de cristales de hielo, en caso de que los datos iniciales sean contínuos.

Conclusiones

En esta memoria se han descrito, modelizado y analizado varios problemas relacionados con el tratamiento de alimentos bajo altas presiones. Hay un amplio rango de problemas que se pueden estudiar relacionados con este tema, que depende de factores como el tipo de alimento, el tamaño y diseño de la máquina de altas presiones, o los efectos deseados del proceso. En particular, en esta memoria nos hemos centrado en problemas para alimentos grandes y pequeños, sólidos y líquidos, y máquinas colocadas vertical y horizontalmente. También se han estudiado procesos de congelación por altas presiones y procesos de crecimiento y maduración de cristales de hielo dentro de un alimento congelado.

Creemos que se ha cubierto un amplio abanico de problemas relacionados con la Industria Alimentaria, usando para ello una gran variedad de técnicas matemáticas. Aún así, todavía hay mucho trabajo por hacer en esta área. De hecho, el trabajo desarrollado en esta memoria podría extenderse en un futuro. Por ejemplo, en los capítulos 4, 5 y 6, los modelos podrían ampliarse para que fuesen válidos para cualquier tipo de alimentos (grande, pequeño, sólido, líquido), y la distribución de temperaturas resultante podrían acoplarse con modelos de inactivación enzimática o bacteriana, como los que se presentan en el capítulo 2, y como se ha hecho en el capítulo 4. Otras extensiones serían, por ejemplo, incluir la dependencia de la temperatura y la presión en los parámetros termofísicos de los materiales en todos los modelos presentado. Aparte, en el capítulo 6, efectos de anisotropía podrían incluirse en la región congelada del alimento y se podría extender el modelo de dos a tres dimensiones. Por otro lado en el capítulo 7 se podría mejorar el modelo incluyendo más términos, haciendo que se pueda usar para sistemas más complejos. Estas ideas son sólo algunas de las posibles extensiones del trabajo presentado en esta memoria.

Bibliography

[1] *Encyclopedia Britannica*. 15th edition, 1989.

[2] *IUPAC: Compendium of Chemical Terminology*. 2nd edition, 1997.

[3] *Encyclopedia McGraw-Hill*. 9th edition, 2002.

[4] E. Alizadeh, N. Chapleau, M. de Lamballeire, and A. Le-Bail. Impact of freezing process on salt diffusivity of seafood: Application to salmon (salmo salar) using conventional and pressure shift freezing. *Food Bioprocess Technol.*, 2: 257–262, 2009.

[5] R. Aris. *Vectors, Tensors, and the Basic Equations of Fluid Mechanics*. Dover Publications, Inc. New York, 1989.

[6] B. R. Becker and B. A. Fricke. Food thermophysical property models. *Int. Comm. Heat Mass Transfer*, 26(5): 627–636, 1999.

[7] R. E. Bird, W. E. Stewart, and E. N. Lightfoot. *Transport Phenomena*. Wiley, 1960.

[8] B. W. Bridgman. Water, in the liquid and five solid forms, under pressure. *Proc. Am. Acad. Arts Sci. XLVIII*, 13: 439–558, 1912.

[9] V. M. Burlakov and L. Kantorovich. Ostwald ripening of binary alloy particles. *The Journal of Chemical Physics*, 134, 2011.

[10] B. Cabane and R. Vuilleumier. The physics of liquid water. *C. R. Geoscience*, 337: 159–171, 2005.

[11] J. C. Cheftel. Effects of high hydrostatic pressure on food constituents: an overview. *In C. Balny, R. Hayashi, K. Heremans, P. Masson, eds. High Pressure and Biotechnology*, 224: 195–209, 1992.

[12] J. C. Cheftel. Review: high-pressure, microbial inactivation and food preservation. *Food Sci. Tech. Int.*, 1(2-3): 75–90, 1995.

[13] J. C. Cheftel and J. Culioli. Effects of high pressure on meat: a review. *Meat Science*, 46(3): 211–236, 1997.

[14] A. C. Cleland and R. L. Earle. Assessment of freezing time prediction methods. *J. Food Sci.*, 49: 1034–1042, 1995.

[15] G. Comini, S. Giudice, R. W. Lewis, and 0. C. Zienkiewicz. Finite element solution of non-linear heat conduction problems with special reference to phase change. *Int. J. Num. Meth. Engin.*, 8: 613–624, 1974.

[16] G. Comini, S. Giudice, and O. Saro. A conservative algorithm for multidimensional conduction phase change. *Int. J. Num. Meth. Engin.*, 30: 697–709, 1990.

[17] J. Crank. *Free and Moving Boundary Problems*. Oxford Science Publications. New York, 1987.

[18] A. Delgado, C. Rauh, W. Kowalczyk, and A. Baars. Review of modelling and simulation of high pressure treatment of materials of biological origin. *Trends in Food Science and Technology*, 19(6): 329–336, 2008.

[19] S. Denys, A. M. Van Loey, and M. E. Hendrickx. A modelling approach for evaluating process uniformity

during batch high hydrostatic pressure processing: Combination of a numerical heat transfer model and enzyme inactivation kinetics. *Innovative Food Science and Emerging Technologies*, 1(1): 5–19, 2000.

[20] S. Denys, A. M. Van Loey, M. E. Hendrickx, and P. Tobback. Modelling heat transfer during high-pressure freezing and thawing. *Biotechol. Prog.*, 13: 413–423, 1997.

[21] S. Denys, L. R. Ludikhuyze, A. M. Van Loey, and M. E. Hendrickx. Modelling conductive heat transfer and process uniformity during batch high-pressure processing of foods. *Biotechnol. Prog.*, 16: 92–101, 2000.

[22] C. Dogan and O. Erkmen. High pressure inactivation kinetics of listeria monocytogenes inactivation in broth, milk, and peach and orange juices. *J. Food Engng.*, 62: 47–52, 2004.

[23] D .P. Donhowe, R. W. Hartel, and Jr. R. L. Bradley. Determination of ice crystal size distribution in frozen desserts. *J. Dairy Sci.*, 74: 3334–3344, 1991.

[24] J. Irudayaraj (Editor). *Food Processing Operations Modeling: Design and Analysis*. Marcel Dekker Inc. New York Basel, 2002. ISBN 0824704886.

[25] R. Van Eldik and J. Jonas. *High-Pressure Chemistry and Biochemistry*. Springer, 1987. ISBN: 9027724571, 9789027724571.

[26] J. R. Elliott and C. T. Lira. *Introductory Chemical Engineering Thermodynamics*. Prentice Hall International Series in the Physical and Chemical Engineering Sciences, 2005.

[27] O. Erkmen and C. Dogan. Kinetic analysis of escherichia coli inactivation by high hydrostatic pressure in broth and foods. *Food Microbiol.*, 21: 181–185, 2004.

[28] D. F. Farkas and D. G. Hoover. High pressure processing. *Journal of Food Science Supplement: Kinetics of microbial inactivation for alternative food processing technologies*, pages 47–64, 2001.

[29] P. P. Fernández, L. Otero, B. Guignon, and P. D. Sanz. High-pressure shift freezing versus high-pressure assisted freezing: Effects on the microstructure of a food model. *Food Hydrocolloids*, 20: 510–522, 2006.

[30] P. P. Fernández, L. Otero, M. M. Martino, A. D. Molina-García, and P. D. Sanz. High-pressure shift freezing: recrystallization during storage. *European Food Research and Technology*, 227(5): 1367–1377, 2008.

[31] U. S. Food, Drug Administration, Center for Food Safety, and Applied Nutrition. Kinetics of microbial inactivation for alternative food processing technologies, 2000. `http://www.fda.gov/Food/ScienceResearch/ResearchAreas/SafePracticesforFoodProcesses/`.

[32] A. G. A. Ghani and M. M. Farid. Numerical simulation of solid-liquid food mixture in a high pressure processing unit using computational fluid dynamics. *Journal of Food Engineering*, 80(4): 13031–1042, 2007.

[33] Dr. S. Gola. *Microbiological results of tests ordered by Esteban Espuña, S.A, to la Stazione Sperimentale per l'industria delle conserve alimentari in Parma*, 5 Marzo 2004.

[34] B. Guignon, C. Aparicio, and P. D. Sanz. Volumetric properties of pressure-transmitting fluids up to 350mpa: Water, ethanol, ehtylene gylcol, propylene glycol, castor oil, silicon oil, and some of their binary mixture. *J. Chem. Eng. Data*, 55: 3017–3023, 2010.

[35] B. Guignon, A. M. Ramos, J. A. Infante, J. M. Diaz, and P. D. Sanz. Determining thermal parameters in the cooling of a small-scale high-pressure freezing vessel. *Int. J. Refrigeration*, 29: 1152–1159, 2006.

[36] C. Hartmann. Numerical simulation of thermodynamic and fluiddynamic processes during the high pressure treatment of fluid food systems. *Innovative Food Science and Emerging Technologies*, 3(1): 11–18, 2002.

[37] C. Hartmann and A. Delgado. Numerical simulation of convective and diffusive transport effects on a high - pressure - induced inactivation process. *Biotechnology and Bioengineering*, 79(1): 94–104, 2002.

[38] C. Hartmann and A. Delgado. Numerical simulation of thermal and fluiddynamical transport effects on a high pressure induced inactivation. *High Pressure Research*, 23: 67–70, 2003.

[39] C. Hartmann, A. Delgado, and J. Szymczyk. Convective and diffusive transport effects in a high pressure induced inactivation process of packed food. *Journal of Food Engineering*, 59(1): 33–44, 2003.

[40] C. Hartmann, J-P. Schuhholz, P. Kitsbun, N. Chapleau, A. Le Bail, and A. Delgado. Experimental and numerical analysis of the thermofluiddynamics in a high-pressure autoclave. *Innovative Food Science and Emerging Technologies*, 5: 399–411, 2004.

[41] R. Hayashi. Utilization of pressure in addition to temperature in food science and technology. *In High pressure and biotechnology; Balny, C., Hayashi, R., Heremans, K., Masson, P., Eds.; Colloque INSERM:*, 224: 185–193, 1992.

[42] Hiperbaric. Hiperbaric: High pressure processing, 2012. `http://www.hiperbaric.com/`.

[43] A. Ibarz-Ribas and G. V. Barbosa-Cánovas. *Operaciones unitarias en la ingeniería de alimentos*. Mundi-Prensa Libros, 2005. ISBN 8484761630, 9788484761631.

[44] I. Indrawati, L. R. Ludikhuyze, A. M. van Loey, and M. E. Hendrickx. Lipoxygenase inactivation in green beans (phaseolus vulgaris l.) due to high pressure treatment at subzero and elevated temperatures. *J. Agric. Food Chem.*, 48: 1850–1859, 2000.

[45] J. A. Infante. *Análisis numérico de modelos matemáticos y problemas inversos en tecnología de alimentos*. PhD thesis, Universidad Complutense de Madrid, Nov. 2009.

[46] J. A. Infante, B. Ivorra, A. M. Ramos, and J. M. Rey. On the modelling and simulation of high pressure processes and inactivation of enzymes in food engineering. *Math. Models Methods Appl. Sci.*, 19(12): 2203–2229, 2009.

[47] G. Job and F. Herrmann. Chemical potential–a quantity in search of recognition. *European Journal of Physics*, 27: 353–371, 2006.

[48] P. Juliano, K. Knoerzer, P. Fryer, and C. Versteeg. *C. Botulinum* inactivation kinetics implemented in a computational model of a high pressure sterilization process. *Biotechnology Process*, 25(1): 163–175, 2008.

[49] B. Klotz, D. Leo Pyle, and B. M. Mackey. New mathematical modeling approach for predicting microbial inactivation by high hydrostatic pressure. *Applied and Enviromental Microb.*, 73(8): 2468–2478, 2007.

[50] K. Knoerzer, R. Buckow, P. Juliano, B. Chapman, and C. Versteeg. Carrier optimisation in a pilot-scale high pressure sterilisation plant – an iterative cfd approach. *Journal of Food Engineering*, 97(2): 199–207, 2010.

[51] K. Knoerzer and B. Chapman. Effect of material properties and processing conditions on the prediction accuracy of a cfd model for simulating high pressure thermal (hpt) processing. *Journal of Food Engineering*, 104: 404–413, 2011.

[52] K. Knoerzer, P. Juliano, S. Gladman, C. Versteeg, and P. J. Fryer. A computational model for temperature and sterility distributions in a pilot-scale high-pressure high-temperature process. *AIChE Journal*, 53(11): 2996–3010, 2007.

[53] K. Knoerzer, P. Juliano, P. Roupas, and Editors C. Versteeg. *Innovative Food Processing Technologies: Advances in Multiphysics Simulation*. Wiley-Blackwell and IFT Press, 2011.

[54] W. Kowalczyk and A. Delgado. Dimensional analysis of thermo-fluid-dynamics of high hydrostatic pressure processes with phase transition. *Int. J. Heat Mass Transf.*, 50: 3007–3018, 2007.

[55] W. Kowalczyk and A. Delgado. On convection phenomena during high pressure treatment of liquid media. *High Pressure Research*, 27(1): 85–92, 2007.

[56] W. Kowalczyk, Chr. Hartmann, and A. Delgado. Modelling and numerical simulation of convection driven high pressure induced phase changes. *Int. J. Heat Mass Transf.*, 47: 1079–1089, 2004.

[57] A. Kupper, E. G. Hauptmann, and M. Iqbal. Combined free and forced convection in a horizontal tube under uniform heat flux. *Solar Energy*, 12: 439–446, 1969.

[58] L. R. Ludikhuyze, I. Van den Broeck, C. A. Weemaes, and M. E. Hendrickx. Kinetic parameters for pressure-temperature inactivation of bacillus subtilis α-amylase under dynamic conditions. *Biotechnol. Prog.*, 13: 617–623, 1997.

[59] L. R. Ludikhuyze, I. Van den Broeck, C. A. Weemaes, C. Herremans, J. F. Van Impe, M. E. Hendrickx, and P. Tobback. Kinetics for isobaric-isothermal inactivation of bacillus subtilis α-amylase. *Biotechnol. Prog.*, 13: 523–538, 1997.

[60] X. Luo and P. V. Schevchenko. A short tale of long tail integration. *Numerical Algorithms*, 56: 577, 2011.

[61] B. Ly-Nguyen, A. M. Loey, C. Smout, S. E. Zcan, D. Fachin, I. Verlent, S. Vu Truong, T. Duvetter, and M. E. Hendrickx. Mild-heat and high-pressure inactivation of carrot pectin methyl-esterase: A kinetic study. *J. Food Sci.*, 68: 1377–1383, 2003.

[62] K. Miyagawa and K. Suzuki. Studies on taka-amylase a under high pressure: Some kinetic aspects of pressure inactivation of taka-amylase a. *Arch. Biochem. Biophys.*, 105: 297–302, 1964.

[63] H. Mujica-Paz, A. Valdez-Fragoso, C. Tonello-Samson, J. Welti-Chanes, and J. A. Torres. High-pressure processing technologies for the pasteurization and sterilization of foods. *Food Bioprocess Technol.*, 4: 969–985, 2011.

[64] T. Norton, A. Delgado, E. Hogan, P. Grace, and Da-Wen Sun. Simulation of high pressure freezing processes by enthalpy method. *J. Food Eng.*, 91: 260–268, 2009.

[65] D. R. Oliver. The effect of natural convection on viscous-flow heat transfer in horizontal tubes. *Chemical Engineering Science*, 17: 335–350, 1962.

[66] L. Otero, M. Martino, N. Zaritzky, M. Solas, and P. D. Sanz. Preservation of microstructure in peach and mango during high-pressure-shift freezing. *J. Food Sci.*, 65: 466–470, 2000.

[67] L. Otero, A. D. Molina-Garcia, A. M. Ramos, and P. D. Sanz. A model for real thermal control in high-pressure treatment of foods. *Notes. Biotechnol. Prog.*, 18: 904–908, 2002.

[68] L. Otero, A. Ousegui, B. Guignon, A. Le Bail, and P. D. Sanz. Evaluation of the thermophysical properties of tylose gel under pressure in the phase change domain. *Food Hydrocolloids*, 20: 449–460, 2006.

[69] L. Otero, A. M. Ramos, C. de Elvira, and P. D. Sanz. A model to design high pressure processes towards a uniform temperature distribution. *J. Food Engng*, 78: 1463–1470, 2007.

[70] L. Otero and P. D. Sanz. High-pressure shift freezing part 1: Amount of ice instantaneously formed in the process. *Biotechnol. Prog.*, 16: 1030–1036, 2000.

[71] L. Otero and P. D. Sanz. Modelling heat transfer in high pressure food processing: a review. *Innovative Food Sci. Emerging Tech.*, 4: 121–134, 2003.

[72] L. Otero and P. D. Sanz. High-pressure-shift freezing: Main factors implied in the phase transition time. *J. Food Engng*, 72: 354–363, 2006.

[73] M. Necati Özisik. *Boundary Value Problems of Heat Conduction.* Dover Publications Inc. New York, 1968.

[74] Q. Tuan Pham. Modelling heat and mass transfer in frozen foods: a review. *Int. J. Refrigeration*, 29: 876–888, 2006.

[75] M. S. Rahman, G. Al-Saidi, N. Guizani, and A. Abdullah. Development of state diagram of bovine gel by measuring thermal characteristics using differential scanning calorimetry (dsc) and cooling curve method. *Thermochim. Acta*, 509: 111–119, 2010.

[76] A. M. Ramos and N. A. S. Smith. Efecto de las altas presiones sobre los microorganismos en relación con la conservación de alimentos. Caso de la *Listeria monocytogenes* en jamón crudo picado. Technical report, Universidad Complutense de Madrid, 2009.

[77] C. Rauh, A. Baars, and A. Delgado. Uniformity of enzyme inactivation in a short-time high-pressure process. *J. Food Engng*, 91: 154–163, 2009.

[78] P. D. Sanz and L. Otero. High-pressure shift freezing part 2: Modelling of freezing times for a finite cylindrical model. *Biotechnol. Prog.*, 16: 1037–1043, 2000.

[79] O. Schlüter, G. Urrutia Benet, V. Heinz, and D. Knorr. Metastable states of water and ice during pressure-supported freezing of potato tissue. *Biotechnol. Prog.*, 20: 799–810, 2004.

[80] H. R. Schwartzberg. Effective heat capacities for the freezing and thawing of food. *J. Food Sci.*, 41: 152–156, 1976.

[81] R. K. Simpson and A. Gilmour. The resistance of *Listeria monocytogenes* to high hydrostatic pressure in foods. *Food Microbiol.*, 14: 567–573, 1997.

[82] J. P. P. M. Smelt. Recent advances in the microbiology of high pressure processing. *Trends Food Sci. Tech.*, 9: 152–158, 1998.

[83] N. A. S. Smith, V. Burlakov, and A. M. Ramos. Publication in preparation.

[84] N. A. S. Smith, K. Knoerzer, and A. M. Ramos. Publication in preparation.

[85] N. A. S. Smith, S. L. Mitchell, and A. M. Ramos. Analysis and simplification of a mathematical model for high-pressure food processes, 2012. Submitted.

[86] N. A. S. Smith, S. S. L. Peppin, and A. M. Ramos. Generalized enthalpy model of a high-pressure shift freezing process. *Proc. Roy. Soc. A*, 468(2145): 2744–2766, 2012.

[87] K. Suzuki and K. Kitamura. Inactivation of enzyme under high pressure: Studies on the kinetics of inactivation of α–amylase of bacillus subtilis under high pressure. *J. Biochem.*, 54: 214–219, 1963.

[88] C. R. Swaminathan and V. R. Voller. A general enthalpy method for modeling solidification processes. *Metallurgical Transactions B*, 23(5): 651–664, 1992.

[89] J. A. Torres and G. Velazquez. Commercial opportunities and research challenges in the high pressure processing of foods. *J. Food Eng.*, 67: 95–112, 2005.

[90] G. Urrutia, O. Schlüter, and D. Knorr. High pressure low temperature processing. suggested definitions and terminology. *Innovative Food Science and Emerging Technologies*, 5: 413–427, 2004.

[91] V. R. Voller, C. R. Swaminathan, and B. G. Thomas. Fixed grid techniques for phase change problems: A review. *Int. J. Numer. Methods Eng.*, 30: 875–898, 1990.

[92] R. Xiong, G. Xie, A. E. Edmondson, and M. A. Sheard. A mathematical model for bacterial inactivation. *J. Food Microbiol.*, 46: 45–55, 1999.